Performance of the ALICE muon spectrometer. Weak boson production and measurement in heavy-ion collisions at LHC.

Zaida Conesa del Valle

Zaida Conesa del Valle. Performance of the ALICE muon spectrometer. Weak boson production and measurement in heavy-ion collisions at LHC.. Nuclear Theory [nucl-th]. Université de Nantes; Universitat Autónoma de Barcelona, 2007. English. NNT : . tel-00198703

HAL Id: tel-00198703
https://theses.hal.science/tel-00198703v1
Submitted on 17 Dec 2007

UNIVERSITÉ DE NANTES
FACULTÉ DES SCIENCES ET TECHNIQUES

ÉCOLE DOCTORALE
SCIENCES ET TECHNOLOGIES DE L'INFORMATION ET DES MATÉRIAUX

Année : 2007

N° attribué par la bibliothèque

Performance of the ALICE muon spectrometer. Weak boson production and measurement in heavy-ion collisions at LHC.

THÈSE DE DOCTORAT
Discipline : Physique Nuclèaire
Spécialité : Physique des Ions Lourds

Présentée et soutenue publiquement par

Zaida CONESA DEL VALLE

Le 12 juillet 2007, devant le jury ci-dessous

Président	K. WERNER, *Professeur, Université de Nantes, SUBATECH, Nantes*
Rapporteurs	E. VERCELLIN, *Professeur, Universita degli Studi di Torino, Torino*
	D. G.-D'ENTERRIA ADAN, *Chargé de recherche, CERN, Genève*
Examinateurs	E. AUGE, *Professeur, Université Paris-Sud XI, LAL, Orsay*
	H. BOREL, *Ingénieur de recherche, CEA, Saclay*

Directeurs de thèse : G. MARTINEZ GARCIA, *Chargé de recherche, CNRS, SUBATECH Nantes*
F. FERNANDEZ MORENO, *Professeur, Universitat Autònoma de Barcelona*

N° ED 366-312

UNIVERSITÉ DE NANTES

Performance du spectromètre à muons d'ALICE. Production et mesure des bosons faibles dans des collisions d'ions lourds auprès du LHC.

Performance of the ALICE muon spectrometer. Weak boson production and measurement in heavy-ion collisions at LHC.

Zaida CONESA DEL VALLE

SUBATECH, Nantes (France), 2007

Universitat Autònoma de Barcelona

Performance of the ALICE muon spectrometer. Weak boson production and measurement in heavy-ion collisions at LHC.

TESIS DOCTORAL

Zaida Conesa del Valle

Directors de tesis:

Ginés Martínez García, *SUBATECH Nantes*

Francisco Fernández Moreno, *Universitat Autònoma de Barcelona*

Grup de Física de les Radiacions, Bellaterra (Spain), 2007

Contents

Acknowledgments

You are rewarding a teacher poorly if you remain always a pupil.

F. Nietzsche

There are lots of people I would like to thank for a huge variety of reasons. Though it is an almost impossible task, I am going to try anyway, and if your name is not listed, rest assured that my gratitude is not less than for those listed below.
I would like to express my gratitude to J. Martino, B. Erazmus and Ginés Martínez García from SUBATECH and Francisco Fernández Moreno from the Universitat Autònoma de Barcelona for giving me the opportunity to work with their groups.
I am specially thankful to my mentor, Ginés Martínez García, for his support, guide and availability. He has always found the time and patience to discuss and to solve my doubts. His knowledge and personal qualities have been of great influence to me both professionally and personally. I am also in debt with the members of the Dimuon group at SUBATECH: to Christian Finck and to Laurent Aphecetche for their support and innumerable advices, and to the latest recruitments, Guillaume Batigne, Philippe Pillot and Nicolas LeBris.
The last chapter of this work has been the fruitful result of the collaboration with Heng-Tong Ding, Andrea Dainese and Daicui Zhou, and partly the outcome of the teachings of Stéphane Peigné. I wish to thank them all, and I look forward to further collaborate with them.
I am grateful to D. d'Enterria and E. Vercellin for accepting to be my *rapporteurs*, for their time and attention while reading this document, and for their remarks and all the discussions which have improved this work. I would also like to thank E. Auge, H. Borel, and K. Werner for being members of my thesis committee.
During the preparation of my thesis I have had the pleasure to work within the ALICE collaboration. The interaction and discussions with their members have been extremely encouraging and formative for me. In particular, I thank to F. Antinori for his many suggestions and stimulating discussions, and to P. Crochet for his availability, enthusiasm and help with this manuscript and all over the last three years.

I have met many people, both in Nantes and in Barcelona, who have accompanied me either physically or electronically, and are responsible of the pleasant working and enjoying

environment. The early support and fondness of Eva A., Eva D., Roger, Andreu, Arnau and Raul from Barcelona encouraged me to follow through this way. The friendship of Jêrome B., Julien and Anneli from Nantes, and of Gustavo, Vladimir, Olivier, Jonathan and all the Ph.D. students from SUBATECH for the company and support they offered me, and for the French culture they have taught me. No doubt that the mini-swimming-dimuon-group has contributed noticeably to create this pleasant environment. I could not forget my electronic companions Rocío and Robert, who are always present and have always comforted me with their affection, support, sincerity, advices and jokes. Last, I wish to thank my family for the support, tenderness and encouragement they bring me, no matter where I am.

Zaida Conesa
Nantes, August 21, 2007

Abstract

> *Science is written in that great book which ever lies before our eyes –I mean the Universe– but we cannot understand it if we do not learn the language and grasp the symbols in which it is written. This book is written in the mathematical language, and the symbols are triangles, circles, and other geometrical figures without whose help it is impossible to comprehend a single word of it, without which one wanders in vain through a dark labyrinth.*
>
> G. Galilei

Nucleus-nucleus collisions are the unique tool available to investigate the QCD matter phase diagram in the laboratory. A lot of work has been devoted to explore it in different domains in the last 3 decades, and the forthcoming LHC collider will contribute to such research increasing the collision center-of-mass energy by a factor 30 and the energy densities by a factor 1-10 with respect to the RHIC collider [C$^+$04, A$^+$06]. Only a comprehensive analysis of a wide spectrum of experimental observables can help to fully characterize the prospected matter. In particular, valuable information is expected from charm and beauty production, the situation from SPS and RHIC charmonia data being puzzling [GdC07, Lei07, A$^+$00a, Sco07], and the $c\bar{c}$ ($b\bar{b}$) yields per central nucleon-nucleon collision being increased from 10 (0.1) to 110 (5) from RHIC to LHC [C$^+$04, MG07]. Whether quarkonia will thermalize, will develop collective motion, will be further suppressed or regenerated are still open questions that LHC data might resolve. In addition, the amount of energy available in the center-of-mass will enable weak bosons production and measurement for the first time in heavy-ion collisions. In chapters 1 & 2 we succinctly expose this canvas, the theoretical basis and the previous experimental results are outlined emphasizing the interest of heavy quarks, quarkonia and weak bosons.

In the first part, the ALICE detector which is a heavy-ion dedicated experiment settled at the LHC [C$^+$04] will be presented (chapter 3). Among other subdetectors, it disposes of a forward muon spectrometer that will allow to investigate the muon related probes (quarkonia, open beauty,...). This thesis work is devoted to exploit its performances to detect dimuons and high transverse momentum (p_T) muons in order to measure quarkonia, open-beauty

and weak bosons production. The apparatus abilities to measure dimuons (explore quarkonia) and high-p_T muons (investigate weak bosons) are discussed in chapter 4. There, factorization techniques are employed to unravel the different contributions to the efficiency; influences from the trigger algorithm, the reconstruction algorithm, the intrinsic chambers efficiency and the dead zones are identified and examined. This methodology promises to be useful to cross-check the goodness of the efficiency calculations with data.

In the second part, weak bosons production in p-p, p-Pb and Pb-Pb collisions at 14, 8.8 and 5.5 TeV respectively are presented (chapter 5) [CMAF06, CdV07]. Some particularities of weak bosons, and the procedures used to generate them with the PYTHIA event generator are exposed. Their yields in the muonic decay channel are obtained in the whole pseudorapidity range as well as within the ALICE muon spectrometer acceptance. Special attention is payed to W production and decay charge asymmetries, as they can be exploited to sign their production. In chapter 6 a compendium of the various sources contribution to the single muon spectra is presented. The reconstructed single muon distribution with the ALICE muon spectrometer for the different collision types are computed, and the expected statistics are estimated.

The last part addresses the utility of weak bosons measurements in nucleus-nucleus collisions (chapter 7). The influence of the medium produced in the collisions on heavy quark and weak bosons production and on the muons in their decay are discussed. Predictions of the single muon suppression in a hot and dense matter are obtained with the help of a gluon-radiation formalism [DDCdVZ07, CdVDD+07]. The nuclear modification factor, the central-to-peripheral ratio and the muon yield ratios are examined. Finally, some possibilities to investigate in-medium effects on Z boson decay particles are mentioned.

Part I

Introduction

Chapter 1

Studying the Quark Gluon Plasma in Heavy Ion Collisions

> *And first of all it seems desirable to find and explain a definition best fitting natural phenomena. For anyone may invent an arbitrary type of motion and discuss its properties...*
>
> G. Galilei

Abstract

We first introduce the theoretical basis behind the Quark Gluon Plasma (QGP) studies in heavy-ion collisions (HIC). We briefly summarize a selection of the experimental results collected so far and the main derived conclusions. All through this chapter we pay particular attention to heavy quark and quarkonia production as hard probes of the QGP formation; to the remaining open questions and to the theoretical predictions for LHC energies. Finally, in the next chapter, we will succinctly note the motivations that push us to investigate weak bosons production at LHC.

1.1 From the Standard Model to the Quark Gluon Plasma

1.1.1 Standard Model and Quantum ChromoDynamics

From the standard model point of view, matter is composed by elementary particles, the fermions[1] and the bosons[2]. The fermions can be classified in 3 families of quarks: (u, d), (c, s), (t, b) and their anti-quarks, and in 3 families of leptons: (ν_e, e), (ν_μ, μ), (ν_τ, τ) and their anti-leptons. The bosons are the mediators of the fundamental interactions; the photon (γ) governs the electromagnetic forces, the $W^\pm$ and Z^0 the weak forces, and the gluon (g) the strong forces. In nature the quarks are confined into hadrons; in quark–anti-quark states ($q\bar{q}$), the mesons, and three quark states (qqq), the baryons, by means of the strong interaction. Quantum ChromoDynamics (QCD) describes the strong interaction by postulating the existence of a strong charge, the color[3], that is associated to quarks and gluons and is responsible of the strong interaction. Two particularities of QCD are the confinement/asymptotic freedom and the chiral symmetry restoration/breaking.

---

[1] The fermions are particles with fractional spin.

[2] The bosons are particles with integer spin.

[3] QCD describes three possible color (charge) states, namely *red*, *blue* and *green*. Quarks have an associated color, anti-quarks an anti-color, and gluons the combination color–anti-color.

Confinement and asymptotic freedom

The intensity of the electromagnetic force is predicted by Quantum ElectroDynamics (QED) to be $\alpha_{em} \approx 1/137$. But as a consequence of vacuum polarization, in QED the coupling constant varies with the momentum transferred in the interaction (Q^2) as

$$\alpha_{QED}(Q^2) = \frac{\alpha_{em}}{1 - \frac{\alpha_{em}}{3\pi} \ln(\frac{Q^2}{m^2})} . \tag{1.1}$$

Thus its intensity augments for high Q, i.e. for short distances.
Similarly, QCD describes the strong interaction as governed by a strong coupling constant α_{QCD}, which is dependent on the momentum transferred in the interaction. In QCD vacuum polarization differs from the QED because besides the screening of quark–anti-quarks pairs there exists anti-screening of gluon pairs, which are color charged particles, whereas the photon is neutral. As a result, the intensity of the strong interaction diminishes at short distances (high energies) as can be observed in Fig. 1.1.

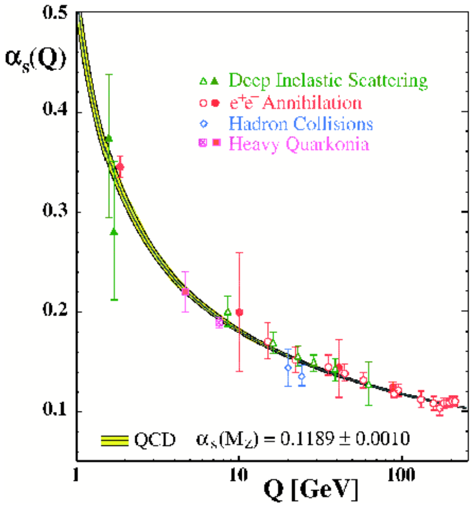

$$\alpha_{QCD}(Q^2) = \alpha_s(Q^2) = \frac{4\pi}{(11 - \frac{2}{3}n_f)\ln(\frac{Q^2}{\Lambda^2_{QCD}})} . \tag{1.2}$$

Figure 1.1: QCD coupling constant α_{QCD} [Bet07].

Therefore, for small values of Q^2, i.e. for small energies, the strong coupling has large values ($\alpha_{QCD} \gg 1$), which explains the magnitude of the strong force and the fact that quarks are confined in neutral color states, the baryons and the mesons. This is known as *color confinement*. On the contrary, for high energies the momentum transferred is large and α_{QCD} becomes small; the quarks behave as quasi-free particles, which is known as *asymptotic freedom* [GW73, Pol73]. Both ingredients are accounted for in the *bag model* which describes hadrons as spherical bags of radius R within which partons can move freely but are prevented to escape outside R by an inwards pressure due to the color confinement [Squ79].

Chiral symmetry restoration

The chiral symmetry refers to the symmetry of the left- and right-handed parts of the quarks. In absence of mass ($m_i \approx 0$), the QCD Lagrangian shows no interaction between left- and right-handed quarks. This symmetry is represented by $SU(3)_L \otimes SU(3)_R$ and is usually

characterized by the chiral condensate $\langle\bar{\psi}\psi\rangle = \langle\bar{\psi}_L\psi_R + \bar{\psi}_R\psi_L\rangle$. In the vacuum, the quarks mass is not null and the right-handed quarks interact with left-handed quarks, the chiral symmetry is spontaneously broken, and the $\langle\bar{\psi}\psi\rangle \neq 0$. But at high energies one expects a restoration of the chiral symmetry[4], $\langle\bar{\psi}\psi\rangle = 0$, so the quarks recover their almost-null mass of the QCD Lagrangian instead of their constituent mass, of the order of ~ 300 MeV [Han01]. Via the chiral symmetry breaking the QCD explains the existence of the 8 Goldstone bosons (π^0, π^+, π^-, K^0, K^+, K^-, $\overline{K}^0$, η_8) with small mass values.
Note that the restoration of a symmetry is a sufficient condition to predict a phase transition related to it.

QCD matter phase diagram

The QCD matter phase diagram as a function of the temperature T and the baryochemical potential μ. The baryochemical potential measures the system net baryonic number[5] (number of baryons minus anti-baryons). Fig 1.2 presents a scheme of the QCD phase diagram. Following the diagram, for high values of T the intensity of the strong force becomes weak; deconfinement sets in, the system degrees of freedom are the quarks and the gluons, which are no longer confined in hadrons, this is called the Quark Gluon Plasma (QGP) phase. Remark that deconfinement does not imply the absence of interaction, it only means to get rid of the requirement to form color neutral bound states [Sat06]. Nevertheless, if we reduce the system temperature the intensity of the strong force grows and QCD matter is formed by confined quarks and gluons; it can be interpreted as a hadron gas. As in the transition from a hadron gas to a deconfined medium the chiral symmetry is restored, this passage should occur via a phase transition. As a matter of fact, since $m_{u,d} \neq 0$ $\langle\bar{\psi}\psi\rangle$ does not strictly vanish but falls steeply in the transition region; thus the transition for high T and small μ is rather characterized as a *cross-over* region: matter suffers a rapid and continuous transition [Han01, Mar06].

Quarkonium binding potential

Since heavy quarks are massive, quarkonium[6] spectroscopy can be studied in non-relativistic quantum mechanics. The confining potential for a $Q\bar{Q}$ pair at a separation distance r can be modeled by [MS86, Sat06]

$$V_{Q\bar{Q}}(r,T) = \sigma(T)\,r - \frac{\alpha_{eff}}{r}\,, \tag{1.3}$$

where $\sigma \simeq 0.216$ GeV^2 is the string tension (for $T \approx 0$), and $\alpha_{eff} \simeq \pi/12$ accounts for the Coulombian-like interaction. At small distances (r small), the Coulombian-like interaction is predominant, whereas at large distances the attractive force of the confinement described by the string tension prevails. The latter increasing linearly with the distance, a big amount

---

[4] Remark that chiral symmetry restoration is predicted for light quarks (u, d and s), but not for heavier quarks (c, b or t), their mass term in the Lagrangian being more important.

[5] The baryonic number is a quantic number associated to quarks. Quarks have a baryonic number $\frac{1}{3}$, and anti-quarks $-\frac{1}{3}$, then baryons have baryonic number 1 and mesons 0.

[6] As quarkonium we refer to heavy quark bound states, that we denote as $Q\bar{Q}$.

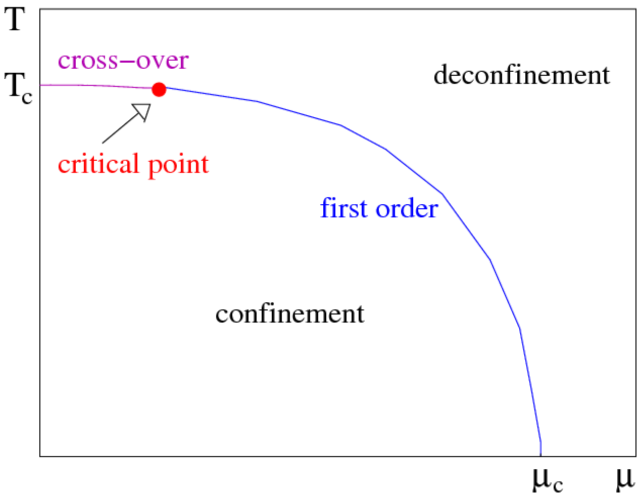

Figure 1.2: QCD matter phase diagram as a function of temperature T and baryochemical potential μ [Sat06].

of energy would be needed to separate the heavy quarks, they are tightly bound.
Above T_c quarks and gluons are no longer confined and the large color charge present in the medium screens the inter-quark potential, the so called *color screening*. The potential is then expected to be described by a Debye-screening form

$$V_{Q\bar{Q}}^{QGP}(r,T) = -\frac{\alpha_{eff}}{r}\, e^{-r/\Lambda_D(T)}\,, \tag{1.4}$$

$\Lambda_D(T)$ being the Debye screening length. $\Lambda_D(T)$ diminishing with the system temperature, the inter-quark potential is reduced accordingly, and when $\Lambda_D(T) < r_{hadron}$ the inter-quark force can not hold the quarks together, and they dissociate.

1.1.2 Lattice QCD calculations

Asymptotic freedom and chiral symmetry restoration

Lattice Quantum ChromoDynamics (lQCD) deals with the challenge to characterize the transition from hadronic matter to a QGP phase [KL94, Han01, Kar02, Kar07]. For this purpose QCD critical behavior has to be considered. On the one hand, the free quark energy is described by the average value of the Polyakov loop L as order parameter, and for $T > T_L$ suggests deconfinement. On the other hand, the chiral symmetry is characterized by the chiral condensate $\langle\bar{\psi}\psi\rangle$ and for $T < T_\chi$ implies chiral symmetry breaking, as we previously discussed. lQCD techniques allow to compute the values of those order parameters to investigate when take place those phenomena. Their results, as shown in Fig. 1.3 [KL94], indicate that both order parameters present a transition at the same temperature that is identified as critical temperature T_c.
lQCD calculations at finite temperature and null baryochemical potential suggest that this transition occur at $T_c \sim$ 170-192 MeV [Shu05, Kar07]. Fig. 1.5 presents the energy density as a function of the system temperature. At the transition point the energy density increases rapidly, which is due to the variation of the system degrees of freedom. From an illustrative point of view, we could recall the Steffan-Boltzman limit for an ideal gas and a QGP. For an

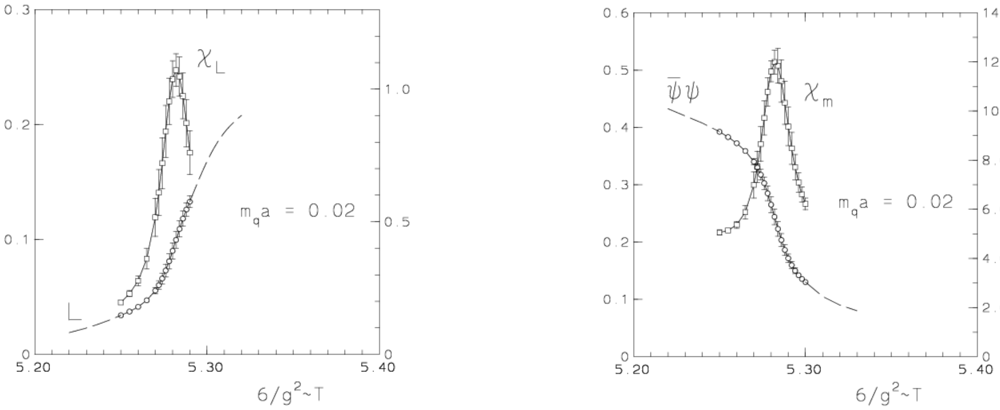

Figure 1.3: Polyakov loop (L) and chiral condensate ($\bar{\psi}\psi$) versus temperature together with their associated susceptibilities, defined by $\chi_L = \langle L \rangle^2 - \langle L^2 \rangle$ and analogously for $\chi_m = \chi_{\bar{\psi}\psi}$ [KL94].

ideal gas of massless pions with N degrees of freedom

$$\epsilon_\pi = N \cdot \frac{\pi^2}{30} T^4 = 3 \cdot \frac{\pi^2}{30} T^4 \simeq T^4 \,, \tag{1.5}$$

where $N = 3$ corresponds to the three possible pion charges. For an ideal QGP [Han01, Mar06] with three massless flavors[7]

$$\epsilon_{QGP} = N \cdot \frac{\pi^2}{30} T^4 = \{(3_f \cdot 2_s \cdot 2_q \cdot 3_c)\frac{7}{8} + (2_s \cdot 8_c)\} \frac{\pi^2}{30} T^4 = 47.5 \cdot \frac{\pi^2}{30} T^4 \simeq 15.6\, T^4 \,.$$

The energy density increases then by more than a factor ten near $T = T_c$. This limit is represented in Fig. 1.5 by the upper-right arrows indicated with ϵ_{SB}/T^4.
Finally, Fig. 1.4 shows lQCD results for the trace anomaly ($\Delta = (\epsilon - 3P)/T^4$) calculated in (2+1)-flavor [Kar07]. This parameter suggests that the 'interaction measure' does not vanish rapidly for $T > T_c$; it is still sizeable for $T \sim 2\, T_c$, indicating a deviation with respect to the ideal QGP (ideal ultra-relativistic gas), and thus a noticeable interaction in the QGP for such temperatures.

Quarkonium binding potential

lQCD can effectuate accurate estimates of the quarkonium binding potential as a function of the system temperature and the inter-quark separation r in the relativistic limit. Such calculations allow them to predict the dissociation temperatures T_d of the quarkonium states. Tab. 1.1 summarizes the results obtained by using the full internal energy (including the entropy term) [Kar05, Sat06]. An illustration of the situation for the charmonium dissociation temperatures is displayed in Fig. 1.6. A 'sequential melting' pattern of the various char-

---

[7] The calculation corresponds to: for gluons 8 color charges ×2 helicity states, for quarks 3 flavors ×2 spin states ×2 charge conjugate states ×3 colors ×7/8 due to the different statistics of quarks and gluons.

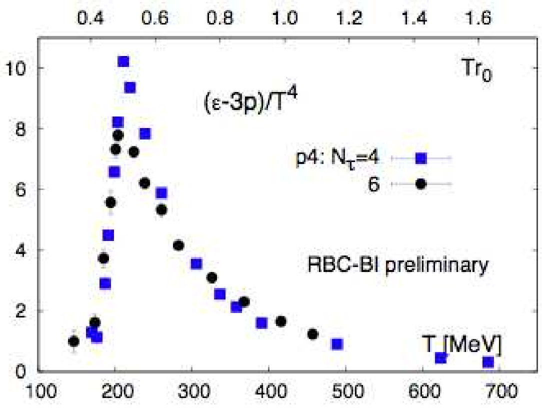

Figure 1.4: $\Delta = (\epsilon - 3P)/T^4$ vs T [Kar07].

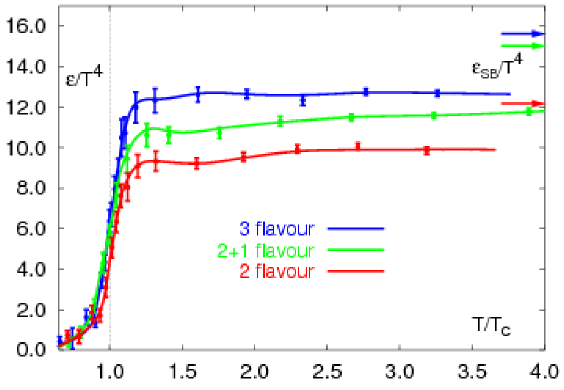

Figure 1.5: Energy density vs T [Kar02].

monium states with their binding energy is observed, the ground state disappearing the last. Recent lQCD calculations support the late dissociation of J/ψ (Υ) at about $T_d/T_c = 1.5$ (3.2) [DHKK07] in agreement with lQCD spectral analysis of the hadron correlation functions [JPPV07].

	J/ψ(1S)	χ_c(1P)	ψ'(2S)	Υ(1S)	χ_b(1P)	Υ'(2S)	χ_b'(2P)	Υ''(3S)
M [GeV]	3.10	3.41	3.69	9.46	9.86	10.02	10.23	10.36
E_s^i [GeV]	0.64	0.20	0.05	1.10	0.67	0.54	0.31	0.20
T_d/T_c	2.1	1.16	1.12	> 4.0	1.76	1.60	1.19	1.17

Table 1.1: Dissociation temperatures of the quarkonium resonances from lQCD. Where E_s^i stands for the binding energy [Kar05, Sat06, Y$^+$06].

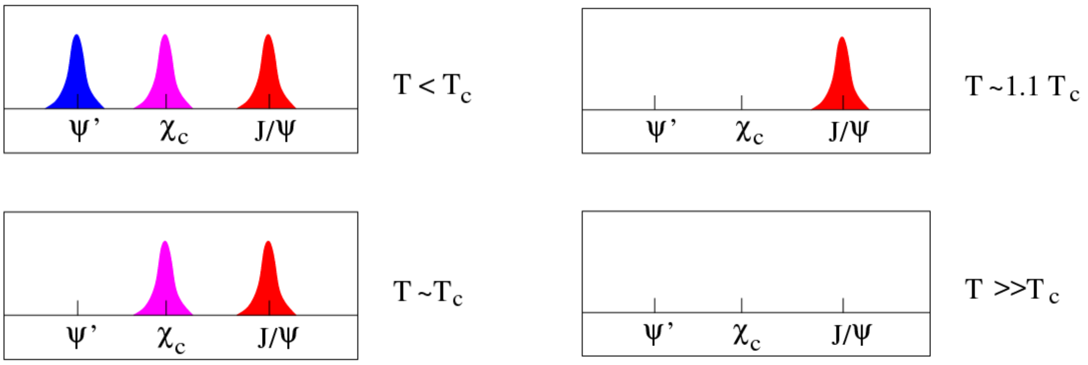

Figure 1.6: Charmonium spectra at different temperatures [Sat06].

1.2 Probing the Quark Gluon Plasma in Heavy-Ion Collisions

Relativistic heavy-ion collisions have been proposed as a tool to create the QGP in the laboratory by reaching energy densities of about (at least) 1 GeV/fm^3 during a long enough time interval. Fig. 1.7 portrays the evolution of an ultra-relativistic heavy-ion collision [Han01]. The colliding nuclei are affected by Lorentz contraction and are conceived as disks in the center-of-mass frame. When nuclei collide, the initial events are hard collisions between nucleons in which many partons are liberated. Nuclei crossing time is thought to be much smaller than the characteristic time of the strong interaction $\tau_{cross} \ll \tau_{strong} \approx 1/\Lambda_{QCD} \sim 1$ fm/c. Thus, after the hard interactions, nuclei pass through leaving behind the created partons. Due to their large amount, those partons can re-scatter redistributing part of the energy deposited in the center-of-mass to thermalize and create a 'fireball'. If the attained energy density exceeds a critical energy density ($\epsilon > \epsilon_c \rightleftharpoons T > T_c$) the QGP might be formed. Then the system tends to expand and cools down towards a hadronic phase. When the energy density is too low to allow inelastic collisions to create particles, the *chemical freeze-out* is attained; the number of particles gets set. The system continues to increase its extent and gets colder; at some point the elastic collisions are no longer possible and the system reaches the *kinetic freeze-out*; the hadrons kinetic properties get set. The hadrons stream then freely till the detectors.

1.2.1 From AGS & SPS to RHIC and LHC

When is a high enough energy density attained? How is it characterized? The expected bulk properties are usually modelized by the Bjorken scenario [Bjo83]. The hypothesis of this scenario are: first that after the initial hard collisions, the partons are created in about $\tau_{strong} \approx 1/\Lambda_{QCD} \sim 1$ fm/c, and at that time the colliding nuclei have already passed through $\tau_{cross} = 2R/\gamma$; second, that the system expands in a homogeneous and longitudinal manner, thus particle multiplicities present a plateau at mid-rapidity. Qualitative estimates of the energy densities obtained in such scenario are summarized in Tab. 1.2 for the different colliding systems. Note that the validity of this scenario at AGS and SPS energies is questionable since there $\tau_{cross} \approx 5.3$ and 1.6 fm/c respectively, which actually violates the hypothesis $\tau_{cross} < \tau_{strong}$ [A$^+$05c]. Therefore, those calculations should just be considered as indicative values. They suggest that at SPS and RHIC the temperatures attained are about

	Nuclei	$\sqrt{s_{NN}}$ [GeV]	ϵ_{Bj} [GeV/fm^3]
BNL-AGS	^{197}Au	5	1.5 [A$^+$05c]
CERN-SPS	^{208}Pb	17.2	2.9 [A$^+$05c]
BNL-RHIC	^{197}Au	130, 200	4-15 [A$^+$05c]
CERN-LHC	^{208}Pb	5500	4-40 [Mar06]

Table 1.2: Estimations of the attained energy density in different colliding systems in the Bjorken scenario.

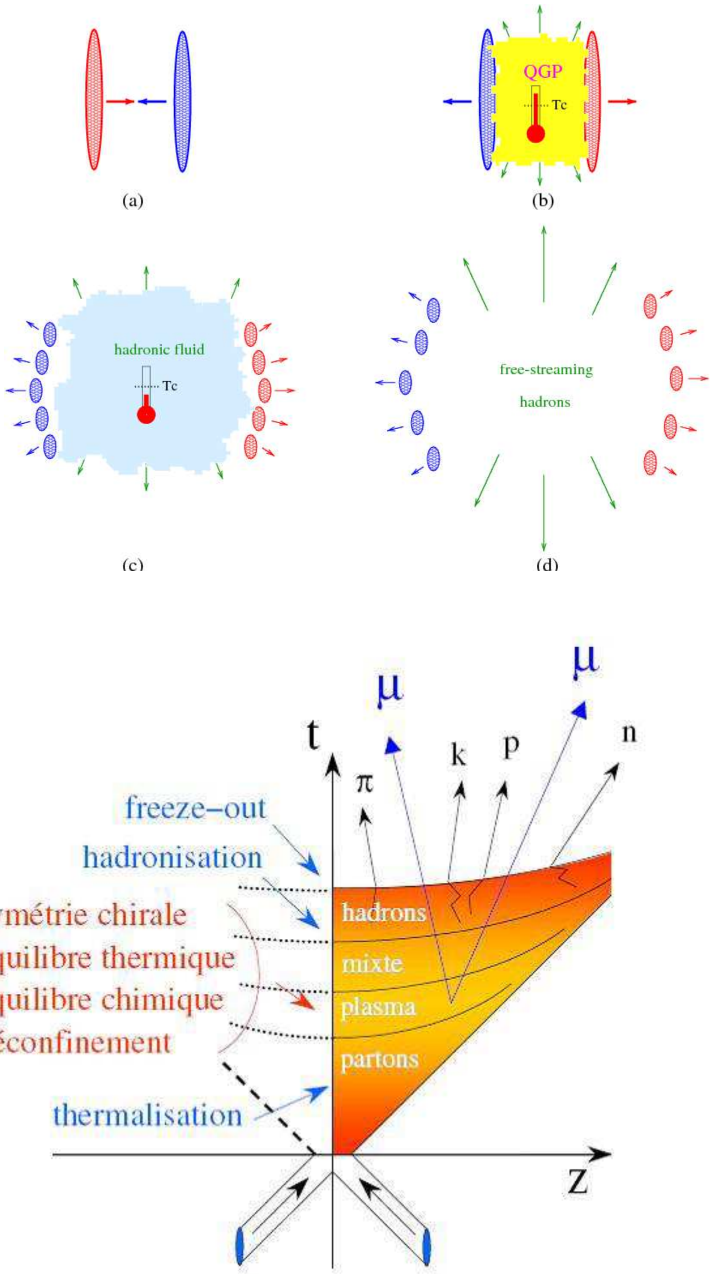

Figure 1.7: Sketch of a heavy-ion collision evolution. Snapshots of the time evolution (upper figure) starting from instants before the collision (a), the formation of a QGP if a high enough energy density is attained (b), the later hadronization (c) and free-streaming of the hadrons towards the detectors (d) [Han01]. Then, (bottom figure) light-cone scheme of the same collision evolution with more precise indication of the different phases of the QGP formation.

$T < 2T_c$ while at LHC $3T_c$ could be reached. This is a crucial point we should bear in mind to interpret $Q\bar{Q}$ production in the sequential melting scenario.

1.2.2 Signatures: experimental observables

Experimentally we study the characteristics of the produced QCD medium analyzing the kinematic and chemical properties of the particles emitted in the reaction. Practically only pions, kaons, (anti-) protons, electrons (positrons), muons, (anti-) neutrons and photons reach the detector, and through analysis techniques the different particles produced in the collision can be identified. Those are the probes that serve us to infer the properties and phases of the matter formed in the collisions. We can classify those probes as: global, initial and final state observables.

Global observables

The global observables provide general information about the collision such as the centrality, the reaction plane, the volume, the expansion velocity and the initial energy density [Mar06]. The measurement of the charged particle multiplicity, the transverse energy and the hadrons kinematic properties (among others) permit those analysis. The reaction centrality can be obtained from measurements of particle multiplicity and of the energy carried by participant and spectator nucleons of the collision. On the other hand, studies of the transverse energy as a function of centrality carry information about the 'fireball' energy density, duration and particles interaction.

Initial state observables

We consider as initial state observables those probes that should not be affected by the QGP formation; those that behave in the same way in the presence of cold nuclear matter (p-A collisions) or the QGP (A-B collisions). Electroweak bosons: high-p_T γ, $W^{\pm}$ and Z^0 are conceived as initial state probes as they do not interact strongly [Mar06]. Weak bosons interest and particularities will be further discussed in Sec. 2 and all through this manuscript we focus on their production at LHC energies and measurement in the ALICE muon spectrometer. With regard to photons, we should distinguish their different production processes. On the one hand, there are direct photons, from which we can separate: the prompt photons, issuing from initial hard collisions, and the thermal photons, emitted in secondary collisions (in the thermal bath), either in the QGP phase or the hadronic phase. On the other hand, there are the decay photons, mainly from π and η decays, that prevail quantitatively over direct photons.

Final state observables

The final state observables are those that provide information on the hadronic and QGP phases. Those are obtained from the hadron yields and kinematic properties. It would be hard to list exhaustively all those probes, since they are many, but we could mention the transverse momentum (p_T) distribution and the relative yield of the hadron species, the flow, the high-p_T particle correlations and the event fluctuations. For instance, due to chiral restoration strange quarks are expected to be lighter at deconfinement, thus strange hadrons are more easily formed; moreover, at deconfinement gluon density also contributes to increase the strange hadrons yields.

Hard probes: As hard probes we refer to those that carry information on the first stages of the collision: the equilibration process, the QGP and its transition [Mar06]. They are produced in the early stages and their life is long enough to become sensitive to the QGP formation before they fragment. As penetrating probes we can point out: high-p_T particles and jets, originating from high-p_T partons fragmentation; resonances with short lifetime that are produced and decay inside the fireball such as the ρ, ω and ϕ mesons; low-p_T photons that could indicate the fireball temperature[8], and heavy quarks and quarkonia that could probe the potential screening and will be discussed in more detail in Sec. 1.3. High-p_T particles and jets may help to describe the partonic phase via studies of their possibly suppressed invariant yield and their angular correlations as a function of the system energy and the reaction plane. On the other hand, the mass and width of the short-lived resonances might be modified by the chiral restoration at deconfinement.

1.2.3 Highlights from the SPS Heavy-Ion program

The CERN-SPS[9] heavy-ion program concerned the NA44, NA45, NA49, NA50, NA52, NA60, WA97 and WA98 experiments among others. They took data in p-p, p-A and A-B collisions (A being a wide variety of nucleus from O, S and In, until Pb) from 40A GeV to 158A GeV (for Pb), where they studied among others the transverse energy, particles multiplicity, strangeness production, direct photons and charmonium production, and they concluded that there was experimental *evidence for the formation of a new state of matter* as their data could not be explained in terms of hadronic degrees of freedom alone [Gon01, HJ00]. Here we just comment on the most significant charmonia results, as they are of interest for the present work.

J/ψ anomalous suppression

At SPS energies, J/ψ production in p-A collisions showed to be in agreement with expectations from 'normal' nuclear absorption. The NA50 experiment evidenced first an anomalous suppression of J/ψ production in central Pb-Pb collisions at 158A GeV with respect to p-A or S-U data [A$^+$00a]. They identified J/ψ and ψ' production through invariant mass analysis of unlike-sign muon pairs and performed a comparison of the J/ψ and Drell-Yan production as a function of the collision centrality. Where the centrality was determined by measuring the transverse energy (E_T), the energy in the zero degree calorimeter (E_{ZDC}) and the charged particle multiplicity; which allow to determine either the length traversed by the charmonium state in nuclear matter L, or the number of nucleon participants in

---

[8] The identification of the thermal photons should permit to probe the temperature of the bath in which they were formed, and their invariant yield as a function of the reaction centrality should indicate the formation of a hottest state of matter in the most central collisions (there should be an excess of thermal photons if the QGP is formed).

[9] SPS stands for Super Proton Synchrotron.

the reaction N_{part}. Later the NA60 experiment completed the studies with In-In data at 158A GeV [P+06, A+05f]. The results of the J/ψ over Drell-Yan ratio as a function of L for different SPS experiments are plotted together in Fig. 1.8, where the red line represents the expectations from nuclear matter absorption considering an absorption cross section of 4.18 ± 0.35 mb [A+05e]. Observe that in the central collisions (large L values) there is a suppression with respect to cold nuclear effects expectations. This suppression attains a factor of 0.5 for the most central reactions, suggesting the formation of a deconfined medium. However, we may note that it does not necessarily mean a suppression of direct J/ψ production, as a considerable amount of ψ' and χ_c decay into J/ψ. As a matter of fact, at SPS energies about 30-40% of the produced J/ψ come from higher resonances decays. The J/ψ anomalous suppression could then indicate a suppression of the higher resonances. Various models can reproduce the observed suppression either taking into account QGP formation or considering hadronic interactions between the charmonium and the hadron gas. It is then a general hope that either RHIC or LHC data could shed some light on this.

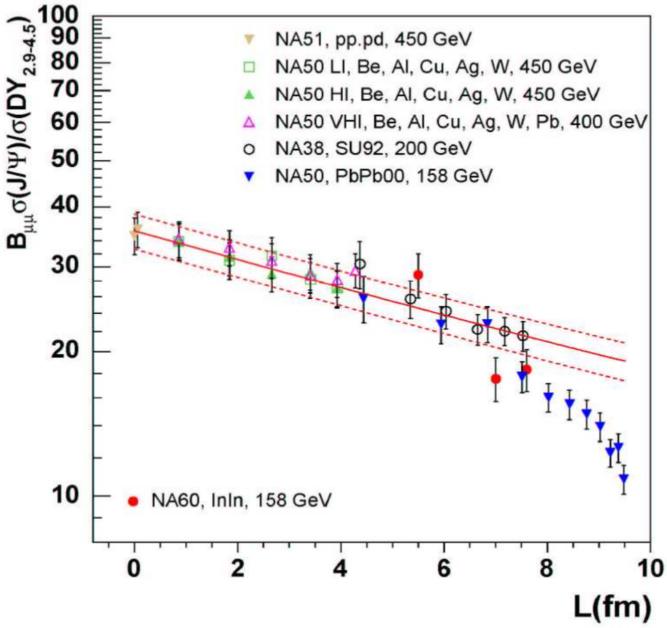

Figure 1.8: J/ψ over Drell-Yan production cross-section ratio as a function of the length traversed by the charmonium in nuclear matter (L) for various colliding systems [P+06].

1.2.4 RHIC results in a nutshell

The RHIC[10] collider has devoted its physics program to the study of nuclear matter under extreme conditions of temperature and energy density. Four experiments have settled there: PHENIX (Pioneering High Energy Nuclear Interaction eXperiment), STAR (Solenoidal Tracker At RHIC), BRAHMS (Broad RAnge Hadron Magnetic Spectrometers experiment) and PHOBOS (the name of the larger and innermost of Mars two moons). They have analyzed p-p, d-Au, Cu-Cu and Au-Au collisions from 19A GeV to 200A GeV (in the center

---

[10] RHIC stands for Relativistic Heavy Ion Collider.

of mass) since 2000 till today, obtaining a wide fan of experimental results. Comprehensive data reviews were published in 2005 by all four experiments, where they all agreed to claim that *a strongly interacting matter was formed* [A$^+$05c, A$^+$05b, A$^+$05g, B$^+$05]. Here I just discuss on some aspects of two of those which I personally consider the most remarkable observations: the jet quenching and the elliptic flow.

Elliptic flow

In reference [Oll92] it was shown that azimuthal anisotropies of particle emission with respect to the reaction plane[11] could be a signature of particles collective motion in heavy-ion collisions, *the collective flow*. In nucleon-nucleon (N-N) collisions the azimuthal distribution of the emitted particles is isotropic. If A-B collisions were an incoherent superposition of N-N collisions, the azimuthal distribution of the particles would also be symmetric. But if there were secondary interactions between the particles produced in the first N-N collisions, the reaction zone anisotropy (see the nucleus overlap area in Fig. 1.9) could induce an azimuthal anisotropy on the emitted particles momenta.

Usually the azimuthal distributions are studied by analyzing the differential production cross-sections in terms of a Fourier decomposition [PV98]

$$\begin{aligned} \frac{dN}{p_T dp_T dy d\phi} &= \frac{1}{2\pi}\frac{dN}{p_T dp_T dy}\left\{1+\sum_{i=1} 2v_i \cos[i(\phi-\Psi_R)]\right\}, \\ v_i &= \langle \cos[n(\phi-\Psi_R)]\rangle , \end{aligned} \tag{1.6}$$

Ψ_R being the reaction plane angle and v_i the Fourier coefficients. The lowest order Fourier terms are the so called *direct flow* (v_1) and *elliptic flow* (v_2). One of the first RHIC measurements on this regard was the elliptic flow at STAR [A$^+$05a]. Fig. 1.9 shows v_2 RHIC results for different particle species. At small p_T ($p_T \lesssim$ 2-3 GeV/c) a good agreement with hydrodynamic calculations is observed; the mass dependence is reproduced, the lighter particles having a more important flow. This together with v_2 dependence on centrality and p_T suggests that equilibrium is reached quickly, and indicate that at those energies a perfect liquid (a strongly interacting liquid), more than an ideal-gas QGP could have been formed [A$^+$05c, A$^+$05b, A$^+$05g, B$^+$05]. However, there is still some open questions to this interpretation.

Jet quenching

Partons produced in initial hard collisions may traverse the QGP before they fragment. Due to their color charge, they may interact with this dense matter loosing part of their energy. Their fragmentation products would then be less energetic (than if no QGP is formed), leading to the so called *jet quenching*. Moreover, as in the parton model of LO-pQCD jets are produced by pairs (with equal impulsion and direction but opposite sense in azimuth), if

---

[11] The reaction plane is determined with respect to the impact parameter vector $\vec{b}$ and the nucleus initial impulsion vector.

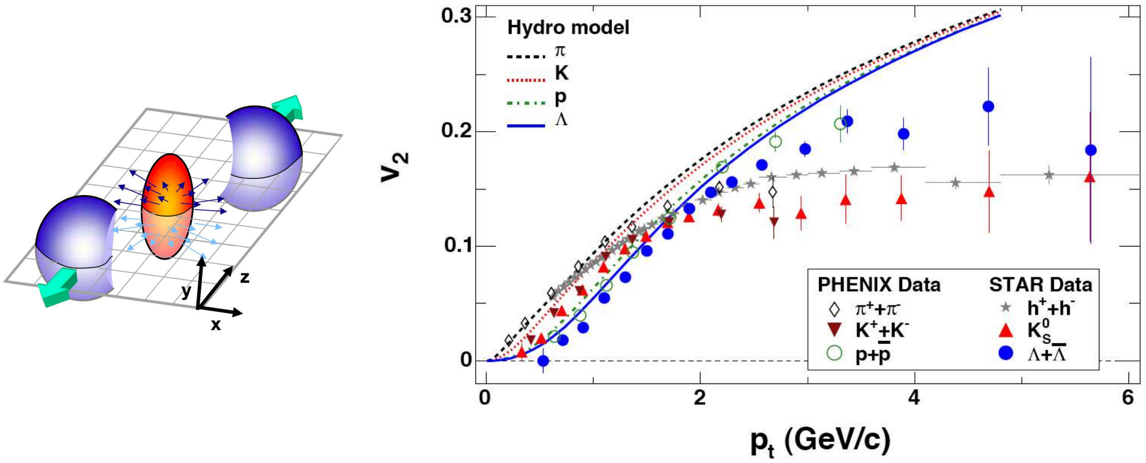

Figure 1.9: Sketch of a heavy-ion collision flow (left-figure). Elliptic flow v_2 distribution as a function of p_T for various particle species at $\sqrt{s_{NN}} = 200$ GeV [A$^+$05a] (right-figure).

one of those jets traverses a longer in-medium path their relative properties could be affected. In the most extreme case they are produced near the bulk surface; one of the jets escape without any modification, whereas the other crosses all the medium and could even be fully screened. Fig. 1.10 presents a sketch of this situation.

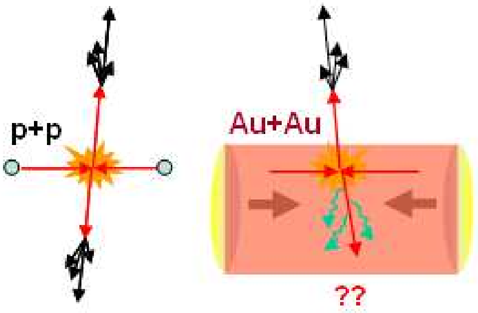

Figure 1.10: Sketch of the back-to-back jets production in p-p collisions and the in-medium influence in A-B collisions.

High-p_T particles suppression: RHIC experiments have performed a detailed systematic study of the nuclear modification factor for various particle species, colliding systems, energies and collision centralities. A snapshot of the obtained results is displayed in Fig. 1.11 [A$^+$03, d'E04, A$^+$05d]. We can observe in the left-hand figure the d-Au nuclear modification factor (R_{dAu}) as measured by PHENIX at $\sqrt{s_{NN}} = 200$ GeV for charged hadrons and neutral pions. An enhancement in the intermediate-p_T region of about 2-8 GeV/c is evidenced and commonly interpreted in terms of the Cronin-effect. It is thought that parton multiple scattering in a cold nuclear medium produces a dispersion and widening of the partons p_T distribution. In addition, the nuclear modification factor of charged hadrons in the most central 0-10% Au-Au collisions (R_{AuAu}) is plotted, exhibiting a strong suppression of about a factor 5 ($R_{AuAu} \sim 0.2$). Charged hadron suppression, which is also observed for the π^0

observable at the same energy, is not noticed neither at lower energies (Fig. 1.11 upper-right plot) nor for direct photon production (Fig. 1.11 bottom-right plot). The high-p_T particle suppression reveals then the effect of the jet quenching phenomena. RHIC results on the nuclear modification factor suggest that a deconfined medium with a high gluon density has been formed, causing a large parton energy loss [Mar06].

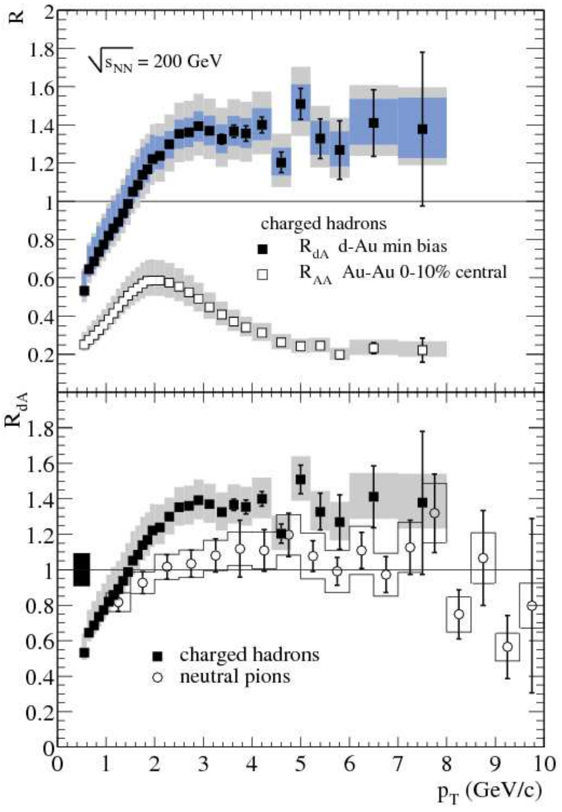

$R_{dA}(p_T)$ and $R_{AA}(p_T)$ (central collisions) for charged hadrons and π^0 at 200 GeV [A+03].

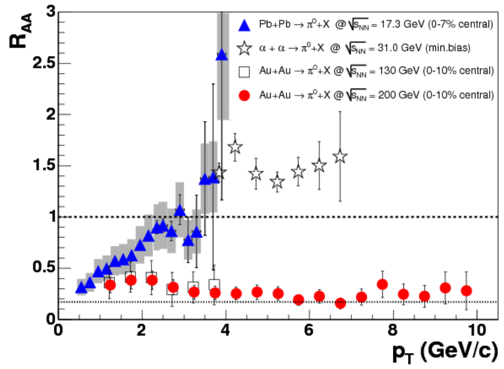

π^0 $R_{AA}(p_T)$ at SPS, ISR & RHIC central collisions [d'E04].

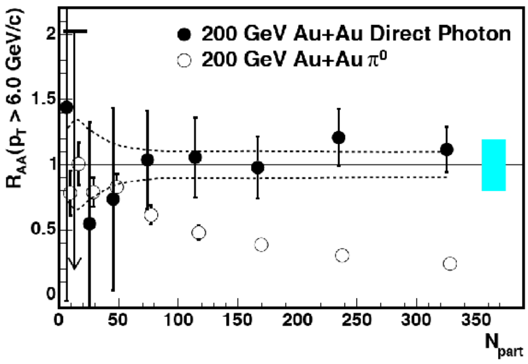

$R_{AA}(p_T)$ for π^0 and direct γ vs centrality [A+05d].

Figure 1.11: Compilation of the jet quenching phenomena results at RHIC. The nuclear modification factor in d-Au collisions at 200 GeV for π^0 and charged hadrons is compared to the one of charged hadrons in Au-Au collisions at the same energy [A+03] (left figure). π^0 $R_{AA}(p_T)$ for the most central heavy-ion collisions at SPS (CERN), ISR (CERN) and RHIC (BNL) energies [d'E04] (right-upper plot). Comparison of R_{AA} for π^0 and direct γ vs collision centrality [A+05d] (right-bottom figure).

1.3 Heavy quarks and quarkonia

In this section we outline the different aspects influencing heavy quark and quarkonia production. A qualitative estimate of their formation and decay times is needed to situate them with respect to the collision evolution stages. Various models/mechanisms that might affect their production in nucleon-nucleon, proton-nucleus and nucleus-nucleus collisions are commented. It should be noticed that this is not an extensive review, just some points are discussed.

1.3.1 Qualitative formation and decay times

It is commonly accepted that at LHC energies the main production mechanism of heavy quark and quarkonia is gluon fusion $gg \longrightarrow Q\bar{Q}$. Gluons from the nucleus wave function will form a $Q\bar{Q}$ pre-resonance in a characteristic (hard) production time t_p

$$t_p(p_T \gg m_Q) \sim \frac{E}{p_T^2} \sim \frac{1}{p_T}\,, \qquad t_p(p_T \lesssim m_Q) \sim \frac{1}{m_Q}\,, \tag{1.7}$$

E being the pair energy. Thus, for $p_T \sim m_Q$ the production time of charm and beauty pre-resonance pairs would be about

$$t_p(p_T \sim m_c) \sim 0.15\,\mathrm{fm/c}\,, \qquad t_p(p_T \sim m_b) \sim 0.05\,\mathrm{fm/c}\,.$$

The production time is then much smaller than 1 fm/c, and they are formed at a relative distance $1/m_Q \ll 1$ fm. Then the $Q\bar{Q}$ pairs travel extremely close and to form a $Q\bar{Q}$ resonance they need to expand till the characteristic size of the resonance. It can be interpreted as the time the pair takes to 'decide' which of the possible $Q\bar{Q}$ bound-states it will couple to (one with mass m_1 or one with m_2). This formation time can be calculated by means of [The94, KT99]

$$t_f \simeq \frac{2E}{m_2^2 - m_1^2}\,. \tag{1.8}$$

Thus the time a $c\bar{c}$ ($b\bar{b}$) pair takes to 'decide' to form a J/Ψ (Υ) rather than a Ψ' (Υ')

$$\begin{aligned} t_f(J/\Psi, E) &\simeq \frac{2\,E}{m(J/\Psi)^2 - m(\Psi')^2}\,, & t_f(\Upsilon, E) &\simeq \frac{2\,E}{m(\Upsilon)^2 - m(\Upsilon')^2}\,, \\ t_f(J/\Psi, 10\,\mathrm{GeV}) &\simeq 1.0\,\mathrm{fm/c}\,, & t_f(\Upsilon, 10\,\mathrm{GeV}) &\simeq 0.36\,\mathrm{fm/c}\,, \\ t_f(J/\Psi, 30\,\mathrm{GeV}) &\simeq 3.0\,\mathrm{fm/c}\,, & t_f(\Upsilon, 30\,\mathrm{GeV}) &\simeq 1.1\,\mathrm{fm/c}\,. \end{aligned}$$

The resonances formation times are thus much larger than the pre-resonances production times. They increase with the particle momentum, ranging from a fraction of fm/c to about 3 fm/c.

Later, the $Q\bar{Q}$ resonance being not a stable particle, it will decay with a characteristic proper time inversely proportional to its width

$$t_d \simeq \frac{1}{\Gamma}\,. \tag{1.9}$$

The J/Ψ and Υ decay time would then be of about

$$t_d(J/\Psi) \simeq \frac{1}{93\,\text{keV}} = 2.1 \cdot 10^3\,\text{fm/c}\,, \qquad t_d(\Upsilon) \simeq \frac{1}{54\,\text{keV}} = 3.7 \cdot 10^3\,\text{fm/c}\,.$$

Theoretical calculations estimate that at LHC energies the QGP might be formed in about 0.1 fm/c and might last ≥ 10 fm/c. The previous calculations suggest that: the $Q\bar{Q}$ pre-resonances are produced while the QGP is formed, but the $Q\bar{Q}$ resonances are formed in coexistence with the QGP, and may decay out of it.

1.3.2 Quarkonia production in nucleon-nucleon collisions

Color Evaporation Model

The Color Evaporation Model (CEM) is a statistical model that describes the probability of charmonia states formation [G+95, AEGH96, AEGH97, GHE97]. It considers that the $Q\bar{Q}$ can either combine with light quarks to form light mesons or bind to form a quarkonia resonance. Focusing on the charmonia production as an example, its hypothesis is that the production cross-section of any charmonium state i (σ_i) is a fixed fraction of the $c\bar{c}$ cross-section $\sigma_{c\bar{c}}$

$$\sigma_i(\sqrt{s}) = f_i\,\sigma_{c\bar{c}}(\sqrt{s})\,, \tag{1.10}$$

f_i being an energy-independent constant to be determined from data. As a consequence it predicts that the production ratios of the different charmonium states must be energy-independent

$$\frac{\sigma_i(\sqrt{s})}{\sigma_j(\sqrt{s})} = \frac{f_i}{f_j} = ctt\,. \tag{1.11}$$

Although this model gives correct quantitative predictions as a function of $\sqrt{s}$, it does not reproduce hidden charm cross-sections and can not describe the space-time evolution of color neutralization [Sat06].

Color Singlet Model

The Color Singlet Model (CSM) [BBB+03, Lan05] uses the non-relativistic QCD formalism (NRQCD) and suggests that the $Q\bar{Q}$ pair is formed in the hard process with the proper quantum numbers. For the J/Ψ formation this requires the emission of a gluon in the final-state to form the color-singlet, $g\,g \longrightarrow J/\Psi\,g$. It underestimates the J/Ψ, Ψ' and Υ states hadroproduction cross-sections by one order of magnitude [BBB+03].

Color Octet Model

The Color Octet Model (COM) [BF95, CGMP95, BR96, Gei98, BFL01] uses the non-relativistic QCD formalism (NRQCD) and proposes that the $Q\bar{Q}$ pair combines with a soft collinear gluon to form a color-singlet $Q\bar{Q} - g$ state, as illustrated in Fig. 1.12. After a relaxation time this state absorbs the gluon and turns into the physical state. It provides a description of the formation process evolution and predicts a transverse polarization. However, the predictions for J/ψ polarization at Tevatron have not been observed [A+00b].

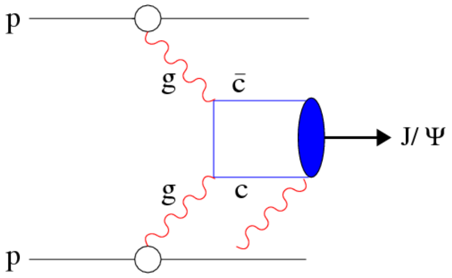

Figure 1.12: Evolution of J/ψ production in the COM [Sat06].

1.3.3 Production in a p-A collisions: cold nuclear effects

When produced in a cold nuclear medium, in p-A collisions, quarkonium and heavy quark production may be affected by the presence of the medium in any of their production stages. In particular we discuss the nuclear shadowing and the nuclear absorption.

Nuclear shadowing

The parton distribution functions (PDFs) describe the probability distribution to find a parton in a proton with a fraction x of the proton momentum. When dealing with nuclei, the high parton density can affect them, resulting in a modification of the PDFs in nuclei. Heavy quark and quarkonia production are mainly influenced by the gluon PDFs. So far model predictions do not severely constrain gluon shadowing [FS99, EKS99, KTH01]. However, PHENIX data favor moderate scenarios such as the EKS one [GdC07]. Nuclear modifications of the gluon distribution functions in a nucleus of $A = 208$ for different values of Q^2 ($R_g^A(x, Q^2)$) are presented in Fig. 1.13. The zone with small values of x ($x < 10^{-2}$) shows a decrease of the PDF that is often called *shadowing* and could lead to a reduction of the pro-

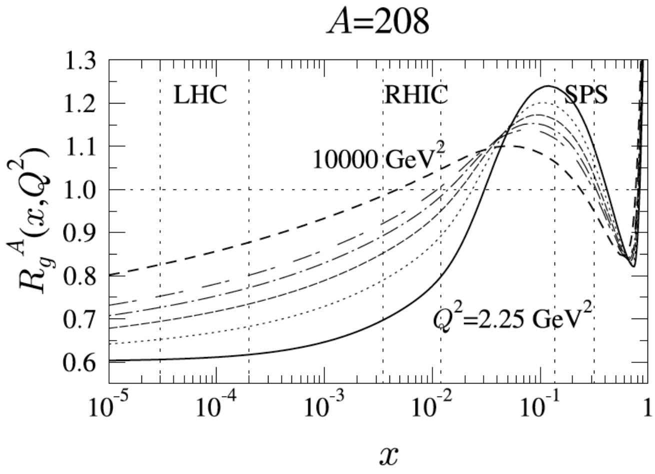

Figure 1.13: Nuclear modification of the gluon distribution functions in a nucleus of $A = 208$ for different values of Q^2; from 2.25 GeV^2 (solid line) to 10000 GeV^2 (dashed line).

duction rate. On the contrary, the x region of between 0.03 and 0.2 presents an increase of the PDFs that is referred to as *anti-shadowing* and could enhance the production rate.

Nuclear absorption

Due to the elevate parton density in the nuclear medium, the $Q\bar{Q}$ state might suffer collisions with the surrounding nucleons either in the pre-resonance or the resonance stage. This might resolve the pair, consequently reducing the quarkonia production rate, and augmenting the open heavy quark mesons production rate. The influence of nuclear absorption should diminish with the collision center-of-mass energy, as the higher the energy of the colliding system, the shorter their crossing time, and the smaller the effect [CF06].

1.3.4 Production in A-B collisions: hot nuclear effects

In a high energy density environment heavy quark and quarkonia produced in hard primary collisions might be affected by the following effects.

Heavy quark energy loss

Heavy quarks crossing through a QGP might interact with the medium and loose energy via various mechanisms. Collisional and radiative energy loss have attracted the theorists attention, the latter being actually considered the most important effect at high-p_T. As we discuss in more detail those effects in Chapter 7, here we just comment that this may reduce high-p_T heavy quarks and quarkonia production rate.

Quarkonia dissociation

Several effects can influence quarkonia production by separating the heavy quarks in the pre-resonance stage and impeding its formation. We can distinguish the comover collisions, the color screening and the parton percolation.

Suppression by comover collisions: [BM88, GV90, GV97, CF05] It was proposed that multiple scattering of the quarkonia with the medium might provoke its dissociation resulting in an effective suppression rate. This effect could occur either in a confined phase via the comover hadrons or in a deconfined phase via the comover partons. An illustration of the expected behavior is shown in Fig. 1.14 as a function of the medium energy density (ϵ). For clarification purposes, in the plot was considered that there is little or no suppression in the hadronic phase ($\epsilon < \epsilon(T_c)$), and that in the deconfined phase (for larger ϵ) the comover partons density increase with ϵ; the quarkonia survival probability decreasing accordingly.

Suppression by color screening: Results of lQCD concerning the quarkonium binding potential have already been discussed in Sec. 1.1.2 [Sat07, Sat06, KKS06]. They suggest that if the QGP is formed, the color field between the heavy quarks gets modified by the presence of the surrounding unbound color charges; the consequence being the sequential dissociation of the different quarkonium states as a function of the medium temperature or energy density schematized in Fig. 1.15 for the J/ψ case (see Tab. 1.1 for the dissociation temperatures for the various quarkonia states). This scenario has also consequences on the mean p_T squared ($\langle p_T^2 \rangle$), predicting its broadening with respect to the number of nucleon-nucleon collisions (N_{coll}^{AB}) as

$$\langle p_T^2 \rangle_{AB} = \langle p_T^2 \rangle_{pp} + N_{coll}^{AB} \delta_0 \tag{1.12}$$

where δ_0 describes the average 'kick' the parton receives in each collision and is determined with p-A data. Figs. 1.15 & 1.16 display the expected pattern of the J/ψ production probability and $\langle p_T^2 \rangle$ behavior as a function of centrality. lQCD calculations are model-independent; nevertheless nothing assures that the medium produced in heavy-ion collisions is the thermal QCD matter studied by lQCD, and moreover the various evolution stages in the nuclear collisions are not accounted for [Sat06].

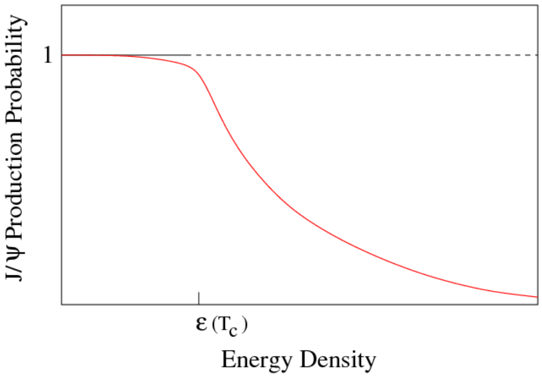

Figure 1.14: J/ψ survival probability suppression by comover collisions [Sat06].

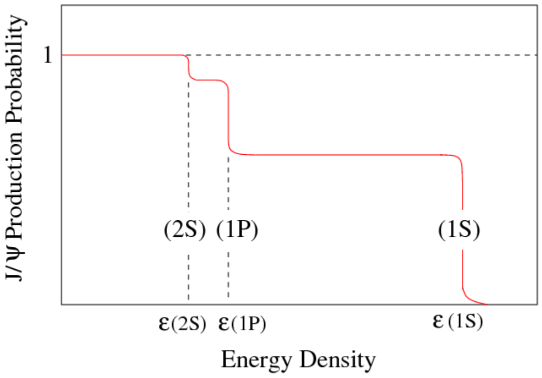

Figure 1.15: Sequential J/ψ survival probability suppression by color screening [Sat06].

The Color Glass Condensate (CGC): [MV94, Mue99, McL03] The increase of A or $\sqrt{s_{NN}}$ comes along with an augmentation of the parton density in the nucleus, the gluons becoming predominant. At high enough A or $\sqrt{s_{NN}}$ the density is so large that there is an overlap of the partons wave functions, and they percolate producing an interconnected network. If the network resolution is sufficient, it could lead to quarkonia dissociation. The CGC allows then to describe the initial conditions in heavy-ion collisions and accounts for the nuclear effects (shadowing, saturation,...). However, to evaluate the effect of the parton resolution scale on quarkonia or heavy quarks production it is model-dependent.

Quarkonia regeneration

In the hadronization phase quarkonia can be formed by the binding of heavy quarks from different nucleon-nucleon collisions as well as from the same [GRB04, BKCS04, ABMRS03, TM06]. If the heavy quarks abundance augments with respect to their thermal conditions, statistical recombination favors quarkonia production with respect to light hadrons, resulting on quarkonia production enhancement. The quarkonia production cross-section increasing faster with the energy than the light hadrons one, the probability of recombination augments with the energy density and the collision centrality. Moreover, in the regeneration picture the mean $\langle p_T^2 \rangle$ is thought to be independent of the centrality since the heavy quarks probably come from different collisions. Fig. 1.16 illustrates the probability of J/ψ production as a function of the medium energy density ϵ compared to the opposite scenario of sequential suppression.

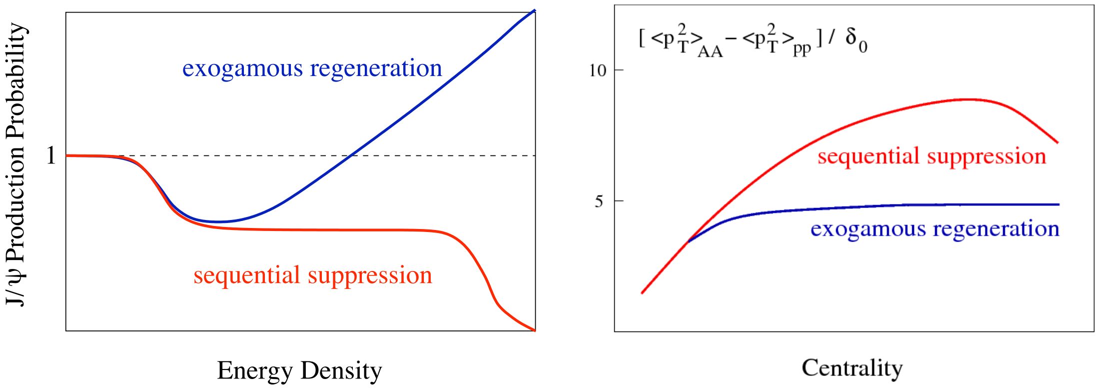

(a) (b)

Figure 1.16: Cartoon of J/ψ enhancement by recombination in front of the sequential dissociation scenarios. Survival probability as a function of the energy density (a) and p_T behavior (b) [Sat07].

1.3.5 Charmonium data interpretation: remarks

CERN-SPS and BNL-RHIC experiments have provided valuable data on charmonium and open-charm production. The (in my opinion) most relevant SPS observations were commented on Sec. 1.2.3 and RHIC data are recent and are still under discussion. Here we just pretend to give the basic lines in a few words. SPS data observed an anomalous J/ψ suppression seemingly in accord with different models, some accounting for the QGP formation and some not. RHIC just provided fresh data of d-Au, Cu-Cu and Au-Au collisions. When compared to SPS results is revealed an intriguing observation: a similar suppression is perceived for both (in the J/ψ over Drell-Yan ratio vs ϵ) while the expected energy densities are increased by a factor 1-5 for RHIC[12] [A$^+$05c]. One interpretation is that even though at RHIC the J/ψ is further suppressed, the recombination of $c\bar{c}$ pairs in the hadronic phase cancels it out. Another is the sequential melting of the quarkonium states; it suggests that direct J/ψ are not suppressed neither at SPS nor at RHIC, and that the observed suppression is due to the decrease of the feed-back contribution from higher resonances which are suppressed earlier and are thought to be melt at both SPS and RHIC energies. The lQCD sequential

---

[12] Note that the comparison is not experimentally trivial, since ϵ calculation is dependent of centrality determination and is model-dependent. Each experiment measures differently the centrality, which could introduce discrepancies.

melting scenario has also consequences on the J/ψ mean p_T squared ($\langle p_T^2 \rangle$), predicting its broadening with respect to the number of nucleon-nucleon collisions (N_{coll}^{AB}). RHIC and SPS data agree with such scenario, so it appears to be on the right track [Sat06]. Nevertheless at the present time we can not discriminate any of the interpretations [GdC07]. More precise data on ψ' production at SPS, on J/ψ production at RHIC energies, and the upcoming LHC data where the lQCD predicted onset of J/ψ dissociation should be attained could be conclusive.

1.3.6 Novel aspects of heavy flavor physics at LHC

The LHC collider will offer the possibility to produce head-on heavy-ion collisions (HIC) increasing the center-of-mass energy by about a factor 30 with respect to RHIC [C$^+$04, A$^+$06]. The large amount of energy available in the center-of-mass will be accompanied by an augmentation of the $c\bar{c}$ and $b\bar{b}$ pairs abundance [C$^+$04, A$^+$06]. Tab. 1.3 reports the expectations: about 115 $c\bar{c}$ pairs and 5 $b\bar{b}$ pairs should be produced in the 0-5% Pb-Pb most central collisions (see App. D and Tab. D.6 for the calculations). That is about 10 times more $c\bar{c}$ pairs and 100 times more $b\bar{b}$ pairs than at RHIC. Heavy flavor will allow to probe rather small values of the gluon Bjorken-x (10^{-5},10^{-3}); for such x values in HIC a large shadowing is expected which could reduce heavy quark production with respect to binary scaling. Moreover, the larger and denser is the matter traversed the larger the heavy quark energy loss. Only about 1% of those heavy quarks will end up in the formation of quarkonia bound states [MG07]. Due to the energies attained at LHC, in HIC the quarkonia nuclear absorption should diminish (the nuclei crossing time is smaller), the dissociation temperatures of J/ψ (and may be even the Υ) in the sequential melting scenario should be reached, and the charmonia recombination processes should also become relevant (the larger the abundance of heavy quarks present in the medium). Bottomonia family which was not accessible at SPS and whose studies at RHIC is under investigation will become a powerful signature at LHC. Whether heavy quarks will thermalize or develop collective motion, and whether quarkonia will be further suppressed or regenerated, are still open questions that LHC data might resolve.

	SPS Pb-Pb Cent	RHIC Au-Au Cent	LHC p-p	LHC Pb-Pb Cent
$N(c\bar{c})$	0.2	10	0.2	115
$N(b\bar{b})$	–	0.05	0.007	5

Table 1.3: Expected number of $c\bar{c}$ and $b\bar{b}$ pairs produced in central heavy-ion and p-p collisions at SPS, RHIC and LHC energies.

The ALICE experiment at LHC has the capability to combine electronic, muonic and hadronic channels to measure heavy flavor (hidden and open charm and beauty), being able to measure quarkonia down to $p_T \sim 0$ [Mar05, Ant07]. Note that ALICE is the unique LHC device able to measure charmonia down to $p_T \sim 0$, and open charm down to $p_T \sim 0.5$ GeV/c in p-p or p-Pb collisions (1 GeV/c in Pb-Pb collisions). The latter would be possible via the reconstruction of the $D^0 \longrightarrow K^- \pi^+$ decays in the central barrel; it will probably bring the most precise measurement of the total charm production cross-section at LHC energies [A+06].

Novelties with the ALICE muon spectrometer

Single muon spectra and the correlated continuum invariant mass will allow to study beauty production from $p_T \sim 1$ to 20 GeV/c [CGMV05, Cro05]. Beauty production cross-section, cold nuclear effects, and beauty energy loss will be studied. An invariant mass resolution of the order of 70 (100) MeV/c^2 will permit to disentangle the resonances of the J/ψ (Υ) family [C+04, A+06]. The resonances yields as a function of centrality and p_T should permit to probe the characteristics of the deconfined medium and might provide tools to discriminate between the various suppression and coalescence models. The expected high J/ψ statistics [SVR07] (about half a million during one Pb-Pb run and 3 millions in a p-p run) will allow to measure it from $p_T \sim 0$ to 30 GeV/c, and investigate its polarization [A+07] and its azimuthal asymmetry with respect to the reaction plane. Polarization measurements in p-p collisions might help to discern between the different models proposed to describe quarkonia production mechanisms: the CSM predicts transverse polarization, the CEM no polarization, and the COM (NRQCD) transverse polarization at large p_T. Moreover, an increase of quarkonium polarization in heavy-ion collisions is expected in case of QGP [IK03]. Another important issue is that Υ(1S) and Υ(2S) will be measured from $p_T \sim 0$ to 8 GeV/c; the novel observable of their relative yield $N_{\Upsilon(2S)}/N_{\Upsilon(1S)}$ will then become accessible [Cro05, DC05]. The resonance ratios as a function of p_T have been suggested to isolate the QGP effects as in the ratio of $N_{\Psi'(2S)}/N_{J/\Psi(1S)}$ or $N_{\Upsilon(2S)}/N_{\Upsilon(1S)}$ the cold nuclear effects are washed out (at least on the p_T evolution). Recent calculations indicate that with the expected Υ(1S) and Υ(2S) statistics their ratio would be sensitive to the QGP [DC05].

Chapter 2

Weak bosons in hadron-hadron collisions

> *The most exciting phrase to hear in science, the one that heralds the most discoveries, is not 'Eureka'! (I found it!) but 'That's funny...*
>
> I. Asimov

From the point of view of nucleus-nucleus collisions, as electroweak bosons do not interact strongly, they are usually considered as medium-blind references and they have been proposed to tag jet energy in back-to-back produced jets (the γ-jet or the Z-jet probes). The concept being to use the electroweak boson energy to estimate the energy loss of its companion-jet[1], as the bosons are not sensitive to the strong interaction and the jets suffer from energy loss while traversing the QGP (see [CB05, MCC$^+$07] and references therein). But, is it enough to only rely on the fact that electroweak bosons do not interact strongly to consider them as medium-blind references? We should remind that they interact electromagnetically, and by the way, we could interrogate about when are they produced and when do they decay? Are these the bosons or their decay products which might cross the QGP? So, could they be influenced by the QGP either electromagnetically or via their decay products? Besides, remember that weak bosons are considered as standard model benchmarks, they are interesting probes by themselves already in p-p collisions. Here and all through this thesis work we will discuss those issues. In this chapter we just draw the attention on those that we consider the most important points, and mainly those related to heavy-ion physics will be developed in this manuscript. To facilitate the comprehension of the whole, here we first discuss the qualitative formation and decay time of weak bosons (Sec. 2.1), then we briefly summarize the main motivations to study weak bosons at LHC energies (Sec. 2.2), and finally we remind the basics of the electroweak theory and the particularities of the weak interaction (Sec. 2.3).

2.1 Qualitative formation and decay times

Weak bosons are formed early due to their large mass: $t_p \sim 1/M \sim 10^{-3}$ fm/c. Their decay time is by definition inversely proportional to their widths

$$t_d(Z^0 \to X) \simeq \frac{1}{2.495\,\mathrm{GeV}} = 0.08\,\mathrm{fm/c}\,, \qquad t_d(W^\pm \to X) \simeq \frac{1}{2.141\,\mathrm{GeV}} = 0.09\,\mathrm{fm/c}\,.$$

---

[1] It is based on the fact that in the parton model of pQCD, at LO jets are always produced by pairs, with equal momenta and opposite sense of movement.

Therefore weak bosons are produced early, before the QGP is formed, and decay either before or within the QGP. As a result their decay products might be sensitive to the QGP. If we focus on their leptonic decays, as leptons do not interact strongly, they should be hardly influenced by the QGP (we will discuss this in more detail in Sec. 7.3). However, if we concentrate on Z beauty decays, which branching ratio is of about 15% [Y⁺06], b-quarks should be sensitive to the QGP, and so the Z invariant mass in this channel (see more details in Sec. 7.5.1).

2.2 Why should we study weak bosons at LHC?

Weak bosons properties have been studied at LEP (CERN), SLC (SLAC) and Tevatron (FNAL) colliders in $p\bar{p}$ and e^+e^- collisions [Y⁺06]. At the LHC, large energy will be available in the center-of-mass, enabling the possibility to produce W and Z bosons in p-p and in nucleus-nucleus (A-A) collisions.

In the lowest order approximation, W and Z bosons are produced by the quark (q) - antiquark ($\bar{q}$) annihilation process:

$$q + \bar{q}' \rightarrow W^{\pm}\,; \qquad q + \bar{q} \rightarrow Z\,.$$

These subprocesses are characterized by the scale $Q^2 = M^2$ and the Bjorken-x values, which can be determined by $x_{1,2} \sim \frac{M}{\sqrt{s}}\,e^{\pm y}$ [TCSG05, CS05], where M is the mass of the weak boson, $\sqrt{s}$ is the center-of-mass energy of the nucleon-nucleon collision, and y is the rapidity.

Their measurements at LHC will provide important information:

- These subprocesses are considered as Standard Model benchmarks. Their production cross-sections are ’known’ with a precision dependent on the parton distribution functions (PDFs) uncertainties. Therefore, they have been suggested as ’standard-candles’ for luminosity measurements, and to improve the evaluation of the detector performances [TCSG05, CS05].

- In proton-proton (p-p) collisions, they will be sensitive to the quark PDFs at high Q^2 ($Q = M_{W/Z}$).

- In proton-nucleus (p-A) collisions, quark nuclear modification effects will become accessible at the same scale.

- Since weak bosons are probes produced in hard primary collisions and if we concentrate in their leptonic decay they do not interact strongly with the surrounding medium created in the collision, they will allow binary scaling cross-checks in A-A collisions.

- They could then be used as a reference for observing medium induced effects on other probes, like the suppression of high transverse momentum (p_T) muons from charm and beauty, or the jet quenching phenomena in the Z-jet observable[2].

W and Z bosons can be measured via their leptonic decay. The decay $W^+ \rightarrow l^+ \nu_l$ ($W^- \rightarrow l^- \bar{\nu}_l$) has a branching ratio of 10.7 %, and the decay $Z \rightarrow l^+ l^-$ has a branching ratio of 3.37 % [Y+06]. All through this thesis work we will bring our efforts to discuss weak boson production at LHC energies, their measurement in the ALICE muon spectrometer, and their utility to study heavy-ion collisions (in particular to investigate the QGP formation in them).

2.3 Basics of the electroweak theory

2.3.1 Historical outline

About 1968 Sheldon Glashow, Steven Weinberg, and Abdus Salam formulated a unified theory of electromagnetism and weak interactions, the electroweak theory (label $SU(2) \times U(1)$), for which they shared the 1979 Nobel Prize in physics [Nob]. The application of the gauge principle to the weak theory (label $SU(2)$) requires three mass-less spin-1 bosons. The electroweak theory postulates then the existence of four mass-less gauge spin-1 bosons: a triplet W^+, W^-, W^0 plus a neutral single particle V^0. The Standard Model predicts the existence of at least one heavy spin-0 boson called the Higgs boson, in which relies the mass-giving mechanism. Such mechanism can break the symmetry of the postulated triplet to give the massive W^+ and W^-, the massive Z^0, and the mass-less photon (γ). The electroweak theory has three parameters: the Fermi coupling constant $G_F/(\hbar c)^3 = 1.166 \cdot 10^{-5}$ GeV^{-2}, the electromagnetic coupling constant e, $\alpha = e^2/\hbar c = 1/137$, and the Weinberg angle θ_W which describes the mixing of the gauge fields to make the four observable bosons, $\sin^2 \theta_W \simeq 0.23$.

Carlo Rubbia and Simon van der Meer were awarded with the Nobel Prize in physics on 1984 for the discovery of the W and Z [Nob]. On the one hand, on 1972 Simon van der Meer published a report entitled 'Stochastic damping of betatron oscillations in the ISR' [dM72]. He is the architect of the 'beam cooling' techniques which permitted to make intense antiproton beams feasible and allowed the discovery of the W and Z. The firsts tests of this technique were carried out at ISR (CERN) on 1974, and an small storage ring was rapidly converted on 1976-77. On the other hand, on 1973, the huge Gargamelle bubble chamber at CERN photographed the tracks of a few electrons suddenly starting to move, seemingly of their own accord. It presented an evidence of the weak neutral currents, showing that the electroweak theory was on the right track. But the discovery of the W and Z had to wait till 1983, when thanks to the 'beam cooling' techniques the SPS collider was able to provide high enough luminosity beams. At that time the experiments UA1 (led by Carlos Rubbia) and UA2 (led by Pierre Darriulat) measured unambiguous signals of W bosons (on January 1983) [A+83a, B+83b] and Z bosons (on May 1983) [A+83b, B+83a].

---

[2] Nevertheless, remark that the production cross-section of this process is relatively small. In Sec. 5.1.1 we will discuss the production cross-sections, and we will observe that the NLO corrections to weak boson production account only for about 13% [FM04].

2.3.2 Introduction to the electroweak theoretical formalism

The electromagnetic interaction is described by a $U(1)_{em}$ symmetry with coupling constant e, where the current is:

$$e\,j_\mu^{em} = e\,\bar{\Psi}\,\gamma_\mu\,Q_f\,\Psi, \tag{2.1}$$

Ψ is the fermion wave-function and Q_f its charge ($Q = +1$ for the electron). The vertex of the interaction is then of the form:

$$-\,i\,e\,Q_f\,\gamma^\mu. \tag{2.2}$$

On the other hand, the weak interaction is described by a $SU(2)_L$ symmetry with coupling constant g, where the charged and the neutral currents can be respectively written as [HM84]:

$$j_\mu^\pm = \bar{\chi}_L\,\gamma_\mu\,\tau_\pm\,\chi_L, \qquad\qquad j_\mu^3 = \bar{\chi}_L\,\gamma_\mu\,\frac{1}{2}\tau_3\,\chi_L, \tag{2.3}$$

χ_L are the spinor doublets, the subscript L denotes the left-handed spinors and records the vector axial nature of the currents, and $\tau_\pm = \frac{1}{2}(\tau_1 \pm i\tau_2)$ being τ_i are the Pauli matrices. The weak vertexes are then of the form:

$$-\,i\,\frac{g}{\sqrt{2}}\,\gamma^\mu\,\frac{1}{2}\,(1-\gamma^5), \qquad\qquad -i\,\frac{g}{\cos\theta_W}\,\gamma^\mu\,\frac{1}{2}\,(c_V^f - c_A^f\gamma^5), \tag{2.4}$$

for the charged and neutral currents respectively, and where

$$c_V^f = T_f^3 - 2\,\sin^2\theta_W\,Q_f, \qquad\qquad c_A^f = T_f^3, \tag{2.5}$$

with T^3 as the third component of the fermion weak isospin charge: $T^3 = \int j_0^3(x)d^3x$. Tab. 2.1 presents the fermions charge and the third component of their weak isospin charge as a function of their chirality state. Observe that the weak isospin component is zero for right-handed fermions. Remark that the chirality operator γ^5 of eq. 2.4 ensures that right-handed neutrinos do not participate on the weak interaction. As a matter of fact, there is no experimental evidence of their existence. One may also notice, by a comparison of the vertex factors for the electromagnetic and the weak interactions (eqs. 2.2 and 2.4), that while the first interaction has a pure vectorial coupling (vertex as γ^μ), the latter contains

Fermion	Q_f	$(T_f^3)_L$	$(T_f^3)_R$
u, c, t	$+\frac{2}{3}$	$+\frac{1}{2}$	0
d, s, b	$-\frac{1}{3}$	$-\frac{1}{2}$	0
ν_l	0	$+\frac{1}{2}$	-
l^-	-1	$-\frac{1}{2}$	0

Table 2.1: Values of the electric charge and the third component of the weak isospin for left-handed and right-handed fermions [HM84].

vector and axial vector parts (vertex as $\gamma^\mu\,(1-\gamma^5)$). This difference explains that while the weak interaction violates parity (P), the electromagnetic interaction does not [3] . Eq. 2.3 also makes evident the pure nature of the vector-axial (V-A) coupling for the case of the charged weak currents, i.e. for W$^\pm$ couplings that are 'maximally' mixed (vertex as $\gamma^\mu\,(1-\gamma^5)$); in contrast to the non-pure V-A nature of the neutral weak current, i.e. for the Z^0 coupling (vertex as $\gamma^\mu\,(c_V^f - c_A^f\gamma^5)$). That means that W$^\pm$ only couple with left-handed fermions (and right-handed anti-fermions), while the Z^0 coupling has also right-handed fermionic (and left-handed anti-fermionic) components.

Finally, the electroweak theory proposed by Glashow, Weinberg and Salam is able to describe both together on a $SU(2)_L \otimes U(1)_Y$ symmetry. According to the theory the electromagnetic interaction 'sits across' the weak interaction and the weak hypercharge. The weak hypercharge (Y) is defined by:

$$Q = T^3 + \frac{Y}{2}, \tag{2.6}$$

and is described by a $U(1)_Y$ symmetry with coupling constant g', so that the weak hypercharge current is [HM84]

$$j_\mu^Y = \bar{\Psi}\,\gamma_\mu\,Y\,\Psi. \tag{2.7}$$

The currents can then be characterized by:

$$j_\mu^{em} = j_\mu^3 + \frac{1}{2}\,j_\mu^Y, \tag{2.8}$$

$$j_\mu^{NC} = j_\mu^3 - \sin^2\theta_W\, j_\mu^{em}, \tag{2.9}$$

where NC stands for neutral current. By imposing the consistency of those equations, one obtains the relationship between the coupling constants

$$e = g\sin\theta_W = g'\cos\theta_W. \tag{2.10}$$

2.3.3 Particularities of the weak interaction

Here we highlight some particularities of the weak interaction that will be useful for the comprehension of the rest of the manuscript.

Feynman diagrams for the weak vertexes

The Feynman diagrams of W and Z vertexes are presented in Fig. 2.1 and Fig. 2.2 together with the rules for the vertex construction. It is important to note that the weak interaction do not mix the lepton generations but do connect the quark generations. ***The W vertex connects two different fermions, either quarks or leptons.*** The electric charge, the lepton generation

---

[3] The parity and charge conjugation transformations deal with space inversion ($\vec{r} \to -\vec{r}$) and charge particle conjugation (particle $\rightleftharpoons$ antiparticle) respectively. Their respective conserved quantities are the parity and the charge conjugation quantum numbers. Thus CP violation is interpreted as a different physical behavior of particles and antiparticles, matter and antimatter.

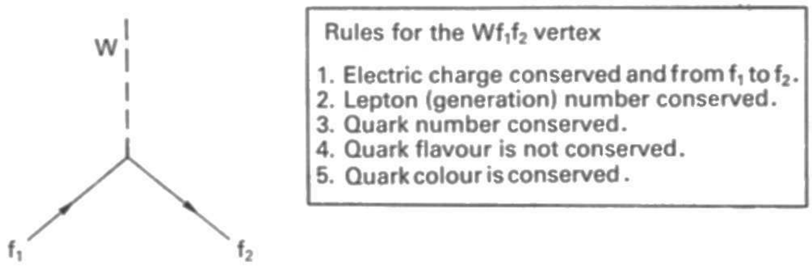

Rules for the Wf_1f_2 vertex

1. Electric charge conserved and from f_1 to f_2.
2. Lepton (generation) number conserved.
3. Quark number conserved.
4. Quark flavour is not conserved.
5. Quark colour is conserved.

Figure 2.1: Feynman diagram for the Wf_1f_2 vertex with the rules for vertex construction [Wil05]. Where f stands for fermions, either quarks or leptons.

number, the quark number and color are conserved on the W vertex while the quark flavor is not. ***In contrast, the Z vertex connects two identical fermions, or a fermion with an anti-fermion***, and on that case besides the conservation rules of the W vertex, the quark flavor is conserved. So, the Z is attached to a fermion current in which the fermion does not change. ***In addition, we should highlight that W bosons only couple with left-handed fermions and right-handed anti-fermions.***

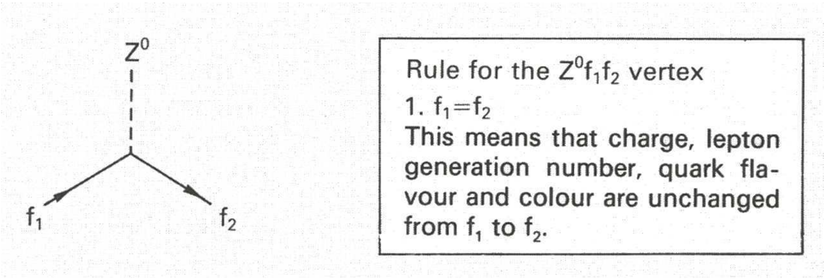

Rule for the $Z^0f_1f_2$ vertex

1. $f_1=f_2$

This means that charge, lepton generation number, quark flavour and colour are unchanged from f_1 to f_2.

Figure 2.2: Feynman diagram for the Zf_1f_2 vertex with the rules for vertex construction [Wil05]. Where f stands for fermions, either quarks or leptons.

Quark mixing on charged weak couplings

Cabibbo first explained the coupling of the quark generations considering just two generations of quarks. He assumed that ***the charged weak current couples 'rotated' quark states and not the quark mass eigenstates***. On that case the charged weak current could be written as [HM84]:

$$j^\mu = \begin{pmatrix} \bar{u} & \bar{c} \end{pmatrix} \frac{\gamma_\mu(1-\gamma^5)}{2} U \begin{pmatrix} d \\ s \end{pmatrix} \qquad \text{with} \qquad U = \begin{pmatrix} \cos\theta_C & \sin\theta_C \\ -\sin\theta_C & \cos\theta_C \end{pmatrix}, \tag{2.11}$$

where U is the rotation matrix and θ_C the Cabibbo angle, the unique parameter that is determined by means of experiments to be $\theta_C = 13.1°$ [Gri04].

Later, Cabibbo-Kobayashi-Maskawa (CKM) generalized the rotation matrix for the case of three quark generations. Thus in the standard electroweak model the left-handed fermion fields $\Psi_i = \begin{pmatrix} \nu_i \\ l_i^- \end{pmatrix}$ and $\begin{pmatrix} u_i \\ d_i' \end{pmatrix}$ of the ith fermion family transform as doublets under $SU(2)$, where $d_i' \equiv \sum_j U_{ij} d_j$ and U is the CKM mixing matrix

$$U = \begin{pmatrix} |U_{ud}| = 0.9738 & |U_{us}| = 0.2272 & |U_{ub}| = 3.96 \cdot 10^{-3} \\ |U_{cd}| = 0.2271 & |U_{cs}| = 0.9722 & |U_{cb}| = 42.2 \cdot 10^{-3} \\ |U_{td}| = 8.1 \cdot 10^{-3} & |U_{ts}| = 41.6 \cdot 10^{-3} & |U_{tb}| = 0.99910 \end{pmatrix}, \tag{2.12}$$

which can be parameterized by three mixing angles and a CP-violating phase [Y$^+$06].

Parity violation

The parity operator (P) deals with space inversion ($\vec{r} \to -\vec{r}$) and has two eigenvalues: ± 1. Pseudo-scalars ($\bar{\Psi}\,\gamma^5\,\Psi$) and vectors ($\bar{\Psi}\,\gamma^\mu\,\Psi$) have associated a parity -1 and scalars ($\bar{\Psi}\,\Psi$) and axial vectors ($\bar{\Psi}\,\gamma^\mu\,\gamma^5\,\Psi$) $+1$. On a two dimensional plane, to perform a parity transformation is equivalent to apply a 180° rotation, that is why it is usually referred to as mirror symmetry.

The particle helicity (h) characterizes the particle spin ($\vec{S}$) projection on the momentum direction ($\vec{p}$), that is

$$h = \frac{\vec{S} \cdot \vec{p}}{|\vec{p}|}. \tag{2.13}$$

As the parity of spin and momentum are opposite: $P(\vec{S}) = \vec{S}$, $P(\vec{p}) = -\vec{p}$, the helicity changes sign under parity $P(h) = -h$. In the extreme relativistic limit or in the case of mass-less particles, the chirality operator (γ^5) is equal to the helicity operator [HM84]. The chirality right-handed and left-handed projection operators are:

$$P_R \equiv \frac{1}{2}(1+\gamma^5), \qquad P_L \equiv \frac{1}{2}(1-\gamma^5). \tag{2.14}$$

Then, for example, the left-handed electron $\frac{1}{2}(1-\gamma^5)\,u = u_L$ corresponds to an electron of negative helicity. So in the ultra-relativistic limit negative helicity corresponds to left chirality, and positive helicity to right chirality. ***As the weak interaction just act with left-handed neutrinos and right-handed antineutrinos, it violates parity***[4].

Parity violation on charged weak couplings was first suggested by Lee and Yang on 1956. One year later the experience proposed by Lee and Yang was achieved by Wu [WAH$^+$57], and Lee and Yang were awarded with the Nobel Prize of physics that year [Nob]. In the Wu experiment represented in Fig. 2.3, the nuclear spins of a sample of ^{60}Co were aligned by an external magnetic field and it was observed an asymmetry on the emission direction of the electrons. The electrons were preferably emitted on the opposite direction to the Cobalt nuclear spin, which testified the parity violation effect. One can understand that observing that on this experiment angular momentum conservation on the Cobalt decay imposes that $J(e^- + \bar{\nu}_e) = 1$. As the antineutrino is right-handed, in order to keep $J = 1$ the antineutrino

---

[4] For instance, if one applies parity transformation to a left-handed neutrino, one should reverse the sense of the spin rotation, then one gets a right-handed neutrino. But right-handed neutrinos do not exist, thus the parity transformation is violated.

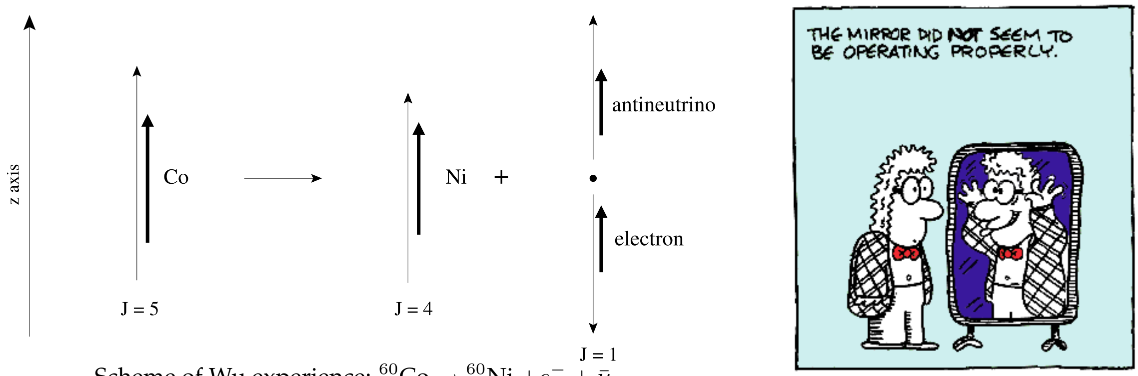

Scheme of Wu experience: $^{60}\mathrm{Co} \to {}^{60}\mathrm{Ni} + e_L^- + \bar{\nu}_R$.

Cartoon of P violation.

Figure 2.3: Sketch to describe the ^{60}Co experiment; where the thin lines represent the movement (momentum) direction, and the thick lines represent the helicity.

is preferably emitted on the direction of the Cobalt nuclear spin, thus the electron tends to be emitted on the opposite direction.

Part II

Experimental apparatus

Chapter 3

The Experiment

> *A spider conducts operations that resemble those of a weaver, and a bee puts to shame many an architect in the construction of her cells. But what distinguishes the worst architect from the best of bees is this, that the architect raises his structure in imagination before he erects it in reality.*
>
> K. Marx

Abstract

This chapter is an introduction to the experimental setup. The LHC collider and the ALICE experiment are briefly described. Special attention is payed to the ALICE muon spectrometer.

3.1 The Large Hadron Collider

The Large Hadron Collider (LHC) is a particle accelerator, which is being installed in a tunnel of 27 km in circumference, buried 50-175 m below ground. It is located between the Jura mountain range, in France, and the Lake of Geneva, in Switzerland. *The tunnel was built in the 1980s for the previous big accelerator, the Large Electron Positron collider (LEP) . The LEP collider was originally foreseen to produce electron-positron collisions at energies up to* 200 *GeV, and achieved a collision energy of* 209 *GeV in its last year of running, in 2000.*

The LHC will produce head-on collisions between two beams of particles, either protons or heavy ions. The beams will be produced and pre-accelerated in CERN's chain of accelerators (see Fig. 3.1), and then injected into the LHC. It will be the first accelerator able to generate proton-proton collisions at $\sqrt{s_{NN}} = 14$ TeV, that is a factor 7 with respect to TEVATRON energies, and lead-lead collisions at $\sqrt{s_{NN}} = 5.5$ TeV, a factor 30 with respect to the RHIC collider. The LHC nominal running conditions in the ALICE experiment interaction point are summarized in Tab. 3.1. This new energy domain will open new insights in particle and nuclear physics.

3.1.1 The beam travel road

In the LHC accelerator, particles circulate in a vacuum tube, are kept in circular orbits using dipole magnets, are focused by means of quadrupole magnets, and are accelerated at LHC cavities with electromagnetic resonators. In Fig. 3.2 can be seen some details of the LHC ring and of the cryodipoles. The maximum energy of the collisions is determined by the dipole

	p-p	Pb-Pb	Ar-Ar	p-Pb
$\sqrt{s_{NN}}$ [TeV]	14	5.5	6.3	8.8
$\langle\mathcal{L}\rangle$ [cm^{-2}s^{-1}]	$3 \cdot 10^{30}$	$5 \cdot 10^{26}$	10^{29}	10^{29}
Rate [s^{-1}]	$2 \cdot 10^{5}$	$4 \cdot 10^{3}$	$3 \cdot 10^{5}$	$2 \cdot 10^{5}$
Runtime [s]	10^{7}	10^{6}	10^{6}	10^{6}
σ_{geom} [b]	0.07	7.7	2.7	1.9

Table 3.1: LHC nominal running conditions at interaction point 2, in the ALICE experiment.

magnet parameters and the collider circumference, in particular by their magnetic rigidity ($B\rho$). The momentum P of the beam particles is given by

$$P = q\,B\rho \qquad \longrightarrow \qquad \frac{P}{A} = \frac{Z}{A} e\,B\rho\,.$$

Since the maximum energy delivered by the LHC for proton beam is 7 TeV, the corresponding maximum energy for lead beams is 2.7A TeV ($Z/A \sim 0.4$).
The travel done by proton and lead ion beams (as an example of heavy ion beam) from their production point till their interaction point following is outlined in Fig. 3.1.

Proton beam The proton beam travel [Sch99] begins at the *Linac2*. Orbiting electrons are stripped off from hydrogen atoms. The protons are sent at an energy of 50 MeV from the *Linac2* to the *Proton Synchrotron Booster* (PSB), and accelerated to 1.4 GeV. Then the beam is fed to the *Proton Synchrotron* (PS) and accelerated to 25 GeV. Later it is injected into the *Super Proton Synchrotron* (SPS), where it is accelerated to 450 GeV. Afterwards the protons are transferred to the LHC where they are accelerated to their nominal 7 TeV energy.

Lead ion beam The lead ions are produced by the *Electron Cyclotron Resonance* sources (ECR) [Mar06] and later transferred to the *Linac3*. The ERC is a plasma device that permits to generate multi-charged ion states with the help of heat, a magnetic field and microwaves. A sample of different charge states with a maximum of Pb^{27+} are produced. These ions are selected, accelerated to 4.2 MeV/nucleon *(energy per nucleon)* and passed through a carbon foil, which strips most of them to Pb^{54+}. The Pb^{54+} beam is accumulated and accelerated to 72 MeV/nucleon in the *Low Energy Ion Ring* (LEIR). It is sent to the PS, which accelerates it to 5.9 GeV/nucleon, passes it through a second foil (which fully strips it to Pb^{82+}) and transfers it to the SPS. Finally the SPS accelerates it to 177 GeV/nucleon and injects it to the LHC, where it is accelerated to the nominal 2.76 TeV/nucleon energy [Sch99, B+04].

3.2 The ALICE Detector

A Large Ion Collider Experiment, i.e. ALICE [C+04, A+06], was designed for the study of heavy ion collisions [Ant07]. The experiment will allow to investigate a wide fan of observ-

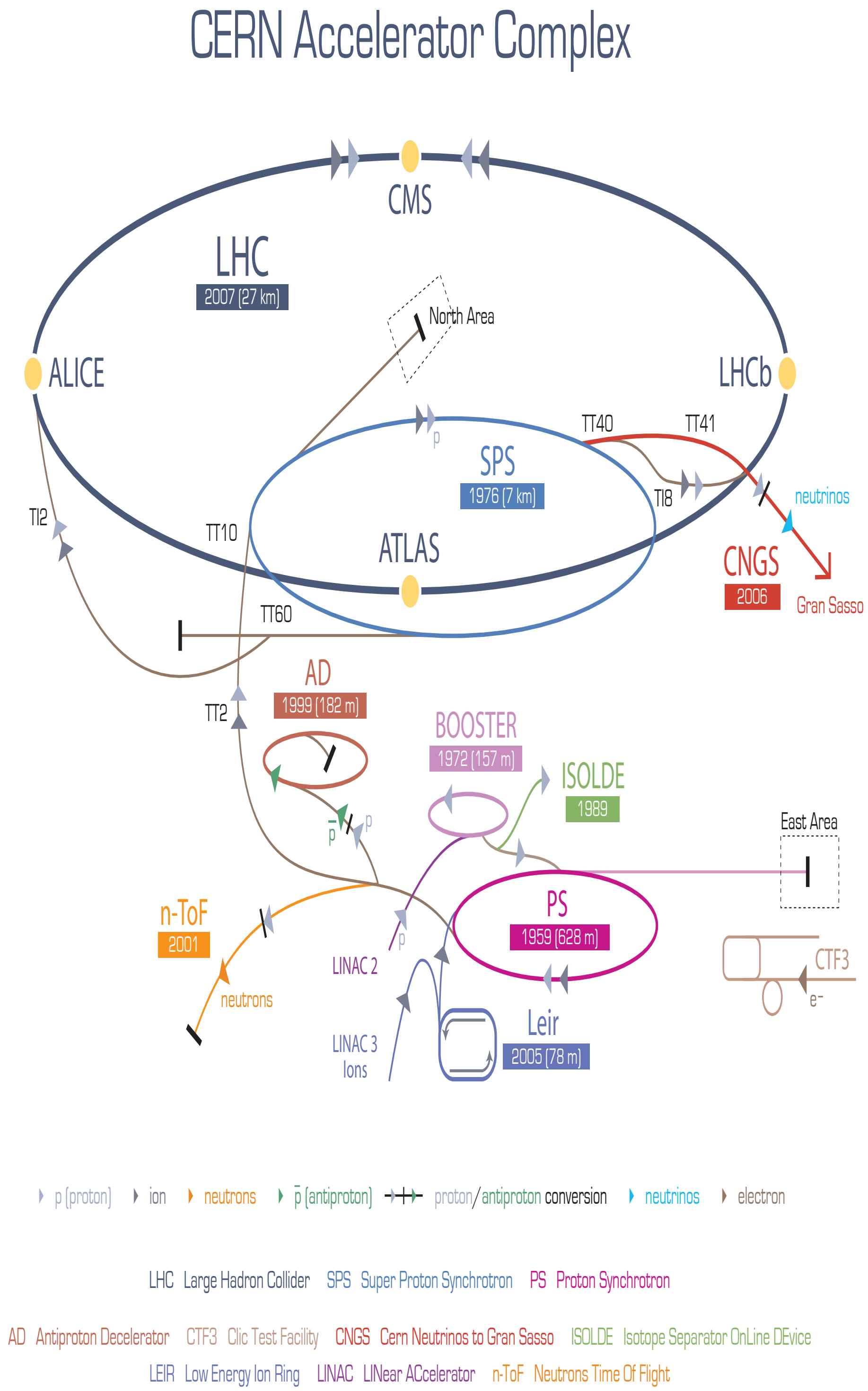

Figure 3.1: CERN Accelarator Complex.

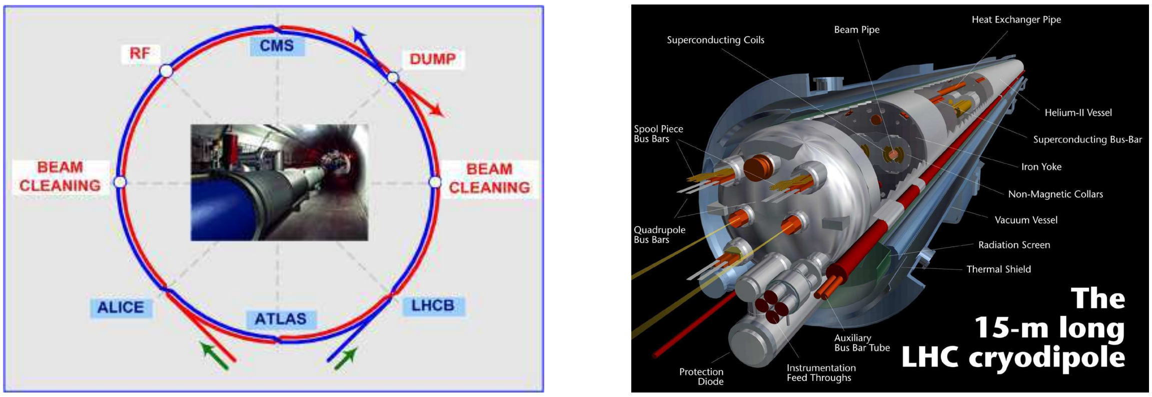

Schema of the LHC ring

The LHC cryodipole

Figure 3.2: Details of LHC collider.

ables from very low (~ 100 MeV/c) up to fairly high (~ 100 GeV/c) transverse momenta, p_T, in a center-of-mass energy domain not explored up to now. It will be able to track and identify particles in this p_T interval and to perform these tasks in a large particle multiplicity environment (up to 8000 particles per unit of rapidity at mid-rapidity[1]).

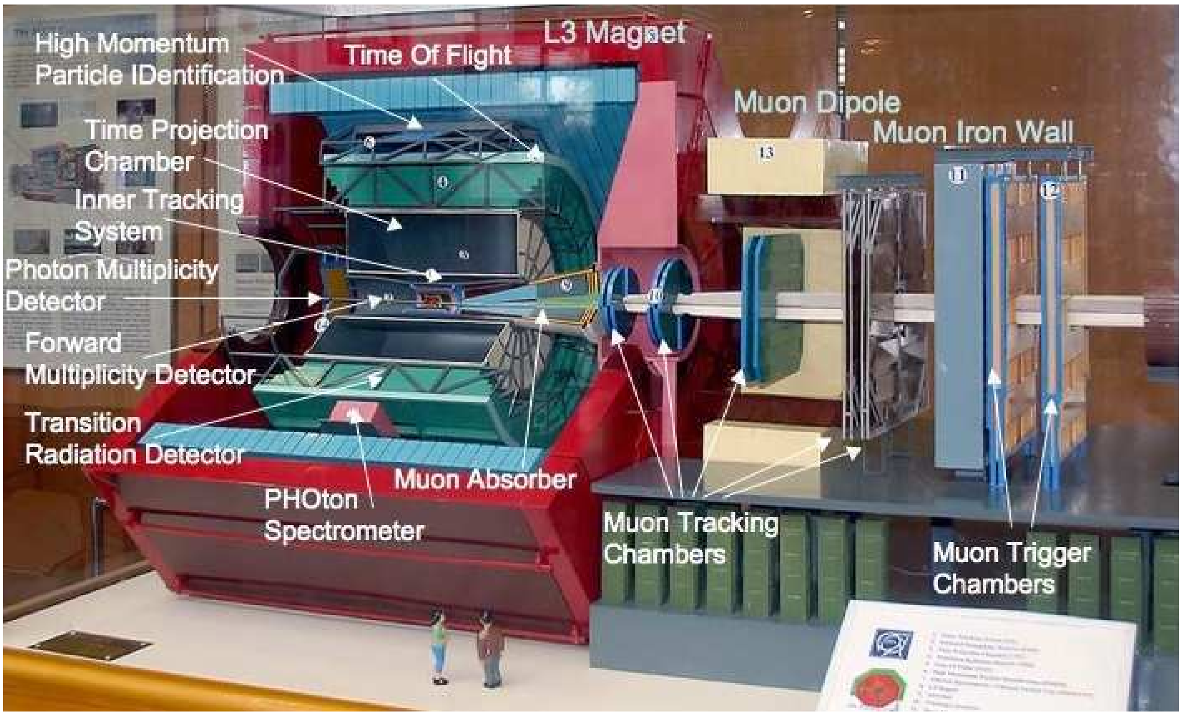

Figure 3.3: ALICE detector layout.

---

[1] The experiment was designed about 10 years ago in order to work in an expected harsh environment of 8000 particles per unit of rapidity at mid-rapidity. Nowadays RHIC data suggest to update the predictions reducing this value by a factor of 4, which assures that ALICE can perfectly cope with the expected particle multiplicities.

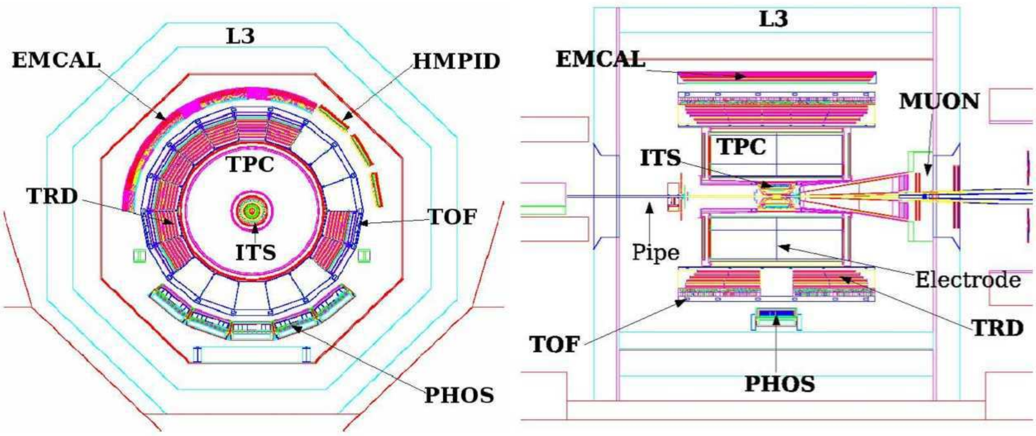

Figure 3.4: ALICE longitudinal and transversal sections, including EMCAL. In PHOS and HMPID coverage regions neither TRD nor TOF detectors are color filled.

The ALICE experiment consists of some detectors for measuring global observables (defined as global detectors), a central barrel and a muon spectrometer. The central barrel covers a pseudo-rapidity range of $|\eta| \leq 0.9$, is flooded by a magnetic field $B \leq 0.5$ T generated by a large solenoidal magnet (L3), and is in charge of tracking and identifying charged particles and photons. From the vertex region to the outer part it is composed by a vertex detector, the Inner Tracking System (ITS), a large Time Projection Chamber (TPC), a Transition Radiation Detector (TRD) for electron identification, and a Time Of Flight detector (TOF) to identify protons, kaons and pions, all of them with full azimuth acceptance. It disposes also of a High Momentum Particle Identification (HMPID) detector to extend the transverse momenta coverage of particle identification, and a Photon Spectrometer (PHOS) to identify photons, both with reduced azimuthal acceptance. The muon spectrometer covers a pseudo-rapidity range of $-4.0 < \eta < -2.5$, has its proper magnetic field of $B \leq 0.7$ T provided by a dipole magnet, and is responsible of muon tracking and reconstruction. For this purpose it consists, from the interaction vertex forwards, of a front absorber, five tracking stations, an muon filter and two trigger stations. In addition, the ALICE global detectors are the Forward Multiplicity Detector (FMD), the Photon Multiplicity Detector (PMD), the V0 and the T0, that take care of event particle multiplicity and beam luminosity measurement, and the Zero Degree Calorimeter (ZDC) in charge of event centrality evaluation. The experiment is completed by an array of scintillators for triggering on cosmic rays (ACORDE) and an ElectroMagnetic CALorimeter (EMCAL)[2]. The detector layout can be seen in Fig. 3.3, and longitudinal and transversal sections can be observed in Fig. 3.4.

---

[2] ALICE EMCAL will cover $|\eta| < 0.7$ and $\pi/3 < \phi < \pi$ but will not be installed the first year of data-taking.

3.2.1 Global detectors

As global detectors we considered the FMD, the PMD, the V0, the T0 and the ZDC. In particular we refer to the ALICE forward detectors as: the FMD, the V0 and the T0. Fig. 3.5 shows their position with respect to the ITS [C+04, ALI04]. Further details of those detectors can be observed on Fig. 3.6.

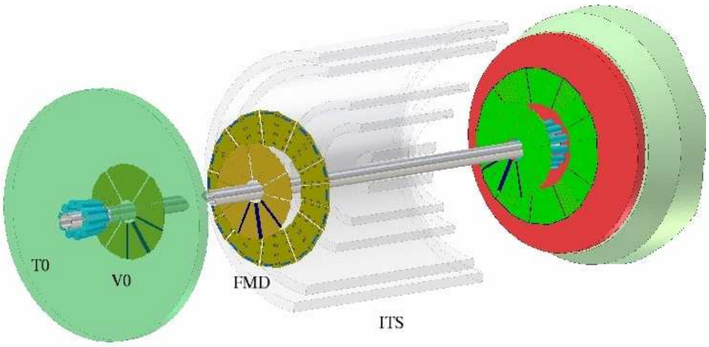

Figure 3.5: Forward detectors location schema. From left to right up to ITS: T0, V0, FMD, ITS.

FMD: Forward Multiplicity Detector

The Forward Multiplicity Detector, FMD, consists of five rings of silicon strip detectors whose dimensions are presented in Tab. 3.2. ***It is in charge of evaluating the charged particle multiplicity in the pseudo-rapidity range*** $-3.4 < \eta < -1.7$ ***and*** $1.7 < \eta < 5.1$***, and it will also permit to determine the reaction plane event-by-event.*** Together, the ITS and the FMD will provide an early charged particle multiplicity measurement for $-3.4 < \eta < 5.1$ in all colliding systems.

In order to reconstruct particle multiplicity with the FMD two approaches can be considered. The Poisson approach assumes that on average each channel will be traversed by about one charged particle per central event[3].

---

[3] The extreme approach of 8000 particles per unit of rapidity at mid-rapidity drives to an evaluation of less than 3 charged particles per strip for all channels, including background.

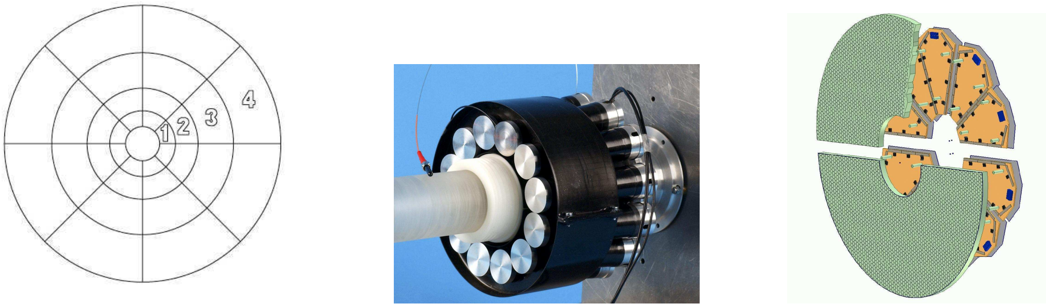

V0 scheme. T0 prototype. FMD scheme.

Figure 3.6: Details of V0, T0 and FMD.

Then multiplicity information can be obtained by comparing the number of occupied and empty channels. That is counting the number of empty channels, and evaluating the charged particle multiplicity by statistics. The other approach, that will be more probably used, is to derive charged particle multiplicity from the measurement of the deposited energy on each strip. This approach supposes that each particle deposes (on average) the same amount of energy (minimum ionizing particles, MIPs).

Ring	z (cm)	R_{in} (cm)	R_{out} (cm)	η coverage
Si1 outer	-75.2	15.4	28.4	$-2.29 < \eta < -1.70$
Si1 inner	-62.8	4.2	17.2	$-3.40 < \eta < -2.01$
Si2 outer	75.2	15.4	28.4	$1.70 < \eta < 2.29$
Si2 inner	83.4	4.2	17.2	$2.28 < \eta < 3.68$
Si3	340.0	4.2	17.2	$3.68 < \eta < 5.09$

Table 3.2: FMD detector dimensions.

V0

The V0 detector is involved on fast trigger and centrality determination tasks. It is made of two arrays of scintillator counters, labeled V0A and V0C, that are segmented into four rings and eight sectors (sectors of 45°). The scheme of one array can be observed in Fig. 3.6. The V0A is located at $z = 340$ cm, and the V0C at $z = -90$ cm, in front of the muon absorber. The rings angular coverage is presented on Tab. 3.3.

	V0A		V0C	
Ring	η_{max}/η_{min}	$\theta_{min}/\theta_{max}$	η_{max}/η_{min}	$(\pi-\theta)_{min}/(\pi-\theta)_{max}$
1	$5.1/4.5$	$0.7/1.3$	$-3.7/-3.2$	$2.8/4.7$
2	$4.5/3.9$	$1.3/2.3$	$-3.2/-2.7$	$4.7/7.7$
3	$3.9/3.4$	$2.3/3.8$	$-2.7/-2.2$	$7.7/12.5$
4	$3.4/2.8$	$3.8/6.9$	$-2.2/-1.7$	$12.5/20.1$

Table 3.3: η coverage and angular acceptance (in deg) of the rings for V0A and V0C.

Each counter consists of scintillator material with embedded WaveLength Shifting (WLS) optical fibers to collect the produced light. These fibers absorb predominantly the blue light and reemit green light. The light is then transmitted through a clear fiber to a photo-multiplier tube (PMT) located at $3-5$ m from the detectors. Each individual counter has a time resolution better than 1 ns and provides time-of-flight and signal charge information. It characterizes the V0 a fast detector. ***The V0 will provide a fast trigger signal and it will permit to validate the muon trigger signal by rejecting beam-gas interactions***[4]. Particularly, as trigger signals it will provide a minimum bias trigger and two centrality triggers

---

[4] Beam-gas interactions can be identified by measuring the time-of-flight difference of V0A and V0C signals.

(on Pb-Pb collisions), as the T0 will. It will also serve as a centrality indicator, and ***it will permit to control the beam luminosity.***

T0

The T0 detector is made of two arrays of Cherenkov counters with 12 individual counters per array. The right array, T0C, is located at $z = -70$ cm (muon spectrometer side) and covers $-2.9 < \eta < -3.3$. The left array, T0A, is located farther from the interaction point, at $z = 350$ cm, and covers $5 < \eta < 4.5$. Each Cherenkov counter is based on a fine-mesh photo-multiplier tube, 30 mm in diameter and 45 mm long, optically coupled to a quartz radiator 30 mm in diameter and 30 mm thick. This detector has a time resolution of about 50 ps (individual counters have a time resolution of 37 ps), and is able to measure the vertex position with a resolution of 1.3 cm. The T0 is in charge of:

- ***Provide a measurement of the collision time, a T0 signal*** that the TOF detector needs.;
- ***Generate a L0 trigger*** by means of a fast vertex position measurement. It helps to discriminate against beam-gas interactions;
- ***Provide an early 'wake-up' signal to the TRD, prior to L0***;
- ***Measure particle multiplicity and generate three possible trigger signals***: minimum bias, and two centrality triggers (as the V0 will).

PMD: Photon Multiplicity Detector

The pre-shower Photon Multiplicity Detector, PMD, ***measures event-by-event photon multiplicity and spatial (η,φ) distribution of photons*** [C+04, ALI99c, ALI03]. It is located at $z = 360$ cm and covers $2.3 \leq \eta \leq 3.5$. Fig. 3.7 presents its structure. It consists of two iden-

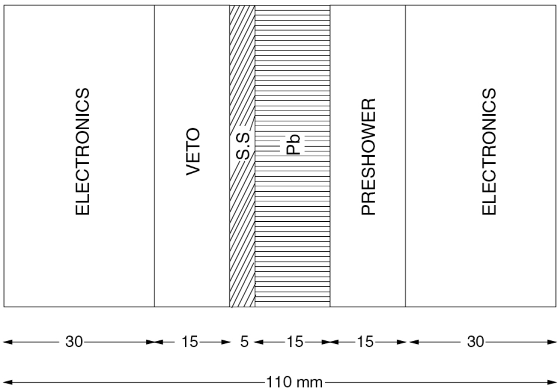

Figure 3.7: Photon Multiplicity Detector structure. S.S. is the support plate for the lead converter plates.

tical planes of detectors with a $3X_0$ lead converter in between them. The detector is a gas proportional counter with wire readout and the particularity of having a honeycomb structure and operating with a mixture of $\mathrm{Ar}/\mathrm{CO}_2$ ($70\%/30\%$). The hexagonal cells have a cross section of 0.22 cm^2, and a depth of 0.5 cm. The detector plane situated on the interaction side is used for vetoing charged particles and is labeled the *veto*, and the other detector plane is called the *pre-shower* and gives both photons and charged hadrons signals. So the photon signal can be disentangled.

ZDC: Zero Degree Calorimeter

The Zero Degree Calorimeter, ZDC, role is to ***measure the number of spectator nucleons and hence to determine the centrality of the interaction*** [C$^+$04, ALI99e]. When an interaction takes place, the spectator nucleons (the nucleons that do not interact) are ejected at forward rapidities. The ZDC measures the number and energy of these spectator nucleons in order to evaluate the number of participants and the event centrality.
The detector is composed by two hadronic calorimeters: the neutron calorimeter (ZN, that measures the spectator neutrons), and the proton calorimeter (ZP, that measures the spectator protons), and by an electromagnetic calorimeter (ZEM, that estimates the participating nucleons). *The hadronic calorimeters are placed at $z = \pm 116$ m and are made of a dense passive material and quartz fibers (Cherenkov detectors) interspersed in the passive material. The spectator nucleons entering the calorimeter generate showers which produce Cherenkov radiation that is detected by the quartz fibers. The ZN is located between the two beam pipes, to profit that neutrons are not deflected by the LHC machine magnetic field. In opposition, the ZP is placed externally to the outgoing beam pipe, on the side where the positive particles are deflected. Fig. 3.8 shows ZP and ZN position with respect to the LHC beam pipes, and Tab. 3.4 presents ZN, ZP and ZEM characteristics. On the other hand, the two ZEMs are placed at $z = 7$ m, in the opposite side of the muon spectrometer, and covers $4.8 < \eta < 5.7$. It evaluates the participating nucleons by measuring the energy of the generated showers. The detector technique is the same that for the ZN and ZP, but it is made of lead planes of 3 mm readout by sandwiched quartz fibers, which are oriented at 45° (where the peak of the Cherenkov produced light is).*

	ZN	ZP	ZEM
z (m)	116	116	7
Dimensions (cm^3)	$7.04 \times 7.04 \times 100$	$12 \times 22.4 \times 150$	$7 \times 7 \times 21$
Absorber material	Tungsten alloy	Brass	Lead
Fiber orientation	0°	0°	45°
Filling ratio	$1/22$	$1/65$	$1/11$

Table 3.4: ZDC calorimeters dimensions and characteristics.

By comparing the energy measured by the ZEM, E_{ZEM}, and the energy of the spectator nucleons $E_{ZDC} = E_{ZN} + E_{ZP}$, one is comparing the number of participants and the number of spectator nucleons. Then, one can determine the centrality of the interaction. As an example, Fig. 3.9 presents a plot where 10 centrality classes have been defined.

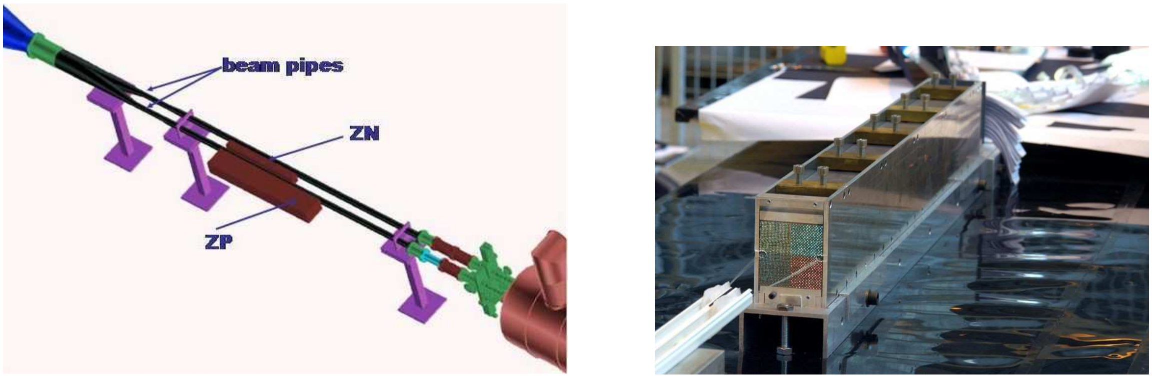

Location of the proton and neutron calorimeters. View of a neutron calorimeter.

Figure 3.8: Details of the ZDC.

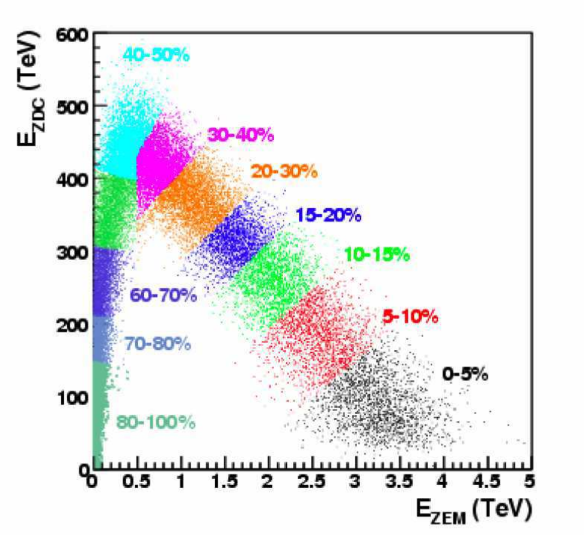

Figure 3.9: Centrality classes determination from ZDC energy and ZEM energy, using fast simulations.

3.2.2 Central Barrel

ITS: Inner Tracking System

The Inner Tracking System, ITS, is the innermost detector of ALICE and its main purpose is to participate in tracking and to provide vertexing measurements to the experiment. It consists of six cylindrical layers of silicon detectors and covers $|\eta| \leq 0.9$ for all vertices located within the length of the interaction diamond ($\pm$ 1 σ, i.e. 10.6 cm along the beam axis) [C+04, ALI99b]. It combines different silicon detector technologies in order to accomplish its design requirements regarding its acceptance coverage, the $\mathrm{d}E/\mathrm{d}x$ measurement, the desired spatial resolution, the need to minimize the amount of material in the active volume, the radiation levels attained at this area, and the readout rate. Thereby, the innermost two layers are equipped with Silicon Pixel Detectors (SPD), the following two layers are equipped with Silicon Drift Detectors (SDD) and the external two layers with double-sided Silicon micro-Strip Detectors (SSD). ITS layout can be observed on Fig. 3.10, and Tab. 3.5 summarizes its dimensions and characteristics. We can point out that the first layer has a wider pseudo-rapidity coverage $|\eta| \leq 1.98$ to permit a continuity on the measurement of charged particle multiplicity at higher rapidities (together with the FMD). On the other hand, the four outermost layers will have analogue readout to allow $\mathrm{d}E/\mathrm{d}x$ measurement for particle identification. Basically, the ITS is able to:

- ***Localize the primary vertex with a resolution much better than*** $100\ \mu$***m***;
- ***Reconstruct secondary vertices*** from decays of hyperons and D and B mesons;
- ***Improve the TPC measurements extending momentum coverage below*** 100 ***MeV and ameliorating the*** (p, θ) ***resolution***.

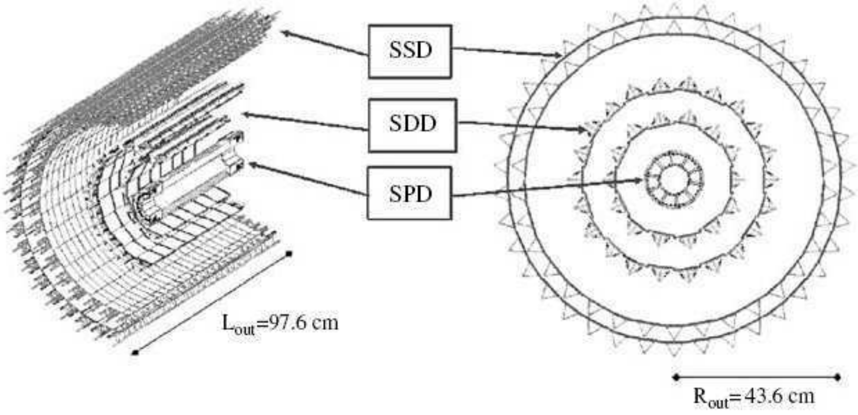

Figure 3.10: ITS layout.

Layer	Type	r (cm)	$\pm\ z$ (cm)	S.P. $r\varphi(\mu\mathrm{m})/z(\mu\mathrm{m})$
1, 2	Pixel	3.9, 7.6	14.1	12/100
3, 4	Drift	15.0, 23.9	22.2, 29.7	38/28
5, 6	Strip	37.8/38.4, 42.8/43.4	43.1, 48.9	20/830

Table 3.5: ITS detector dimensions and characteristics [C+04], where S.P. stands for spatial precision.

TPC: Time Projection Chamber

The ALICE Time Projection Chamber, TPC, is the main tracking detector of the ALICE central barrel [C+04, ALI00b]. ***It is in charge of tracking and determining charged particle mo-***

menta with a good two-track separation, to enable particle identification and event vertex position evaluation. It will be able to determine charged particles p_T from 100 MeV/c (with $1\% - 2\%$ resolution) up to 100 GeV/c (with $\sim 5\%$ resolution if ITS is also used). The harm of using the TPC is its memory time, which limits the luminosity that the ALICE experiment can afford.

The TPC is a cylindrical cage of 510 cm long (z position between ± 255 cm), internal radius of 84 cm and external radius of 246 cm. It covers $|\eta| \leq 0.9$ (up to $|\eta| \sim 1.5$ for tracks with a small track length). Fig. 3.11 presents a scheme of the TPC layout. *It is characterized by having a central high-voltage electrode of* 100 *kV and two opposite axial potential degraders, providing a highly uniform electrostatic field of* 400 $V\ cm^{-1}$ *in the common gas volume, which is filled with* 88 m^3 *of a* Ne/CO_2 *mixture* ($90\%/10\%$)*. Those characteristics result on a maximum drift time of* 88 μs *which limit the memory time of the TPC. The end-plates of the detector are equipped with multi-wire proportional chambers with cathode pad readout, structured in 18 trapezoidal sectors at each end-plate. Those sectors are radially segmented into two chambers at radii* $84.1, 132.1, 246.6$ *cm. The readout chambers pad sizes are of* 4×7.5, 6×10 *and* 6×15 mm^2*. Those chambers are closed by a gating grid, located above the cathode wire grid, with alternate wires connected together electrically. When there's a L1 trigger* (6.5 μs *after the collision), the gates are opened for the duration of the drift time. That means that the wires are held at the same potential, permitting the pass of the electrons generated in the drift region into the amplification region. Otherwise the gate is closed, the grid is biased by a bipolar field, preventing the electrons to enter the amplification region and stopping the ions created by avalanche processes in the amplification region. The gates have then the mission to prevent TPC space charge.*

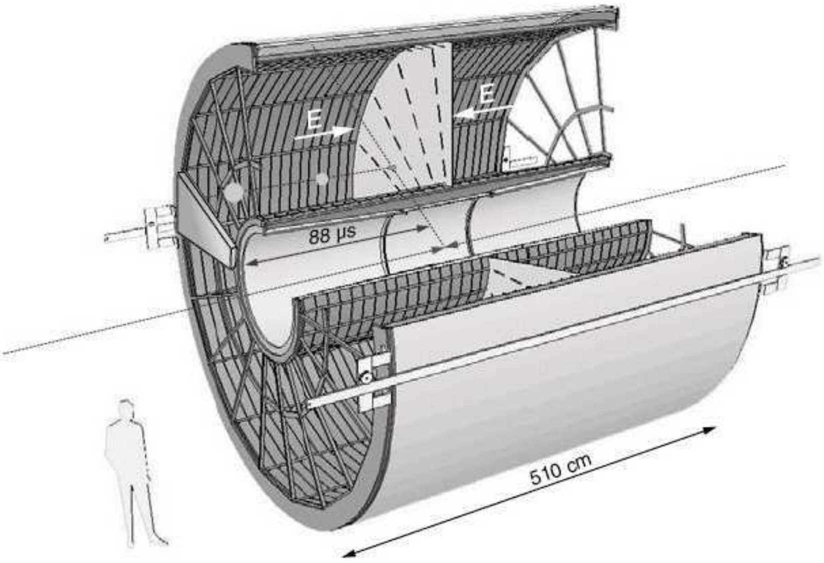

Figure 3.11: TPC layout.

TRD: Transition Radiation Detector

The Transition Radiation Detector, TRD, covers $|\eta| \leq 0.9$ and is situated between the TPC and the TOF detectors, that is at a radius of $(2.9, 3.7)$ m and $|z| < 3.5$ m [C⁺04, ALI01]. It is composed by 18 sectors (as the TPC), and each sector is made of 6 layers and 5-fold segmentation along the beam axis (that is a total of $18 \times 6 \times 5 = 540$ modules). The module consists of a radiator of 4.8 cm thickness and a multi-wire proportional chamber (MWPC) with cathode pad readout. The chambers are filled with a gas mixture of Xe/CO_2 $(85\%/15\%)$, and the typical pad size is of $6 - 7$ cm^2. The detector $r\varphi$ resolution is about 400 μm. The TRD momentum resolution in standalone mode is:

$$\frac{\Delta P}{P} \approx 2.5\% \oplus 0.5(0.8)\% \cdot P(\mathrm{GeV/c}) \qquad \text{for } \frac{dN_{ch}}{d\eta} = 2000(8000)$$

The principle of the radiation detector comes from the fact that when a relativistic charged particle traverse the boundary of two media of different dielectric constant, it produces transition radiation. It depends strongly on the relativistic γ factor, which makes it suitable for particle discrimination. In particular, for the P range $1 - 100$ GeV/c just the electrons produce transition radiation. Radiation that is in form of X-rays (energy in the keV range) and has a peaking angle of the order of $1/\gamma$ relative to the particle's path.

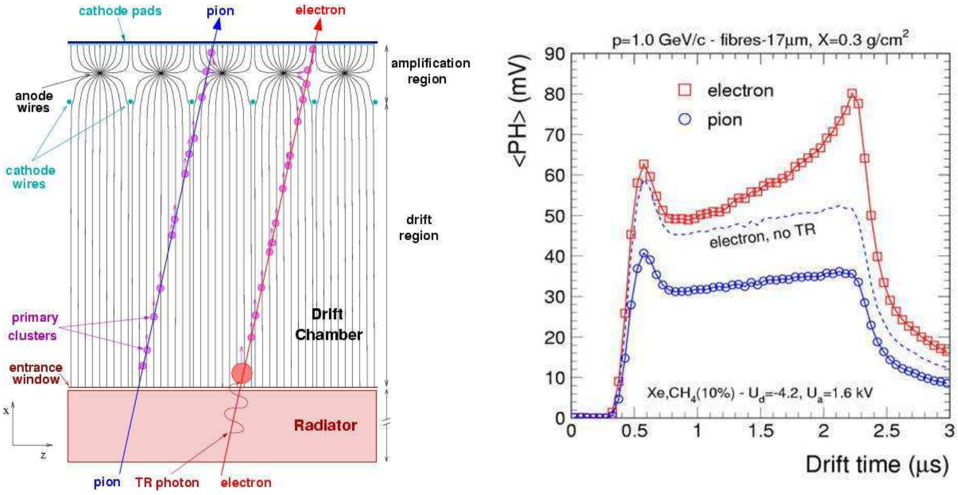

Schema of a TRD.

Measured signal vs time for π and e.

Figure 3.12: Schema of a TRD module and of the measured signal vs time spectra for e and π with and without the radiator.

Fig. 3.12 presents a sketch of a TRD module and a figure of the measured signal versus time for electrons and pions. The electron signal with and without the presence of the radiator is plotted. The pion signal represent the signal of a charged particle crossing the MWPC, where the peak in the first μs *comes from the particles ionized in the multiplication region. On the other hand, for the chosen gas mixture, when there's transition radiation produced the X-rays are absorbed at the beginning of the MWPC, so their signal reaches the pads on the latest moments (with respect to the drift time). This characteristic makes possible the electron identification with the TRD.*

The TRD main functionality is to provide electron identification for $P > 1$ GeV/c by having a good π rejection capability (π suppression of 10^{-2})[5]. As it is a fast tracker, it can serve as trigger for high p_T electrons (L1 trigger for single tracks of $p_T > 3$ GeV/c), and for electron pairs (online PID), and it helps to improve the hadron P measurement and identification.

TOF: Time Of Flight

The Time Of Flight detector, TOF, covers $|\eta| \leq 0.9$ and takes care of particle identification in the intermediate momentum range ($0.2 < P < 2.5$ GeV/c) [C+04, ALI02b, ALI02a]. Together with the ITS and the TPC (for vertex reconstruction and $\mathrm{d}E/\mathrm{d}x$ measurement at low P), they will permit event-by-event identification of pions, kaons and protons. It is composed by 18 sectors (in φ) of 5 segments each (in z) of Multi-gap Resistive Plate Chambers (MRPC) $r\varphi$ oriented. It is localized at a radius of $3.70 < r < 3.99$ m, has a total length of 7.45 m, and its chambers pad size is of 3.5×2.5 cm^2. ***The TOF is characterized by a time resolution better of 40 ps, with permits to identify π, K for $0.2 - 2.5$ GeV/c, p for $0.4 - 4.5$ GeV/c, and e for $0.1 - 0.5$ GeV/c.***

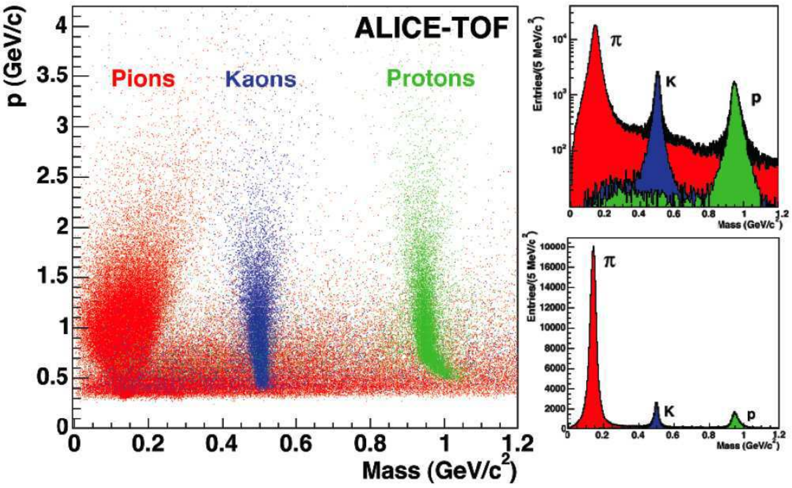

Figure 3.13: Mass separation as a function of momentum with the TOF detector, for 200 HIJING central PbPb events and with a simulated overall TOF time resolution of 80 ps. The right plots present the mass distributions for $0.5 < P < 4.2$ GeV/c in linear and logarithmic scales [A+06].

The identification of the hadrons resides in their different time of flight vs P behavior. The ITS-TPC reconstructed tracks are projected into the TOF, and for the matched particles the travel length (l) is calculated from the track momentum (P). The time of flight (t) allows to evaluate the particle mass as: $m = P\sqrt{t^2/(l^2-1)}$ [ALI02b]. Particles are then entered in a P versus m plot, as the one of Fig. 3.13, which permits to identify them.

---

[5] That means that for each 100 hadrons, just 1 would be labeled as an electron by the TRD.

HMPID: High Momentum Particle IDentification

The High Momentum Particle IDentification, HMPID, is one of the outer detectors of ALICE [C+04, ALI98]. It is located at a radius of 5 m and its azimuthal and pseudo-rapidity coverage are of $\Delta\varphi = 57.61^\circ$ and $|\eta| \leq 0.6$. It consists of 7 modules of 1.5×1.5 m^2 of proximity-focusing Ring Imaging Cherenkov (RICH) counters. The physics basis of the RICH detectors reside on the fact that when a charged particle crosses a dielectric medium (a radiator) at a higher speed than the speed of light in the medium, the particle emits Cherenkov radiation. Radiation which is characterized by an emission angle of $cos\theta = 1/n\beta$ ($\beta = v/c$, n is the refractive index of the medium).
The HMPID radiator is a 15 *mm thick layer of* C_6F_{14} *liquid, corresponding to a* $\beta_{min} = 0.77$*, a momentum threshold of* 1.21 m *(where* m *is the particle mass). The Cherenkov photons are detected by a photon counter, that consists of a multi-wire pad chamber (MWPC) with CsI deposited onto the pad cathode. This photo-detector is filled with methane, and its pads size is of* 8×8.4 *mm*^{2}*. In particular, the electrons generated by ionization in the proximity gap are prevented from entering the MWPC by a positive polarization of the collection cathode close to the radiator. On the other hand, the light cones reach the CsI, which converts them into photo-electrons, that are detected by the MWPC. Once the Cherenkov rings are detected, the Cherenkov angles can be measured with an accuracy of a few mrad.* The correlation between the Cherenkov angle and the particle momenta allows to identify π, K and p. ***Therefore, this detector enables inclusive measurements of identified hadrons for*** $p_T > 1$ ***GeV/c, and extends*** π/K ***discrimination to*** 3 ***GeV/c and*** K/p ***to*** 5 ***GeV/c on a track-by-track analysis.***

PHOS: PHOton Spectrometer

The ALICE PHOton Spectrometer, PHOS, is situated in the bottom part of the central barrel, at 460 cm of the interaction point. It covers $|\eta| \leq 0.12$, and $\Delta\varphi = 100^\circ$ [C+04, ALI99d]. It is composed by two different elements, the Charged-Particle Veto (CPV) and the ElectroMagnetic Calorimeter (EMC). The EMC is made of lead-tungstate crystals ($PbWO_4$ or PWO) of $22 \times 22 \times 180$ mm^3, readout by Avalanche Photo-Diodes (APD). The CPV is located in front of the EMC at a distance of about 5 mm, and consists of multi-wire proportional chambers (MWPC) with cathode pad readout, operated with a mixture of Ar/CO_2 ($80\%/20\%$).

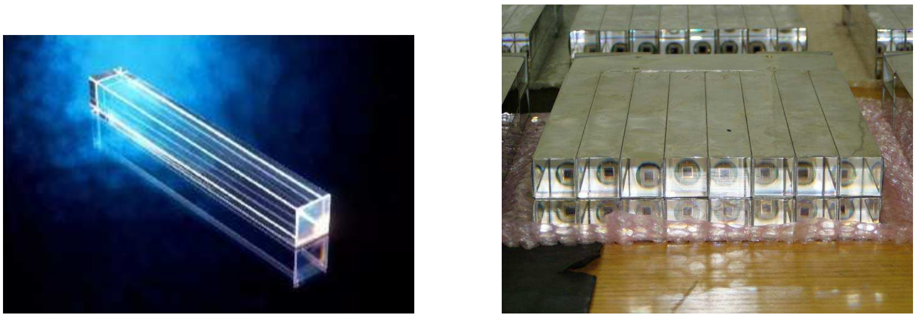

PHOS PWO crystal.

EMC module of the PHOS detector.

Figure 3.14: PHOS details.

The CPV detects the charged particles with an efficiency of 99% and a spatial precision of 1.6 mm. Then, one considers that a photon is detected and identified when the EMC detects an electromagnetic shower and the CPV does not. A posteriori, the measurement of the time of flight with a precision of a few ns enables to distinguish photons from baryons, which is particularly useful for neutron discrimination. ***Hence, PHOS provide photon and neutral meson (through the two photon decay channel) identification from a few hundreds of MeV/c to several tens of GeV/c, and it will procure a fast trigger.***

3.2.3 Muon Spectrometer

The ALICE Muon Spectrometer was designed in order to measure the spectra of the quarkonia, the J/ψ and Υ families (that is J/ψ, ψ' and Υ, Υ', Υ'') as well as the ϕ meson, by means of their muonic decay. In order to disentangle the resonances of the Υ family an invariant mass resolution of 100 MeV/c^2 at about 10 GeV/c is required. ***Then, its mission is to identify and reconstruct muons in the angular range from*** $171°$ ***to*** $178°$***, that corresponds to an interval of*** $-4.0 \leq \eta \leq -2.5$ [C$^+$04, ALI99a, ALI00a]. This angular coverage is restricted by the beam shield, which protects the tracking chambers from secondary particles, and by the TPC volume. The muon spectrometer layout is represented in Fig. 3.15. It is composed by

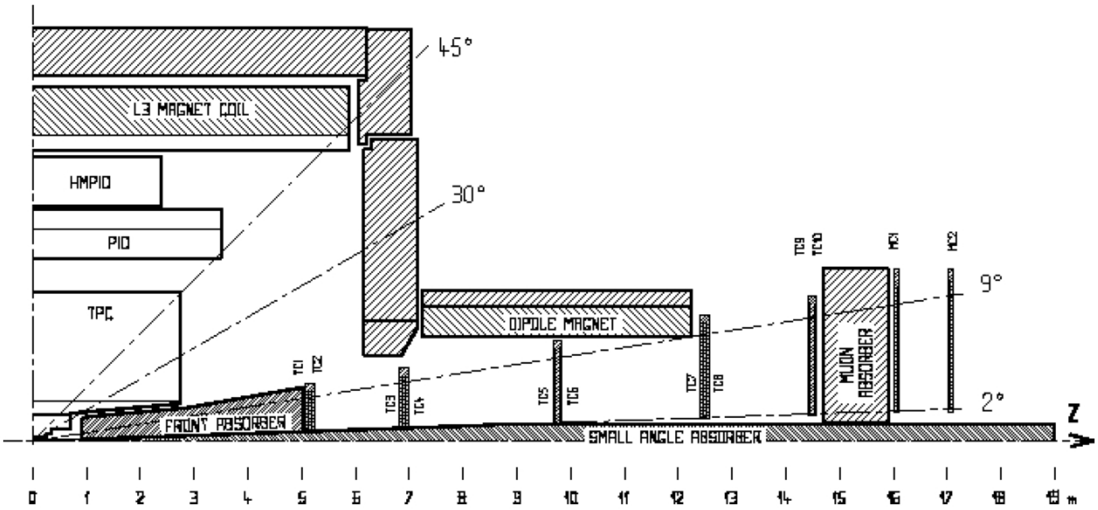

Figure 3.15: Muon spectrometer layout with respect to the interaction point.

some passive elements: the front absorber, the beam shield and the muon filter, to reduce the background to identify muons; by a dipole magnet, which allows to evaluate muon momenta; and some active elements: the trigger and tracking chambers, which generate the trigger signal and permit muon tracking. It should be noticed that the muon trigger system relies on the V0 detector as fast trigger to reduce the background from beam-gas interactions.

The absorbers: Front absorber, Beam shield, Muon filter

The front absorber has 4 m of length ($\sim 10\ \lambda_{int}$) and is placed inside the L3 magnet, as close as possible from the interaction point[6], at 90 cm, in order to ***reduce the background of muons from π and K decays in the tracking chambers.*** As can be observed on Fig. 3.16 it is made predominantly of carbon and concrete, and it can be divided in three parts: a central cone, and an inner and an outer shield. The central cone has a front part (close to the interaction point) made of low atomic number (Z) materials (carbon), to limit multiple scattering, and concrete. The central cone back part (near to the tracking chambers) is made of high Z materials (lead, tungsten), to absorb the particle showers, the secondaries produced in the absorber itself, and the low energy neutrons. It also permits to reduce the tracking chambers background from photons and low energy electrons. On the other hand, the inner shield is composed by lead and tungsten and protects from beam particles, and the outer shield is made of high density materials and protects the central barrel detectors from the absorber recoiling particles.

The beam shield is made of tungsten, lead and stainless steel. It envelopes the beam pipe and has a 'pencil shape': it has an angular coverage aperture of 2° till it attains 30 cm of diameter, then it keeps this diameter till the end of the spectrometer. It ***shields the muon chambers from high rapidity particles and from secondary particles.***

Whereas the front absorber and the beam shield are enough to protect the tracking chambers, the trigger chambers need further protection. **The muon filter** is an iron wall of 1.2 m thick ($\sim 7.2\ \lambda_{int}$) situated between the tracking and the trigger chambers, at 15 m from the interaction point. Its dimensions are $5.6 \times 5.6 \times 1.2\ \mathrm{m}^3$ and it ***reduces further the hadronic background on the trigger chambers.***

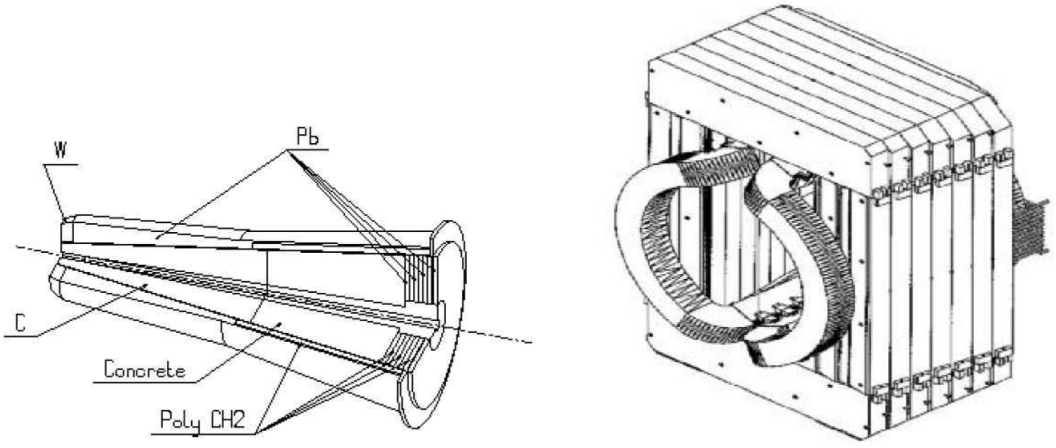

Absorber schema.

Magnetic dipole schema.

Figure 3.16: Schemes of the muon front absorber and the muon dipole.

---

[6] The closest location of the front absorber with respect to the interaction point is constrained by geometrical issues, as the ITS geometrical volume.

The dipole magnet

The magnetic field is a key element of the muon spectrometer. Charged particles passing through a magnetic field are deflected. Then, the measurement of their curvature allows the determination of the particle momenta and charge.
The dipole magnet is equipped with resistive coils on a horseshoe shape (see Fig. 3.16). It is at 7 m from the interaction vertex, has about 5 m of longitude, an aperture of 3.9 m (acceptance from 171° to 178°) and a weight of 900 tons. It provides an axial magnetic field $B \leq 0.7$ T, and the field integral from the interaction point to the muon filter is 3 Tm.

The tracking chambers

The tracking system is formed by five stations of two planes of Cathode Pad Chambers (CPC) each, that's a total of ten detection planes. Two tracking stations are placed before the dipole magnet, one inside, and two after. Fig. 3.17 presents a CPC layout. The CPC are composed by two pad cathode planes separated of 5 mm (on stations 3, 4 and 5) and a wires anode plane situated in the middle. A difference of potential of about 1650 V is applied between them, creating an electric field on the active volume, which is filled with a mixture of Ar/CO_2 ($80\%/20\%$). When a charged particle crosses the detector ionizes the gas, and the created electrons travel to the anode wires driven by the electric field. Close to the anode wires, and due to the higher electric field in this region, the electrons are able to ionize the gas in its turn, creating an avalanche. The mean number of electrons created per incident electron in the amplification process defines the chamber gain. But on the CPCs the readout is effectuated on both cathode planes. The planes corresponding to the bending plane (cathode 2 on Fig. 3.17) have smaller pad sizes than the pads of the non-bending planes. ***The two cathode plane readout capability of the detector with high granularity (see segmentation at Tab. 3.6) allows a*** $\sim 40\mu$***m position resolution [Bou04].***
Stations 1 & 2 cover a small area and suffer high density particles flux, so a high granularity is required. For this reason, these stations are of quadrant type, and their electronics is situated on the surface of the chambers (see Fig. 3.18). Stations 3, 4 & 5 are not exposed to a high density particle flux. The station 3 is inside the dipole, so its constraints are to minimize the multiple scattering for a good momentum determination. Stations 3, 4 & 5 are of slat type (see Fig. 3.18). They are composed by a set of slats of a size from 40×80 cm^2 to 40×240 cm^2.

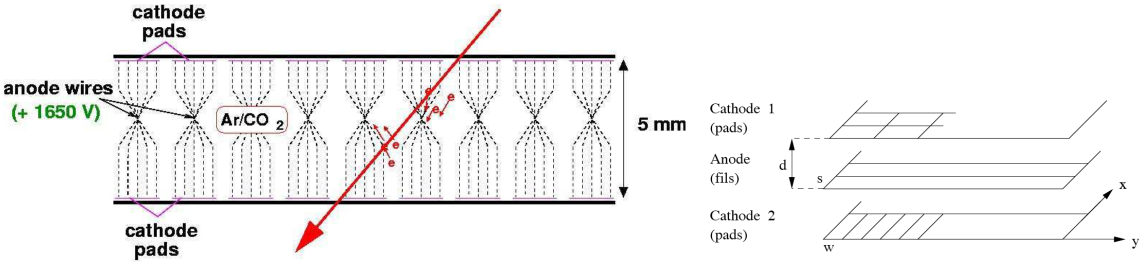

Figure 3.17: Cathode Pad Chamber layout.

Station	Bending pads size [mm^2]	A-C gap [mm]
1	$4 \times 6.4\,,\ 4 \times 12\,,\ 4 \times 24$	2.1
2	$5 \times 7.5\,,\ 5 \times 15,\ 5 \times 30$	2.5
3, 4 & 5	$5 \times 25\,,\ 5 \times 50\,,\ 5 \times 100$	2.5

Table 3.6: Muon tracking chambers characteristics, where A-C gap stands for anode-cathode gap distance.

Half tracking chamber of station 4.

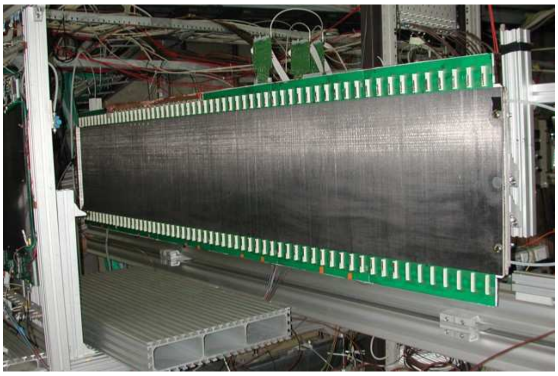

Tracking chamber slat.

Quadrant tracking chamber of station 2.

Figure 3.18: Muon spectrometer tracking chambers.

As the electronics are on their sides, the slats are overlapped to avoid dead zones on the detector.

The Front End Electronics (FEE) of the tracking chambers consists of MANU cards (MANU12 for the slats, and MANU345 for the quadrants), equipped with four MANAS chips and one MARC chip (see Fig. 3.19). About 450 MANU12 are needed to equip one quadrant, and 800 MANU345 to equip one half-chamber for stations 3, 4 & 5. A total of 16828 MANU cards,

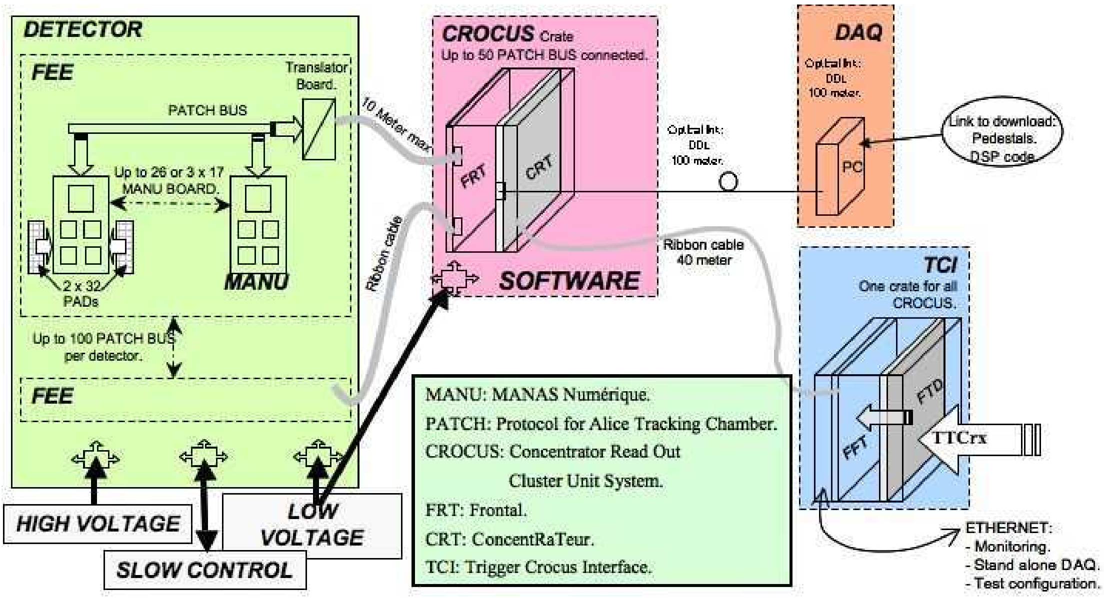

CROCUS read-out.

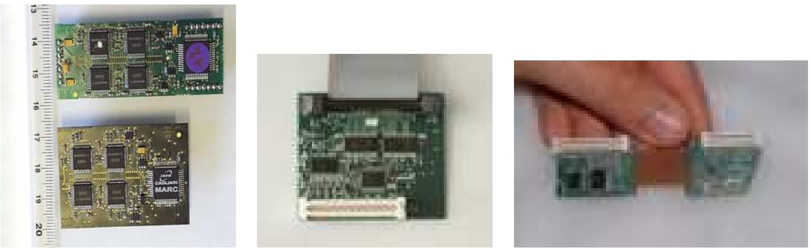

MANU cards. Translator card. Bridge card.

Figure 3.19: Details of muon tracking chambers readout.

67312 MANAS chips and 1064008 electronic channels. The bridge cards connect different PCBs, and groups of one, two or three PCBs are jointly readout by the translator cards. The translator cards send their signal to the 20 Concentrator Read Out Cluster Unit System (CROCUS) crates, that are in charge of transmitting the signal to the Data AcQuisition (DAQ), permitting the monitoring and signal recording (see Fig. 3.19). Another important element of the electronics are the Trigger Crocus Interface (TCI) cards, which give the trigger signal to the CROCUS crates for the readout the tracking chambers.

The tracking capability of the chambers depends strongly on the precision of their position knowledge. The measurement of the deformations and of the relative displacements of the rigid modules (the frames and the intermediate supports) of the tracking system is carried out by the Geometry Monitoring System, GMS, and used to correct the track coordinates in the offline analysis. *The GMS evaluates the in-plane deformations and the displacements of stations* 1 *&* 2*, and the displacements of stations* 3*,* 4 *&* 5 *(the carbon fiber material of these stations frames result on a very weak thermal expansion). First, and before installing the quadrants and the half-chambers on the experimental hall, the photogrammetry technique is used to evaluate its geometry. Then, to monitor their position on the ex-*

periment, 2D sensors are fixed on the rigid modules, on the quadrants supports and the half-chambers frames, outside of the spectrometer acceptance. The positions of the rigid modules are measured with respect to the laser beams crossing consecutively the 2*D semi-transparent sensors. Moreover, the overall position with respect to the ALICE coordinate system, is controlled by monitoring the positions of the laser collimators with respect to the benchmarks placed on the ALICE hall.* The whole measure the chambers relative positions with a resolution better than 20μm, and the chambers planarity with about 70μm.

The trigger chambers

The trigger system is composed by two stations of two planes each of single gap Resistive Plate Chambers (RPC). They are placed behind the muon filter, at 16 m (station 1) and 17 m (station 2) from the interaction point. The distance between the two stations is of 1 m, and the size of each plane is of 6×6 m^2. In Pb-Pb collisions they will be operated in streamer mode, while for p-p collisions where higher counting rates are expected, they will be operated in a highly saturated avalanche regime.

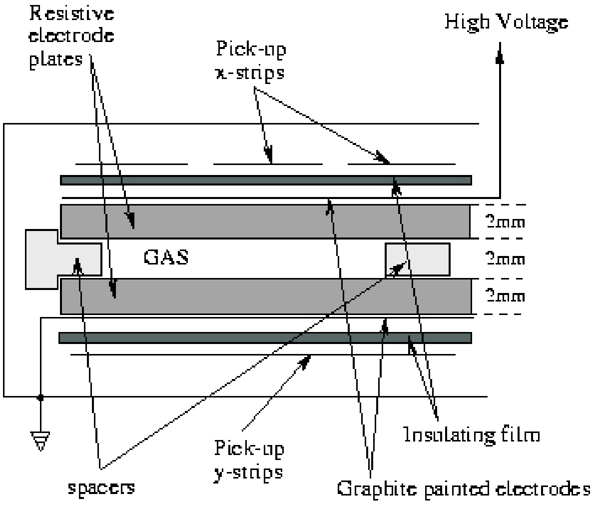

Figure 3.20: Resistive Plate Chamber layout.

The RPCs are formed by two low-resistive bakelite electrodes, 2 mm of gas, two graphite films submitted to high voltage and readout strip planes on the X and Y direction. For the streamer mode the gas mixture is of Ar/$C_2H_2F_4$/i-butane/SF_6 (49%/40%/7%/1%), and the strip pitch on the bending plane is of 10.6, 21.2, 42.5 mm on the station 1. The spatial position resolution attained is better than 1 cm. ***The chambers response is fast: the signal rise time is about* 2 *ns, and the time resolution is of the order of* 1-2 *ns*** . This allows a fast signal treatment and a short dead time. Moreover, as in a time window of 20 ns after the fast muons just 50% of charged particles, 10% of photons and 1% of neutrons reach the detector, it allows a reduction of the background. To fulfill those requirements the RPCs are equipped with dual-threshold front-end discriminators (ADULT). The discriminators send the signal to the trigger electronics which will be treated in Sec. 4.2.1 while describing the muon trigger decision in detail.

The trigger system identifies candidate muon and/or dimuon tracks above a certain p_T. The p_T cut is applied in two levels: first, by fast specialized circuits, and then by fast processors, that apply a more precise cut. It is able to trigger for single muon and/or dimuon tracks of low and high p_T, which corresponds to a cut of 1 and 2 GeV/c respectively. It is also able to do a first evaluation of the particle charge, permitting to identify positive and negative single muon tracks and like and unlike sign muon pairs (dimuons). During data taking period, five trigger types are foreseen: low and high p_T like and unlike sign dimuons, and single muons of all p_T (low and high p_T cuts).

Table 3.7: *Summary table of properties, functions and characteristics of ALICE detectors.*

Element	η	$\Delta\varphi$	z	*Main Functions-Characteristics*
				Magnetic Fields:
L3	± 0.9	360°		Radial field $B \leq 0.5$ T
Muon Dipole	$(-4.0, -2.4)$	360°	-7 m	Axial field of $B \leq 0.7$ T
				Trigger and Centrality:
FMD	$(-3.4, -1.7)$ $(1.7, 5.1)$	360°	$-62, -75$ cm $75, 83, 340$ cm	Event-by-event particle multiplicity and event plane determination.
T0	$(-3.3, -2.9)$ $(4.5, 5.0)$	360°	-70 cm 350 cm	Provide a collision initial time (T_0), L0 trigger ($\sigma < 50$ ps), particle multiplicity and 3 centrality triggers.
V0	$(-3.7, -1.7)$ $(2.8, 5.1)$	360°	-90 cm 340 cm	Fast trigger ($\sigma < 1$ ns), centrality indicator and control beam luminosity.
PMD	$(2.3, 3.5)$	360°	360 cm	Event-by-event photon multiplicity and spatial distribution.
ZDC			116 & 7 m	Event centrality determination.
				Vertexing:
ITS	± 0.9		± 49 cm	Primary vertex ($\sigma < 100 \mu$m) secondary vertices, track and identify particles with $P < 100$ MeV.
				Particle Tracking:
TPC	± 0.9	360°	± 255 cm	Track, identify and determine charged particles momenta (100 MeV < $p_T < 100$ GeV)
				Particle Identification:
TRD	± 0.9	360°	± 3.5 m	e/π rejection for $P > 1$ GeV/c L1 trigger for $P > 3$ GeV/c single tracks and electron pairs.
TOF	± 0.9	360°	± 3.75 m	Identify π, K for $0.2 - 2.5$ GeV/c p for $0.4 - 4.5$ GeV/c and e for $0.1 - 0.5$ GeV/c
HMPID	± 0.6	57.61°	r=5 m	Extends π/K discrimination to 3 GeV/c and K/p to 5 GeV/c
				Electromagnetic calorimetry:
PHOS	± 0.12	100°	r=4.6 m	Identify photons and neutral mesons
				Muon Spectroscopy:
Tracking	$(-4.0, -2.5)$	360°	-5,-7,-10, -12.5,-14.5 m	Track and identify muons of $p_T > 4$ GeV/c
Trigger	$(-4.0, -2.5)$	360°	-16, -17 m	Trigger for single and dimuon low and high p_T muons (1 & 2 GeV/c)

Chapter 4

Performance of the muon spectrometer: J/Ψ and high-p_T muon measurements

> *Theory is when we know something but it doesn't work. Practice is when everything works and don't know why.*
>
> A. Einstein

Abstract

In this chapter we center our interest in the efficiency determination for J/Ψ and high-p_T muons. Muon spectrometer trigger decision and track reconstruction algorithm are briefly reviewed. Possible inefficiency sources and causes of momenta resolution deterioration with the muon spectrometer are discussed. Acceptance correction and global efficiency evaluation via an iterative procedure are exposed. The factorization of the different terms contributing to the efficiency in the ALICE muon spectrometer is developed. Results of those techniques are presented for dimuons, with the J/Ψ as example, and high-p_T single muons.

4.1 Physics motivations

The ALICE experiment was designed with the main purpose to investigate the properties of matter under extreme conditions, i.e. the possible formation and characteristics of the Quark Gluon Plasma in the most central and violent heavy-ion collisions. To achieve such objective it is equipped, among other detectors, of a forward muon spectrometer that will be able to trigger, track and identify muons. This apparatus will allow to measure single muon and dimuon spectra so to examine heavy flavor production via the muon decay channel. Heavy quark and quarkonia are hard probes of the collision. In particular, quarkonia were early pointed out by Matsui and Satz [MS86] as medium-sensitive probes. They have been studied at CERN in the SPS heavy-ion program, are being currently measured and investigated at RHIC collider experiments and have motivated a wide fan of theoretical interpretations. Future LHC measurements will provide additional information in a new energy domain that will help to shed light on the puzzle. In particular, the ALICE muon spectrometer will allow to measure the quarkonia families: an invariant mass resolution of the order of 70 (100) MeV/c^2 is required to separate the individual states of the J/Ψ (Υ) families. The Υ family will be measured and disentangled for the first time in heavy-ion collisions, the quarkonia spectra will be measured down to $p_T \sim 0$: p_T and rapidity shape, centrality dependence and novel observables such as J/Ψ polarization and the relative yield of $\Upsilon(2S)/\Upsilon(1S)$ will become accessible with the expected statistics (see [MG07, Cro05] and references therein). The spectrometer will also permit to examine open beauty production through the single muon and dimuon spectra with unprecedent details (see [Cro05] and references therein). The feasibility of those measurements is obviously strongly related to the accuracy of acceptance and efficiency corrections. For that reason in this chapter we focus on the procedure employed for acceptance and efficiency determination and estimate the expected performances of the muon spectrometer for J/Ψ measurements (p_T from 0 to 20 GeV/c) and single muon high-p_T measurements (from 1 to 80 GeV/c), Sec. 4.3 and 4.4. We shall note that we are particularly interested on the high p_T part of the single muon spectra since the last part of this work will be focused on weak bosons production as medium-blind references that mostly contribute to p_T from 25 to 50 GeV/c. We note that the performances of the muon spectrometer up to such p_T values are investigated in this work for the first time. In addition we will develop and adapt a factorization procedure to the spectrometer in order to facilitate the identification of the various contributions to the efficiency and enable an easier trigger and tracking chambers intrinsic efficiency determination, Sec. 4.5.

4.2 Basics of track reconstruction with the muon spectrometer

Experimentally the performance of an apparatus to measure a particular observable are determined by: its geometrical acceptance, its capability to trigger on the specific probe (its efficiency for rejecting background sources that could hide it), and certainly the ability to properly reconstruct and identify the particles, the detection efficiency. In this section we will first focus on the spectrometer trigger decision aptitudes, Sec. 4.2.1. Then we will briefly describe the track reconstruction algorithm, Sec. 4.2.2, and we will discuss the various sources that can influence the momentum resolution and can cause inefficiencies in the spectrometer, Sec. 4.2.3. The acceptance and efficiency determination via global and factorization methods will be examined later, in Sec. 4.3 and 4.4 & 4.5 respectively.

4.2.1 Trigger decision

The trigger decision in the ALICE muon spectrometer will be taken by the muon trigger chambers composed by RPCs (for more details on the detector see Sec. 3.2.3). ***The trigger system is able to select in about*** 650 ***ns candidate muon or dimuon tracks (like-sign or unlike-sign) above a certain transverse momentum.*** Note that this p_T cut is justified to reduce the background of muons from pion and kaon decays, which are predominant at low p_T. The selection of candidate tracks is effectuated by an algorithm on the electronics level. Roughly, the algorithm takes the measured position on the first trigger station, that corresponds to (X_1,Y_1,Z_1) in Fig. 4.1. It considers a straight line trajectory for the track with origin in the interaction vertex[1], and evaluates which is the deviation of the measured position in the second trigger station (X_2,Y_2,Z_2) with respect to this straight line trajectory. The

---

[1] The straight line trajectory would be the trajectory followed by a muon of infinite transverse momentum, which would not be deviated at all by the dipole magnetic field.

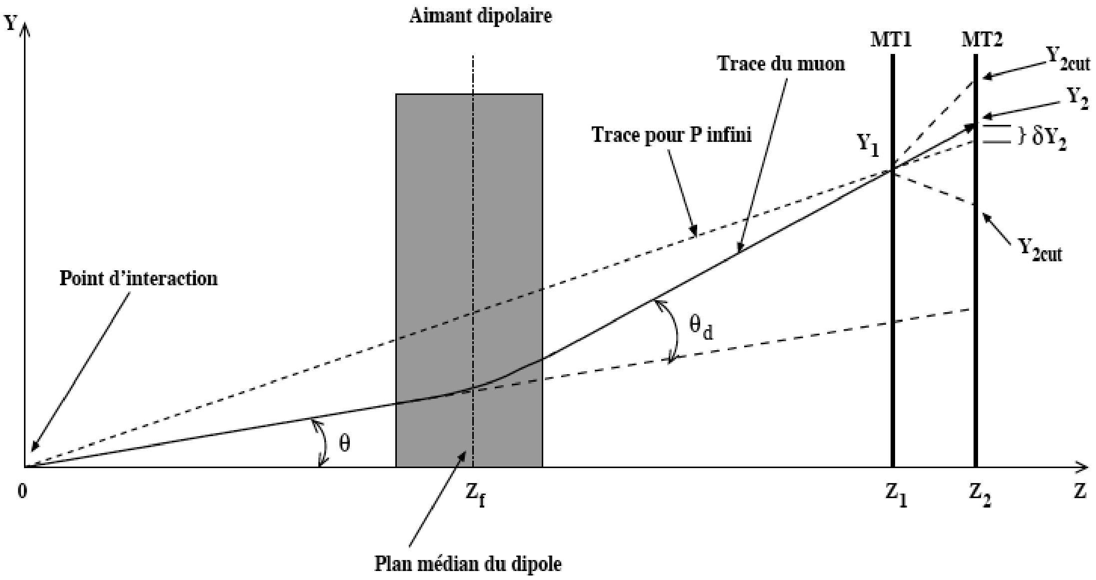

Figure 4.1: Sketch of the tracks transverse momentum determination by the ALICE muon spectrometer trigger system [Gue06].

measured deviation in the Y plane (bending plane), labeled as δY_2 in the figure, should be smaller than a certain cut, $(\delta Y_2)_{cut}$, which corresponds to the p_T cut [Gue06, G$^+$06]. The tracks deviation angle, θ_d, is calculated by means of [Gue06]:

$$\theta_d = \frac{1}{Z_F}\left(\frac{Z_1 Y_2 - Z_2 Y_1}{Z_2 - Z1}\right), \tag{4.1}$$

where Z_F is the z coordinate of the dipole. Thus in the small angle approximation the track transverse momentum can be obtained as

$$p_T \approx qBL\,\frac{(Z_2 - Z_1)}{Z_1}\,\frac{\sqrt{X_F^2 + Y_F^2}}{\delta Y_2}, \qquad Y_F = Y_1\frac{Z_F}{Z_1} - \delta Y_2\left(\frac{Z_1 - Z_F}{Z_2 - Z_1}\right). \tag{4.2}$$

B and L are the dipole magnetic field and length. To fulfill the design requirements the trigger system disposes of a three-level electronics. First the local cards with a decision time of 250 ns treat the information coming from a portion of the detector surface and provide a 'local trigger', deciding whether: there is no trigger, there is trigger for positive particles, there is trigger for negative particles, or trigger with no deviation. Second the regional cards collect the local cards information and evaluate if there is one candidate track (with which sign), or two or more candidate tracks like-sign or unlike-sign. Finally, the global cards are in charge of coordinate regional cards information and provide five trigger signals that will be sent to the Central Trigger Processor (CTP) [Gue06]. ***The five possible muon input trigger signals for the CPT are:***

- ***like-sign dimuon candidate of low p_T:*** PairLikeLPt ***trigger,***
- ***like-sign dimuon candidate of high p_T:*** PairLikeHPt ***trigger,***
- ***unlike-sign dimuon candidate of low p_T:*** PairUnlikeLPt ***trigger,***
- ***unlike-sign dimuon candidate of high p_T:*** PairUnlikeHPt ***trigger,***
- ***single muon candidate of low or high p_T:*** SingleLPt ***or*** SingleHPt ***triggers.***

In particular, there are two trigger p_T cuts: the Low ***p_T cut and the*** High ***p_T cut that correspond to a p_T threshold of 1 GeV/c and 2 GeV/c respectively.*** Those cuts are not abrupt, the intrinsic trigger efficiency is not an ideal step function, as can be seen in Fig. 4.2 from [Gue06]. In fact they are associated to the p_T value for which the trigger efficiency attains 50%. Nevertheless the efficiency increases sharply and reaches a plateau of about $99\%(98\%)$ at $3(5)$ GeV/c for the Low (High) p_T trigger cut [Gue06]. Those p_T cuts combined with the possibility that the trigger offers to disentangle particles' charge permits to define the five trigger signals. Notice that when the trigger has difficulties to identify the particle charge sign it considers both signs to avoid any trouble. The Low p_T cut is optimized for the J/Ψ physics and the High p_T cut for the Υ physics. Moreover there is also a minimum cut on p_T that is defined by the maximum deviation that the local electronics can afford. This cut is labeled as All p_T cut and corresponds to about 0.5 GeV/c.

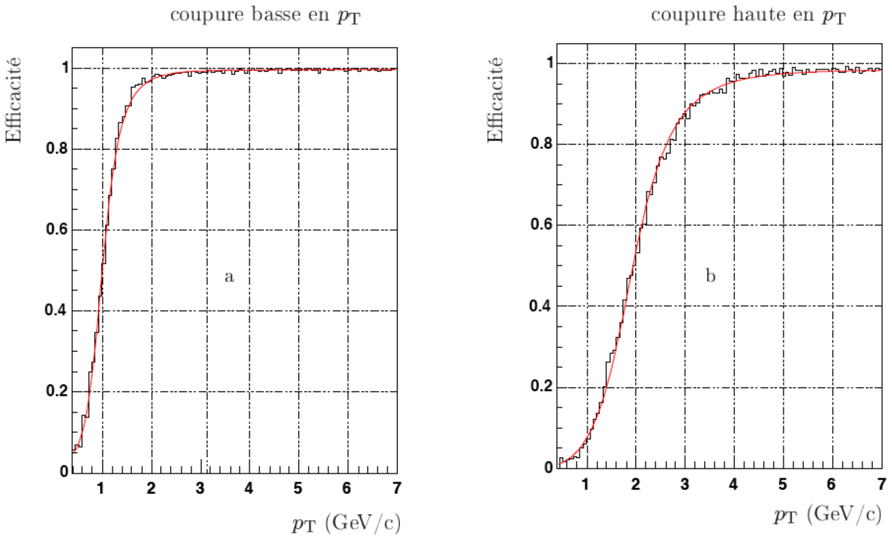

Figure 4.2: Single muon trigger efficiency as a function of p_T for the Low p_T trigger cut (a) and the High p_T trigger cut (b) [Gue06].

The CTP receives the trigger signals from detectors, coordinates their information and decides whether the whole trigger conditions identify that an 'interesting' event takes place. This decision is taken while considering the physics characteristics of the events, which define a certain combination of detectors that should trigger, and the available band-width. In reference [Gue06] can be found the detail of the different trigger configurations defined at the present time, even though this point is still under discussion within the collaboration. Once we got a trigger signal from the CTP, the tracking and trigger stations are readout and the information is saved in the form of Raw data.

4.2.2 Reconstruction algorithm

With the Raw data as input, the cluster-finder algorithm takes the relay in order to associate clusters to the detector digits, and later the tracking algorithm deals with the reconstruction to evaluate the muon tracks, their trajectory and associated properties. ***The cluster-finder algorithm begins with the information of the digits and fits the charge induced on the pads of the CPCs by the charged particles with a Mathieson-function-based expression*** [A+06, Z+03b, Mat88]. Thus the clusters coordinates can be extracted from those fits. The tracking algorithm takes as input the clusters information. In the ALICE muon spectrometer two independent algorithms for track reconstruction have been developed. One is based on the *Kalman filter* first proposed by R. E. Kalman on 1960 [Kal60, Kal] and developed by A. Zinchenko [Z+03a], and the other is based on the *traditional tracking* algorithms that fit the position of the track associated clusters to reconstruct the track. ***The* Kalman filter *is the default option in our reconstruction algorithm.*** Here we will just outline the algorithms procedure and distinctions at the present time. ***The restrictions applied by the code are:***

- ***The first estimation of track momenta should be*** $3\ \mathrm{GeV/c} < \mathrm{P} < 3\ \mathrm{TeV/c}$***;***
- ***A*** χ^2 ***cut is considered to associate a cluster to a track, and also a*** χ^2 ***cut on the track;***
- ***The condition of* reconstructible *track is set to:*** 1 ***over*** 2 ***clusters on stations 1, 2 & 3, and*** 3 ***over*** 4 ***clusters on stations 4 & 5.***

The track reconstruction begins on the two last tracking stations (stations 4 and 5) because these stations are exposed to much less noise than the first ones. The algorithm begins linking cluster pairs on stations 4 and 5 (independently) and creating segments by joining the two clusters position by a straight line[2]. Those segments are extrapolated in the magnetic field to the vertex position to have an initial guess of the track momentum, P, through the usual Lorentz-law derived relationship in the case of having only a magnetic field perpendicular to the particle momenta

$$\vec{F} = \frac{d\vec{P}}{dt} = q(\vec{E} + \vec{v} \wedge \vec{B}) \qquad \longrightarrow \qquad P[\mathrm{GeV/c}] = 0.3 \cdot B[\mathrm{T}] \cdot \rho[\mathrm{m}]\,, \tag{4.3}$$

where B stands for the magnetic field and ρ for the radius of curvature. Here comes the first restriction of both tracking algorithms: tracks with $P < 3$ GeV/c or $P > 3$ TeV/c are rejected. The second step is to consider as departure the guessed track from station 5 (station 4) clusters and extrapolate it to the station 4 (station 5). The algorithm searches for at least

---

[2] The distance between the two detection planes of station 4 or 5 is small with respect to their distance to the interaction point, about 30 cm [Tou07] in front of around 12-14 m, whereas the magnetic field is very small, thus the straight line trajectory is a good approximation.

one cluster on that station that could be associated to the track (condition of $3/4$ clusters on stations 4 & 5). The restriction applied to associate clusters to tracks is a χ^2 cut. The *Kalman* based reconstruction algorithm considers all clusters that pass the criteria, while the *traditional* one usually considers the best associated cluster[3], the one with the lowest χ^2. Once a cluster is associated the track parameters are re-calculated. The *Kalman* algorithm uses the *Kalman filter* procedure, and the *traditional* algorithm needs to fit again the associated clusters to evaluate the new parameters. The next step is the track extrapolation to the station 3. As before, a χ^2 cut is imposed as cluster selection criteria and a χ^2 cut on the track is also applied. A minimum of one cluster has to be associated to the track for it to be considered (condition of $1/2$ clusters on station 3) and then the track parameters are re-evaluated. The remaining tracks are now extrapolated to the station 2, and later to the station 1. The selection criteria are the same: the χ^2 cut on the clusters and the track and a minimum of 1 associated cluster on both stations (condition of $1/2$ clusters on stations 1 & 2). Afterwards, for some physics analysis the tracks can be extrapolated, if needed, to the vertex position provided by the ITS detector (specifically by the SPD detector) in order to refine the track parameters. With this extrapolation the mean energy lost by the particles while crossing the absorber is estimated and a correction is applied to the particle momenta following the Bethe-Bloch formula for the stopping power [Wil05]. In addition, the deviation suffered by the tracks through multiple Coulomb scattering in the absorber is also accounted for by correcting the initial track orientation[4]. This last extrapolation to the vertex position is important for invariant mass analysis of muon pairs, in particular for J/Ψ or Υ reconstruction, as the invariant mass depends on the pair relative angle. In a two particle system

$$m_{12}^2 = (\sum E_i)^2 - (\sum \vec{p}_i)^2 = m_1^2 + m_2^2 + 2(E_1E_2 - p_1p_2\cos\theta_{12})\,. \tag{4.4}$$

4.2.3 Sources of inefficiency and various contributions to momenta resolution

It is important to bear in mind which could be the various sources contributing to the worsening of the spectrometer measurements. Here we want to introduce some of them and differentiate those contributing to the efficiency from those that might influentiate the measured momentum resolution.

Sources of inefficiency

First, the muon spectrometer acceptance is defined as the angular range $171^\circ < \theta < 178^\circ$, and inside this acceptance are situated the so called dead zones, as the tracking and trigger chambers supports. Then, the front absorber can stop low energy particles, impeding them to reach the tracking chambers. In addition, the magnetic field deflects charged particles and could eventually throw them out of the spectrometer acceptance. Those effects can be studied via simulations with good accuracy. In particular, the influence of the dead zones

---

[3] There exists also the possibility to run the *traditional* reconstruction algorithm considering all the clusters that pass the selection criteria, even though it is not done by default due to the increase of the CPU time.

[4] Note that if the SPD detector provides the interaction vertex position the effect of Coulomb scattering is better constrained, as we consider that muons come from the interaction vertex.

will be discussed when dealing with the efficiency factorization, in Sec. 4.5. It has been estimated that the absorber restrains the spectrometer to measure charged particles of $P > 4$ GeV/c. And the effect of the magnetic field deflection is small and affects mainly the low p_T particles.
However, ***intrinsic trigger and tracking chambers efficiency will be the main sources of inefficiency***. Non-responding electronic-cards, -channels and/or detectors and the detector occupancy will play an important role.

Contributions to momenta resolution

Different issues contribute to the momentum resolution. Namely the magnetic field, the correction for the energy loss and multiple scattering in the absorber, and the chambers spatial resolution.

Magnetic field mapping. Particles momenta can be measured thanks to their deflection when a magnetic field is applied. Thus a proper magnetic field mapping is needed for good momenta estimations. As a matter of fact, from eq. 4.3 we can derive the momenta resolution

$$\delta P = 0.3\sqrt{(\delta B \cdot \rho)^2 + (B \cdot \delta\rho)^2} \qquad \longrightarrow \qquad \frac{\delta P}{P} = \sqrt{\left(\frac{\delta B}{B}\right)^2 + \left(\frac{\delta\rho}{\rho}\right)^2}\,, \tag{4.5}$$

observing that it is directly dependent on the magnetic field and the radius of curvature resolution. Note that the magnetic field mapping has been measured precisely, minimizing the effect of this term, that will be constant. The ρ resolution is discussed below.

The front absorber effects. As explained in Sec. 3.2.3, the mission of the front absorber is to reduce the background from pion and kaon decays in the tracking chambers in order to identify muons. It is made of high density materials such as the Pb and low density materials such as the C. Charged particles crossing the absorber lose energy and might suffer multiple Coulomb scattering.
Concerning the energy loss, we know that there will be competition between the collisional energy loss (energy loss by ionization characterized by the Bethe-Bloch formula [Wil05]) and the bremsstrahlung energy loss (radiative energy loss). It is also accepted that at very high energies the latter phenomena is predominant and at intermediate energies the energy loss by ionization is the most important process. We have estimated the muon critical energy[5] in Pb to be about 140 GeV and in C to be around 1.06 TeV (see Appendix. B for details on the calculation). Since the front absorber is mainly composed of C, in the region of interest (p_T from 0 to 100 GeV/c) the ionization energy loss will be predominant, even though the probability of bremsstrahlung for high p_T muons begins to be noticeable in the lead region of the absorber, close to the first tracking station. This justifies that in the track reconstruction algorithm just the energy loss by ionization in the absorber has been considered so far.
Moreover, the energy loss is not a smooth process, it can fluctuate from the expected value,

---

[5] The critical energy is defined as the energy at which radiative and ionization loss rates are equal.

and we usually refer to these fluctuations as straggling [Wil05]. In very thick absorbers the distribution of energy loss is expected to be governed by a Gaussian probability distribution. For thin absorbers the Landau probability distribution describe the process. We cannot correct the measured track momenta for this effect, thus it contributes to momenta resolution. If we do consider that it does not depend on the initial particle energy, the momenta resolution due to straggling will be determined by the σ of the distribution. The resolution will then be given by a constant that we denote A

$$(\delta P)_{Stragg} \approx A \qquad \longrightarrow \qquad \left(\frac{\delta P}{P}\right)_{Stragg} \approx \frac{A}{P}\,. \tag{4.6}$$

Furthermore, charged particles passing through the absorber and the detection planes might suffer from multiple Coulomb scattering, that might deviate their trajectories. In the front absorber it only affects the initial muon direction measurement, and we can partly account for it via the measurement of the interaction vertex position with the SPD detector. In any case, for small angles the Gaussian approximation is valid [Leo93] and the angular width can be described by [Y$^+$06]

$$(\delta\theta)_{Scatt} = \frac{13.6\,\mathrm{MeV}}{\beta c P} z \sqrt{x/X_0}\Big(1 + 0.038\, ln\Big(\frac{x}{X_0}\Big)\Big) \tag{4.7}$$

where βc and z are the velocity and charge of the incident particle and x/X_0 is the thickness of the scattering medium in radiation lengths.
In Appendix. B the front absorber influence on momenta resolution is discussed in more extent.

Tracking chambers resolution. As we stated in eq. 4.5, track momenta resolution is directly dependent on the radius of curvature resolution. In its turn the measurement of the radius of curvature is strongly related to the detector segmentation, to the precise positioning of the detector active volumes, and to a correct understanding the detector and electronics response. A correct calibration and alignment will help to maximize the resolution. In the muon spectrometer, alignment is first taken in charge by the Geometry Monitoring System system (GMS, see Sec. 3.2.3) that provides information of the active zones location, and will be later refined via offline analysis of specific runs without magnetic field. Recent studies indicate that alignment will not have an important impact on the resolution [Cas07].
We would like to evaluate the influence of the tracking chambers spatial resolution on the measured momenta resolution and estimate which is the uppermost momenta we can detect with the muon spectrometer spatial resolution. Fig. 4.3 shows a qualitative sketch of the effect of the magnetic dipole on a charged particle trajectory. For simplicity we have considered muons emitted from the vertex position (0,0,0) that cross the five tracking stations (STi for $i = 1, 2, ..5$) and a magnetic dipole that produce a constant field $\oint Bdl = B \cdot L = 3$ Tm over the dipole length L. We have neglected the sagitta effect on the third tracking station. The particle momenta being perpendicular to the magnetic field, from eq. 4.3 the momenta

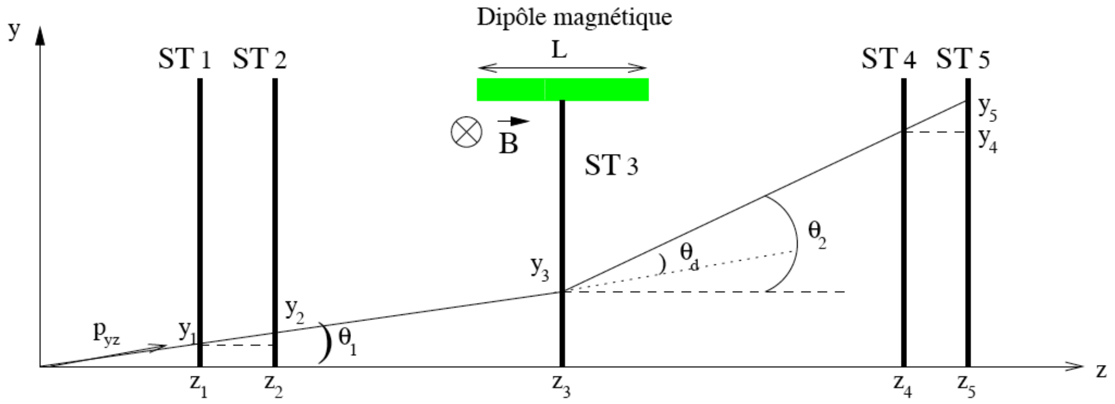

Figure 4.3: Qualitative sketch the magnetic dipole effect on a charged particle trajectory in the ALICE muon spectrometer [Bou04].

can be written as

$$P[\mathrm{GeV/c}] = 0.3 \cdot B[\mathrm{T}] \cdot \frac{L[\mathrm{m}]}{\theta_d}\,. \tag{4.8}$$

For small deviations we can express the deviation angle due to the magnetic field, θ_d, as a function of the measured positions on the tracking stations [Bou04]

$$\theta_d \simeq \frac{y_5 - y_4}{z_5 - z_4} - \frac{y_2 - y_1}{z_2 - z_1}\,. \tag{4.9}$$

The z coordinates of the stations being fixed ($z_i = 5.357, 6.860, 9.830, 12.920, 14.221$ m) [C+04, Tou07], the momenta resolution depends on the y coordinate resolution. Consequently the momenta resolution from the tracking chambers spatial resolution is given by

$$\text{(from eq. 4.8)}\quad \delta P = 0.3 \cdot B \cdot L \cdot \frac{\delta\theta_d}{\theta_d^2} \qquad \longrightarrow \qquad \frac{\delta P}{P} = \frac{\delta\theta_d}{\theta_d}\,, \tag{4.10}$$

$$\text{(and from eq. 4.9)}\quad (\delta^2\theta_d)_{Spatial} \simeq 2\delta^2 y\left(\frac{1}{(z_5 - z_4)^2} + \frac{1}{(z_2 - z_1)^2}\right), \tag{4.11}$$

$$\text{thus}\quad \left(\frac{\delta P}{P}\right)_{Spatial} = \left(\frac{\delta\theta_d}{\theta_d}\right)_{Spatial} = \frac{1}{0.3BL} \cdot P \cdot \delta\theta_d \approx 8 \cdot 10^{-5}[\mathrm{GeV^{-1}c}] \cdot P\,. \tag{4.12}$$

Besides, to estimate the maximum momenta we suppose a critical case, the one where θ_1 is close to 0 ($y_1 = y_2$), where there is not initial deviation of the track and the particle deviation due to the magnetic field θ_d is very small. If we consider a station spatial resolution[6] of 50 μm, to be able to disentangle the y coordinates on stations 4 and 5 the distance between

---

[6] Notice that it is a pessimistic approach, since station spatial resolution has been estimated to be $50/\sqrt{2}\,\mu$m [Bou04].

them should be larger than $100\ \mu$m, so

$$\theta_d \simeq \frac{y_5 - y_4}{z_5 - z_4} \geq \frac{100\ \mu\mathrm{m}}{z_5 - z_4} = 7.686 \cdot 10^{-5} \equiv \theta_d^{critical} . \tag{4.13}$$

This implies that momenta should be smaller than

$$P \leq \frac{0.3 \cdot 3}{\theta_d^{critical}} \approx 11.7\ \mathrm{TeV/c} . \tag{4.14}$$

As far as we can determine the track deviation we can estimate the particle momenta and the charge sign. Of course the resolution and efficiency diminish with the track momenta, as we have explained. The momentum resolution for $P = 11$ TeV/c (1 TeV/c) considering just the tracking chambers spatial resolution amounts to about 10 TeV/c (80 GeV/c) and can be obtained from eq. 4.12. ***If we impose that momentum resolution has to be better than*** 20% ***(***10%***), then particle momenta has to be lower than*** 2.5 ***(***1.2***) TeV/c to be measured in the muon spectrometer.***

In summary, three terms have a noticeable influence on momentum resolution: the straggling, the multiple scattering in the tracking chambers and the tracking chambers spatial resolution. Qualitatively, the total momentum resolution is then proportional to

$$\begin{aligned} \left(\frac{\delta P}{P}\right)^2_{total} &\propto \left(\frac{\delta P}{P}\right)^2_{Stragg} + \left(\frac{\delta P}{P}\right)^2_{Scatt} + \left(\frac{\delta P}{P}\right)^2_{Spatial} \\ \left(\frac{\delta P}{P}\right)^2_{total} &\propto \left(\frac{A}{P}\right)^2 + (B)^2 + \left(8 \cdot 10^{-5}[\mathrm{GeV}^{-1}\mathrm{c}] \cdot P\right)^2 , \end{aligned} \tag{4.15}$$

where the multiple scattering contribution has been evaluated from eq. 4.7 to be a constant B. In reference [Bou04] were estimated the muon spectrometer tracking chambers momenta and angular resolution in more detail, and Fig. 4.4 presents their results for the momentum resolution. ***Notice that, as expected, multiple scattering contribution to muon momentum resolution remains constant over all the interval. The energy loss in the absorber is the most important effect at low momenta (***$P < 40$ ***GeV/c) and the tracking chambers spatial resolution gets significant at high momenta (***$P > 100$ ***GeV/c).*** It should be noticed that at low momenta the resolution is related to the angle of the track because the energy loss in the absorber for small angle tracks is larger due its non-homogeneity. Close to the beam tube the absorber is composed by denser materials to reduce the background from the beam pipe in the tracking stations.

4.3 Acceptance determination

The acceptance provides information about the proportion of muons or dimuons that are emitted in the detector angular coverage, i.e. $171° < \theta < 178°$ ***for the muon spectrometer, and that could be a priori reconstructed, if they pass the reconstruction criteria.*** When referring to single muons the acceptance is an ideal step function: either they are inside

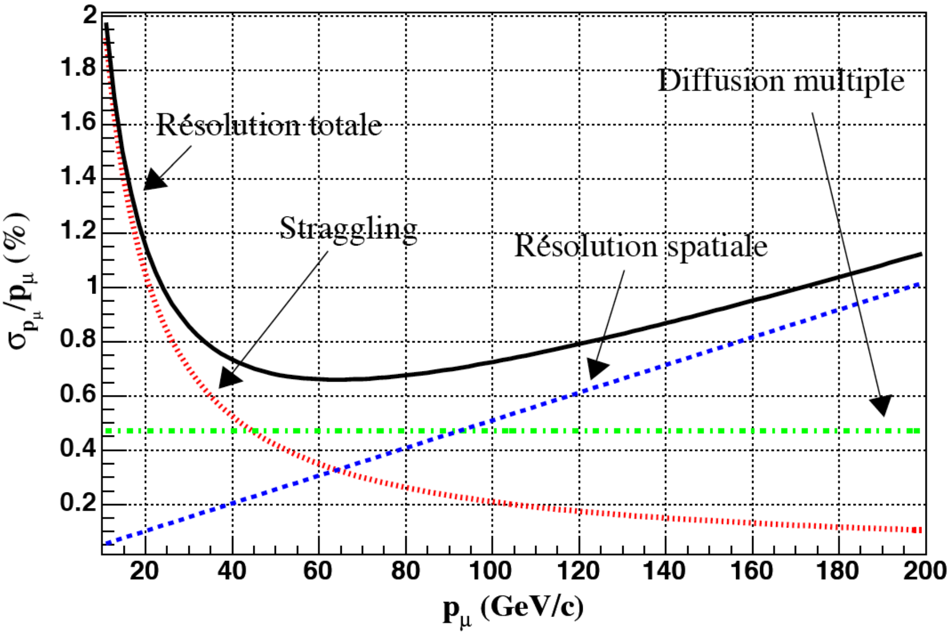

Figure 4.4: Momentum resolution with the muon spectrometer tracking system indicating the contribution of the different physical processes [Bou04].

the spectrometer angular coverage or they are not. On the other hand, when dealing with dimuons from a resonance decay, for instance the J/Ψ, we will be interested in estimating the portion of J/Ψ produced in the muon spectrometer angular coverage that decay into two muons in this range, and also the fraction of J/Ψ produced outside this interval whose decay muons enter inside the spectrometer angular window. An example of the latter would be a resonance produced in the beam direction with $p_T \sim 0$, i.e. outside the detector angular coverage; the muons should decay symmetrically with respect to the beam axis and there would a non null probability that both end up in the detection window.
The acceptance correction has to be evaluated with high precision because it depends strongly on the rapidity, transverse momentum and polarization of the particle. Furthermore, it has to be estimated by means of simulation, thus it can be evaluated now, in advance to the upcoming data-taking.

4.3.1 The J/Ψ acceptance

J/Ψ acceptance[7] is presented in Fig. 4.5. It has been estimated simulating a J/Ψ distribution in the muon spectrometer and evaluating how many of those decay into two muons in the spectrometer angular coverage with the help of the PYTHIA event generator [S^+02]. The rapidity[8] and transverse momentum dependences have been evaluated, while the pos-

---

[7] J/Ψ acceptance can be found in AliRoot in the PWG3 module, class AliQuarkoniaAcceptance.

[8] Note that while dealing with resonances we estimate the acceptance as a function of y and not η to account for the pair p_T influence, i.e. when a resonance is produced outside the detector angular coverage but its p_T push the decayed muon pair inside it.

sible effect of the polarization has been ignored because recent calculations estimate it to be lower than 5% [A+07]. Observe that, as expected, the acceptance presents big variations. One can also notice a minimum located around the J/Ψ mass ($p_T \sim m_{J/\Psi}$) due to kinematical reasons. Consider a J/Ψ produced at high-rapidities; if the J/Ψ $p_T \sim 0$, the dimuon decay is symmetric with respect to the beam axis. When one of the decayed muons is in the spectrometer acceptance, the other is also probably inside the acceptance. As the J/Ψ p_T increases, the $\mu^+ - \mu^-$ opening angle increases, decreasing the probability to find both in the spectrometer acceptance. With a $p_T \gg m_{J/\Psi}$ this effect is negligible and the muons tend to be collinear to the J/Ψ direction, thus the fraction of muon pairs in the spectrometer augments. The obtained averaged value of the acceptance amounts to 40%, but notice that if it would be calculated with respect to the whole phase space it would be close to 5%.

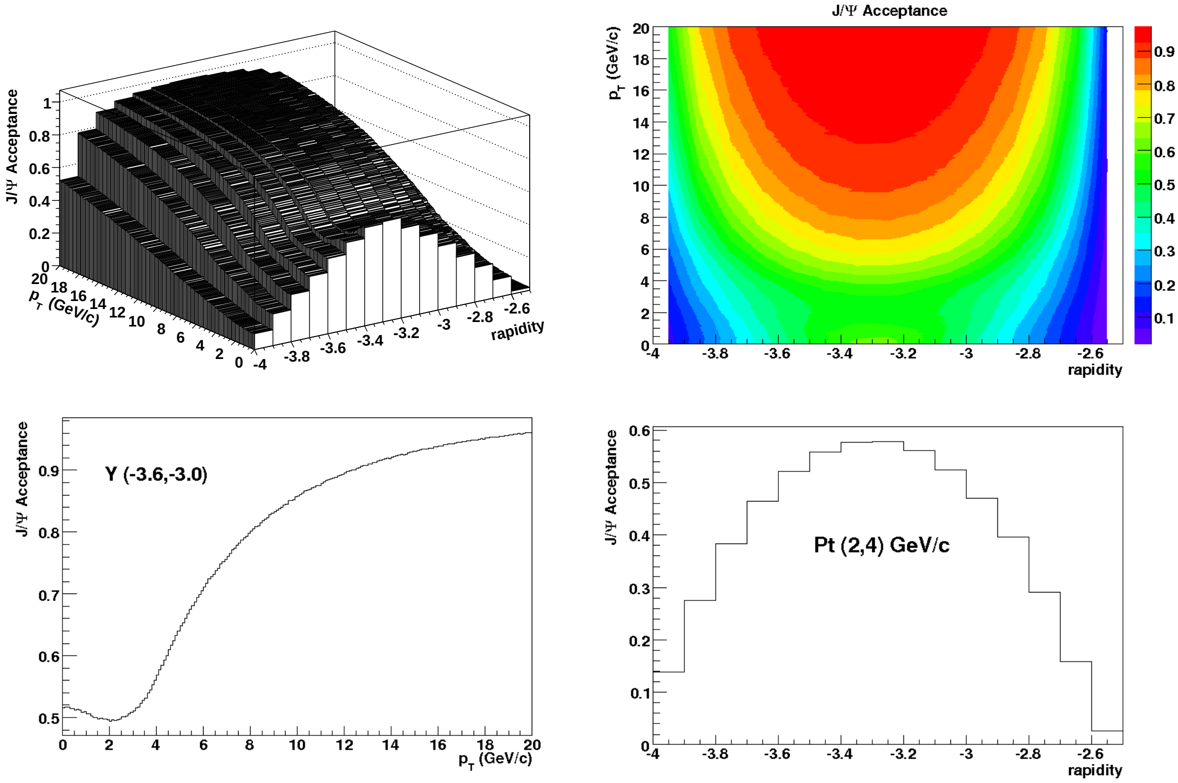

Figure 4.5: J/Ψ acceptance as a function of p_T and rapidity (upper figures). Projection of J/Ψ acceptance for $-3.6 < y < -3.0$ and $2 < p_T < 4$ GeV/c (down figures).

4.4 Global efficiency evaluation

The detector efficiency is a basic information for the majority of the physics analysis. For instance, without the efficiency correction no value of cross-section could be extracted. The physics distribution we would like to estimate can be expressed as

$$\frac{d^2N(p_T,y)}{dp_Tdy} = \frac{d^2N_{rec}(p_T,y)}{dp_Tdy} \cdot \frac{1}{A(p_T,y)} \cdot \frac{1}{\epsilon(p_T,y)} \cdot \frac{1}{N_{events} \cdot \epsilon_{MB}^{Obs}} \;, \tag{4.16}$$

where $d^2N_{rec}(p_T,y)/dp_Tdy$ stands for the reconstructed yield, $\epsilon(p_T,y)$ is the reconstruction efficiency, N_{events} stands for the number of reactions and ϵ_{MB}^{Obs} is the minimum bias trigger efficiency for a given 'observable'[9]. The acceptance correction $A(p_T,y)$ being already treated in Sec. 4.3, we can consider it independently

$$\frac{d^2N^{Acc}(p_T,y)}{dp_Tdy} = \frac{d^2N(p_T,y)}{dp_Tdy} \cdot A(p_T,y) \;, \tag{4.17}$$

$$\frac{d^2N^{Acc}(p_T,y)}{dp_Tdy} = \frac{d^2N_{rec}(p_T,y)}{dp_Tdy} \cdot \frac{1}{\epsilon(p_T,y)} \cdot \frac{1}{N_{events} \cdot \epsilon_{MB}^{Obs}} \;. \tag{4.18}$$

Therefore, from now onwards we will be concerned by the distributions in the detector acceptance. Thus for readiness we will adapt the notation by dropping the index Acc in the formulas though we will be working with the distributions in the acceptance. Besides, we will ignore the effect of the last term of the equation, the number of reactions and the minimum bias trigger efficiency for the studied observable. Consequently, in this section we shall concentrate on the reconstruction efficiency term.

The reconstruction efficiency will be dependent on the muon trigger[10] used and can be evaluated globally for each physics analysis. By globally we understand with a global, general, unique term that could be in form of histogram and depends on the rapidity and transverse momentum of the particle. Practically it should be determined by means of simulation. Simulating a realistic distribution of the particle spectra, reconstructing the spectra with the same algorithm than on 'real-data' and with the same trigger. Note that an accurate geometry, a realistic mapping, the electronics noise, the background sources and the detector dead zones during data-taking must be considered. In a first approximation the efficiency would just be the ratio of what we get from reconstruction with respect to what we have simulated. Naively

$$\text{Efficiency} \approx \frac{\text{Reconstructed spectra}}{\text{Simulated spectra}} \;.$$

But in reality the reconstructed distribution is

$$\frac{d^2N_{rec}(p_T,y)}{dp_Tdy} = \iint F(p_T^{ini},y^{ini},p_T,y)\,\frac{d^2N(p_T^{ini},y^{ini})}{dp_T^{ini}dy^{ini}}\,dp_T^{ini}dy^{ini} = \epsilon(p_T,y)\,\frac{d^2N(p_T,y)}{dp_Tdy} \;, \tag{4.19}$$

---

[9] The minimum bias efficiency for a given 'observable' shall not be the same regardless of the process. For instance, the probability of an inelastic and a hard process to start a trigger signal might vary.

[10] Remark that in general the trigger signal for the muon spectrometer will be given by the muon trigger chambers plus a minimum bias trigger by the global detectors. Here we separated their influence on the global efficiency; the muon trigger is considered in $\epsilon(p_T,y)$, while the minimum bias trigger in ϵ_{MB}^{Obs}. We ignore the latter and discuss the former.

$F(p_T^{ini}, y^{ini}, p_T, y)$ being the detector response function, which is dependent on the initial variables of the particle (p_T^{ini}, y^{ini}) and also the reconstructed ones (p_T, y). ***We would like to unfold these terms to obtain the efficiency*** $\epsilon(p_T, y)$ ***from the detector response function and get rid of the terms cross-dependences. The difficulty to do so is that we do not really know which is the initial particle distribution in the detector acceptance***, $d^2N(p_T, y)/dp_T dy$. As a matter of fact, this distribution is what we are trying to measure, the physics distribution. ***We have different ways to bypass this issue and one of them is to employ an iterative technique*** which we decided to exploit and explain on Sec. 4.4.1.

4.4.1 Unfolding the efficiency with an iterative method

Let's denote $(C_i; i = 1, 2, ..., n_c)$ several independent causes, that can produce an effect E. $P(E|C_i)$ is the conditional probability that the *ith* cause C_i has produced the effect, and $P(C_i)$ is the initial probability of the causes. Thus the Bayes' theorem describes the probability that an effect has been produced by the *ith* cause C_i, $P(C_i|E)$, as the product of the probability of the cause times the probability of the cause to produce the effect [D'A95]

$$P(C_i|E) = \frac{P(E|C_i)\, P(C_i)}{\sum_{j=1}^{n_c} P(E|C_j)\, P(C_j)} \,. \tag{4.20}$$

In our case, the effect could be the reconstruction of a given number of particles in a certain bin of p_T and y ($\Delta N_{rec}/\Delta p_T \Delta y$), and the causes all the possible cells of the physics values ($dN/dp_T dy$). Eq. 4.20 makes evident the dependence of $P(C_i|E)$ on the initial probability of the causes $P(C_i)$, the physics spectra. We can overcome the need of the initial distribution by applying an iterative procedure.

Remember that we want to measure the physics distribution

$$\frac{d^2N(p_T, y)}{dp_T dy} = \frac{1}{\epsilon(p_T, y)} \left(\frac{d^2N(p_T, y)}{dp_T dy} \right)_{rec} , \tag{4.21}$$

$\epsilon(p_T, y)$ being the efficiency and where the subindex rec denotes the reconstructed spectra. The procedure we follow is:

1. By means of Monte Carlo simulations we can evaluate an initial guess of the efficiency distribution $\epsilon^0(p_T, y)$ from an initial guessed distribution

$$\epsilon^0(p_T, y) = \frac{\left(\frac{d^2N(p_T,y)}{dp_T dy}\right)^0_{rec-sim}}{\left(\frac{d^2N(p_T,y)}{dp_T dy}\right)^0_{sim}} \,. \tag{4.22}$$

   Practically we simulate a guessed distribution $(d^2N(p_T, y)/dp_T dy)^0_{sim}$ and we reconstruct it through the usual reconstruction chain taking into account all the possible sources of inefficiency to get $(d^2N(p_T, y)/dp_T dy)^0_{rec-sim}$, and deduce $\epsilon^0(p_T, y)$;

2. With the reconstructed measured spectra (denoted by rec without any other index)

and the initial guess of the efficiency we estimate the physics distribution as

$$\left(\frac{d^2N(p_T,y)}{dp_T dy}\right)^0 = \frac{1}{\epsilon^0(p_T,y)}\left(\frac{d^2N(p_T,y)}{dp_T dy}\right)_{rec} ; \tag{4.23}$$

3. Now we have to compare the estimated physics distribution at step 2 $(d^2N(p_T,y)/dp_T dy)^0$ with the simulated distribution used as input for the efficiency calculation at step 1 $(d^2N(p_T,y)/dp_T dy)^0_{sim}$. In reference [D'A95] a χ^2-like comparison is suggested;

4. If the distributions compared (in step 3) do not agree, then one has to go back to step 1, substitute the input distribution for efficiency evaluation by the estimated distribution at step 2 and start again, so

   $$\left(\frac{d^2N(p_T,y)}{dp_T dy}\right)^{i+1}_{sim} \equiv \left(\frac{d^2N(p_T,y)}{dp_T dy}\right)^{i} . \tag{4.24}$$

   The iteration has to be done until the results stabilize, i.e. until

   $$\left(\frac{d^2N(p_T,y)}{dp_T dy}\right)^{i}_{sim} \approx \left(\frac{d^2N(p_T,y)}{dp_T dy}\right)^{i} . \tag{4.25}$$

The agreement tend to converge constantly with the number of iterations and the true distribution is recovered. Event though usually a good agreement is reached after a few iterations (the number of needed iterations depend on the response function), a limitation to the maximum number of iterations has to be obviously imposed, as there are some pathological cases for which it would be too difficult to achieve this. For example, in the case of low statistics the estimated true distribution would fluctuate around the true distribution. One technique to avoid the problems caused by successive iterations is to smooth the results before feeding them to the next iteration step. In our case, a rough smoothing will be done by fitting the estimated physics spectra before feeding it into the next iteration step. Reference [D'A95] justifies the smoothing and estimate that 20 iterations would be a logical value for the maximum number of iterations. Fig. 4.6 presents schematically the iterative procedure. *The departure point on that scheme is the initial guessed distribution in the detector acceptance* $(d^2N/dp_T dy)^i_{sim}$ *(where the race green light is) that is fed to* AliRoot *to simulate the detector and reconstruct the correspondent spectra to estimate the first guess of the efficiency* ϵ^i*. That correspond to the step 1. Then one evaluates the physics spectra* $(d^2N/dp_T dy)^i$ *and later compares to the input distribution for efficiency analysis. The rest of the scheme can be easily interpreted (the goal being to reach the race end flag).*

Note that there exist other methods to unfold the efficiency. For example reference [Sch94] propose the χ^2 minimization method.

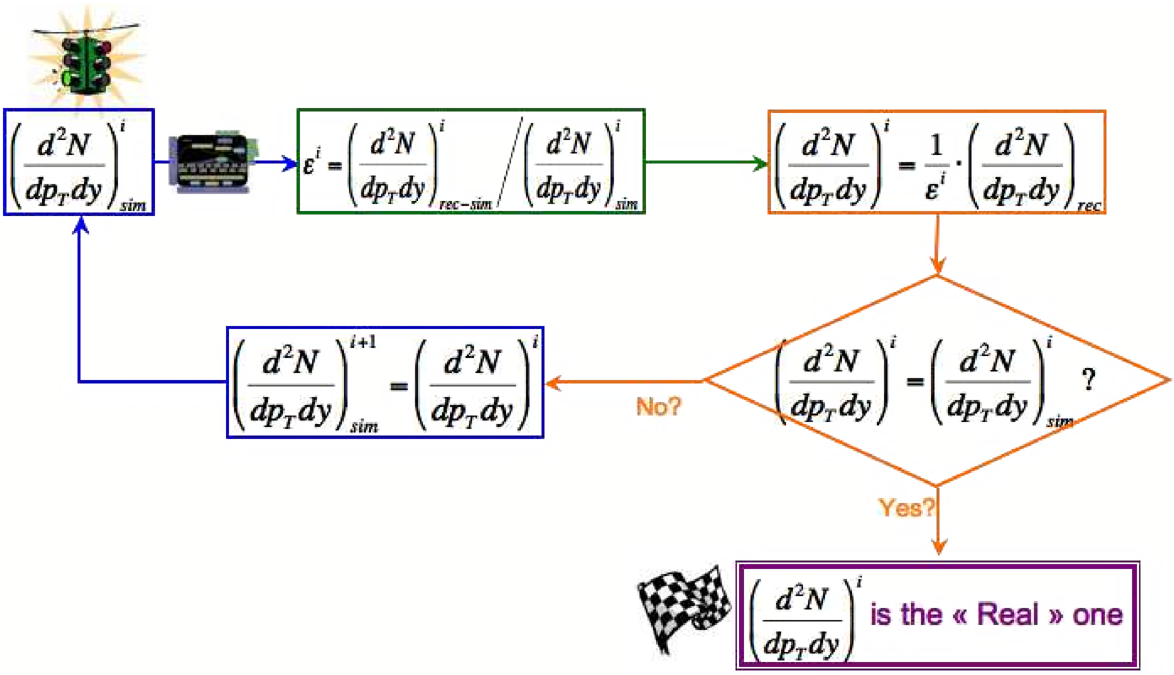

Figure 4.6: Sketch of the iterative method procedure to evaluate the efficiency.

The weight technique

We have argued that the iterative procedure is a useful method to unfold experimental distributions. Its weak point is the need of CPU time and disk space which could be overcome by a weight technique. ***It consists on making a first guess of the initial distribution in the first step of the iterative procedure, and in the second and further iterations, instead of re-doing the whole simulation, apply a weight*** y ***and*** p_T ***dependent to each particle.*** The weight associated to each particle has to be related to the initial particle properties – remember the dependence on the initial spectra – and represents the probability from 1.0 to 0.0 of this particle to be in the physics spectra. Practically it is traduced by:

- Only one complete simulation is done;
- At the end of the iteration the evaluated physics spectra is fitted;
- Then at the next iteration a weight is associated to each simulated particle relative to the previous fit (y^{ini} and p_T^{ini} dependent). That weight is applied to each particle from the first simulation step till the final reconstruction.

An enormous advantage of the weight technique is then the saving of CPU time and disk space, and the fact that used with a flat p_T ***distribution permits to estimate the efficiency at high*** p_T ***without need to generate huge statistics.*** A flat p_T simulation provides the same statistical error over the whole p_T distribution.

4.4.2 Results on dimuon pairs: the J/Ψ case

The objective being to calculate the efficiency for a realistic J/Ψ spectra, we have simulated a J/Ψ flat distribution in the spectrometer angular coverage[11] – remember we unfolded the acceptance term – for $p_T \in (0, 20)$ GeV/c. First, we have evaluated the correspondent efficiency y and p_T dependent for the flat distribution. Second, we should estimate the initial physics distribution and fit it. For the J/Ψ case[12] , the transverse momentum distribution has been extrapolated from CDF data in p-p̄ collisions at 1.8 TeV and it is of the form

$$\frac{d\sigma}{dp_T} \propto \frac{p_T}{(1+(p_T/a)^2)^b} \, ,$$

where a and b are the free parameters. The estimates indicate that for p-p collisions at 14 TeV $a = 5.355$ and $b = 3.821$, while for 5.5 TeV $a = 4.703$ and $b = 3.826$ [SVR07]. Rapidity distributions are predicted by the Color Evaporation Model [BBB+03] and shadowing effects should be accounted for in the extrapolation to the nucleus-nucleus collisions. We have then associated a weight from 1.0 to 0.0 (y and p_T dependent) to each simulated particle relative to the physics distribution and we have estimated again the efficiency. Fig. 4.8 presents a projection of the considered distribution in the first and second iterations (labeled as flat and weighted distributions) and the obtained efficiency for a realistic J/Ψ spectra is displayed in Fig. 4.7. In this example no further iterations are needed as we knew the true J/Ψ distribution shape. The mean efficiency obtained at the first iteration (for the flat distribution) is about 89% and in the second iteration (for the realistic spectra) it amounts to 85% without any trigger consideration. ***The efficiency distribution obtained with the* PairUnlikeLPt *trigger can be observed in Fig. 4.7 and the calculations indicate that the mean value amounts to* 76% *and* 58% *with a flat and realistic distribution respectively.*** The decrease of the mean efficiency when estimated with a realistic physics spectra is expected because this distribution is peaked at low p_T, the most sensitive zone. Note that for kinematical reasons of the J/Ψ decay, the reconstruction efficiency falls locally around $p_T \sim M_{J/\Psi}$. This exercise has been done with the disposable fits relative to 14 TeV and also 5.5 TeV J/Ψ distributions and for different trigger types[13]. Tab. 4.1 summarizes the estimated mean values.

A detailed comparison of the obtained efficiency distributions in the first and second iterations is presented in Fig. 4.8 in the form of the ratio of both distributions (realistic over flat efficiency spectra) for the PairUnlikeLPt trigger. ***The parameterization effect on the efficiency seems to be negligible.*** The rapidity shape is clearly flat, while the p_T pattern oscillate around a mean value. Anyway an overall reduction factor of the order of 2% is observed.

---

[11] Practically, within AliRoot it can be done with EVGEN/AliGenBox class.

[12] The J/Ψ physics distribution fit can be found in EVGEN/AliGenMUONlib class within AliRoot.

[13] The resultant efficiencies are accessible within AliRoot in the PWG3 module in the AliQuarkoniaEfficiency class.

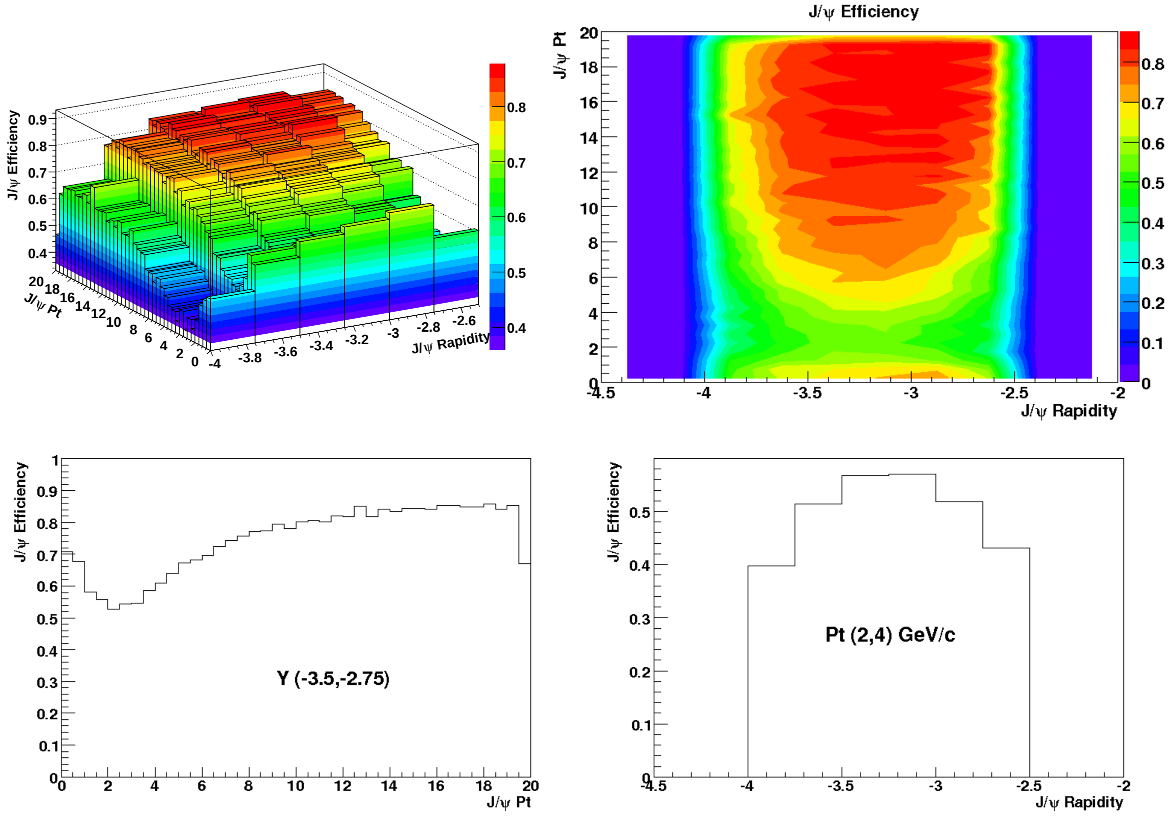

Figure 4.7: J/Ψ efficiency at 14 TeV as a function of p_T and rapidity for the PairUnlikeLPt trigger (upper figures), and the projections for $-3.5 < y < -2.75$ and $2 < p_T < 4$ GeV/c (lower figures).

Distribution	no trigger	PairUnlikeLPt	PairUnlikeHPt	PairUnlikeAPt
Flat	89%	76%	61%	82%
CDF extrap. to 14 TeV	85%	58%	27%	73%
CDF extrap. to 5.5 TeV	85%	57%	24%	73%

Table 4.1: Mean global efficiency values for J/Ψ production with different parameterizations and muon trigger types. Where PairUnlikeLPt, PairUnlikeHPt & PairUnlikeAPt refer to the MUON pair unlike low, high & all p_T trigger (see details in Sec. 4.2.1).

Invariant mass resolution evolution

Another important issue that will quantify the quality of the reconstructed invariant mass spectra and the goodness and adequacy of simulations is the resonance peak position and invariant mass resolution. We should be able to reproduce it with simulations to trust our analysis. With such devise the J/Ψ invariant mass has been studied over different rapidity intervals as a function of its transverse momentum for two different distributions of the resonance (the flat and CDF extrapolation to 14 TeV distributions). A Gaussian plus Landau

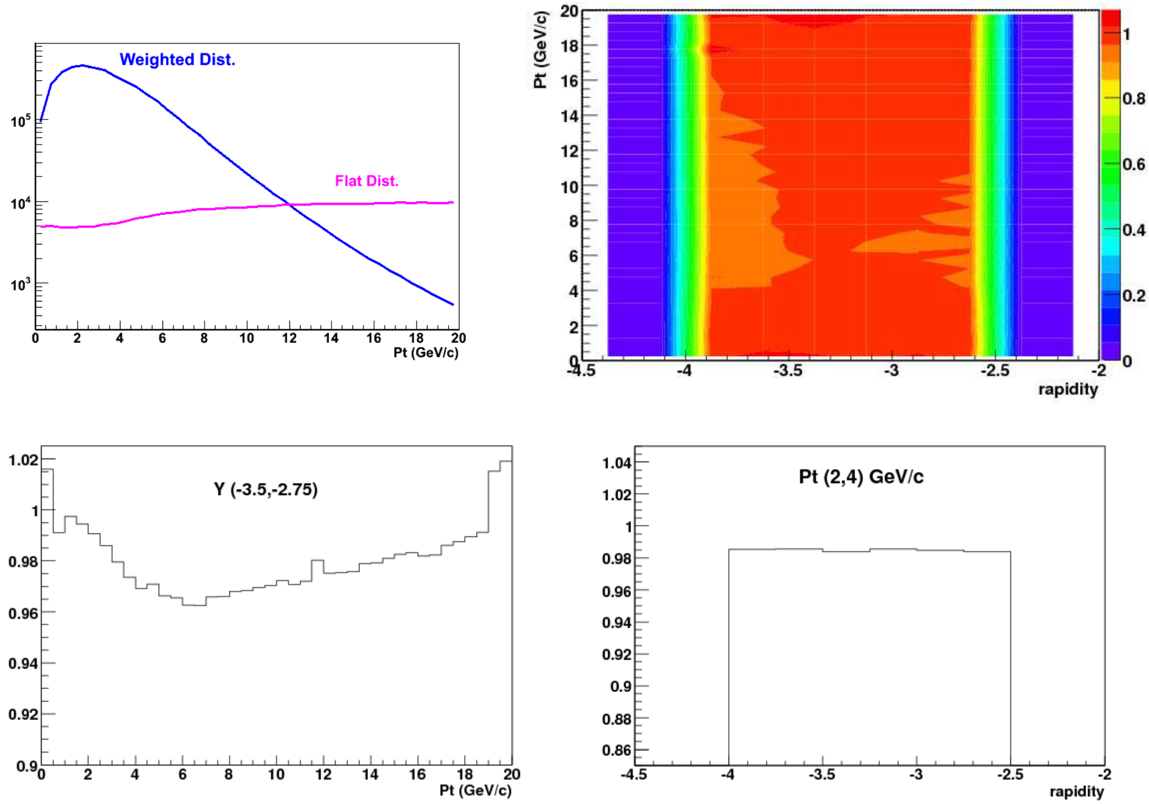

Figure 4.8: Comparison of J/Ψ efficiency for the PairUnlikeLPt trigger with and without applying weights (for 14 TeV). Upper left plot presents the projection of J/Ψ distribution for $-3.6 < y < -3.1$ with and without considering weights with an arbitrary normalization. The rest of the figures show the ratio of the efficiency distribution with over without weights as a function of p_T and rapidity, and the projections for $-3.5 < y < -2.75$ and $2 < p_T < 4$ GeV/c.

convolution function has been used to fit the spectra, where the Landau component accounts for the straggling in the front absorber. An example of the fit can be observed in Fig. 4.9. The position of the maximum value of the peak and of its full-width-half-maximum extracted from the fit have been summarized in Fig. 4.10 & 4.11 for the flat and CDF extrapolated distributions. Through the fitting procedure of all the intervals analyzed we observed that the Landau contribution to the fit decreases as the J/Ψ p_T increases, which evidences that the straggling influence on the spectra diminish when the resonance p_T augments. Accordingly, results indicate that the invariant mass peak position augments smoothly with p_T, about a 2% in 20 GeV/c, regardless of its rapidity and parameterization (from Fig. 4.10). Nevertheless, from the invariant mass fit the full-width-half-maximum pattern do not present a clear behavior with the transverse momentum (from Fig. 4.11). Anyhow, an overall reduction of the fit full-width-half-maximum for smaller rapidities seems quite clear. No distinction of the fit results with the various parameterizations is observed.

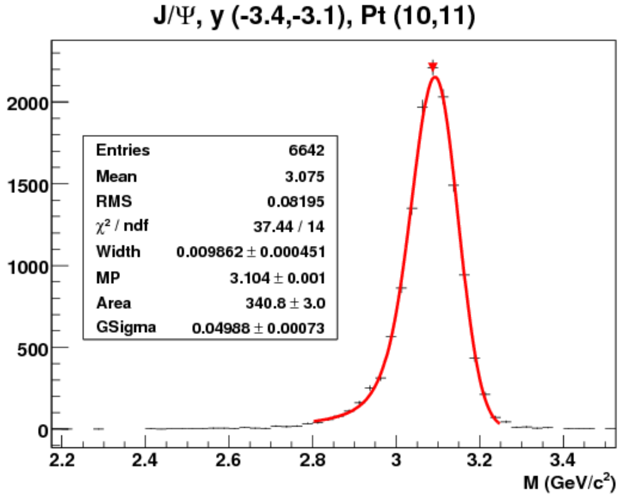

Figure 4.9: J/Ψ invariant mass for rapidity (-3.4,-3.1) and transverse momenta (10,11) for the CDF extrapolation to 14 TeV. The fit corresponds a Gaussian plus Landau convolution and gives a peak position of 3.092 ± 0.001 and a FWHM 0.136 ± 0.001 GeV/c^2.

4.4.3 Results on single muons

We have estimated the global single muon efficiency in p-p collisions at 14 TeV with the iterative procedure. For this purpose we have simulated a flat muon distribution[14] in the spectrometer angular coverage for $p_T \in (1, 100)$ GeV/c. In the first iteration, the efficiency has been evaluated for the flat distribution, and the physics spectra has been estimated with the PDC06 reconstructed spectra provided by N. Bastid and Ph. Crochet [15]. This spectra has been fitted with a power law like function of the form

$$\frac{d\sigma}{dp_T} \propto \frac{p_T}{(a + (p_T/b))^c} ,$$

with a, b, and c as free parameters. It corresponds predominantly to beauty, charm, kaon and pion decay contributions in p-p collisions at 14 TeV. Moreover, the electroweak contribution to the single muon spectra has been fitted separately from the simulations as will be explained in the next chapter. This 'second part' of the fit has been done by a linear plus polynomial function and added to the final fit used to estimate the weights in the second iteration for $p_T \in (1, 80)$ GeV/c. The muon p_T patterns used in the first and second iterations can be compared in Fig. 4.13. Even a third iteration has been done, but no important effect has been observed in that or in further iterations because the statistical fluctuations were predominant. The determined single muon global efficiency is shown in Fig. 4.12 for the SingleLPt trigger, and the results obtained for different triggers are summarized in Tab. 4.2. Remark that studying a muon distribution of p_T larger than 1 GeV/c noticeable variations with the trigger types should not be observed for the flat distribution, while the realistic one being peaked at low p_T and decreasing in a power law form presents large variations with the trigger type. With a SingleHPt trigger the single muon efficiency for a realistic distribution is lower than 50%. We must highlight that for the same reason the results might be

---

[14] Practically, within AliRoot it can be done via the EVGEN/AliGenBox class.

[15] PDC06 stands for Physics Data Challenge and refers to the campaign done by the ALICE-Grid team to test and develop the grid capabilities during 2006.

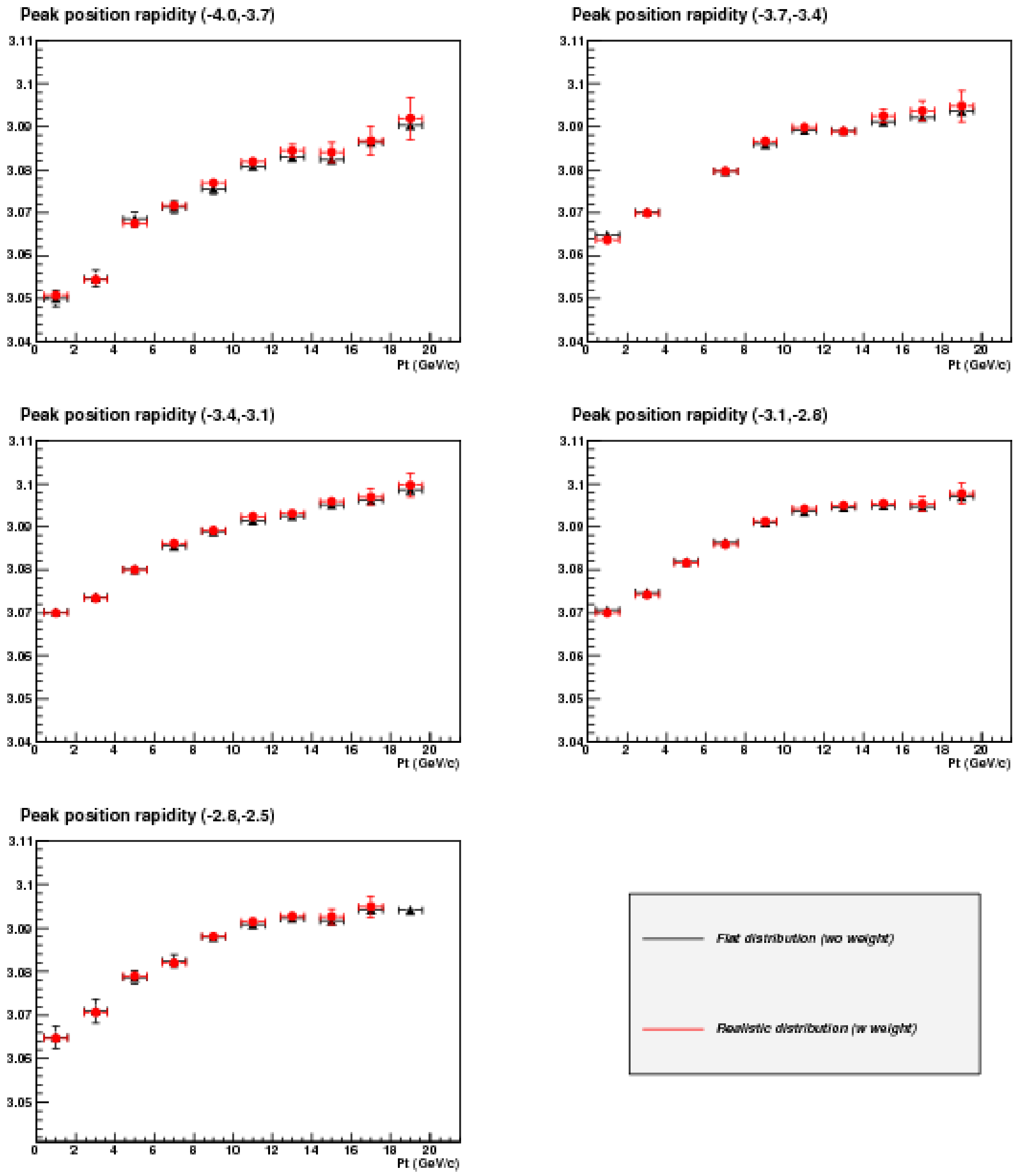

Figure 4.10: Results of J/Ψ invariant mass fit peak position in various rapidity intervals as a function of its transverse momenta for the flat and CDF extrapolated distributions, plotted with full triangles and circles respectively.

distinct if evaluated with a distribution from $p_T \sim 0$.

Fig. 4.13 presents a comparison of the efficiencies obtained with the flat and realistic distribution by means of plotting their ratio (realistic over flat efficiency distributions). ***As in the previous case, we can conclude that the choice of the input distribution does not mod-***

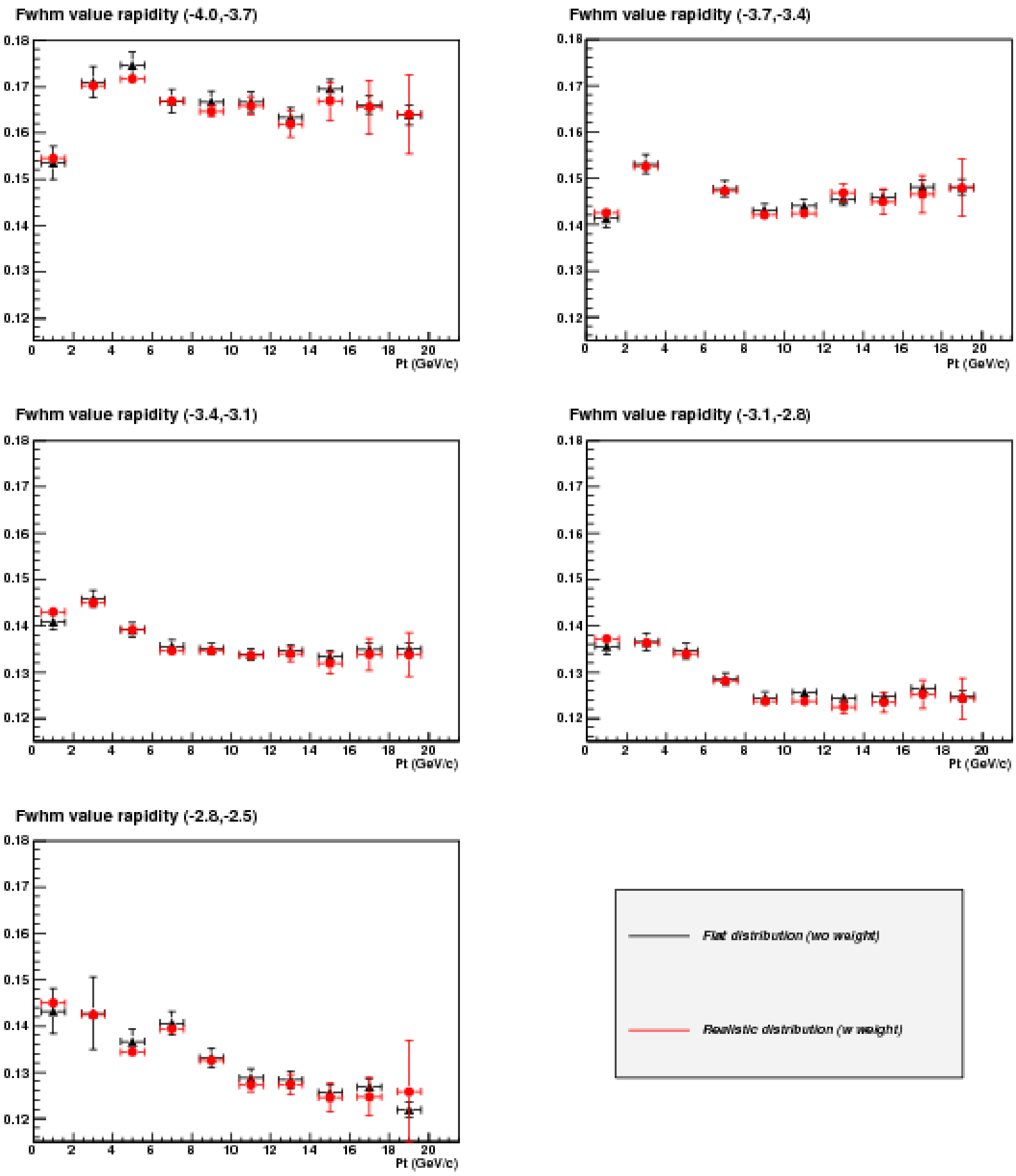

Figure 4.11: J/Ψ invariant mass fit results of the full-width-half-maximum in various rapidity intervals as a function of its transverse momenta for the flat and CDF extrapolated distributions, plotted with full triangles and circles respectively.

ify strongly the efficiency pattern with the considered detector response function. In any case, and particularly from the p_T pattern, we can realize the influence of the used fit stability on the estimated efficiency. It is obvious that increasing the statistics the fit and the results will be improved. Our concern was to effectuate a feasibility study of high p_T muons

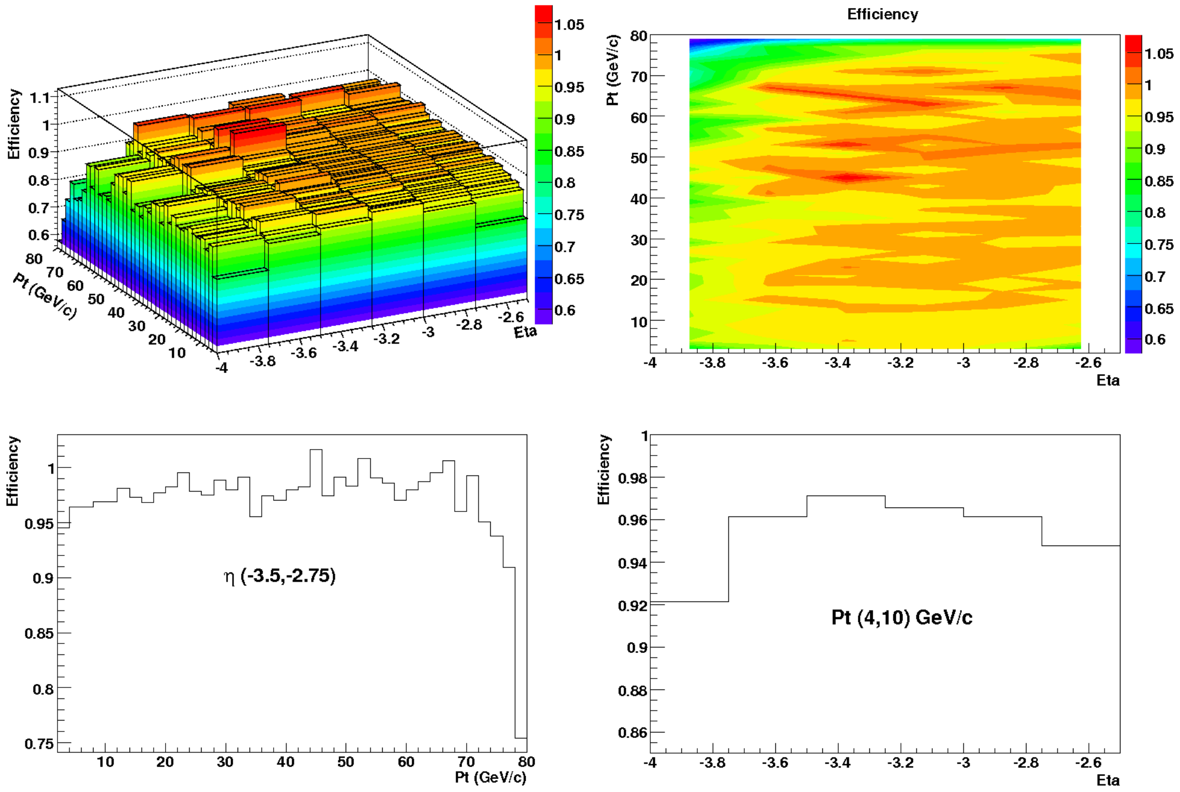

Figure 4.12: Single muon efficiency as a function of p_T and pseudo-rapidity for the SingleLPt trigger (upper figures), and the projections for $-3.5 < \eta < -2.75$ and $4 < p_T < 10$ GeV/c (lower figures).

Distribution	no trigger	SingleLPt	SingleHPt	SingleAPt
Flat	95%	94%	93%	94%
PDC06 + EW	88%	76%	45%	83%

Table 4.2: Mean global efficiency values for single muon production in different collision and trigger types for muons with $p_T > 1$ GeV/c in p-p collisions at 14 TeV. Where SingleLPt, SingleHPt & SingleAPt refer to the MUON single low, high & all p_T trigger (see details in Sec. 4.2.1).

in the spectrometer, thus we considered it to have no influence in our conclusions.

In addition, we have calculated the muon global efficiency for positive and negative charge as a function of p_T. Fig. 4.14 shows the results for the SingleHPt trigger, indicating that μ^+ ***and*** μ^- ***global efficiency have a similar and uniform behavior and that the spectrometer is able to reconstruct the muon charge up to high*** p_T***. We have estimated that in the*** $p_T \in (5, 60)$ ***GeV/c domain the mean efficiency amounts to about*** 97% ***without trigger considerations and it is around*** 96% ***with trigger***[16]. This values are in agreement with the

---

[16] Remark that for p_T larger than 5 GeV/c the mean efficiency will be the same for all the triggers.

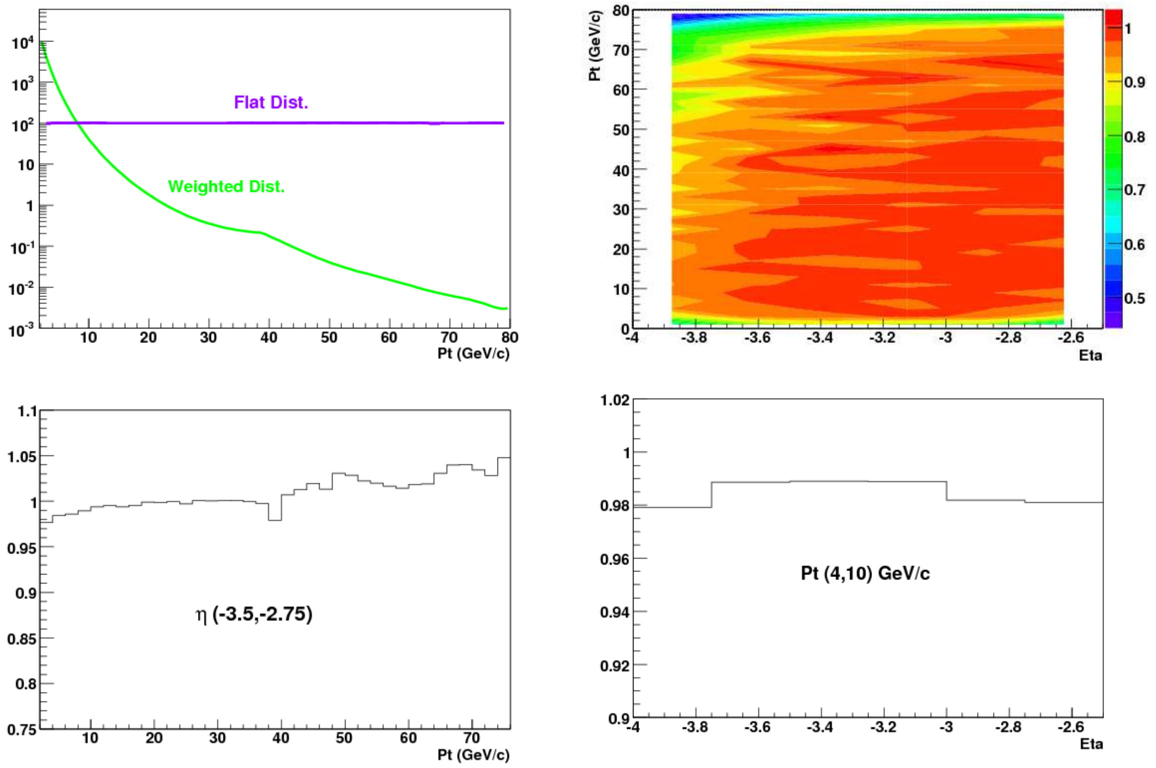

Figure 4.13: Single muon p_T distribution shape with and without applying weights (up-left figure), with arbitrary normalization. The rest of the figures present a comparison of the efficiency obtained for the SingleLPt trigger with and without applying weights in the form of the ratio of efficiency with weight over efficiency without weight. Up-right plot is the 2 dimensional histogram and the projections are the lower figures.

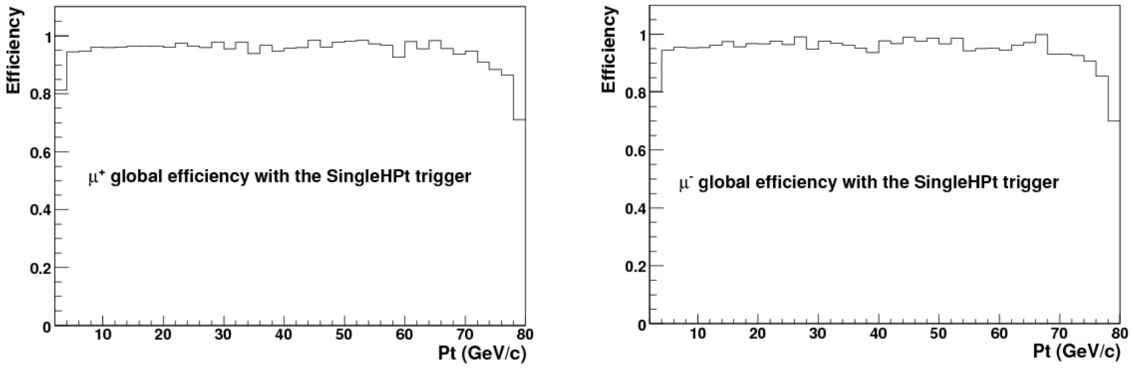

Figure 4.14: Single muon efficiency as a function of p_T for μ^+ (left plot) and μ^- (right plot) for the SingleHPt trigger.

fact that at high p_T the intrinsic trigger plateau reaches about 99% efficiency (see Sec. 4.2.1, [Gue06]).

4.5 Factorized efficiency approach

Over the last section we have exposed and observed the utility to estimate the acceptance independently of the efficiency, and that the latter can be evaluated globally as a function of the trigger type. Now the point is that ***there are still multiple effects taking part in the efficiency itself and we would like to disentangle them with the purpose to facilitate the detection of possible of problems and bugs in the code, to take advance on some points that can be studied before the first data-taking and to enable an easier determination of the trigger and tracking chambers intrinsic efficiency with 'real-data'.*** In the 'real-life', with 'real-data', both simulation and data should be considered to evaluate the efficiency, and the factorization technique offers the possibility to unfold them. Moreover, it will be a good manner to evaluate the goodness of the simulation code, as will be explained in the next subsection.

4.5.1 Efficiency factorization in the muon spectrometer

In the ALICE muon spectrometer we decided to unfold the efficiency ϵ in five distinct terms as follows,

$$\begin{aligned}\epsilon &= \epsilon(\text{triggerable}) \cdot \epsilon(\text{trigger}) \cdot \epsilon(\text{trackeable}) \cdot \epsilon(\text{reconstructible}) \cdot \epsilon(\text{reconstructed}) \qquad (4.26)\\ &= \frac{\mathrm{Y}(\text{triggerable})}{\mathrm{Y}(\text{simulated})} \cdot \frac{\mathrm{Y}(\text{trigger})}{\mathrm{Y}(\text{triggerable})} \cdot \frac{\mathrm{Y}(\text{trackeable})}{\mathrm{Y}(\text{trigger})} \cdot \frac{\mathrm{Y}(\text{reconstructible})}{\mathrm{Y}(\text{trackeable})} \cdot \frac{\mathrm{Y}(\text{reconstructed})}{\mathrm{Y}(\text{reconstructible})},\end{aligned}$$

where Y stands for the muon invariant yield. Each term accounts for different aspects of the global efficiency, particularly:

- The first term, $\epsilon(\text{triggerable})$ ***estimates if the simulated tracks pass the trigger algorithm criteria to be considered***, that is 3 over 4 hits on stations 6 & 7. We refer to those tracks as *triggerable* tracks. This efficiency term will evoke the trigger chambers dead zones (by construction), the magnetic field deflection and the energy lost by the tracks while traversing the muon absorber and the muon filter before they reach the trigger stations. Note that this term is trigger type independent.

  Practically we will evaluate this contribution observing if the simulated muons are able to pass through the muon front absorber, the tracking chambers and the muon filter inside the magnetic field, and reach the trigger chambers while accomplishing the trigger algorithm criteria. In AliRoot *it corresponds to analyze the muon* TrackRefs*;*

- The second term, $\epsilon(\text{trigger})$ ***evaluates the intrinsic trigger chambers response***, i.e. if a certain trigger is fired in the cases where there are *triggerable* tracks. It estimates the trigger algorithm response, and in the 'real-life', i.e. with 'real-data', this term will also account for the trigger chambers response: the electronics dead-channels, the high-level voltage variations, the non-responding detectors,... Note that from this term onwards all efficiency terms will be trigger type dependent.

  We can get the trigger information from the Digits *level. In* AliRoot*, the trigger chambers response is* *stored as* AliMUONGlobalTrigger*. However, the current plans to evaluate the intrinsic trigger chambers response with real-data are to profit of non-muon-triggered events, take the reconstructed muon tracks and extrapolate them to the trigger chambers, to estimate if they pass trigger algorithm criteria and if the trigger has been fired. This work is being carried on by D. Stocco [S⁺07];*

– In analogy to $\epsilon(\text{triggerable})$, $\epsilon(\text{trackeable})$ ***estimates if the tracks (for triggered events) fulfill the criteria (described in Sec. 4.2.2) requested by the tracking algorithm. It takes into account the tracking chambers dead zones (by construction).*** Remark that the muon spectrometer tracking and trigger dead zones related to the passive elements (i.e. the supports) have been optimized to maximize the whole active area, i.e. the supports angular position coincide over all the stations. In addition, the magnetic field deflection and the energy lost by particles crossing the absorber has already been accounted for in $\epsilon(\text{triggerable})$, thus we expect high values for this term of the efficiency.
In the simulations the information to estimate this term is obtained from the TrackRefs *level in* AliRoot*;*

– The next term, $\epsilon(\text{reconstructible})$***, takes in charge the intrinsic tracking chambers response***. It estimates which of the *trackeable* tracks are *reconstructible* tracks, i.e. which of the *trackeable* tracks produced clusters on the detector in accord with the tracking algorithm criteria. In fact with 'real-data' it will account for the slats/quadrants response (electronics, voltage,...).
Practically, we can estimate this contribution from the detector reconstructed points (the clusters). In AliRoot *they are stored in* AliRawCluster*. With 'real-data' the plans are to launch the track reconstruction algorithm ignoring a chamber. From the reconstructed tracks we observe if they cross the ignored chamber. Then we can check if there are reconstructed points (clusters) on that chamber and, thus obtain the intrinsic chamber efficiency. N. LeBris is taking in charge those studies [L⁺07];*

– Finally, $\epsilon(\text{reconstructed})$ ***accounts for the track reconstruction algorithm efficiency***. It evaluates which ones of the *reconstructible* tracks end up reconstructed, and with which precision.

Some of those terms have to be estimated by means of simulation and can be studied before the upcoming data-taking: $\epsilon(\text{triggerable})$ ***and*** $\epsilon(\text{trackeable})$, and the geometrical acceptance, as was explained in Sec. 4.3.1. ***Other terms must be evaluated with 'real-data', we refer to*** $\epsilon(\text{trigger})$ ***and*** $\epsilon(\text{reconstructible})$ ***that involve trigger and tracking chambers intrinsic response***. Finally $\epsilon(\text{reconstructed})$ can be calculated either with simulations or with 'real-data'. The intrinsic trigger and tracking chambers response should be properly reproduced by simulations. If this is not the case, we should re-consider the optimization of the code till the results converge. Moreover, at the present time we can study which would be the effect of a non-perfect intrinsic response, and with 'real-data' this technique offers the possibility to evaluate these terms independently of the rest and 'plug' them by hand. Thereby, the factorization allows for easier cross-checks of simulations and data and becomes a way to evaluate the goodness of the simulation code. ***In conclusion, the factorization is a useful tool to unfold and identify the different terms affecting the efficiency and to test the goodness of the simulation code.***

4.5.2 Results on dimuon pairs: the J/Ψ case

We have estimated the different terms taking part on J/Ψ efficiency. We did this with the realistic distributions – as realistic we understand the ones weighted with the disposable fits (of EVGEN/AliGenMUONlib, see Sec. 4.4.2) – for CDF extrapolation at 14 and 5.5 TeV and for the various dimuon unlike-sign trigger types. The results for 14 TeV are presented in Fig. 4.15 for the PairUnlikeLPt trigger as two dimensional plots and are summarized in Tab. 4.3 with their mean values. As the results with the two parameterizations are similar, for 5.5 TeV we just indicate the mean efficiency values in Tab. 4.4. We can observe that

	PairUnlikeLPt	PairUnlikeHPt	PairUnlikeAPt
$\langle\epsilon$ global$\rangle$	58%	27%	73%
$\langle\epsilon$(triggerable)$\rangle$	84%	84%	84%
$\langle\epsilon$(trigger)$\rangle$	72%	34%	91%
$\langle\epsilon$(trackeable)$\rangle$	98%	98%	97%
$\langle\epsilon$(reconstructible)$\rangle$	99%	99%	99%
$\langle\epsilon$(reconstructed)$\rangle$	100%	100%	99%

Table 4.3: Results of J/Ψ average factorized efficiency contributions in different trigger types for CDF extrapolation at 14 TeV. See trigger definitions in Tab. 4.1 or in Sec. 4.2.1.

	PairUnlikeLPt	PairUnlikeHPt	PairUnlikeAPt
$\langle\epsilon$ global$\rangle$	57%	24%	73%
$\langle\epsilon$(triggerable)$\rangle$	83%	83%	83%
$\langle\epsilon$(trigger)$\rangle$	71%	30%	91%
$\langle\epsilon$(trackeable)$\rangle$	97%	98%	97%
$\langle\epsilon$(reconstructible)$\rangle$	99%	99%	99%
$\langle\epsilon$(reconstructed)$\rangle$	100%	100%	99%

Table 4.4: Results of J/Ψ average factorized efficiency contributions in different trigger types for CDF extrapolation at 5.5 TeV. See trigger definitions in Tab. 4.1 or in Sec. 4.2.1.

ϵ(triggerable) and ϵ(trigger) are the terms that contribute the most to the global efficiency. This is the expected behavior in simulations, where the the intrinsic chambers efficiency is close to 100%. The detail of ϵ(triggerable) in Fig. 4.15 evidences a reduction of the efficiency around $p_T \sim m_{J/\Psi}$ due to kinematical reasons (see Sec. 4.3.1 for further explanations) that is more pronounced at larger rapidities. Low angle tracks (high-rapidity tracks) may pass by the inner shield of the absorber or may even cross through the beam shield traversing larger density materials and loosing more energy than higher angle tracks. The probability of those tracks to attain the trigger chambers and fulfill the minimum trigger algorithm conditions is then diminished. The ϵ(trigger) 2D plot clarifies the effect of the PairUnlikeLPt trigger. The

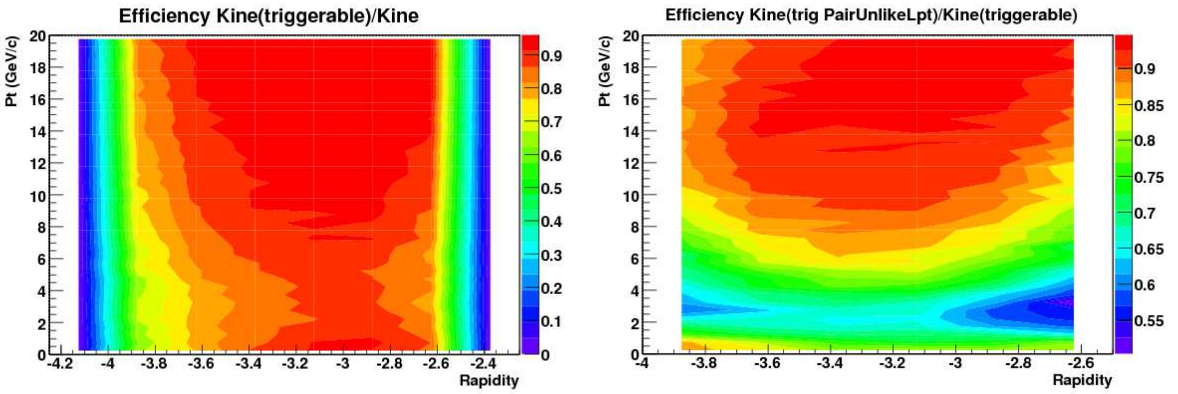
Efficiency Kine(triggerable)/Kine

Efficiency Kine(trig PairUnlikeLpt)/Kine(triggerable)

ϵ(triggerable) ϵ(trigger) for the PairUnlikeLpt trigger

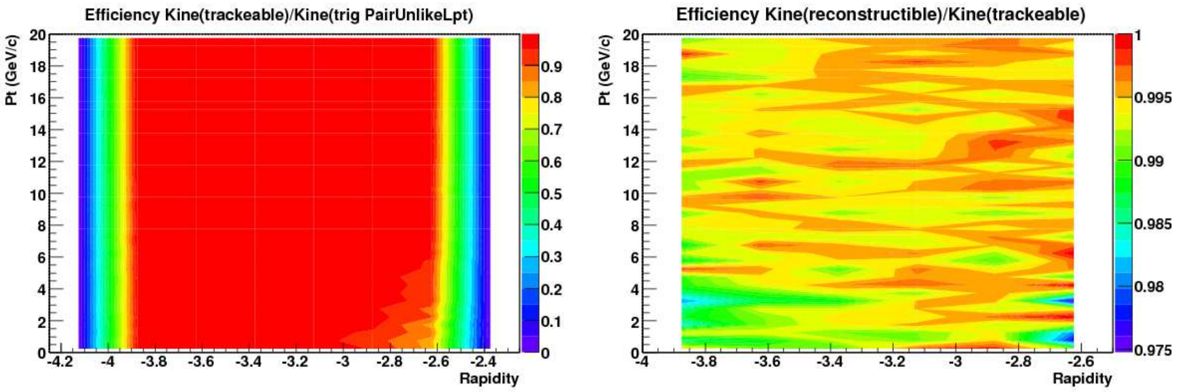
Efficiency Kine(trackeable)/Kine(trig PairUnlikeLpt)

Efficiency Kine(reconstructible)/Kine(trackeable)

ϵ(trackeable) for the PairUnlikeLpt trigger ϵ(reconstructible) for the PairUnlikeLpt trigger

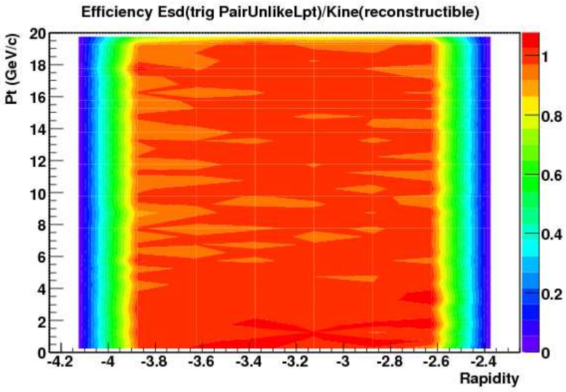
Efficiency Esd(trig PairUnlikeLpt)/Kine(reconstructible)

ϵ(reconstructed) for the PairUnlikeLpt trigger

Figure 4.15: Qualitative results of J/Ψ efficiency factorization for CDF extrapolation at 14 TeV and the PairUnlikeLpt trigger.

low p_T cut reduces drastically the muon tracks below 1 GeV/c[17]. The mean value estimations are of 72%, 34% and 91% for the PairUnlikeLPt, PairUnlikeHPt and and PairUnlikeAPt triggers and are in agreement with those of reference [Gue06, G$^+$06]. In general, the rest of the efficiency terms present a quite homogeneous pattern. ϵ(trackeable) is about 98% prov-

---

[17] For clarification, notice that the desired effect of the PairUnlikeLPt trigger is to reduce the background sources and optimize the J/Ψ over background rejection power of the trigger.

ing that the majority of the trigger and tracking chambers passive elements angular coverage are in common, as expected. $\epsilon(\text{reconstructible})$ is stable around 99% showing that this part of the code is in good shape. Finally $\epsilon(\text{reconstructed})$ attains even higher values, about 100%, with tiny fluctuations. This shows the goodness of the track reconstruction algorithm, in particular the *Kalman filter* algorithm that has is used by default in the spectrometer.

4.5.3 Intrinsic tracking chambers efficiency

To evaluate the effect that a non-perfect intrinsic tracking chambers response function could have on the J/Ψ reconstruction pattern we have considered two different values for the mean intrinsic efficiency: 90% and 97%, and we have estimated the $\epsilon(\text{reconstructible})$ term variations. Practically, it means that we have associated to each reference hit (defined as the point where the particle crosses and touches the detector) an arbitrary probability to produce a hit on the detector, and we force that only a fraction of the reference hits related to the intrinsic efficiency can produce a detector hit. By statistics we can estimate the impact caused on the single and dimuon tracks. In fact if we consider an intrinsic efficiency of 90% [97%]

- The probability that 1 over 2, $1/2$, hits gives signal is $P(1/2) = 1 - 0.10 \times 0.10 = 0.99$ [0.9991], and the contrary is 0.01 [0.0009];
- The probability that $3/4$ planes get touched is the probability that the four are touched plus four times the probability that three of them are touched and one is not (because this might happen in four different ways). One obtains $P(3/4) = 0.90^4 + 4 \times 0.90^3 \times 0.10 = 0.9477$ [0.9948];
- As a consequence, following the tracking algorithm criteria the single track probability is $P(\text{track}) = P(1/2) \cdot P(1/2) \cdot P(1/2) \cdot P(3/4) = 0.9196$ [0.9921];
- And the two track probability is $P(\text{pair}) = P(\text{track}) \cdot P(\text{track}) = 0.8456$ [0.9843].

Results of the simulation done for the J/Ψ case and the PairUnlikeApt trigger are presented in Fig. 4.16. They evidence homogeneous patterns in close agreement with the statistical expectations. Remark that the effect observed here is non negligible, a tracking chamber intrinsic efficiency of 90% would imply $\epsilon(\text{reconstructible}) \sim 84\%$. Single and dimuon reconstruction could be seriously affected by the intrinsic chambers response. As previously said, this term has to be evaluated with 'real-data' but this test could already persuade us of its importance. The dimuon collaboration is doing efforts to be ready for those studies.

4.5.4 Results on single muons

We have calculated the various factors contributing to the single muon efficiency with the same simulation as in Sec. 4.4.3 to study the efficiency mapping up to high p_T. That is with a flat θ and p_T distribution weighted to account for a realistic distribution from PDC06 + EW distributions for p-p collisions at 14 TeV. Fig. 4.17 shows the factorization results in the

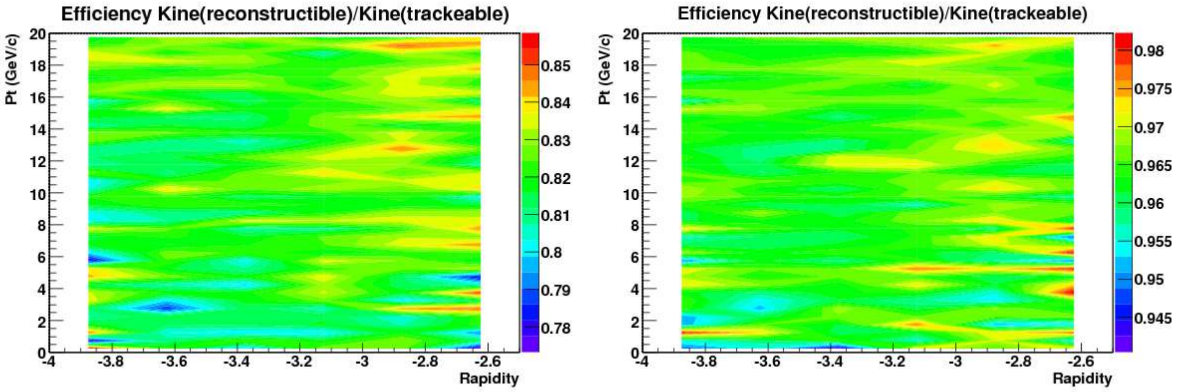

Intrinsic efficiency 90% Intrinsic efficiency 97%

Figure 4.16: Intrinsic efficiency test for the J/Ψ efficiency with the PairUnlikeApt trigger.

form of two dimensional plots for the SingleLPt trigger, and Tab. 4.5 their mean values for the different single muon trigger types. Remark that in this study we have just considered muons with p_T larger than 1 GeV/c, therefore results – particularly those concerning trigger types – may not coincide with other studies done down to $p_T = 0$ and should be interpreted carefully. Observe that $\epsilon(\text{triggerable})$ and $\epsilon(\text{trigger})$ have the major effect on the global efficiency, as expected and observed for J/Ψ production. $\epsilon(\text{triggerable})$ has a mean value of 93% and diminishes at small angles with respect to the beam axis, i.e. at high pseudo-rapidity, due to the more probable pass of the tracks through the inner part of the absorber losing more energy than large angle tracks, which reduce the probability of those to attain the last trigger station and fulfill the required trigger criteria. As may be guessed, this effect is more pronounced at low p_T. $\epsilon(\text{trigger})$ exhibit an uniform behavior – observe the color scale going from 97.5% to 100% – though the effect of small angle tracks can still be perceived. The SingleLPt trigger threshold is situated around 1 GeV/c (see Sec. 4.2.1), this is the reason why its effect can not be clearly seen here. $\epsilon(\text{trackeable})$ presents a flat pattern with mean value around 98% showing that, as observed for the J/Ψ, the trigger and tracking passive

	SingleLPt	SingleHPt	SingleAPt
$\langle\epsilon$ global$\rangle$	76%	45%	83%
$\langle\epsilon(\text{triggerable})\rangle$	93%	93%	93%
$\langle\epsilon(\text{trigger})\rangle$	86%	50%	96%
$\langle\epsilon(\text{trackeable})\rangle$	98%	99%	98%
$\langle\epsilon(\text{reconstructible})\rangle$	100%	100%	100%
$\langle\epsilon(\text{reconstructed})\rangle$	97%	98%	95%

Table 4.5: Results of single muon average factorized efficiency contributions in different trigger types for muons with $p_T > 1$ GeV/c in p-p collisions at 14 TeV. See trigger definitions in Tab. 4.2 or in Sec. 4.2.1.

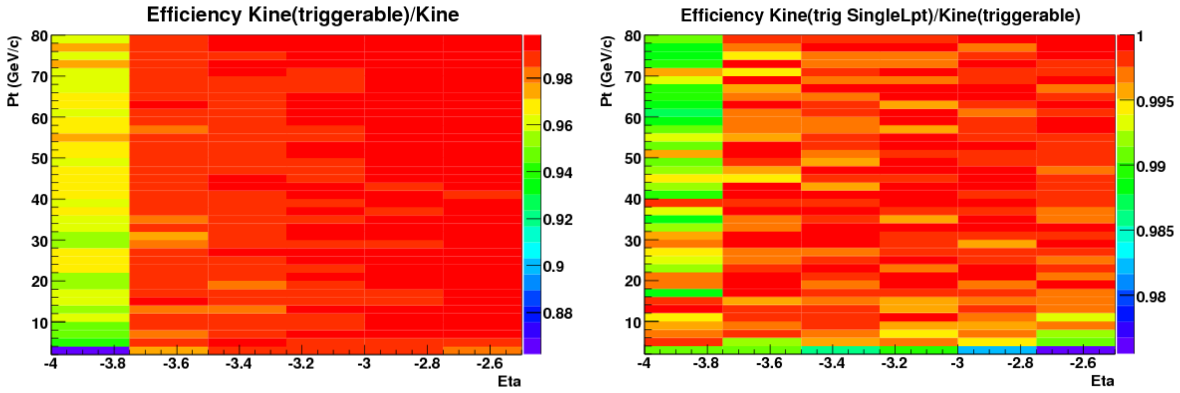
Efficiency Kine(triggerable)/Kine

Efficiency Kine(trig SingleLpt)/Kine(triggerable)

ϵ(triggerable)

ϵ(trigger) for the SingleLPt trigger

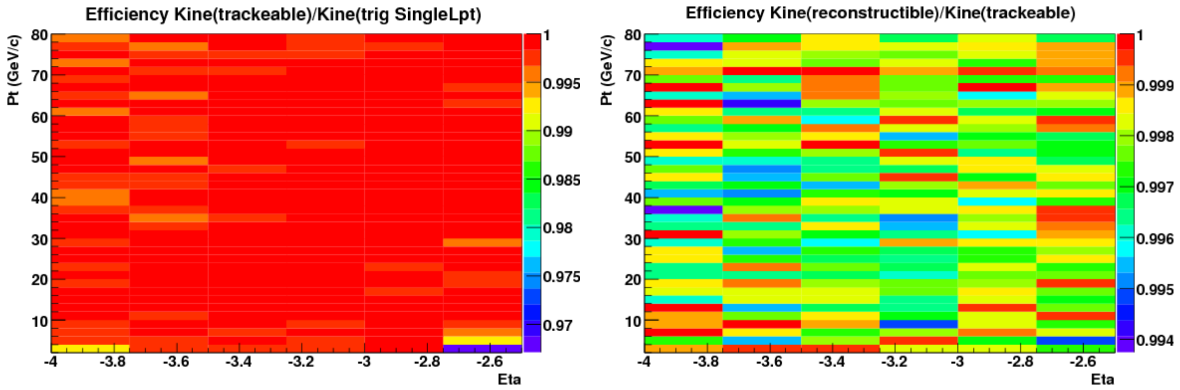
Efficiency Kine(trackeable)/Kine(trig SingleLpt)

Efficiency Kine(reconstructible)/Kine(trackeable)

ϵ(trackeable) for the SingleLPt trigger

ϵ(reconstructible) for the SingleLPt trigger


Efficiency Esd(trig SingleLpt)/Kine(reconstructible)

ϵ(reconstructed) for the SingleLPt trigger

Figure 4.17: Qualitative results of single muon efficiency factorization for p-p collisions at 14 TeV and the SingleLpt trigger for muons with $p_T > 1$ GeV/c.

elements are common. ϵ(reconstructible) distribution is even more homogeneous than the previous with a mean value of 100% – the color scale goes from 99.4% to 100% –, as expected since in these simulations the intrinsic tracking chambers efficiency is the ideal one. Finally, ϵ(reconstructed) fluctuates smoothly around its mean value 97%. Retain that in this term is included the reconstruction algorithm response. The calculated mean values as a function of the trigger type are affected by the hard analysis cut ($p_T^{Ana} > 1$ GeV/c) and decrease with

the trigger p_T cut. We estimated that the mean tracking algorithm efficiency for SingleHPt $>$ SingleLPt $>$ SingleAPt. Due to the straggling of the energy loss in the absorber not included in the tracking algorithm the p_T of the reconstructed tracks can oscillate around their initial one. The lower the initial p_T track considered (with $p_T > 1$ GeV/c) the higher the probability to reconstruct it below 1 GeV/c, where the analysis cut actuate. Thus the lower is the initial p_T track considered, the smaller will be the mean reconstruction algorithm efficiency – remind that the distribution is peaked at low p_T, then those bins contribute the most to the mean value –. Besides, the straggling effect can also be observed in the $\epsilon(\text{reconstructed})$ plot for the higher p_T bins, as in the analysis a higher p_T cut has also been considered.
It is important to bear in mind that this exercise has been done with the purpose to study the efficiency mapping up to high p_T. If one envisage to study the whole p_T interval without any analysis cut or the low p_T region one should repeat the study for that region.

4.6 Remarks

In this chapter we have outlined the trigger decision and the reconstruction algorithm procedures and the sources of inefficiency. We can highlight that the muon spectrometer should be able to measure charged tracks from 4 GeV/c momenta (due to energy loss in the front absorber) up to a higher approximative limit of 2.5 TeV/c (with a resolution of 20%). We have argued that the acceptance correction can be evaluated independently of the efficiency determination, and we have widely discussed the latter. We exposed that the efficiency can be estimated globally as a function of the trigger type, but if the initial physics distribution is not known we need to employ an adapted method to unfold the efficiency. We have shown that the use of an iterative procedure combined with a weight technique turned out to be a good alternative giving appropriate results and saving CPU time and disk space. Furthermore, we developed and adapted a factorization technique for the muon spectrometer identifying the various contributions to the efficiency. It facilitates the detection and identification of possible problems and enables an easier intrinsic chamber efficiency determination with 'real-data'. Results indicate that the intrinsic chambers efficiency could have a noticeable effect on the global efficiency with 'real-data', and reveal that the spectrometer dead zones ($\epsilon(\text{triggerable})$) and the trigger efficiency ($\epsilon(\text{trigger})$) contribute the most to the global efficiency when estimated via simulations. In addition, the use of the factorization method for dimuons and single muons has allowed us to 'isolate' the reconstruction algorithm efficiency that has demonstrated to be in a good-shape presenting small fluctuations.

Part III

Weak boson production

Chapter 5

Weak boson production at the LHC

> *Tell me and I'll forget; show me and I may remember; involve me and I'll understand.*
>
> Chinese proverb

Abstract

Some relevant aspects of the physics processes involved in weak boson production are discussed. The tools and techniques used to simulate W and Z bosons are explained. Weak boson spectra at LHC in the muonic decay channel in different collision types are presented. Special emphasis is given to the charge asymmetries and the expected statistics in the ALICE muon spectrometer acceptance.

5.1 Generation of weak bosons at LHC energies

In this section we review the physics processes that contribute to weak boson production at LHC energies and determine the simulation tools and techniques that will be used to evaluate the feasibility of their measurement. Particularly, we will be interested in weak boson studies in p-p collisions at 14 TeV, p-Pb collisions at 8.8 TeV and Pb-Pb collisions at 5.5 TeV.

5.1.1 Production physics processes

As weak bosons are massive particles, they are produced in initial hard collisions, where the available energy in the center-of-mass is maximum. ***The lowest order process for W/Z production, is the quark - anti-quark annihilation process*** (see Fig. 5.1):

$$f_i + \bar{f}_j \to W\,, \qquad\qquad f_i + \bar{f}_i \to Z.$$

Higher order processes involve gluon and photon initial and final state radiation (i.e. QCD and QED radiation). Second order processes are:

$$\begin{aligned} f_i + g &\to W + f_k\,, \qquad & f_i + g &\to Z + f_i\,, \\ f_i + \bar{f}_j &\to W + g\,, \qquad & f_i + \bar{f}_i &\to Z + g\,, \end{aligned}$$

$$\begin{aligned} f_i + \gamma &\rightarrow W + f_k\,, & \qquad f_i + \gamma &\rightarrow Z + f_i\,, \\ f_i + \bar{f}_j &\rightarrow W + \gamma\,, & \qquad f_i + \bar{f}_i &\rightarrow Z + \gamma\,. \end{aligned}$$

The respective Feynman diagrams for the W are shown in Figs. 5.2. In reference [ADMP04] are computed W and Z production cross sections taking into account the LO, NLO and NNLO contributions that are represented in Fig. 5.3. ***Although there are some discrepancies [ADMP04], it has been estimated that NLO corrections amount to*** $13\ \%$ ***of the complete NLO cross-section [FM04].*** Cross-sections variations due to a change of the scales

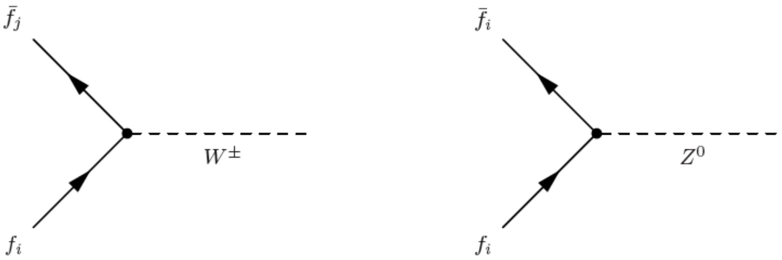

Figure 5.1: Lowest order diagram for W/Z production in hadron-hadron collisions.

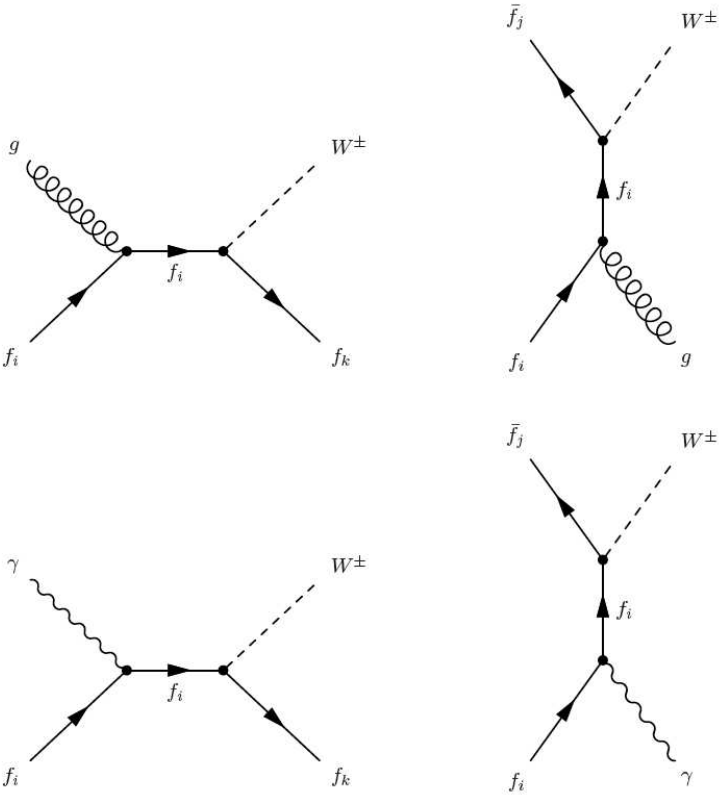

Figure 5.2: Second order diagrams for W production.

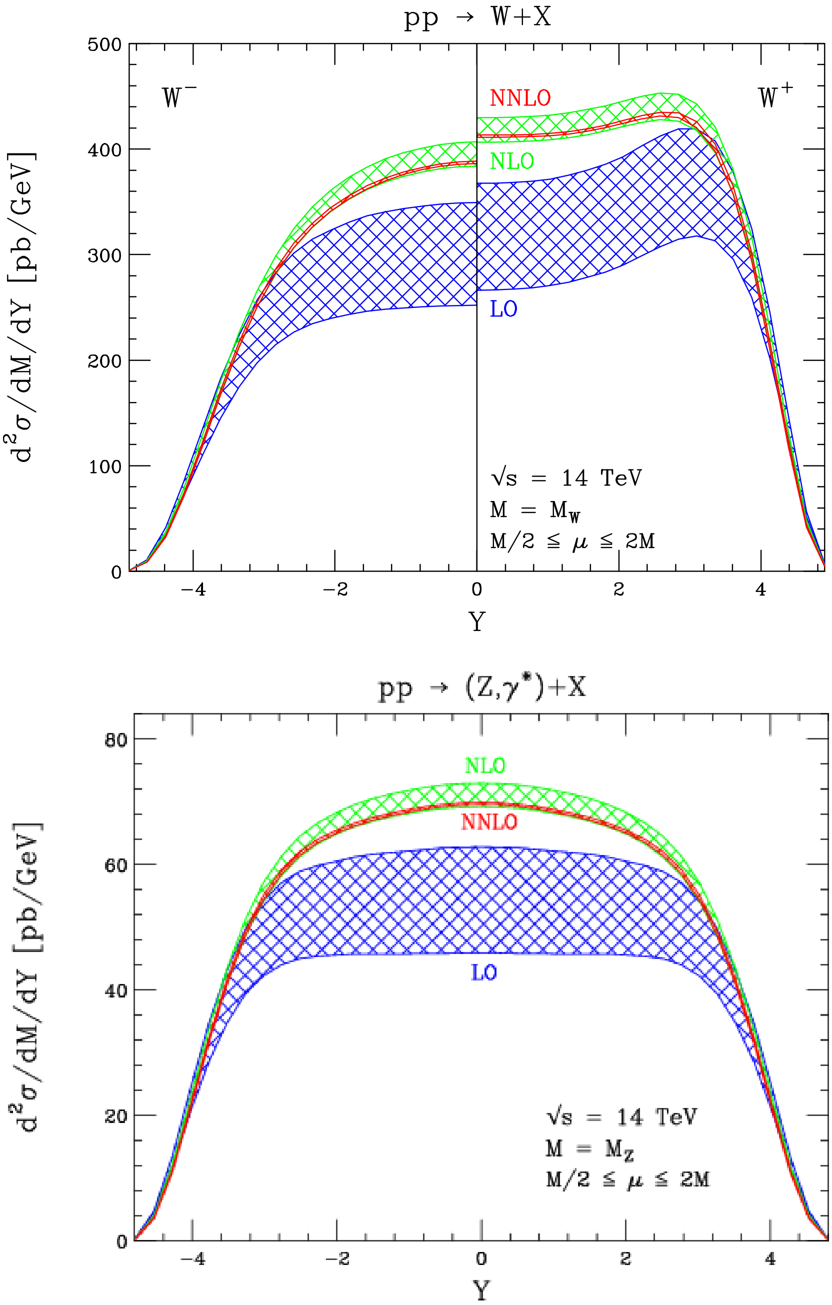

Figure 5.3: W and Z rapidity distributions at LO, NLO and NNLO for the MRST PDF sets [ADMP04]. The bands indicate a common variation of the re-normalization and factorization scales in the range $M/2 \leq \mu \leq 2M$.

(re-normalization and factorization) have been evaluated to be a few percent, and NNLO corrections are small and are dominated by the uncertainty of the Parton Distribution Functions (PDFs) [ADMP04]. PDF uncertainties have been estimated to be about $2-8\%$, and the theoretical yields of NNLO predictions to be better than one percent [ADMP04]. Thus electroweak production at LHC can provide valuable information helping to disentangle be-

tween different sets of PDFs.
Fig. 5.4 presents W and Z production cross sections flavor decomposition at LO. The dominant contribution to W production comes from u-d scattering. Nevertheless, s-c scattering contribution to the total production cross section at LHC amounts to approximately 17% for W^+ and 23% for W^- [MRST00] and the remaining processes contribute between 1% and 3%. The corresponding situation for Z^0 production is simpler. At LHC energies it is predominantly produced by either the coupling of $u\bar{u}$ or $d\bar{d}$, and contributions from heavier quarks turn out to be smaller (i.e. $u\bar{u} \sim d\bar{d} \gg s\bar{s} \gg c\bar{c}$).

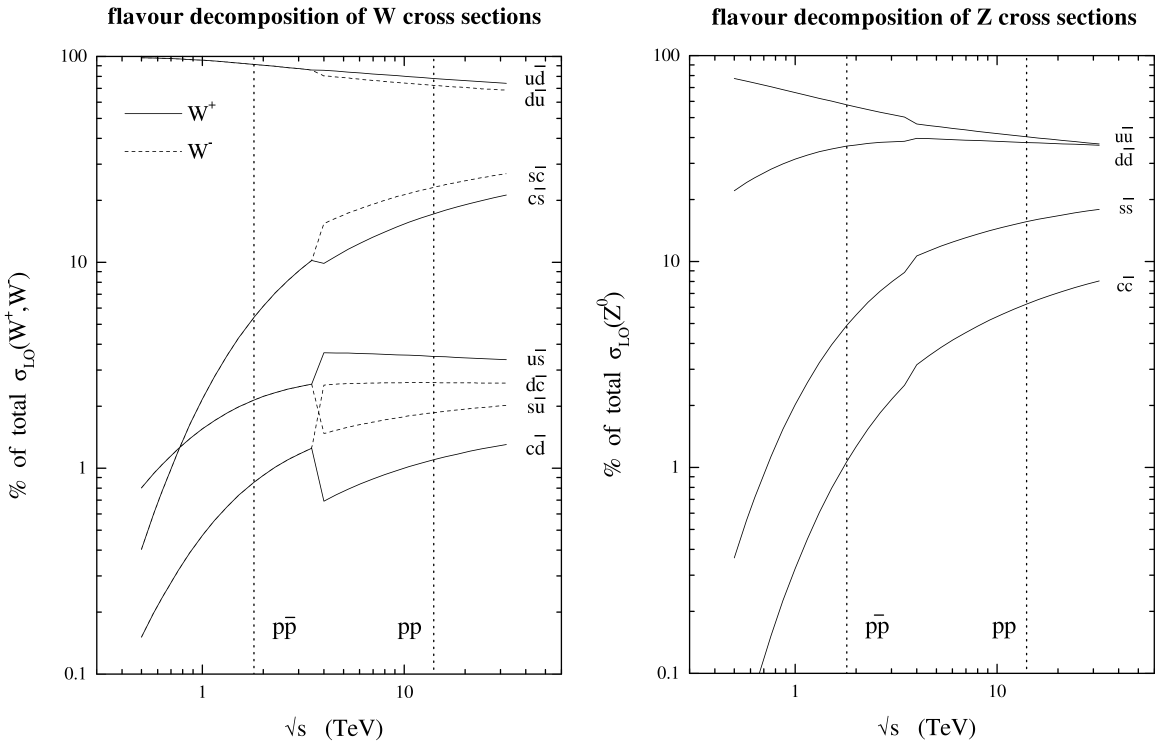

Figure 5.4: Flavor decomposition of $W^\pm$ and Z^0 production cross sections at LO [MRST00].

W production charge asymmetry

W and Z bosons are produced by initial hard collisions between partons and in the LO approximation gluons do not take part on their production (Fig. 5.1). Thus at LO W^+ bosons can only be produced by the coupling of $u\bar{d}'$ and $c\bar{s}'$, while W^- are produced by the coupling of $d'\bar{u}$ and $s'\bar{c}$ (where d' and s' are the 'Cabibbo-rotated' states [Gri04], see also Sec. 2.3.3). ***So the isospin content of the colliding nuclei (see PDFs in Fig. 5.5) may differentiate positive and negative W production depending on the colliding system.*** Till now W production has been studied in e^+-e^- and p-p̄ collisions at LEP (CERN), SLC (SLAC) and Tevatron (FNAL) [Y^+06]. In those conditions the net isospin content of the colliding system is null, and the total W charge is also null. In the future p-p, p-Pb and Pb-Pb collisions at LHC the colliding nuclei net isospin will not be null, so there could be a difference on the positive and

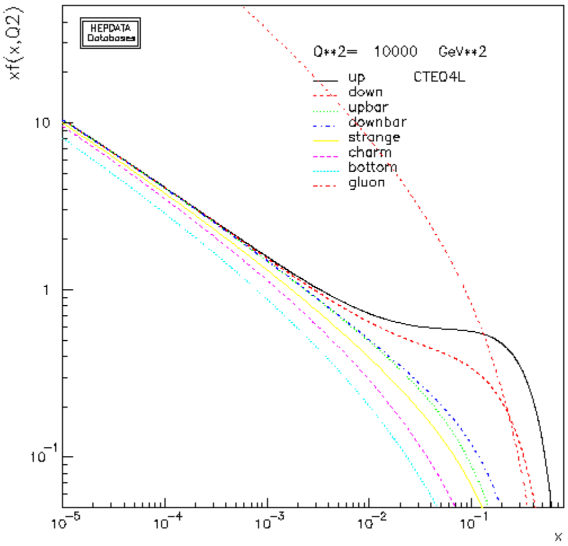

Figure 5.5: CTEQ4L parton distribution functions at $Q = 100$ GeV.

negative W produced charge. For instance, as protons are made up of uud valence quarks ($N_u = 2N_d$), in p-p collisions W$^+$ production will be favored with respect to that of W$^-$. One can evaluate the Bjorken-x values contributing to the production of a W boson at a given rapidity y as

$$x_{1,2} = \frac{M_W}{\sqrt{s_{NN}}} \cdot e^{\pm y} \,, \tag{5.1}$$

where M_W is the W mass and $\sqrt{s_{NN}}$ is the center-of-mass energy. A W boson at mid-rapidity is produced by low values of $x_{1,2}$ (i.e. $x_{1,2} \ll 0.1$, e.g. in p-p collisions at 14 TeV for $y = 0$, $x_{1,2} = 5.7 \cdot 10^{-3}$), so it is mainly produced by sea quarks interactions. But W production at high-rapidity concerns at least one high value of x (i.e. $x \geq 0.1$, e.g. in p-p collisions at 14 TeV for $y = 3$, $x_1 = 0.12$ and $x_2 = 2.9 \cdot 10^{-4}$), then valence quarks contribution is predominant. Therefore, in p-p collisions at 14 TeV one expects that at high-rapidity at most $N_{W^+} = 2N_{W^-}$. On the contrary, in Pb-Pb collisions at 5.5 TeV we should consider proton (uud) and neutron (udd) valence quark contents. Thus, $(2Z + N)$ u valence quarks and $(Z + 2N)$ d valence quarks are involved. On those reactions at high-rapidity at most

$$\frac{N_{W^-}}{N_{W^+}} = \frac{Z + 2N}{2Z + N} \qquad N_{W^-} = 1.15\, N_{W^+} \qquad \text{(for Pb-Pb collisions)}.$$

Parity violation on W leptonic decays

The weak interaction only couples left-handed fermions with right-handed anti-fermions. Following the LO diagram, W bosons will be polarized in the direction of the anti-quark momentum. W bosons emitted at high rapidities will be produced in parton-parton collisions with $x_1 \lesssim 1$ and $x_2 \ll 1$, and partons with $x \sim 1$ will probably be quarks. There-

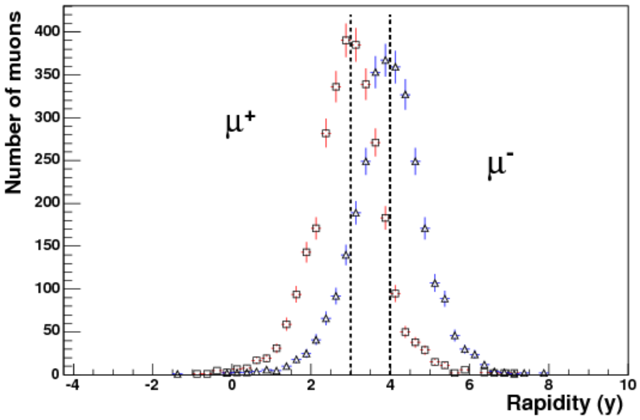

Figure 5.6: Muon rapidity distribution for W bosons decays at $y_w \in (3.0, 4.0)$.

fore, the W bosons will tend to be polarized in the opposite direction to their momentum (they will predominantly be left-handed). With regard to its leptonic decay: $W^+ \to l^+\nu_l$, $W^- \to l^-\bar{\nu}_l$, the fact that antineutrinos are right-handed will favor the emission of leptons in the opposite direction of the W polarization and anti-leptons in its polarization direction. In this respect, ***W$^-$ bosons produced at high rapidities will preferably emit negative muons in its momentum direction and W$^+$ bosons will preferably emit positive muons in the opposite direction to its momentum***. This is certainly the effect that we observe in the simulations. For example, Fig. 5.6 reproduce the muon rapidity spectra for W$^+$ and W$^-$ simulated at $y \in (3.0, 4.0)$ with the PYTHIA event generator. For the same W$^\pm$ distribution at high-rapidities, the μ^+ distribution tends to be shifted to mid-rapidity, and the μ^- to higher rapidities. These effects are explained in more detail in Appendix C.

Parton Distribution Functions

Electroweak measurements will allow to explore the parton distribution functions at $Q^2 \sim M_W^2$ and $Q^2 \sim M_Z^2$. Tab. 5.1 report Bjorken-x values for W production at 14 TeV in proton proton collisions as a function of W rapidity. We observe that, for p-p collisions, the quark distribution functions will be probed (at $Q = M_W$) in the regions $x \in (1.1 - 4.7) \cdot 10^{-4}$ and $x \in (2.1 - 5.7) \cdot 10^{-3}$ by the ALICE muon spectrometer ($-4.0 < \eta < -2.5$) and by the central barrel ($|\eta| < 0.9$) respectively. In Pb-Pb, p-Pb and Pb-p collisions we will be able to probe nuclear modification effects in lead nuclei. Bjorken-x values for these collisions are presented in Tabs. 5.2, 5.3 and 5.4. Note that for asymmetric colliding systems we have to take into account the shift of the center of mass rapidity with respect to the laboratory reference system due to the different energy of the colliding beams ($|\Delta\eta| = 0.5$). Then, ALICE central barrel covers $-0.5 < \eta < 1.5$ ($-1.5 < \eta < 0.5$) and the muon spectrometer covers $-3.5 < \eta < -2.0$ ($-4.5 < \eta < -3.0$) in p-Pb (Pb-p) collisions.

Similar calculations can be done to evaluate the kinematic region that will be explored by Z production, obtaining values close to those probed by W production. For instance, in

y (rapidity)	$x_1\,(p)$	$x_2\,(p)$
0.0	$5.7{\cdot}10^{-3}$	$5.7{\cdot}10^{-3}$
1.0	$1.6{\cdot}10^{-2}$	$2.1{\cdot}10^{-3}$
2.5	$7.0{\cdot}10^{-2}$	$4.7{\cdot}10^{-4}$
3.0	$1.2{\cdot}10^{-1}$	$2.9{\cdot}10^{-4}$
4.0	$3.1{\cdot}10^{-1}$	$1.1{\cdot}10^{-4}$

Table 5.1: Average Bjorken-x values for W production in **p-p collisions** at $\sqrt{s_{NN}} = 14$ TeV as a function of W rapidity.

y (rapidity)	$x_1\,(Pb)$	$x_2\,(Pb)$
0.0	$1.5{\cdot}10^{-2}$	$1.5{\cdot}10^{-2}$
1.0	$4.0{\cdot}10^{-2}$	$5.4{\cdot}10^{-3}$
2.5	$1.8{\cdot}10^{-1}$	$1.2{\cdot}10^{-3}$
3.0	$2.9{\cdot}10^{-1}$	$7.3{\cdot}10^{-4}$
4.0	$8.0{\cdot}10^{-1}$	$2.7{\cdot}10^{-4}$

Table 5.2: Average Bjorken-x values for W production in **Pb-Pb collisions** at $\sqrt{s_{NN}} = 5.5$ TeV as a function of W rapidity.

y (rapidity)	$x_1\,(Pb)$	$x_2\,(p)$
1.5	$4.0{\cdot}10^{-2}$	$2.0{\cdot}10^{-3}$
0.0	$9.1{\cdot}10^{-3}$	$9.1{\cdot}10^{-3}$
-0.5	$5.5{\cdot}10^{-3}$	$2.0{\cdot}10^{-2}$
-2.0	$1.2{\cdot}10^{-3}$	$7.0{\cdot}10^{-2}$
-3.0	$4.6{\cdot}10^{-4}$	$1.8{\cdot}10^{-1}$
-3.5	$2.8{\cdot}10^{-4}$	$3.0{\cdot}10^{-1}$

Table 5.3: Average Bjorken-x values for W production in **p-Pb collisions** at $\sqrt{s_{NN}} = 8.8$ TeV as a function of W rapidity (x_2 refers to proton, and x_1 to lead nuclei).

y (rapidity)	$x_1\,(p)$	$x_2\,(Pb)$
0.5	$2.0{\cdot}10^{-2}$	$5.5{\cdot}10^{-3}$
0.0	$9.1{\cdot}10^{-3}$	$9.1{\cdot}10^{-3}$
-1.5	$2.0{\cdot}10^{-3}$	$4.0{\cdot}10^{-2}$
-3.0	$4.6{\cdot}10^{-4}$	$1.8{\cdot}10^{-1}$
-3.5	$2.8{\cdot}10^{-4}$	$3.0{\cdot}10^{-1}$
-4.5	$1.0{\cdot}10^{-4}$	$8.2{\cdot}10^{-1}$

Table 5.4: Average Bjorken-x values for W production in **Pb-p collisions** at $\sqrt{s_{NN}} = 8.8$ TeV as a function of W rapidity (x_1 refers to proton, and x_2 to lead nuclei).

p-p collisions at 14 TeV Z production will permit to test $x \in (1.2 - 5.3) \cdot 10^{-4}$ and $x \in (2.4 - 6.5) \cdot 10^{-3}$ by the ALICE muon spectrometer and by the central barrel respectively.

5.1.2 Generation with PYTHIA

PYTHIA 6.2 [S+02] event generator and its interface in AliRoot [Ali] have been used to simulate W and Z production at LHC energies. W and Z production have been implemented in AliRoot/PYTHIA6/AliPythia with the cases *kPyW* and *kPyZ* [1]. PYTHIA default parameters for electroweak production have been considered: $2 \rightarrow 1$ processes and turn on initial and final state radiation. $2 \rightarrow 1$ processes generate electroweak production at LO, and the showers, initial and final state radiation, permit the interaction with gluons and photons in the initial and final state allowing the boson to have a non null p_T and ranking with NLO processes. In references [MS99, BHP01, S+02] it is shown that in this way PYTHIA reproduces W and Z p_T distribution in p-$\bar{p}$ collisions at Tevatron energies.

---

[1] *kPyW* implementation was committed on March 2005, from CVS Tag v4-03-00.
kPyZ was committed on February 2006, from CVS Tag v4-04-00.

Moreover, in order to enhance the Monte Carlo statistics for particular W and Z decay channels, four AliDecayer *cases have been implemented:* kWToMuon, kWToCharm, kWToCharmToMuon *and* kZDiMuon [2]*. The first one,* kWToMuon*, forces W bosons to decay directly into muons. The second one,* kWToCharm*, forces W to decay into a charm quark plus anything.* kWToCharmToMuon *combines forcing W to decay into a charm quark and forcing charmed hadrons to decay into muons. Finally,* kZDiMuon *forces Z bosons to decay in the dimuon channel.*

Simulations in nucleus-nucleus collisions

In order to properly simulate electroweak boson production in any nucleus-nucleus (A-B) collision it is essential to correctly take into account valence quarks composition of colliding nuclei. PYTHIA MonteCarlo generator is not able to simulate any A-B collision, in particular p-A and A-B collisions, as it does not consider that nuclei have protons and neutrons, and that their quark composition is different. But PYTHIA is able to simulate p-p, n-n, p-n and n-p collisions at given $\sqrt{s_{NN}}$. Therefore, ***we decided to simulate A-B reactions as a combination of weighted p-p, n-n, p-n and n-p collisions***, according to

$$\begin{aligned}\frac{d^2\sigma_{NN}}{dp_T dy} \approx\ & \frac{Z_1 Z_2}{A_1 A_2} \times \frac{d^2\sigma_{pp}}{dp_T dy} + \frac{(A_1 - Z_1)\cdot(A_2 - Z_2)}{A_1 A_2} \times \frac{d^2\sigma_{nn}}{dp_T dy} + \\ & \frac{Z_1 \cdot (A_2 - Z_2)}{A_1 A_2} \times \frac{d^2\sigma_{pn}}{dp_T dy} + \frac{(A_1 - Z_1)\cdot Z_2}{A_1 A_2} \times \frac{d^2\sigma_{np}}{dp_T dy}\,,\end{aligned} \tag{5.2}$$

that for the A-A case gets simplified to

$$\begin{aligned}\frac{d^2\sigma_{NN}}{dp_T dy} \approx\ & \frac{Z^2}{A^2} \times \frac{d^2\sigma_{pp}}{dp_T dy} + \frac{(A - Z)^2}{A^2} \times \frac{d^2\sigma_{nn}}{dp_T dy} + \\ & \frac{Z \cdot (A - Z)}{A^2} \times \left\{ \frac{d^2\sigma_{pn}}{dp_T dy} + \frac{d^2\sigma_{np}}{dp_T dy} \right\}.\end{aligned} \tag{5.3}$$

Where $\frac{d^2\sigma_{NN}}{dp_T dy}$ represents the differential production cross section per nucleon-nucleon collision in A-B reactions, $\frac{d^2\sigma_{pp}}{dp_T dy}$ stands for differential production cross section in p-p collisions (the same notation is applied to n-n, p-n and n-p collisions), and A and Z are the mass number and the atomic number of the nuclei.

From now on, all results concerning A-B simulations will be presented in terms of production cross sections per nucleon-nucleon collision. ***Total A-B production cross sections can be derived from the nucleon-nucleon ones by means of binary scaling*** [GM70, d'E03]. In minimum bias hard collisions:

$$\sigma_{AB}^{hard} = \int d^2\overrightarrow{b}\left(1 - e^{-\sigma_{NN}^{hard}\cdot T_{AB}(b)}\right) \approx \int d^2\overrightarrow{b}\ \sigma_{NN}^{hard} \cdot T_{AB}(b)\,; \tag{5.4}$$

---

[2] *kWToMuon*, *kWToCharm*, *kWToCharmToMuon* were committed on July 2005, from CVS Tag v4-03-03. *kZDiMuon* wad committed on February 2006, from CVS Tag v4-04-00.

$$T_{AB}(b) = \int 2\pi b\, T_A(s) T_B(|\overrightarrow{b} - \overrightarrow{s}|)\, db\ ; \qquad T_A(b) = \int_{-\infty}^{+\infty} dz\, \rho_A(b,z)\ ; \qquad \int_0^{\infty} d^2\overrightarrow{b}\, T_A(b) = A\ ;$$

where $\rho_A(b,z)$ is the nuclear density of nucleus A, $T_A(b)$ is the nuclear thickness function of nucleus A at impact parameter b, and $T_{AB}(b)$ is the nuclear overlap function of nuclei A and B at impact parameter b (see Fig. 5.7 for an sketch of an A-B collision). This formalism permits to calculate A-B hard production cross sections and yields for a given centrality class, CC, as follows:

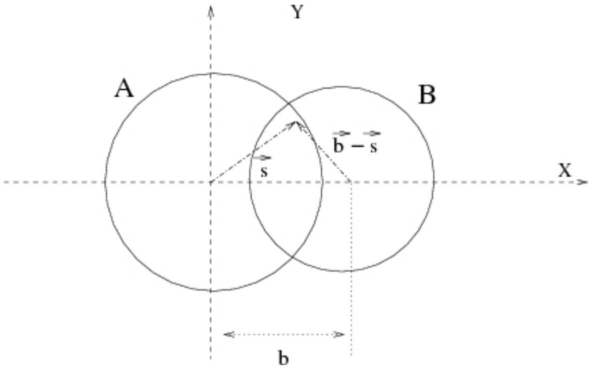

Figure 5.7: Scheme of a A-B collision in the transverse plane to the beam line.

$$\left(\frac{d^2\sigma_{AB}^{hard}}{dp_T dy}\right)^{CC} \approx \langle T_{AB}\rangle^{CC} \cdot (\sigma_{AB}^{inel})^{CC} \cdot \frac{d^2\sigma_{NN}^{hard}}{dp_T dy}\ ; \tag{5.5}$$

$$\left(\frac{d^2 N_{AB}^{hard}}{dp_T dy}\right)^{CC} \approx \langle N_{coll}\rangle^{CC} \cdot \frac{d^2 N_{NN}^{hard}}{dp_T dy}\ ; \qquad \langle N_{coll}\rangle^{CC} = \langle T_{AB}\rangle^{CC} \cdot \sigma_{NN}^{inel}\ .$$

Appendix D presents a more detailed treatment of this model and its associated formalism. Note that PDFs in nucleus-nucleus collisions could be modified with respect to p-p collisions by nuclear effects. In the simulations this has been taken into account by considering EKS98 shadowing parameterization [EKS99].

5.2 Results on W boson production at LHC energies

The production of W bosons at LHC energies in the muonic decay channel is presented in this section. p-p collisions at 14 TeV, p-Pb collisions at 8.8 TeV and Pb-Pb collisions at 5.5 TeV are studied. In all cases CTEQ4L PDFs [LHK+97] have been used and spectra have been absolutely normalized to NLO calculations of the production cross section that can be found in Tab. 5.5 [FM04, Vog01, Vog02].

5.2.1 Proton-proton collisions at 14 TeV

According to PYTHIA, the W production cross section in p-p collisions at 14 TeV, including the muonic branching ratio, is 17.2 nb. Theoretical calculations estimate this production

collision ($\sqrt{s_{NN}}\,[TeV]$)	p-p (14)	p-Pb (8.8)	Pb-Pb (5.5)	p-p (5.5)
$\sigma^{W}_{NN} \times BR_{\mu\nu}$ [nb]	20.9 [FM04]	11.3 [Vog01]	6.56 [Vog01]	7.34 [Vog01]
$\sigma^{Z}_{NN} \times BR_{\mu^+\mu^-}$ [nb]	1.9 [TCSG05]	1.1 [Vog01]	0.63 [Vog01]	0.68 [Vog01]

Table 5.5: W and Z production cross-sections per nucleon-nucleon collision from NLO calculations. Shadowing is included in Pb-Pb and p-Pb calculations.

cross section to be 18.27 nb in the LO approximation and 20.90 nb in the NLO approximation [FM04]. Higher order corrections are expected to have a negligible influence on the spectra shape and on the integrated cross section [ADMP04].
W differential production cross-section is presented in Fig. 5.8 as a function of rapidity[3], where the error bars are only statistical. We observe that:

- ***More W$^+$ than W$^-$ are produced***, as expected from the valence quark composition of the colliding particles (there are more u than d valence quarks in p-p collisions);
- ***W$^+$ production is peaked at high-rapidity while W$^-$ production is peaked at mid-rapidity.*** In particular, for $y = 3.5$, $N_{W+} \sim 2N_{W-}$, as we should expect if valence quarks are the main contributors to W production cross section in this rapidity domain. In contrast, at mid-rapidity, for $y = 0$, $N_{W+} \sim N_{W-}$, pointing out the sea-sea quark interaction dominance. Those results are in accord with predictions from Fig. 5.3, where for $y = 0$ $N_{W+} \approx 1.05\, N_{W-}$ and for $y = 3$ $N_{W+} \approx 2\, N_{W-}$;

In addition, in Fig. 5.9 muon production differential cross section as a function of rapidity is presented. We remark that:

- ***More μ^+ than μ^- are produced*** because more W$^+$ than W$^-$ are produced;
- In the muon spectrometer pseudo-rapidity range ($-4.0 < \eta < -2.5$) we should be able to observe the asymmetry in the production of μ^+/μ^-;
- ***μ^+ rapidity distribution is narrower than that of W$^+$ while μ^- distribution is wider than that of W$^-$.*** This is mainly due to polarization (parity violation) effects. For more details see Sec. 5.1.1 and/or Appendix C.

The transverse momentum distribution of muons emitted in W decays inside the spectrometer acceptance[4] is shown in Fig. 5.10. As expected, this distribution shows a peak in the region between 30 and 50 GeV/c, corresponding to about $M_W/2$. Finally, Fig. 5.11 shows the ratio of positive and negative muon yields (the muon charge asymmetry) as a function of p_T in the whole rapidity range and in the muon spectrometer acceptance. ***The muon spectrometer acceptance has an important effect on the shape of the muon charge asymmetry***

---

[3] We have simulated W production with AliRoot version AliRoot-pro-4.01.04 and PYTHIA 6.2. PYTHIA cross-sections have been absolutely normalized to NLO theoretical calculations [FM04].

[4] It is worth noting that here the muon spectrometer acceptance has been defined by a pseudo-rapidity range of $-4.0 < \eta < -2.5$, a transverse momenta $p_T > 1$ GeV/c, and a total momentum $p > 4$ GeV/c.

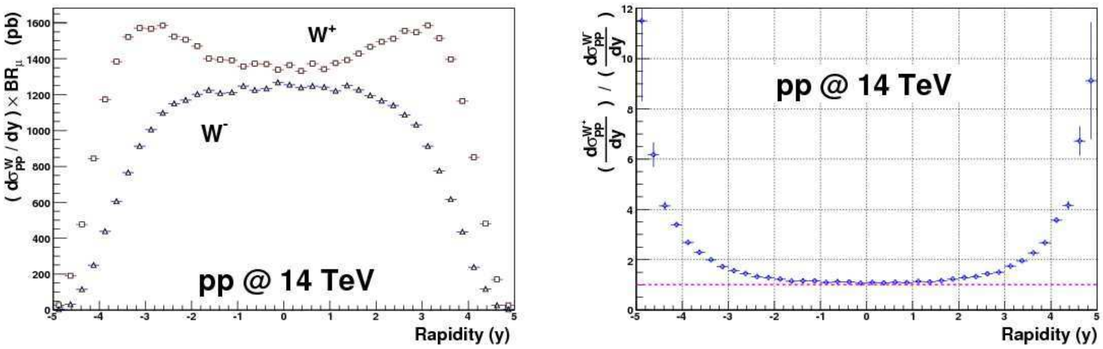

Figure 5.8: On the left, W bosons differential production cross section as a function of rapidity for **p-p collisions** at $\sqrt{s_{NN}} = 14$ TeV, in the case of **W muonic decay**. Squares represent W$^+$ and triangles W$^-$. On the right, W$^+$/W$^-$ differential production cross section ratio.

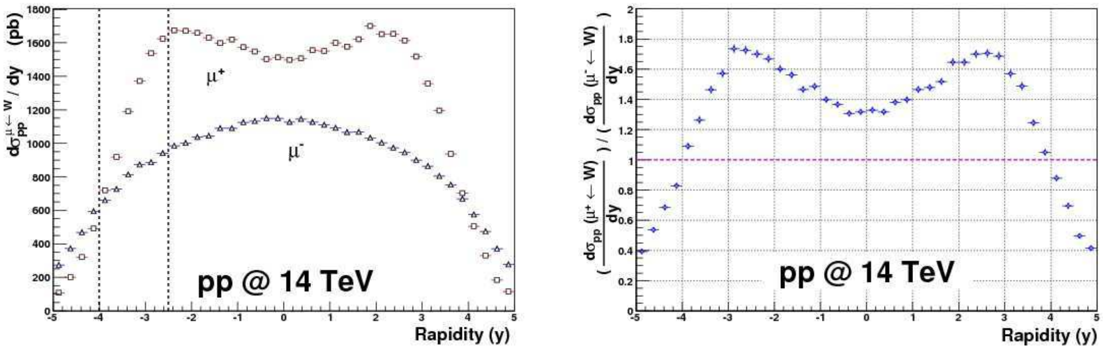

Figure 5.9: On the left, muon differential production cross section as a function of rapidity in **p-p collisions** at $\sqrt{s_{NN}} = 14$ TeV for **W muonic decays**. Squares represent μ^+ and triangles μ^-. The dashed lines indicate the muon spectrometer acceptance. On the right, μ^+/μ^- differential production cross section ratio.

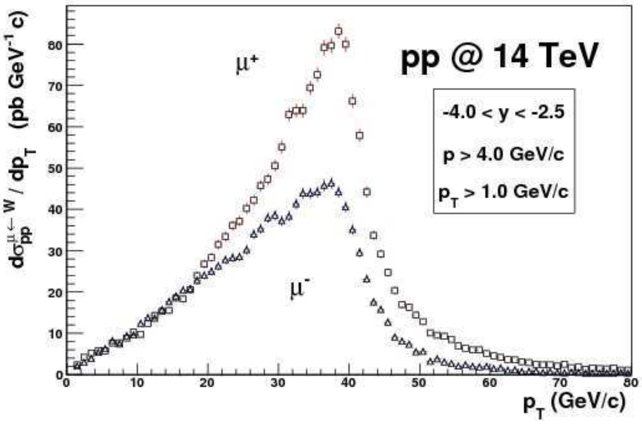

Figure 5.10: Muon differential production cross section from **W muonic decays** in the ALICE muon spectrometer acceptance as a function of transverse momentum in **p-p collisions** at $\sqrt{s_{NN}} = 14$ TeV. Squares represent μ^+ and triangles μ^-.

distribution. The ratio μ^+/μ^- is close to the unity at low p_T and grows around half the W mass (where the muon peak is situated).

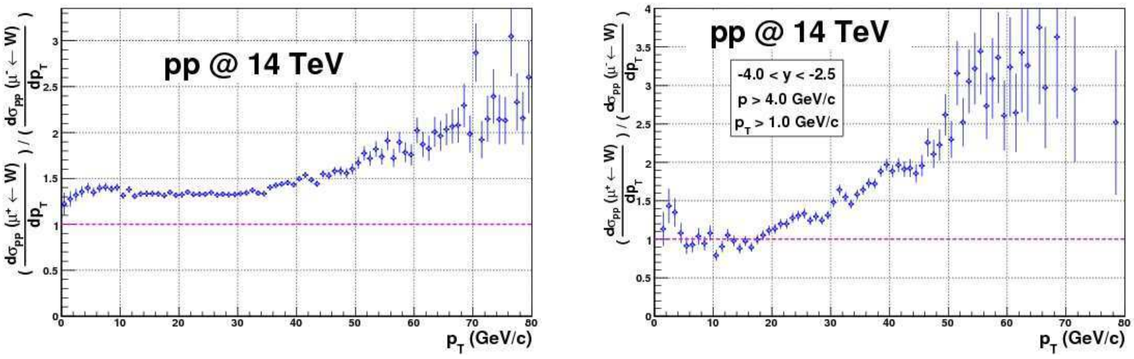

Figure 5.11: Ratio of single muons (μ^+/μ^-) production cross section over the whole rapidity range (left figure) and in the muon spectrometer acceptance (right figure) for **W muonic decays** as a function of transverse momentum in **p-p collisions** at $\sqrt{s_{NN}} = 14$ TeV.

Expected muon yields in the muon spectrometer acceptance

In standard data-taking conditions, the p-p integrated luminosity in ALICE will be $\mathcal{L} = 3 \cdot 10^{37}$ cm^{-2} (that is 30 pb^{-1}) in one year of data-taking (which corresponds to $t \sim 10^7$ s), see [C$^+$04, Mar05] or Tab. 3.1. So, considering the NLO production cross section of 20.9 nb, we estimate that about $6.3 \cdot 10^5$ muons from W muonic decays will be produced in the whole rapidity range. This corresponds to $8.9 \cdot 10^4$ muons in the muon spectrometer acceptance. Out of them, $5.1 \cdot 10^4$ muons will fall in the p_T range $(30, 50)$ GeV/c. These results are summarized in Tab. 5.6.

Collision	$N_{\mu\leftarrow W}$	$N^{Acc}_{\mu\leftarrow W}$
p-p	$6.3 \cdot 10^5$	$8.9 \cdot 10^4$ ($\sim 14\%$ Acc)
Restricting p_T range to $(30, 50)$ GeV/c		
p-p	$3.3 \cdot 10^5$	$5.1 \cdot 10^4$

Table 5.6: Estimated number of muons produced in the ALICE acceptance in **p-p collisions** for W boson muonic decays. $N_{\mu\leftarrow W}$ stands for number of produced muons in $4\,\pi$ per year of data-taking, and $N^{Acc}_{\mu\leftarrow W}$ stands for number of produced muons in the ALICE muon spectrometer acceptance per year of data-taking. Values have been computed assuming an integrated luminosity $\mathcal{L} = 3 \cdot 10^{37}$ cm^{-2} [C$^+$04, Mar05].

5.2.2 Lead-lead collisions at 5.5 TeV

We have simulated W boson production in Pb-Pb collisions[5] following the techniques described in Sec. 5.1.2 to account for the isospin of the colliding nuclei. Shadowing effects in nuclear PDFs in Pb-Pb conditions have been studied in references [Vog01, Vog02] in the NLO approximation. In the simulations they have been considered by using the EKS98 parameterization [EKS99]. It has been estimated that the production cross section of W bosons for p-p collisions at 5.5 TeV is $\sigma^W_{pp} \simeq 69.28$ nb and for Pb-Pb collisions is $\sigma^W_{NN} \times C_{shad} \simeq 61.84$ nb including shadowing [Vog01, Vog02]. That is a production cross section of muons from W decays of $\sigma^W_{NN} \times C_{shad} \times BR_\mu \simeq 6.56$ nb for Pb-Pb collisions. Hence, shadowing effect reduces the production cross section of 10 % in 4 π [Vog01, Vog02]. In the spectrometer acceptance, the shadowing influence diminishes the production cross section by ~ 16 %.

In Fig. 5.12 W bosons distributions as a function of rapidity in p-n collisions at 5.5 TeV are presented. The asymmetry between W^+ and W^- production is different from the one observed in p-p collisions (Fig. 5.8), as expected from valence quark contribution to W production (isospin effects). Notice that as in p-n collisions the proton beam comes from the muon spectrometer side (that is negative rapidity sign), and W^+ production is boosted towards the direction of the proton beam, W^+ yield is peaked on the positive rapities. The same effect can be observed on W^- yield which is peaked at negative rapidities, in the direction of the neutron beam. The spectra have been absolutely normalized to the NLO theoretical predictions of the production cross section per nucleon-nucleon collision for Pb-Pb reactions to guide the eye in further comparisons.

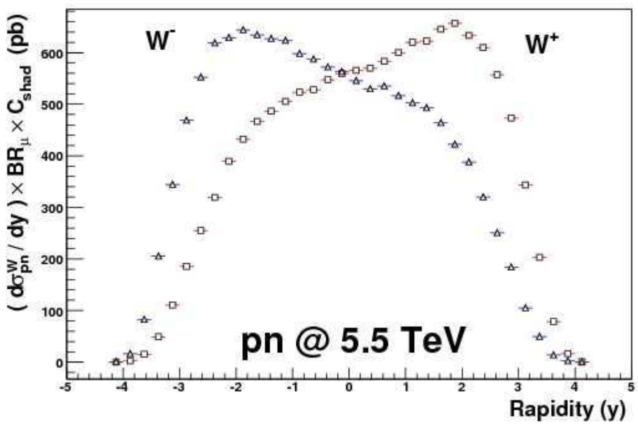

Figure 5.12: W bosons differential production cross section as a function of rapidity in **p-n collisions** at $\sqrt{s_{NN}} = 5.5$ TeV in the case of **W muonic decays**. Squares represent W^+, and triangles W^-.

The W rapidity distributions in Pb-Pb collisions, shown in Fig. 5.13, indicate that ***the nuclei isospin induce a smaller W^+ and W^- production asymmetry in Pb-Pb collisions than in p-p collisions. Even more W^- than W^+ are produced, in contrast to p-p collisions where***

---

[5] We have simulated W bosons in Pb-Pb collisions with AliRoot-pro version v4-01-Rev04, and PYTHIA 6.2.

much more W$^+$ than W$^-$ are produced. Indeed, at $y = 2$ there are $\sim 11\%$ more W$^-$ than W$^+$, as expected from isospin dependence ($(Z + 2N)/(2Z + N) = 1.15$).
Muon differential production cross section per nucleon-nucleon collision from W muonic decays is plotted in Fig. 5.14. We observe that ***μ^+ distribution is narrower than that of W$^+$ while μ^- distribution is wider than that of W$^-$***. Therefore, in the muon spectrometer acceptance much more μ^- than μ^+ from W are observed. Those asymmetries are caused by parity violation effects on W production and decays. See Sec. 5.1.1 and/or Appendix C for further explanations.
Fig. 5.15 represents muon differential production cross section per nucleon-nucleon collision as a function of p_T in the muon spectrometer acceptance. Finally, in Fig. 5.16 we can observe the muon charge asymmetry as a function of p_T over the whole rapidity range and in the muon spectrometer acceptance. ***As in the case of p-p collisions, the effect of the muon spectrometer acceptance on the spectra shape can be observed. In contrast to p-p collisions, for Pb-Pb collisions the ratio μ^+/μ^- is lower than unity.***

Expected muon yields in the muon spectrometer acceptance

In standard Pb-Pb data-taking conditions, the expected integrated luminosity is $\mathcal{L} = 5 \cdot 10^{32}$ cm^{-2} (that is 0.5 nb^{-1}), see [C$^+$04, Mar05] or Tab. 3.1. In these conditions and considering NLO production cross section (which includes shadowing), we evaluate that about $1.4 \cdot 10^5$ muons will be produced in the whole rapidity range in Pb-Pb collisions by W muonic decays. A total of $7.5 \cdot 10^4$ muons will be in the high p_T range ($p_T \in (30, 50)$ GeV/c). About $1.4 \cdot 10^4$ muons will be produced in the ALICE muon spectrometer acceptance; out of them, about $6.9 \cdot 10^3$ muons will fall in the high p_T range (30-50 GeV/c). Tab. 5.7 summarizes these estimations.

Collision	$N_{\mu\leftarrow W}$	$N^{Acc}_{\mu\leftarrow W}$
Pb-Pb	$1.4 \cdot 10^5$	$1.4 \cdot 10^4$ ($\sim 11\%$ Acc)
Restricting p_T range to $(30, 50)$ GeV/c		
Pb-Pb	$7.5 \cdot 10^4$	$6.9 \cdot 10^3$

Table 5.7: Estimated values of the number of muons produced in the ALICE muon spectrometer acceptance in **Pb-Pb collisions** by means of W boson muonic decays. $N_{\mu\leftarrow W}$ stands for number of produced muons in $4\ \pi$ per year of data-taking, and $N^{Acc}_{\mu\leftarrow W}$ stands for number of produced muons in the ALICE muon spectrometer acceptance per year of data-taking. Values computed assuming an integrated luminosity $\mathcal{L} = 5 \cdot 10^{32}$ cm^{-2} [C$^+$04, Mar05].

5.2.3 Proton-lead collisions at 8.8 TeV

W boson production in p-Pb collisions has been simulated with the same procedure used for Pb-Pb collisions to include the isospin of the colliding nuclei[6]. Shadowing effects in nu-

---

[6] We used AliRoot-Head of January 2006, PYTHIA 6.2 and the techniques described in Sec. 5.1.2.

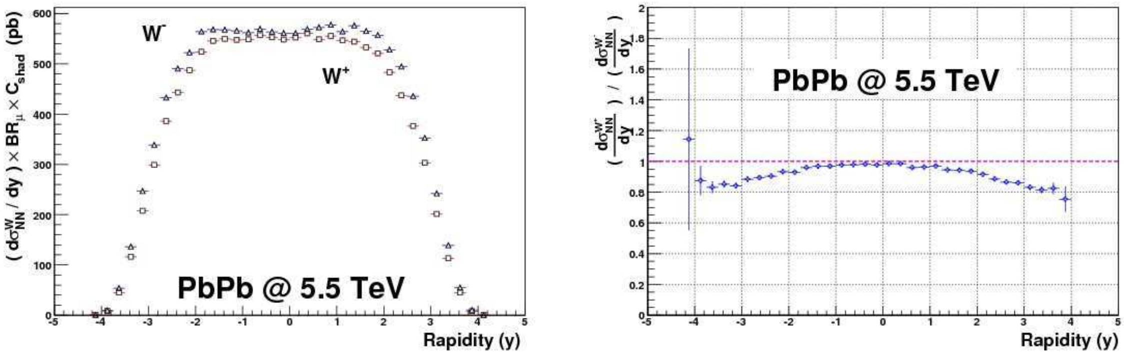

Figure 5.13: On the left, W bosons differential production cross section per nucleon-nucleon collision as a function of rapidity in **Pb-Pb reactions** at $\sqrt{s_{NN}} = 5.5$ TeV for **W muonic decays**. Squares represent W$^+$ and triangles W$^-$. On the right, W$^+$/W$^-$ differential production cross section ratio.

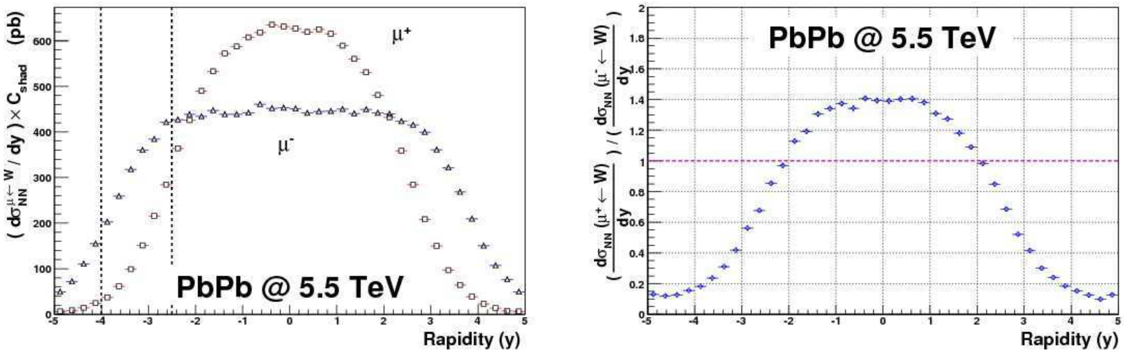

Figure 5.14: On the left, muon differential production cross section per nucleon-nucleon collision as a function of rapidity in **Pb-Pb reactions** at $\sqrt{s_{NN}} = 5.5$ TeV for **W muonic decays**. Squares represent μ^+ and triangles μ^-. The dashed lines indicate the muon spectrometer acceptance. On the right, μ^+ / μ^- differential production cross section ratio.

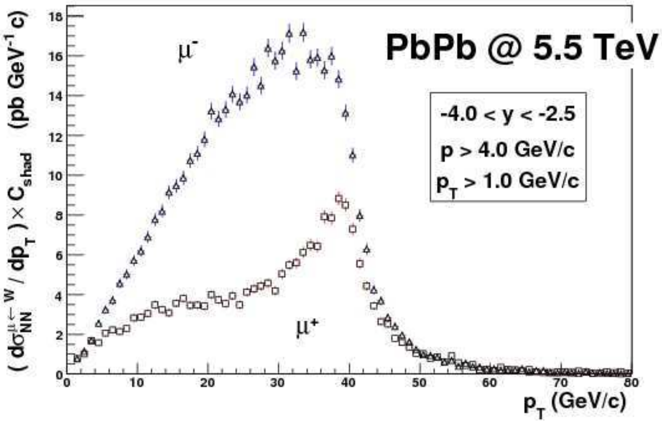

Figure 5.15: Differential production cross section per nucleon-nucleon collision of muons from **W muonic decays** in the ALICE muon spectrometer acceptance as a function of transverse momenta in **Pb-Pb collisions** at $\sqrt{s_{NN}} = 5.5$ TeV. Squares represent μ^+ and triangles μ^-.

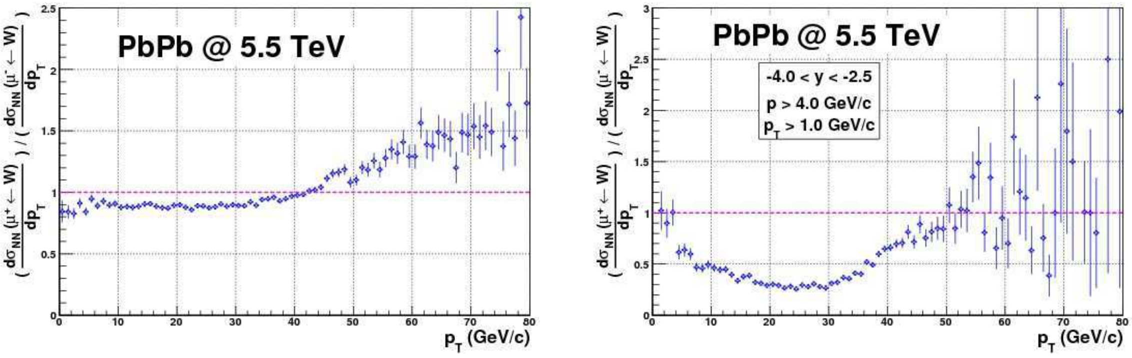

Figure 5.16: Ratio of single muons (μ^+/μ^-) production cross section over the whole rapidity range (left figure) and in the muon spectrometer acceptance (right figure) for **W muonic decay** as a function of transverse momentum in **Pb-Pb collisions** at $\sqrt{s_{NN}} = 5.5$ TeV.

clear PDFs in p-Pb conditions have been studied in references [Vog01, Vog02] in the NLO approximation. In the simulations they have been considered by using the EKS98 parameterization [EKS99]. The W bosons production cross-section in p-p collisions at 8.8 TeV has been estimated to be $\sigma^W_{pp} \simeq 114.5\,\mathrm{nb}$ and for p-Pb collisions is $\sigma^W_{NN} \times C_{shad} \simeq 107.0\,\mathrm{nb}$ including shadowing [Vog01, Vog02]. Which implies a production cross section of muons from W decays of $\sigma^W_{NN} \times C_{shad} \times BR_\mu \simeq 11.3\,\mathrm{nb}$ for p-Pb collisions. Shadowing effect reduces the production cross section of $7\,\%$ in $4\,\pi$ [Vog01, Vog02].

W differential production cross section per nucleon-nucleon collision in p-Pb reactions is presented in Fig. 5.17. Notice that for p-Pb reactions we considered that the proton comes from the 'negative z-axis' direction and the lead from the 'positive z-axis' direction, the former being on the muon spectrometer side. ***Isospin effects of the colliding nuclei can be perceived on the W charge production asymmetry, as expected and as it has also been observed for the cases of p-p, p-n and Pb-Pb collisions.*** Notice that the correspondent plots for Pb-p reactions would be their mirror images with respect to the rapidity axis.

The muon rapidity distributions, plotted in Fig. 5.18, reflect the effects of parity violation on W production and decays, as expected and already observed on the other reactions (Sec. 5.1.1 and/or Appendix C). ***In the muon spectrometer acceptance slightly more μ^- than μ^+ are produced, both for p-Pb collisions (marked by dashed lines in the plot) and for Pb-p collisions (marked by dot-dashed lines in the plot).*** Fig. 5.19 represents the muon distributions in the spectrometer acceptance as a function of the transverse momentum for p-Pb collisions. The muon production charge asymmetry in the whole rapidity range and in the spectrometer acceptance can be observed in Fig. 5.20. ***The effect of the muon spectrometer acceptance on the shape of the μ^+/μ^- ratio is non negligible. In particular, while the μ^+/μ^- ratio is slightly larger than one when integrated over the whole rapidity range (because globally there is more W$^+$ than W$^-$), it turns to be below one in the spectrometer acceptance.***

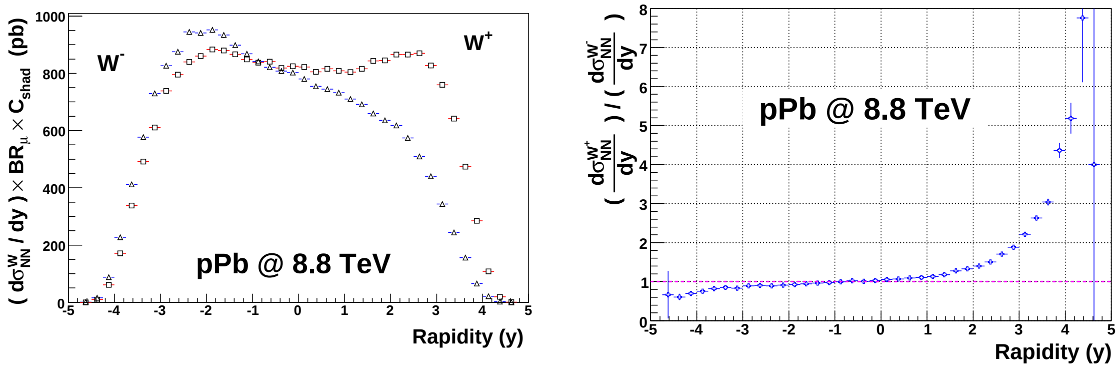

Figure 5.17: On the left, W bosons differential production cross section per nucleon-nucleon collision as a function of rapidity in **p-Pb reactions** at $\sqrt{s_{NN}} = 8.8$ TeV for **W muonic decays**. Squares represent W$^+$ and triangles W$^-$. On the right, W$^+$/W$^-$ differential production cross section ratio.

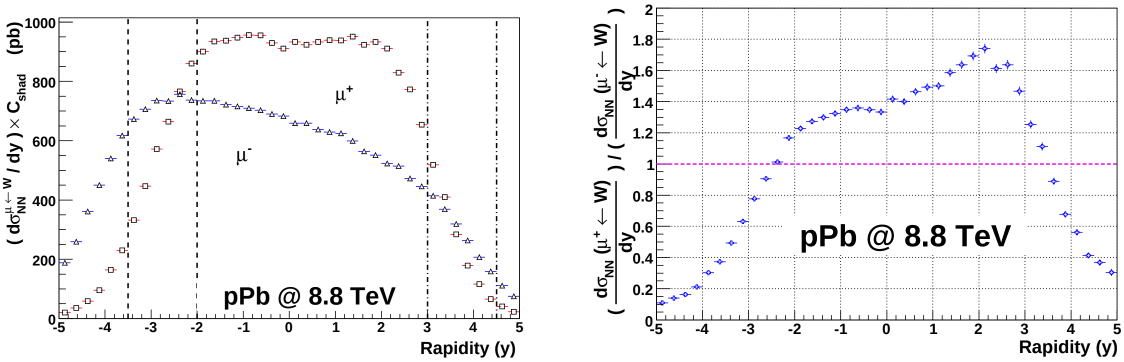

Figure 5.18: On the left, muon differential production cross section per nucleon-nucleon collision as a function of rapidity in **p-Pb reactions** at $\sqrt{s_{NN}} = 8.8$ TeV for **W muonic decays**. Squares represent μ^+ and triangles μ^-. The dashed (dot-dashed) lines indicate the muon spectrometer acceptance in p-Pb (Pb-p) collisions. On the right, μ^+/μ^- differential production cross section ratio.

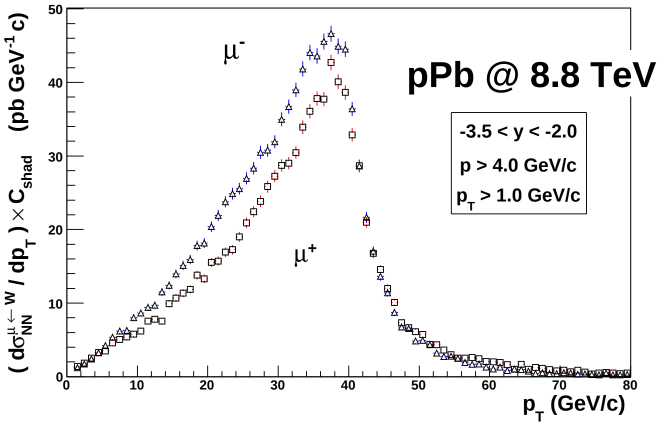

Figure 5.19: Differential production cross section per nucleon-nucleon collision of muons from **W muonic decays** in the ALICE muon spectrometer acceptance as a function of transverse momenta in **p-Pb collisions** at $\sqrt{s_{NN}} = 8.8$ TeV. Squares represent μ^+ and triangles μ^-.

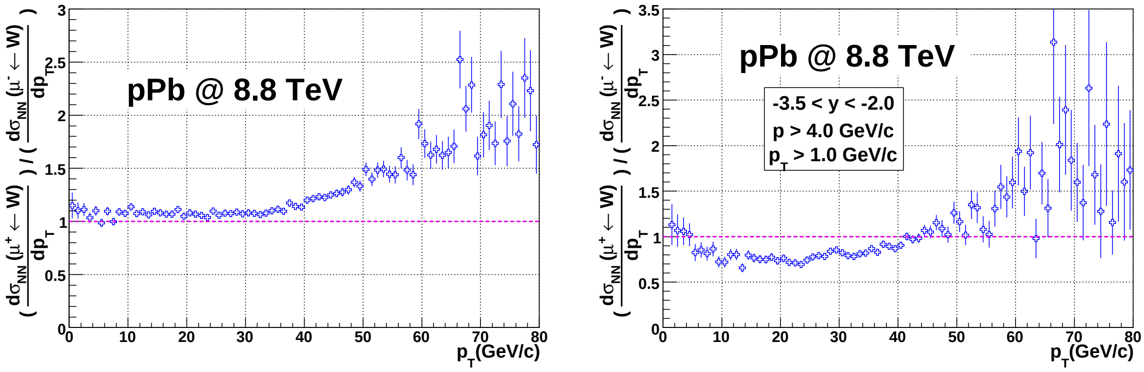

Figure 5.20: Ratio of single muons (μ^+/μ^-) production cross section over the whole rapidity range (left figure) and in the muon spectrometer acceptance (right figure) for **W muonic decays** as a function of transverse momentum in **p-Pb collisions** at $\sqrt{s_{NN}} = 8.8$ TeV.

Expected muon yields in the muon spectrometer acceptance

In standard p-Pb data-taking conditions, the expected integrated luminosity is $\mathcal{L} = 10^{35}$ cm^{-2} (that is 0.1 pb^{-1}), see [C$^+$04, Mar05] or Tab. 3.1. Therefore, considering NLO production cross section we estimate that about $2.3 \cdot 10^5$ muons from W decays will be produced in the whole rapidity range in p-Pb collisions, and about half of them $1.2 \cdot 10^5$ will be in the high p_T range ($p_T \in (30, 50)$ GeV/c). In the muon spectrometer acceptance about $4.1 \cdot 10^4$ muons will be produced. Out of them $2.1 \cdot 10^4$ muons will fall in the high p_T range. Tab. 5.8 summarizes these estimations for p-Pb and Pb-p collisions.

Collision	$N_{\mu\leftarrow W}$	$N^{Acc}_{\mu\leftarrow W}$
p-Pb	$2.3 \cdot 10^5$	$4.1 \cdot 10^4$ ($\sim 17\%$ Acc)
Pb-p	$2.3 \cdot 10^5$	$1.7 \cdot 10^4$ ($\sim 7\%$ Acc)
Restricting p_T range to $(30, 50)$ GeV/c		
p-Pb	$1.2 \cdot 10^5$	$2.1 \cdot 10^4$
Pb-p	$1.2 \cdot 10^5$	$8.3 \cdot 10^3$

Table 5.8: Estimated values of the number of muons produced in the ALICE muon spectrometer acceptance in **p-Pb and Pb-p collisions** by means of W boson muonic decays. $N_{\mu\leftarrow W}$ stands for number of produced muons in $4\,\pi$ per year of data-taking, and $N^{Acc}_{\mu\leftarrow W}$ stands for number of produced muons in the ALICE muon spectrometer acceptance per year of data-taking. Values computed assuming an integrated luminosity $\mathcal{L} = 10^{35}$ cm^{-2} [C$^+$04, Mar05].

5.3 Results of Z boson production at LHC energies

In this section Z production at LHC energies in the dimuon decay channel for p-p collisions at 14 TeV and Pb-Pb collisions at 5.5 TeV is presented. In all cases CTEQ4L PDFs [LHK$^+$97] have been used and PYTHIA spectra have been absolutely normalized to NLO calculations of the production cross section, see Tab. 5.5 [TCSG05, CS05, Vog01, Vog02]. In references [BHP01, S$^+$02] was shown that in this way PYTHIA reproduces Z p_T distribution in p-$\bar{p}$ collisions at Tevatron energies.

5.3.1 Proton-proton collisions at 14 TeV

Theoretical calculations determine the Z production cross-section in p-p collisions at 14 TeV to be $\sigma_{pp}^{Z} \times BR_{\mu^+\mu^-} \simeq 1.9$ nb including the dimuon branching ratio [TCSG05, CS05]. Its production has been simulated[7] following the techniques described in Sec. 5.1.2.

The Z boson differential production cross-section is presented in Fig. 5.21 as a function of rapidity. The invariant mass distribution of unlike sign muons over the whole rapidity range is also shown. To give a first estimate of the spectra shape, the invariant mass distribution has been fitted with a Breit-Wigner distribution function

$$f(E) = \frac{\Gamma}{2\pi[(E-M)^2 + (\Gamma/2)^2]} \,. \tag{5.6}$$

This probability distribution function is considered by PYTHIA [S$^+$02] and is often used to model resonances in high energy physics [HM84]. Fig. 5.22 reproduces the muon differential production cross-section as a function of rapidity. Observe that, in contrast to the W production case, neutral current weak decays violate only partially parity conservation rules. Thus, ***the production pattern of positive and negative muons does not differ too much***. Even if we plot the μ^+ / μ^- production cross-section ratio as a function of rapidity there is not a clear difference. Notice that the largest (even though small) gap is observed at high-rapidity. ***The muon p_T spectra (Fig 5.23) and the μ^+ / μ^- production cross-section ratio as a function of p_T over the whole rapidity range and in the muon spectrometer acceptance (see Fig. 5.24) assure the similar behavior of positive and negative muons from Z decays in the regions of interest.*** The ratios are in concordance with the unity in both rapidity intervals.

Expected muon yields in the muon spectrometer acceptance

ALICE expects to accumulate an integrated luminosity of $\mathcal{L} = 3 \cdot 10^{37}$ cm^{-2} (that is 30 pb^{-1}) during one year of standard data-taking conditions, see [C$^+$04, Mar05] or Tab. 3.1. To this extent, we evaluate that $5.7 \cdot 10^4$ muon pairs from Z dimuon decays will be produced in the whole rapidity range. Out of them $2.5 \cdot 10^3$ pairs will be produced within the muon spectrometer acceptance. Tab. 5.9 summarizes these estimates.

---

[7] We have simulated Z production in p-p collisions at 14 TeV with AliRoot-Head of January 2006, PYTHIA 6.2.

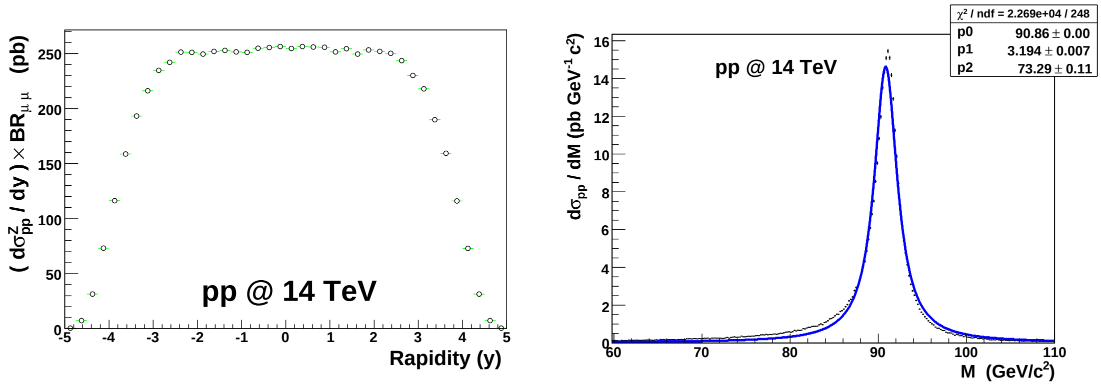

Figure 5.21: Z bosons differential production cross section per nucleon-nucleon collision as a function of rapidity and invariant mass in **p-p reactions** at $\sqrt{s_{NN}} = 14$ TeV for **Z dimuon decays**.

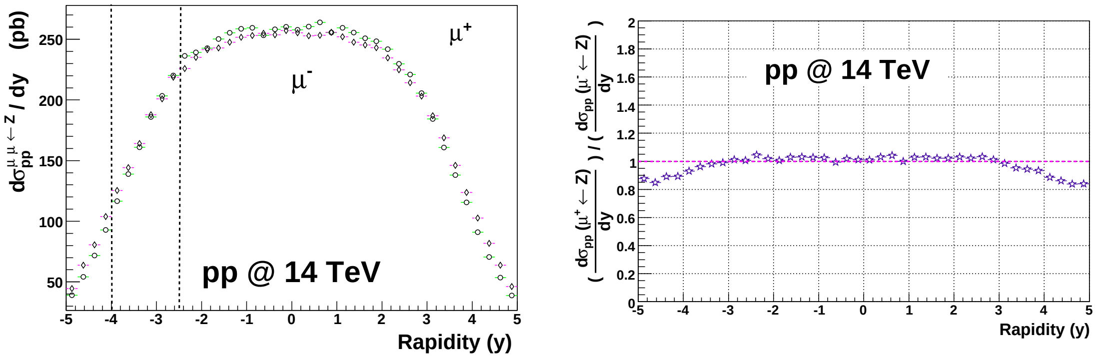

Figure 5.22: On the left, muon differential production cross section per nucleon-nucleon collision as a function of rapidity in **p-p reactions** at $\sqrt{s_{NN}} = 14$ TeV, in the case of **Z dimuon decays**. Circles represent μ^{+} and diamonds μ^{-}. The dashed lines indicate the muon spectrometer acceptance. On the right, μ^{+}/μ^{-} differential production cross section ratio.

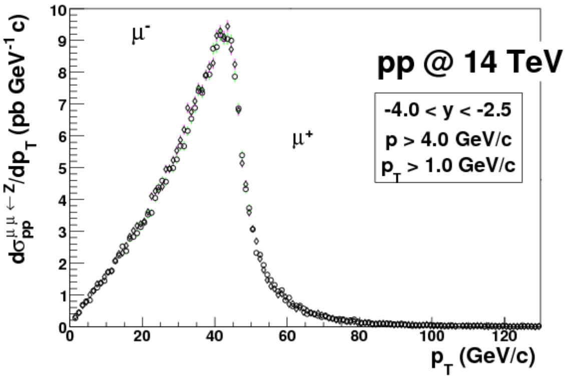

Figure 5.23: Differential production cross section per nucleon-nucleon collision of muons from **Z dimuon decays** in the ALICE muon spectrometer acceptance as a function of transverse momenta in **p-p collisions** at $\sqrt{s_{NN}} = 14$ TeV. Circles represent μ^{+} and diamonds μ^{-}.

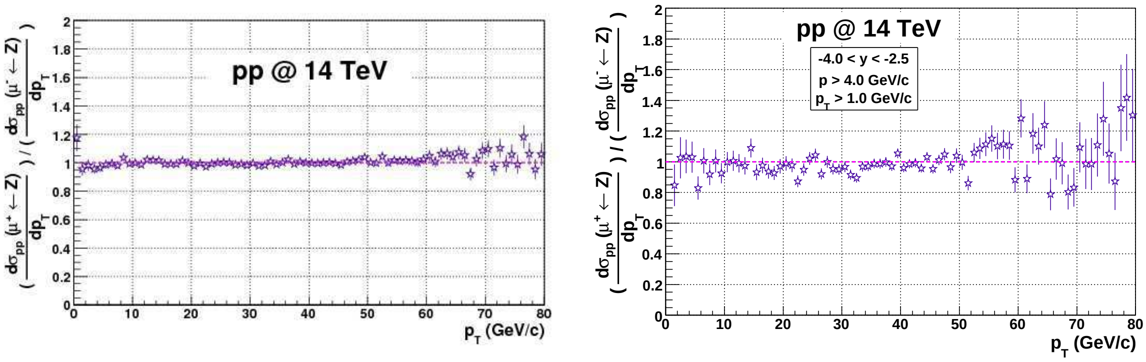

Figure 5.24: Ratio of single muons (μ^+/μ^-) production cross section over the whole rapidity range (left figure) and in the muon spectrometer acceptance (right figure) for **Z dimuon decays** as a function of transverse momentum in **p-p collisions** at $\sqrt{s_{NN}} = 14$ TeV.

Collision	$N_{\mu^+\mu^-\leftarrow Z}$	$N^{Acc}_{\mu^+\mu^-\leftarrow Z}$
p-p	$5.7 \cdot 10^4$	$2.5 \cdot 10^3$ ($\sim 4.4\%$ Acc)

Table 5.9: Estimated values of the number of muon pairs produced in the ALICE muon spectrometer acceptance in **p-p collisions** by means of Z boson dimuon decays. $N_{\mu^+\mu^-\leftarrow Z}$ stands for number of produced pairs in $4\ \pi$ per year of data-taking, and $N^{Acc}_{\mu^+\mu^-\leftarrow Z}$ stands for number of produced pairs in the ALICE muon spectrometer acceptance per year of data-taking. Values computed assuming an integrated luminosity $\mathcal{L} = 10^{37}\ \mathrm{cm}^{-2}$ [C+04, Mar05].

5.3.2 Lead-lead collisions at 5.5 TeV

Here we present Z production in Pb-Pb collisions[8]. Shadowing influence in nuclear PDFs have been studied in references [Vog01, Vog02] in the NLO approximation. In the simulations we account for them by using the EKS98 parameterization [EKS99]. Theoretical calculations estimate that Z boson production cross-section in p-p collisions at 5.5 TeV is $\sigma^Z_{NN} \simeq 20.7\,\mathrm{nb}$ and in Pb-Pb collisions is $\sigma^Z_{NN} \times C_{shad} \simeq 18.7\,\mathrm{nb}$ including shadowing [Vog01, Vog02], which implies a reduction of $\sim 10\%$ of the production cross-section. Thus, in the dimuon decay channel the Z boson production cross-section in Pb-Pb collisions is $\sigma^Z_{NN} \times C_{shad} \times BR_{\mu^+\mu^-} \simeq 0.63\,\mathrm{nb}$.

The invariant mass distribution of unlike sign muons over the whole rapidity range is represented in Fig. 5.25. The spectra has been fitted with a Breit-Wigner distribution function (Eq. 5.6), as expected for PYTHIA simulations. The differential production cross-section of Z bosons and muons are presented in Figs. 5.25 and 5.26 as a function of rapidity. ***In concordance to Z production in p-p collisions and in opposition to W production, the pattern of positive and negative muons is similar***, as expected due to the partial ('pure') violation of parity conservation rules in Z (W) decays. In Fig. 5.26, that show μ^+ / μ^- production

---

[8] It has been simulated with AliRoot-Head of January 2006, PYTHIA 6.2 and following the techniques described in Sec. 5.1.2.

cross-section ratio as a function of rapidity, we can observe that the biggest discrepancies on their production (even though they are small) are presented in the high-rapidity region (like in p-p collisions). In the muon spectrometer acceptance the muon differential production cross-section spectra (Fig. 5.27) and the μ^+ / μ^- ratio as a function of p_T (Fig. 5.28) prove that the difference is negligible.

Expected muon yields in the muon spectrometer acceptance

In standard Pb-Pb data-taking conditions ALICE expects to accumulate an integrated luminosity of $\mathcal{L} = 5 \cdot 10^{32}$ cm^{-2} (that is 0.5 nb^{-1}), see [C$^+$04, Mar05] or Tab. 3.1. In such conditions we estimate that $1.4 \cdot 10^4$ muon pairs from Z decays will be produced in the whole rapidity range. Out of them just about 240 pairs will be in the muon spectrometer acceptance. Conditions that make difficult Z measurement in the muon spectrometer in one year of data-taking. Nevertheless, it could become feasible by accumulating the statistics of multiple data-taking periods. Tab. 5.10 summarizes these estimates.

Collision	$N_{\mu^+\mu^- \leftarrow Z}$	$N^{Acc}_{\mu^+\mu^- \leftarrow Z}$
Pb-Pb	$1.4 \cdot 10^4$	$2.4 \cdot 10^2$ ($\sim 1.8\%$ Acc)

Table 5.10: Estimated values of the number of muon pairs produced in the ALICE muon spectrometer acceptance in **Pb-Pb collisions** by means of Z boson dimuon decays. $N_{\mu^+\mu^- \leftarrow Z}$ stands for number of produced pairs in $4\,\pi$ per year of data-taking, and $N^{Acc}_{\mu^+\mu^- \leftarrow Z}$ stands for number of produced pairs in the ALICE muon spectrometer acceptance per year of data-taking. Values computed assuming an integrated luminosity $\mathcal{L} = 0.5$ nb^{-1} [C$^+$04, Mar05].

5.3.3 Preliminary studies in argon-argon collisions at 6.3 TeV

PYTHIA Z production cross-section in the dimuon decay channel in p-p collisions at 6.3 TeV is about $\sigma^Z_{NN} \times C_{shad} \times BR_{\mu^+\mu^-} \simeq 0.6$ nb [Blu06]. Preliminary studies [Blu06] indicate that the muon spectrometer acceptance in such collisions is about 2.3 %. Thus, considering that in standard data-taking conditions ALICE expects to accumulate an integrated luminosity of $\mathcal{L} = 10^{35}$ cm^{-2} (that is 0.1 pb^{-1}) [C$^+$04] we estimate that about $9.6 \cdot 10^4$ muon pairs will be produced in the whole rapidity range. Out of them about 2200 pairs will be produced in the muon spectrometer acceptance. This is roughly a factor of 10 more muon pairs than in Pb-Pb collisions. Notice that we have considered a lower-limit value of Z production cross-section, that is PYTHIA LO calculation for p-p collisions. NLO calculations tend to increase the value of the production cross-section. We would then have larger estimates for the number of muon pairs produced on those conditions. All that make of Ar-Ar collisions an interesting situation for Z studies in nucleus-nucleus collisions.

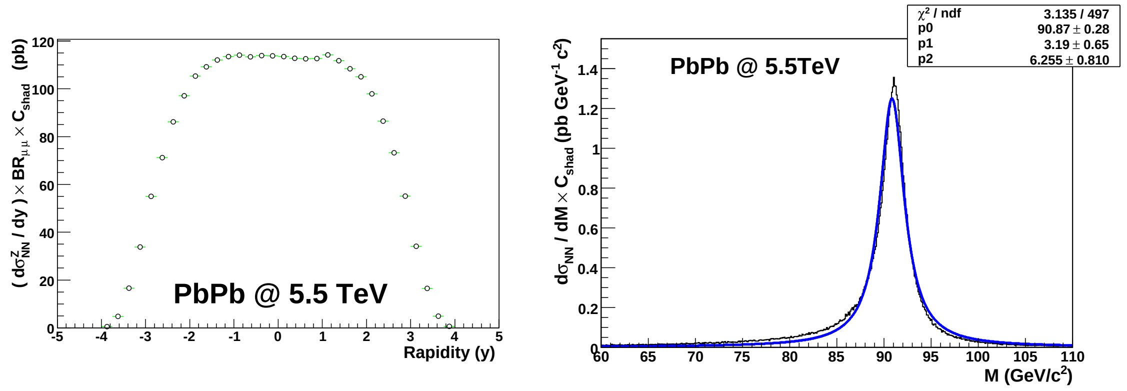

Figure 5.25: Z bosons differential production cross section per nucleon-nucleon collision as a function of rapidity and invariant mass in **Pb-Pb reactions** at $\sqrt{s_{NN}} = 5.5$ TeV in the case of **Z dimuon decays**.

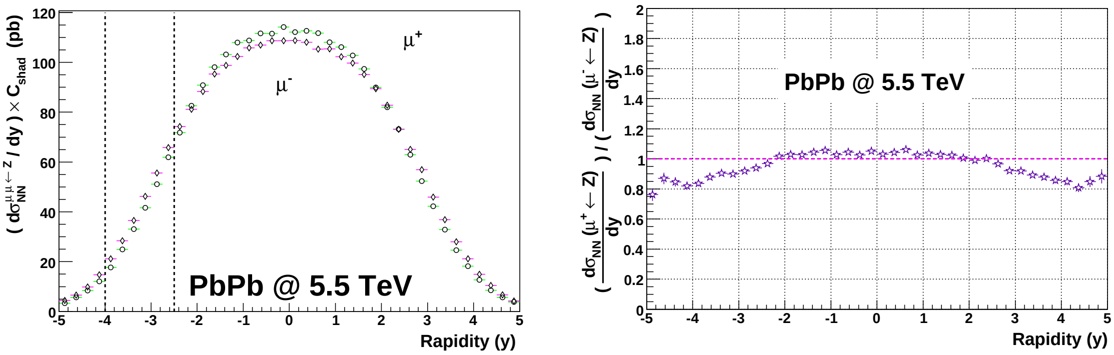

Figure 5.26: On the left, muon differential production cross section per nucleon-nucleon collision as a function of rapidity in **Pb-Pb reactions** at $\sqrt{s_{NN}} = 5.5$ TeV for **Z dimuon decays**. Circles represent μ^+ and diamonds μ^-. The dashed lines indicate the muon spectrometer acceptance. On the right, μ^+ / μ^- differential production cross section ratio.

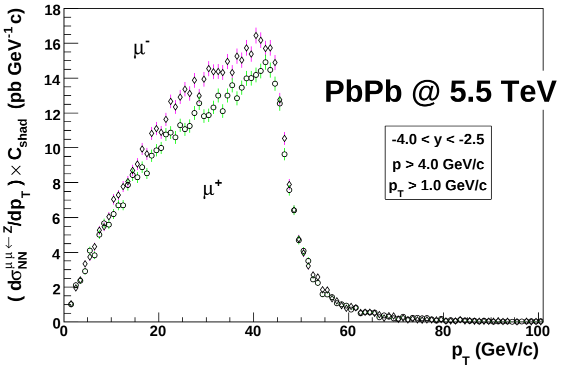

Figure 5.27: Differential production cross section per nucleon-nucleon collision of muons from **Z dimuon decays** in the ALICE muon spectrometer acceptance as a function of transverse momenta in **Pb-Pb collisions** at $\sqrt{s_{NN}} = 5.5$ TeV. Circles represent μ^+ and diamonds μ^-.

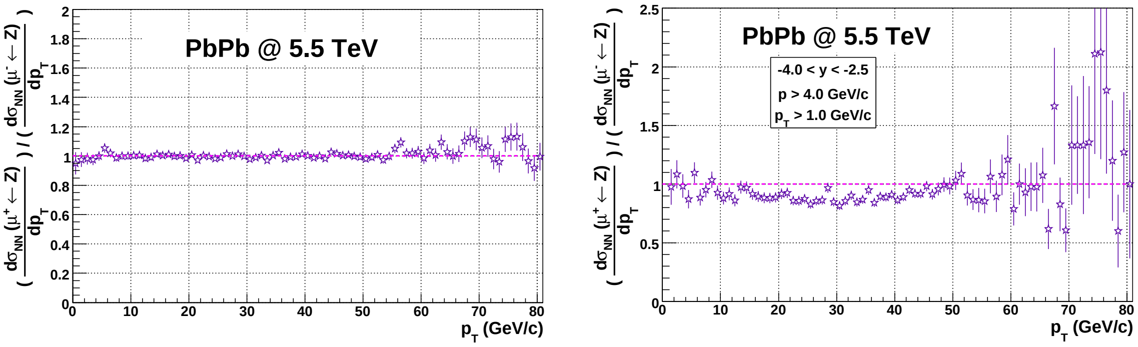

Figure 5.28: Ratio of single muons (μ^+/μ^-) production cross section over the whole rapidity range (left figure) and in the muon spectrometer acceptance (right figure) for **Z dimuon decays** as a function of transverse momentum in **Pb-Pb collisions** at $\sqrt{s_{NN}} = 5.5$ TeV.

5.4 Remarks

From all learned in Sec. 5.2 and Sec. 5.3 we can highlight some aspects:

- The kinematic range (rapidity interval) allowed for W and Z production increases with the collision energy, as expected from energy conservation rules;
- The p_T spectra of muons from W and Z decays is peaked around half the boson mass $M/2$, as expected;
- The isospin of the colliding system influences positive and negative W charge production and their rapidity spectra shape, as predicted from the LO production process. In p-p collisions more W$^+$ than W$^-$ are produced, in Pb-Pb and p-Pb collisions the proportion of positive and negative W charge is similar even though there are slightly more W$^-$ (W$^+$) in Pb-Pb (p-Pb) collisions;
- Parity violation effect in charged weak decays influences positive and negative muon rapidity pattern. W bosons at high-rapidity tend to emit positive muons towards mid-rapidity while negative muons are preferentially emitted at high-rapidities.
- The asymmetry on positive and negative muon yields from W decays can be observed in the muon spectrometer acceptance and depends on the colliding system. Thus it could be a tool of W measurements. In p-p collisions the μ^+/μ^- yield ratio in the spectrometer is above one, and in Pb-Pb and p-Pb it is below one;
- Z production does not introduce any asymmetry on muon charge yields;
- There seems to be enough statistics to measure W and Z bosons[9] in the muon spectrometer, if the experimental setup is able to detect them and the background is not too large (see next chapter).

---

[9] Results indicate that Z bosons could be measured in the muon spectrometer in p-p and Ar-Ar collisions.

Chapter 6

Weak boson measurement with the muon spectrometer

> *Nature is pleased with simplicity, and affects not the pomp of superfluous causes.*
>
> I. Newton

Abstract

The feasibility of the measurement of the weak bosons in the ALICE muon spectrometer is addressed. The various muon contributions to the spectra are presented: Z, W, beauty, charm, hadronic and Drell-Yan decays. Particular properties of the single muon spectra from W decay are discussed, such as the single muon charge asymmetry. The expected statistics reconstructed in the muon spectrometer for W and Z production are estimated.

6.1 Muon sources at LHC energies

In order to determine the feasibility of weak bosons measurement, we need to evaluate the various production mechanisms that will contribute to the muon spectra at LHC energies. In this section we detail those contributions that populate the muon high transverse momenta range in which we are interested. Z, W, beauty, charm, hadronic and Drell-Yan decays are discussed.

6.1.1 W and Z bosons decays

Apart from the direct W and Z bosons muonic decay modes:

$$W^{+} \rightarrow \mu^{+} \nu_{\mu}\,, \qquad W^{-} \rightarrow \mu^{-} \bar{\nu}_{\mu}\,, \qquad Z^{0} \rightarrow \mu^{+} \mu^{-}\,, \tag{6.1}$$

other secondary (cascading) decay channels can end up contributing to the muon spectra, and here we evaluate their impact. Weak bosons decay modes are presented in Tab. 6.1. The most important contribution to the muon yields are from the leptonic and from the charmed decays; in particular the beauty channel remains a sizeable fraction of the Z total decays.

Decay mode	Fraction (Γ_i/Γ)
$W^+ \longrightarrow l^+\,\nu$	$(10.80 \pm 0.09)\,\%$
$W^+ \longrightarrow \mu^+\,\nu_\mu$	$(10.57 \pm 0.15)\,\%$
$W^+ \longrightarrow \tau^+\,\nu_\tau$	$(11.25 \pm 0.20)\,\%$
$W^+ \longrightarrow$ hadrons	$(67.60 \pm 0.27)\,\%$
$W^+ \longrightarrow c\,X$	$(33.4 \pm 2.6)\,\%$
$W^+ \longrightarrow c\,\bar{s}$	$(31\,^{+13}_{-11})\,\%$
$Z \longrightarrow l^+\,l^-$	$(3.3658 \pm 0.0023)\,\%$
$Z \longrightarrow \mu^+\,\mu^-$	$(3.366 \pm 0.007)\,\%$
$Z \longrightarrow \tau^+\,\tau^-$	$(3.370 \pm 0.008)\,\%$
$Z \longrightarrow$ hadrons	$(69.91 \pm 0.06)\,\%$
$Z \longrightarrow c\,\bar{c}$	$(12.03 \pm 0.21)\,\%$
$Z \longrightarrow b\,\bar{b}$	$(15.12 \pm 0.05)\,\%$

Table 6.1: W and Z decay modes, from the Particle Data Group report [Y+06]. W$^-$ decay modes are the charge conjugates of the W$^+$ decay modes.

W and Z muonic decays

The W leptonic decays have a branching ratio (BR), of $BR = 10\%$ and Z leptonic decays amount to $BR = 3.3\%$. In the last chapter we showed that muons from 'direct' W and Z decays populate the high p_T part of the spectrum, they have a mean p_T close to half the boson mass ($p_T \sim m/2$), a characteristic that allows to study their production.

W and Z tau decays

W tau decays ($W^+ \longrightarrow \tau^+\,\nu_\tau$) can also end up producing muons; the $BR\,(\tau \rightarrow l\,\nu_l\,\nu_\tau)$ being about 17%. As an example, we have simulated W tau decays[1], and the resultant single muon transverse momentum spectra can be observed in Fig. 6.1. As expected, those secondary muons contribute to the low p_T part of the muon distribution and are negligible in the high-p_T interval ($p_T \sim m_w/2$).
Similarly, we can anticipate that muons from Z tau decays ($Z \longrightarrow \tau^+\,\tau^-$) will populate the low p_T region, being of little relevance for our studies.

W and Z charmed decays

W charmed decay has a significant BR of about 33%, while the Z charmed decay BR is smaller, of 12% (see Tab. 6.1). Charmed hadrons can decay into leptons[2], and particularly

---

[1] We did those simulations with AliRoot v4.04.Rev.07 version and PYTHIA 6.2.

[2] The semileptonic charm decay branching ratio is $BR_{c\rightarrow lX} \sim (9.5 \pm 0.6)\,\%$. The semimuonic charm decay branching ratio is $BR_{c\rightarrow \mu X} \sim (9.0 \pm 0.7)\,\%$ [A+99].

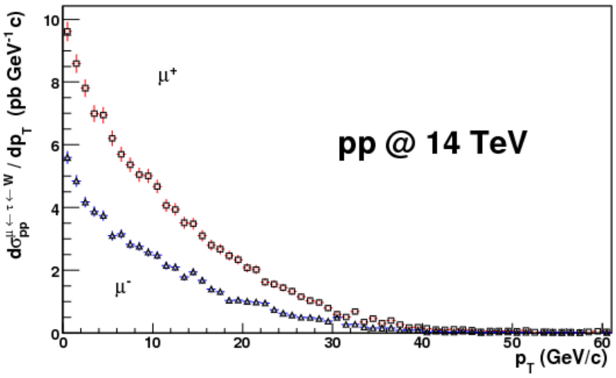

Figure 6.1: Single muon transverse momentum spectra from **W tau decays** in **p-p collisions** at $\sqrt{s_{NN}} = 14$ TeV. Squares represent μ^+ and triangles μ^-.

into muons that will contribute to the muon yields

$$W^{\pm} \rightarrow c\,X \rightarrow \cdots \rightarrow \mu^{\pm}\,Y\,, \qquad Z^0 \rightarrow c\,\bar{c} \rightarrow \cdots \rightarrow \mu^+\,\mu^-\,Y\,.$$

We have simulated W charmed decays[3] and found that muon production cross section for W charmed decays is three times lower than the one for W muonic decays (6.2 nb in front of 20.9 nb for p-p collisions at 14 TeV). Muon differential production cross section is presented in Fig. 6.2 as a function of p_T. In comparison to the W muonic decays (Fig. 5.10), its contribution is shifted to lower p_T as expected due to c-quark fragmentation into D hadrons before decaying into muons. Similarly, Z charmed decays will end up producing low p_T muons. Hence, we won't pay any attention to weak bosons charmed decays either for W or Z feasibility studies. Note that W charmed decays were discussed in more detail in reference [CMAF06].

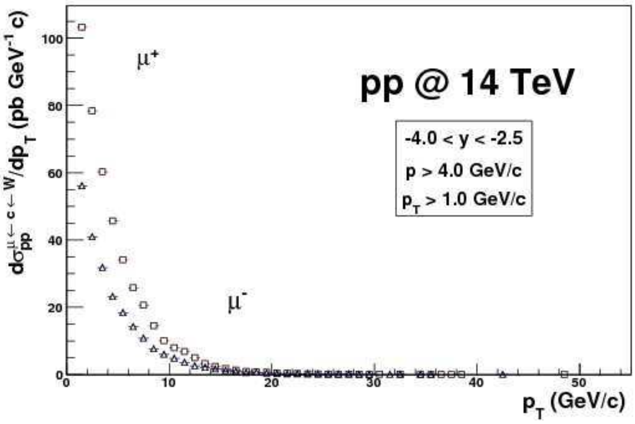

Figure 6.2: Single muon transverse momenta distribution from **W charmed decays** in the ALICE muon spectrometer acceptance in **p-p collisions** at $\sqrt{s_{NN}} = 14$ TeV. Squares represent μ^+ and triangles μ^-.

---

[3] We have simulated W charmed decays with AliRoot-head-200605 version and PYTHIA 6.2.

Z beauty decays

Z bosons have also a considerable probability to end up into $b\bar{b}$ pairs, the BR is about 15% (see Tab. 6.1). Like the $c\bar{c}$ pairs, $b\bar{b}$ pairs might fragment into B hadrons before decaying into muons. The muons will then populate the low transverse momentum spectra. Moreover, their production cross-section will be about a factor 10 smaller than for the Z muonic decays. They are thus of little importance for our studies.

6.1.2 Beauty and charm muonic decays

Remember that beauty and charm are hard probes of the collision that can provide important information about the possible formation of the QGP in the most violent heavy-ion collisions (see Chapter 1, Sec. 1.3). Charm and beauty will be abundantly produced at LHC energies (see production cross-sections in Tab. 6.2). Charm cross-section in p-p collisions at 14 TeV amounts to 11.2 mb, and beauty cross-section to 0.51 mb [A+06]. Therefore, we expect that about 115 / 4.6 $c\bar{c}$ / $b\bar{b}$ pairs will be formed in the most central (0-5%) Pb-Pb collisions at 5.5 TeV (see e.g. Appendix D Tab. D.6 for the $c\bar{c}$ calculations). c-quarks can decay into muons with a BR of about 9% [A+99], and b-quarks can decay semi-leptonically with a BR of about 10% [Y+06], but they can also decay into c-quarks (D mesons) which in their turn end up into muons. ***Due to their abundances, these sources will be the main contributors to the muon spectra at intermediate p_T.*** We have simulated beauty and charm in p-p and Pb-Pb collisions at 14 TeV and 5.5 TeV with[4] tuned PYTHIA parameters in order to reproduce NLO pQCD results at order $O(\alpha_s^3)$ (theoretical predictions from the HVQMNR program) [A+06, Dai03]. EKS98 [EKS99] shadowing parameterizations have been considered to account for the PDFs nuclear modifications when necessary. Inclusive b and c quarks rapidity and transverse momentum distributions can be observed in Figs. 6.3 and 6.4 as obtained from the HVQMNR program [A+06]. Their respective single muon distributions will be discussed in the next section (Sec. 6.2).

collision ($\sqrt{s_{NN}}$ [TeV])	p-p (14)	p-Pb (8.8)	Pb-Pb (5.5)	p-p (5.5)
$\sigma_{NN}^{c\bar{c}}$ [mb]	11.2 [A+06]	7.16 [A+06]	4.32 [A+06]	6.6 [A+06]
$\sigma_{NN}^{b\bar{b}}$ [mb]	0.51 [A+06]	0.27 [A+06]	0.18 [A+06]	0.21 [A+06]
$\sigma_{NN}^{W} \times BR_{\mu\nu}$ [nb]	20.9 [FM04]	11.3 [Vog01]	6.56 [Vog01]	7.34 [Vog01]
$\sigma_{NN}^{Z} \times BR_{\mu^+\mu^-}$ [nb]	1.9 [TCSG05]	1.1 [Vog01]	0.63 [Vog01]	0.68 [Vog01]

Table 6.2: Charm, beauty, W and Z production cross-sections per nucleon-nucleon collision from NLO calculations. Shadowing is included in Pb-Pb and p-Pb calculations.

With regard to the dimuon invariant mass spectra, recent studies [A+06, CGMV05] estimated the various sources contribution. Their results suggest that the invariant mass spectra for $0 < M_{\mu\mu} < 5$ GeV/c^2 will be dominated by opposite-sign muons from a b-decay chain;

---

[4] We have used AliRoot version AliRoot-pro-4.01.04 and PYTHIA 6.2.

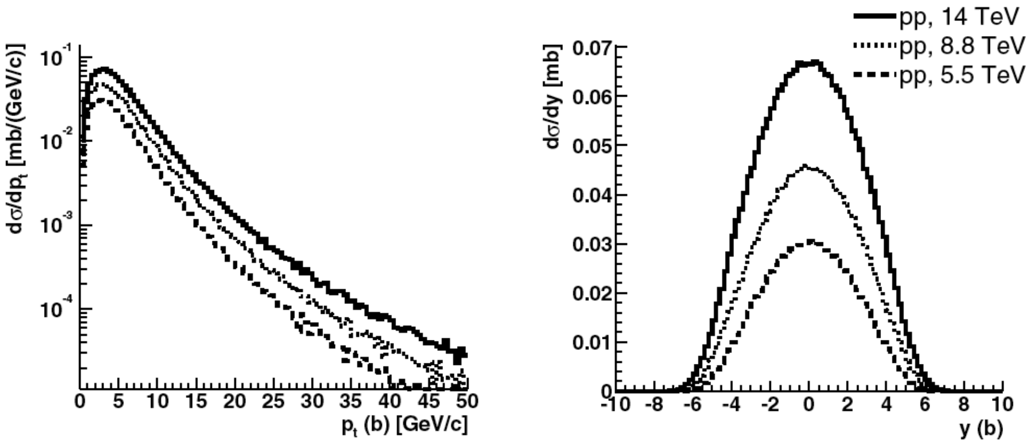

Figure 6.3: Inclusive b quark p_T and rapidity distributions obtained from the HVQMNR program [A+06].

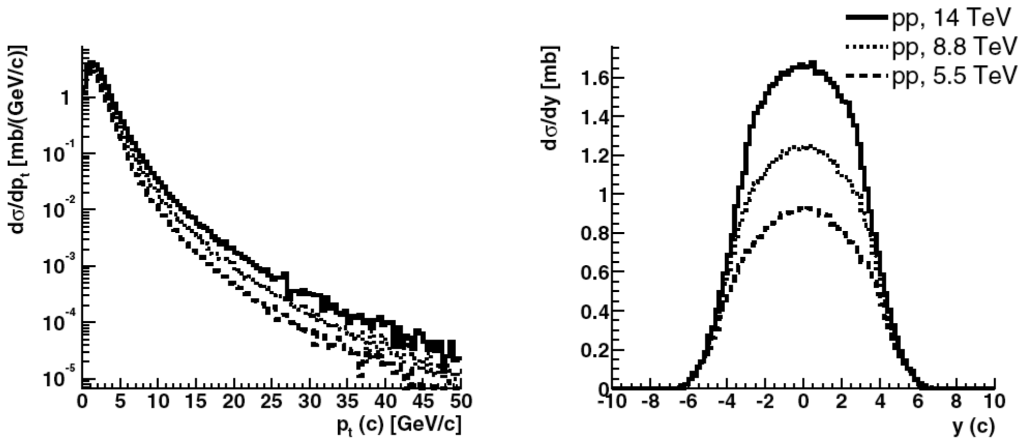

Figure 6.4: Inclusive c quark p_T and rapidity distributions obtained from the HVQMNR program [A+06].

i.e. the muons μ_1 and μ_2 come one from B direct decays[5], and another from B-D decays: $B \longrightarrow \mu_1 + D(\longrightarrow \mu_2 + Y) + X$. However, the interval $5 < M_{\mu\mu} < 20$ GeV/c^2 will be mainly populated by the the combination of the primary muons from b and $\bar{b}$ decays.

6.1.3 Hadronic decays contribution

Light flavor and strange hadrons (pions, kaons,...) can end up producing muons but with a relatively low transverse momenta. In reference [A+06] these sources have been studied in detail. The resulting muon spectrum in Pb-Pb 0-5% central collisions is represented in Fig. 6.5, where the p_T distribution of muons coming from π/K decays is compared to those of charm and beauty decays. It has been concluded that in the muon spectrometer they

---

[5] B mesons direct decays are also called primary decays. We refer to $B \longrightarrow \mu + X$.

dominate the spectra for $p_T < 2\text{-}3$ GeV/c. Therefore in our analysis we will neglect their contribution.

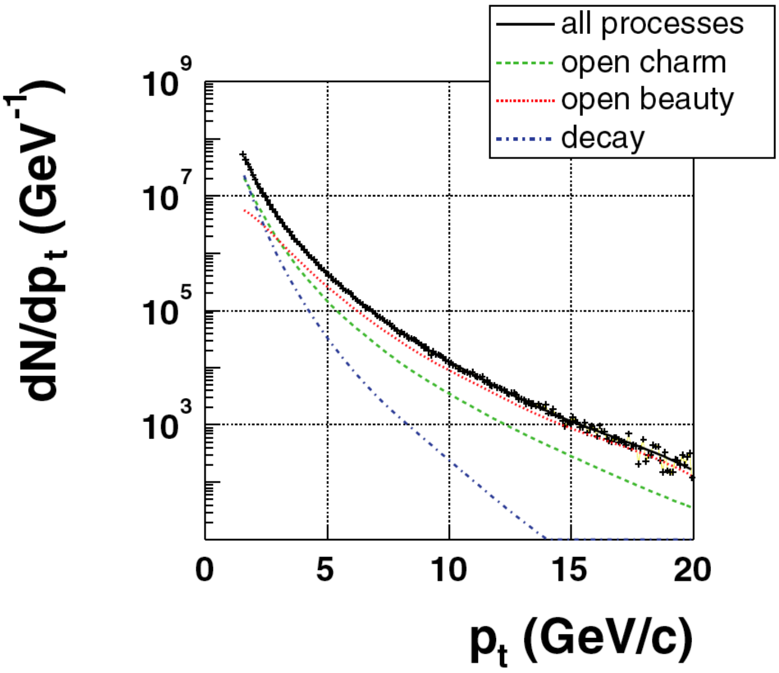

Figure 6.5: Inclusive muon transverse momentum distribution in 5% most central Pb-Pb collisions at 5.5 TeV [A+06]. The contributions from beauty, charm and π/K decays are shown.

6.1.4 Drell-Yan contribution

The Drell-Yan process: $q\,\bar{q} \;\rightarrow\; l^+\,l^-$ also contributes to the single muon and dimuon spectra. In reference [B+00] it has been evaluated its impact on both spectra (see Fig. 6.6). Although muons from Drell-Yan are not important for low transverse momentum measurements because their production cross-section is much smaller than the beauty or the charm ones, the muon p_T slope is harder (flatter) and it could become of interest at high p_T. The single muon p_T distribution computed in reference [B+00] for the CMS experiment is shown in Fig. 6.6 with the left-hand plot, showing that we can ignore its contribution if we restrict ourselves to $p_T \lesssim 50\text{-}60$ GeV/c. For larger p_T its influence could become noticeable, though it should be studied in more detail, and in particular in the rapidity window covered by ALICE muon spectrometer, to draw further conclusions.

The dimuon invariant mass spectrum at LHC energies is displayed in the right-hand plot of Fig. 6.6. Here it becomes evident that Drell-Yan will be the predominant source contributing to the dimuon invariant mass after the Z^0 peak. Nevertheless, it does not represent a problem for investigating the Z^0 peak.

6.2 Single muon p_T distribution in hadron-hadron collisions

We decided to explore the feasibility of W measurements through the single muon spectra at LHC energies, and in this section we expose the results of those studies. Figure 6.7

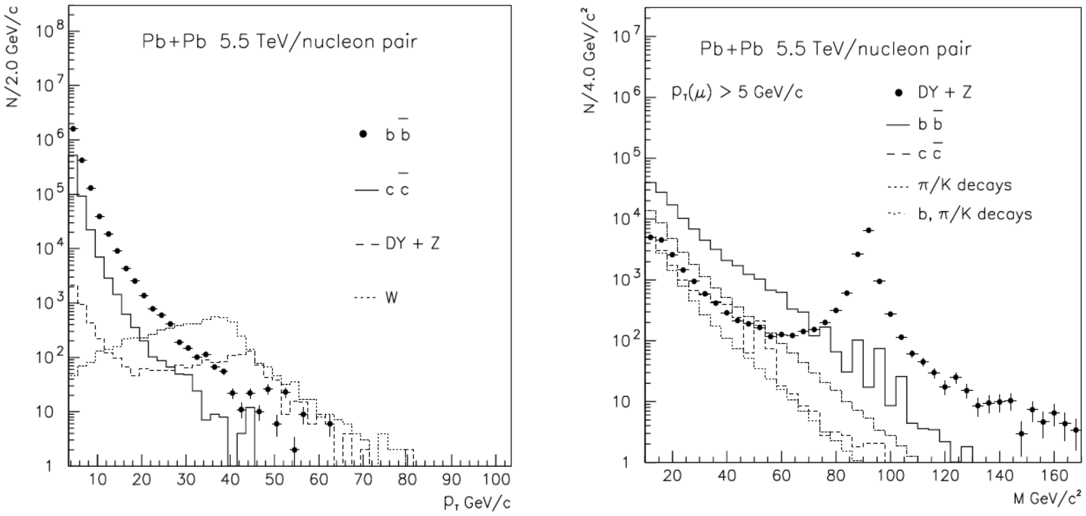

Figure 6.6: On the left, transverse momentum distribution of muons from heavy flavor, Drell-Yan, Z and W produced in Pb-Pb collisions at the CMS experiment for muons of $p_T \geq 3.5$ GeV/c and $|\eta| \leq 2.5$ [B+00]. On the right, invariant mass distribution of $\mu^+\mu^-$ pairs for muons of $p_T > 5$ GeV/c in the same conditions [B+00].

summarizes the different contributions to the single muon transverse momentum differential production cross-section in p-p collisions at 14 TeV in the whole phase space. Charm, beauty, and W, Z weak decays have been included. Analogously, the muon differential production cross-section in Pb-Pb collisions in the whole phase space is shown in Fig. 6.8. Note that, as discussed in Sec. 6.1.1, W charmed decays populate the low p_T region and are negligible for these studies (from Fig. 6.7). ***Direct muons from charm decays are predominant in the low p_T range, for $p_T \in (2, 4)$ GeV/c*[6]*. For $p_T \in (4, 30)$ GeV/c beauty decays prevail and at larger p_T the W decays have the greatest influence on the single muon spectra.*** The crossing-points from W-b and W-c decays evolve smoothly with the center-of-mass energy of the collision. Moreover we can observe the distribution from beauty charmed decays ($b \to c \to \mu$) is softer than the one from beauty or charmed 'direct' decays ($b \to \mu$, $c \to \mu$). Z decayed muon pattern is similar to the W one, but due to its smaller cross-section it is not dominant and it won't be visible through the single muon spectra. ***All this bring us to conclude that W production could be studied via the high-p_T muons***. In the next subsection we will apply acceptance and efficiency corrections to draw up further conclusions.

On the other hand, in Sec. 5.2 we discussed the muon charge asymmetry driven by W bosons, and we are interested in evaluating it with the different muon sources to estimate if it could really be a tool for W measurements or if the background muon sources will hide it. Results in the whole rapidity range are shown in Fig. 6.9 for p-p and Pb-Pb collisions showing the W and the sum of all muon contributions behavior. As guessed, in the low transverse momenta range the W muon charge asymmetry gets screened by the background distributions, but at high-p_T its charge asymmetry prevails. This muon charge asymmetry

---

[6] Remind that for $p_T < 2$ GeV/c the hadronic contribution dominates the single muon spectra.

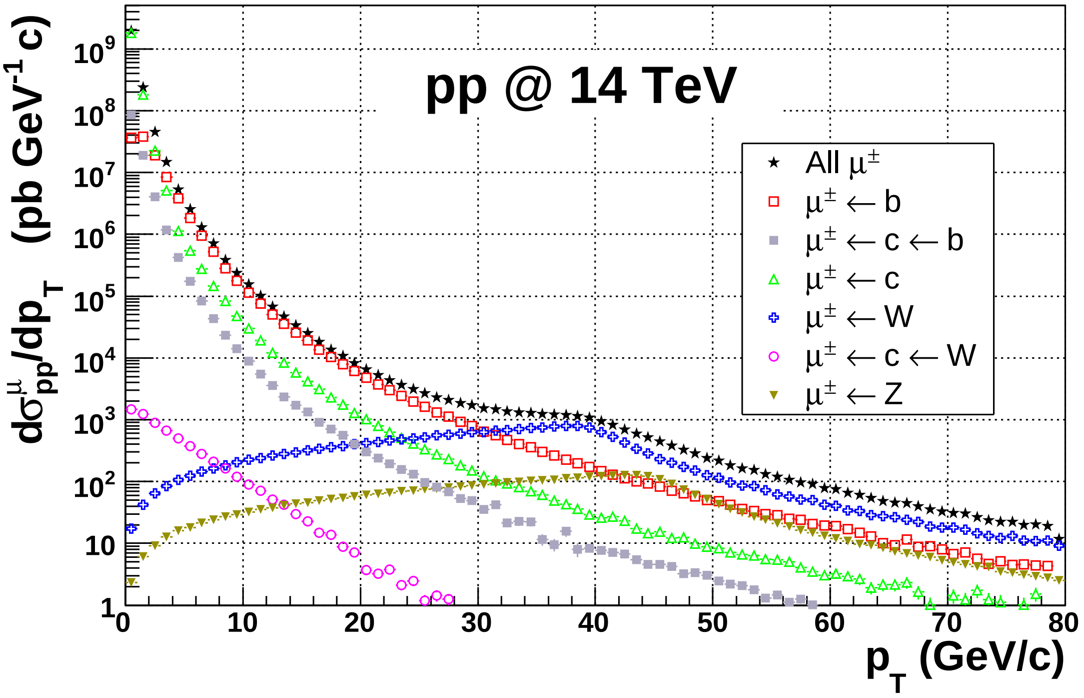

Figure 6.7: Single muon differential production cross-section as a function of the transverse momentum for p-p collisions at 14 TeV in the whole phase space.

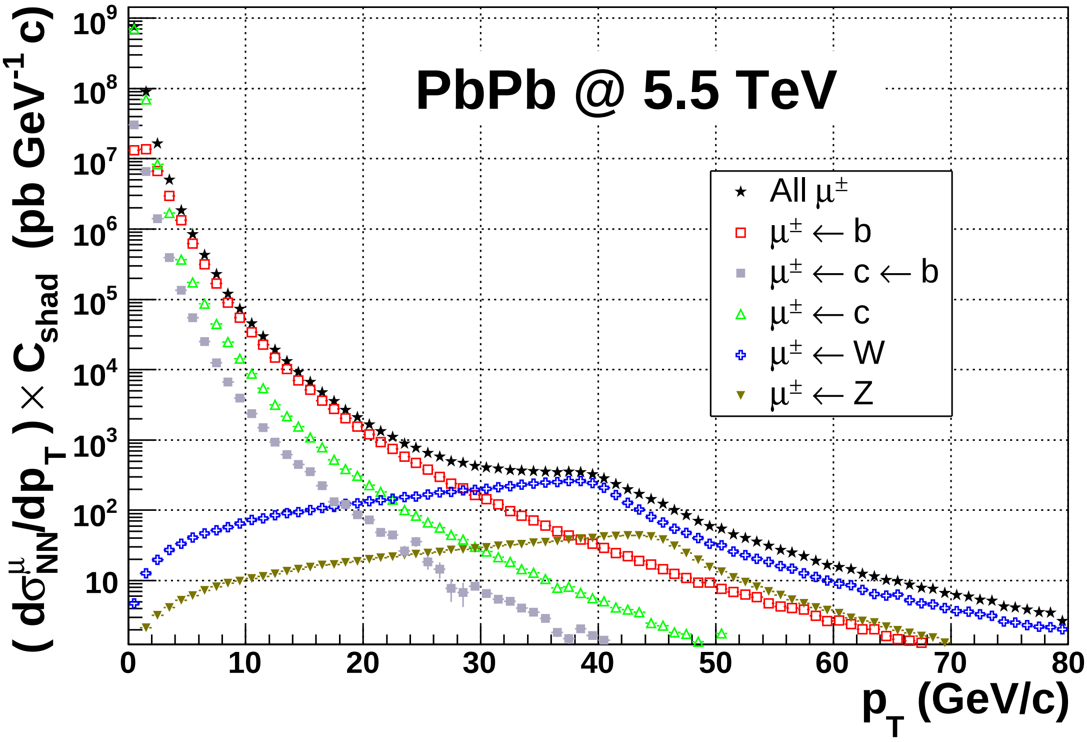

Figure 6.8: Single muon differential production cross-section as a function of the transverse momentum for Pb-Pb collisions at 5.5 TeV in the whole phase space.

for $p_T > 30$ GeV/c could testify W production at LHC energies. Furthermore, the muon charge asymmetry varies with the colliding system, which makes of it a suitable signature for W detection.

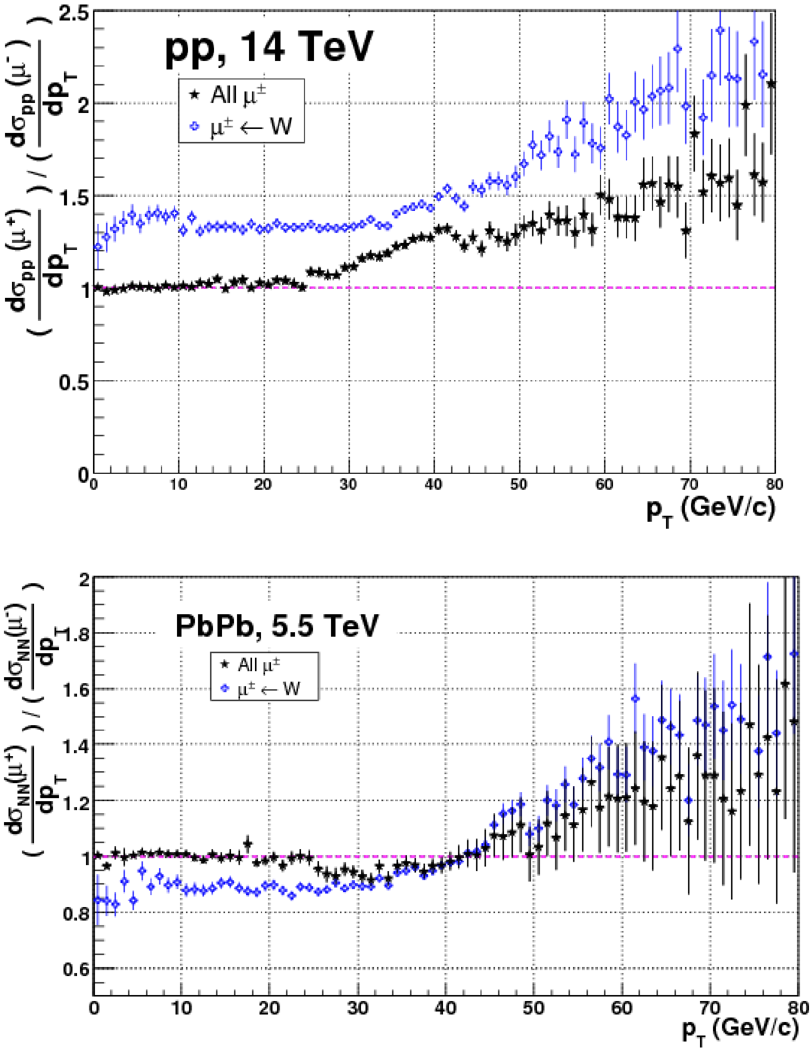

Figure 6.9: Single muon charge asymmetry μ^+/μ^- as a function of p_T for p-p and Pb-Pb collisions in the whole phase space. The sum of the different considered sources and also the W contribution are plotted.

6.2.1 Single muon measurement with the muon spectrometer

To investigate which will be the measured spectra with the ALICE muon spectrometer we need to account for the acceptance and the efficiency effects as explained in Chapter 4. Remind that in this chapter we were interested in recovering the physics distribution from the reconstructed spectra. In contrast, here we have the physics spectra (Figs. 6.7 & 6.8) and we would like to estimate the reconstructed spectra.

Efficiency

In Chapter 4, and more particularly in Sec. 4.4.3 and 4.5.4, we demonstrated that the spectrometer should be able to detect and reconstruct single muons and identify its charge up to high p_T, and we calculated the efficiency from $p_T = 1$ GeV/c up to 80 GeV/c. The efficiency mapping proved that the trigger affects predominantly the low p_T part of the distribution and has no important effect on the high p_T muons. Therefore, here we decided to make no a priori assumption on the trigger used and employ the efficiency without any trigger constraints (we will discuss this issue in more detail later on). The computed single muon reconstruction efficiency is shown in Fig. 6.10 as a function of p_T. It suggests that the mean efficiency is about 97% for $p_T \in (5, 60)$ GeV/c (see results of the left plot). In hadron-hadron collisions the reconstruction efficiency will be subjected to the background conditions because the detector occupancy can diminish the efficiency. As a matter of fact, in Pb-Pb peripheral collisions there is no need to account for occupancy effects because the situation is similar to p-p reactions, but it is not the case in Pb-Pb central collisions. We evaluated the efficiency taking into consideration an extreme case, corresponding to top 5% Pb-Pb central collision that involves about 3500 particles per unit of rapidity at mid-rapidity with the HIJING parameterization available in AliRoot. The resulting efficiency in the $p_T \in (5, 60)$ GeV/c range amounts to 95% as can be seen on the right plot of Fig. 6.10. Observe that the background conditions of hadron-hadron collisions have a greater impact on the lower part of the p_T spectra, as expected. So independently of the number of particles per unit of rapidity considered we do not expect them to have a strong influence on the high-p_T interval of interest. Moreover, one should notice that to properly interpret its effect on the low-p_T range we would need higher statistics on this interval.

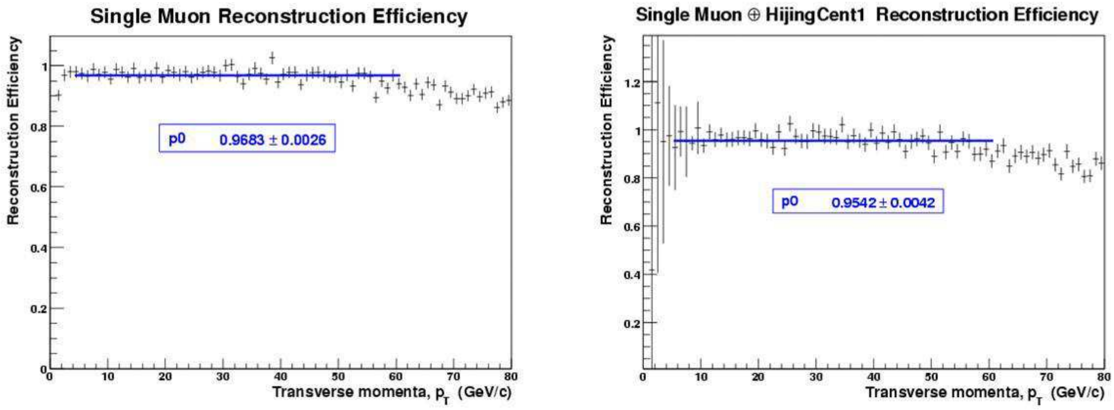

Figure 6.10: Single muon efficiency as a function of p_T estimated with a muon flat distribution (left figure) and considering the background contribution for PbPb central collisions (right figure).

Acceptance

The acceptance influence has been estimated by means of simulation for all the muon sources. All the contributions have been simulated over the whole rapidity and transverse momenta range and an analysis cut over the muon angular position of $171^\circ < \theta < 178^\circ$, the momenta of $P > 4$ GeV/c and transverse momenta of $p_T > 1$ GeV/c have been applied to account for the spectrometer angular coverage and mimic the front absorber effect.

Reconstructed spectra

Once the apparatus acceptance and efficiency were estimated, we computed the expected muon statistics from W decays in different collision types. Tab. 6.3 shows the values of the number of muons produced in the whole rapidity range and reconstructed in the muon spectrometer during one year of data-taking in nominal conditions (see Tab. 3.1) from W muonic decays. Figs. 6.11 and 6.12 present the resulting spectra obtained for the number of muons reconstructed in the ALICE muon spectrometer in p-p and Pb-Pb collisions at 14 TeV and 5.5 TeV. From those plots and tables ***we can conclude that there will be enough statistics and that the muon spectrometer should be able to detect weak bosons in the single muon spectra***, those being the main contributors for p_T larger than 30 GeV/c. In addition, Tab. 6.4 show the estimated number of reconstructed muons from W decays and all the considered muon sources in p-p and Pb-Pb collisions for different centrality classes in the whole p_T range and in the $(30, 50)$ GeV/c interval. Notice that in order to evaluate the expected statistics for different centralities just binary scaling has been considered, and not the possible modifications of nuclear shadowing with the centrality class[7]. From the expectations it is evident that approximately half of muons from W decays are in the $(30, 50)$ p_T interval, and that in this range their contribution amounts to about 70% (80%) of the total for p-p (Pb-Pb) collisions. ***Furthermore, from those calculations we can observe that minimum bias, and*** 0-5% ***as central and*** 40-70% ***as peripheral centrality classes provide appropriate statistical samples for minimum bias, central and peripheral reactions***.

Collision	$N_{\mu\leftarrow W}$	$N^{Reco}_{\mu\leftarrow W}$
p-p at 14 TeV	$6.3 \cdot 10^5$	$8.6 \cdot 10^4$
p-Pb at 8.8 TeV	$2.3 \cdot 10^5$	$4.0 \cdot 10^4$
Pb-p at 8.8 TeV	$2.3 \cdot 10^5$	$1.7 \cdot 10^4$
Pb-Pb at 5.5 TeV	$1.4 \cdot 10^5$	$1.4 \cdot 10^4$

Table 6.3: Estimated number of muons from W decays in ALICE during one year of data-taking. Statistics in $4\ \pi$ ($N_{\mu\leftarrow W}$) and evaluated number of reconstructed muons ($N^{Reco}_{\mu\leftarrow W}$) in the muon spectrometer.

---

[7] PDFs nuclear modifications could be affected for the centrality of the collision. This modifications seem to have a small influence on the gluon PDFs and to be negligible for quark's.

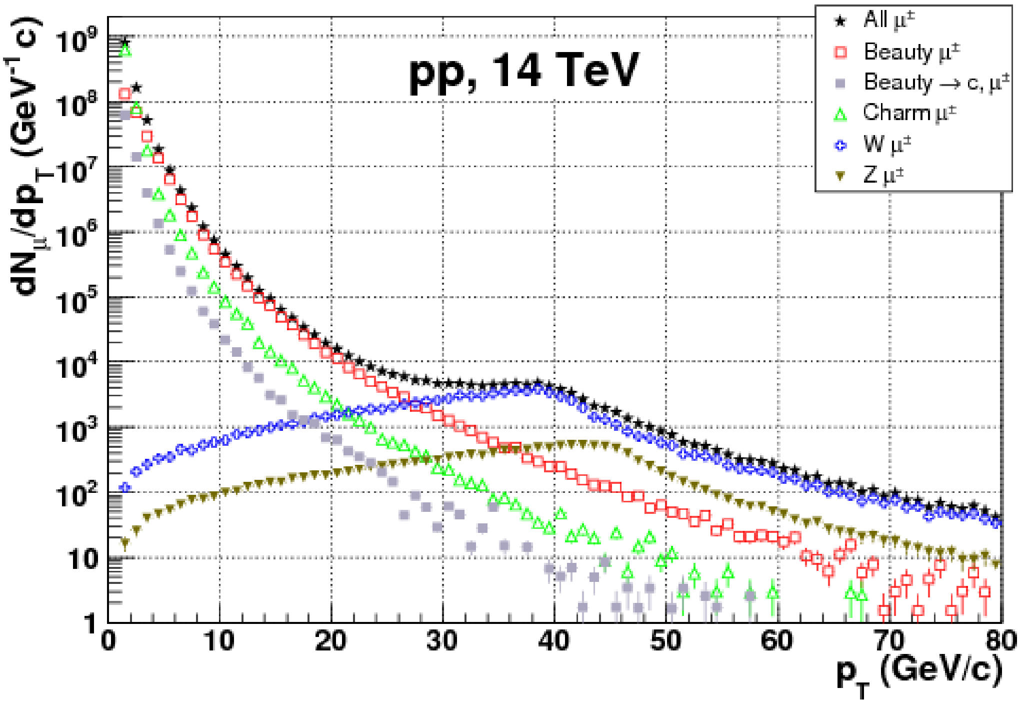

Figure 6.11: Estimated number of reconstructed muons as a function of p_T for p-p collisions at 14 TeV.

Collision	C.C.	p_T [GeV/c]	$N^{Reco}_{\mu\leftarrow W}$	N^{Reco}_{μ}
p-p at 14 TeV	MB	(1,80)	$8.6 \cdot 10^4$	$1.1 \cdot 10^9$
		(30,50)	$5.0 \cdot 10^4$	$7.0 \cdot 10^4$
Pb-Pb at 5.5 TeV	MB	(1,80)	$1.4 \cdot 10^4$	$2.9 \cdot 10^8$
		(30,50)	$6.7 \cdot 10^3$	$8.4 \cdot 10^3$
	0-5%	(0,80)	$3.4 \cdot 10^3$	$4.1 \cdot 10^7$
		(30,50)	$1.6 \cdot 10^3$	$2.0 \cdot 10^3$
	0-10%	(1,80)	$6.0 \cdot 10^3$	$7.4 \cdot 10^7$
		(30,50)	$2.9 \cdot 10^3$	$3.6 \cdot 10^3$
	40-70%	(1,80)	$1.0 \cdot 10^3$	$1.3 \cdot 10^7$
		(30,50)	$4.9 \cdot 10^2$	$6.1 \cdot 10^2$
	50-70%	(1,80)	$4.2 \cdot 10^2$	$5.1 \cdot 10^6$
		(30,50)	$2.0 \cdot 10^2$	$2.5 \cdot 10^2$

Table 6.4: Estimated number of reconstructed muons in ALICE during one year of data-taking from W decays ($N^{Reco}_{\mu\leftarrow W}$) and all muon sources ($N^{Reco}_{\mu}$) as a function of the p_T range and centrality class (C.C.), where MB stands for minimum bias.

Finally, we want to observe how the muon charge asymmetry evolves in the muon spectrometer acceptance as a function of p_T. Fig. 6.13 displays the pattern of W muons and all muon

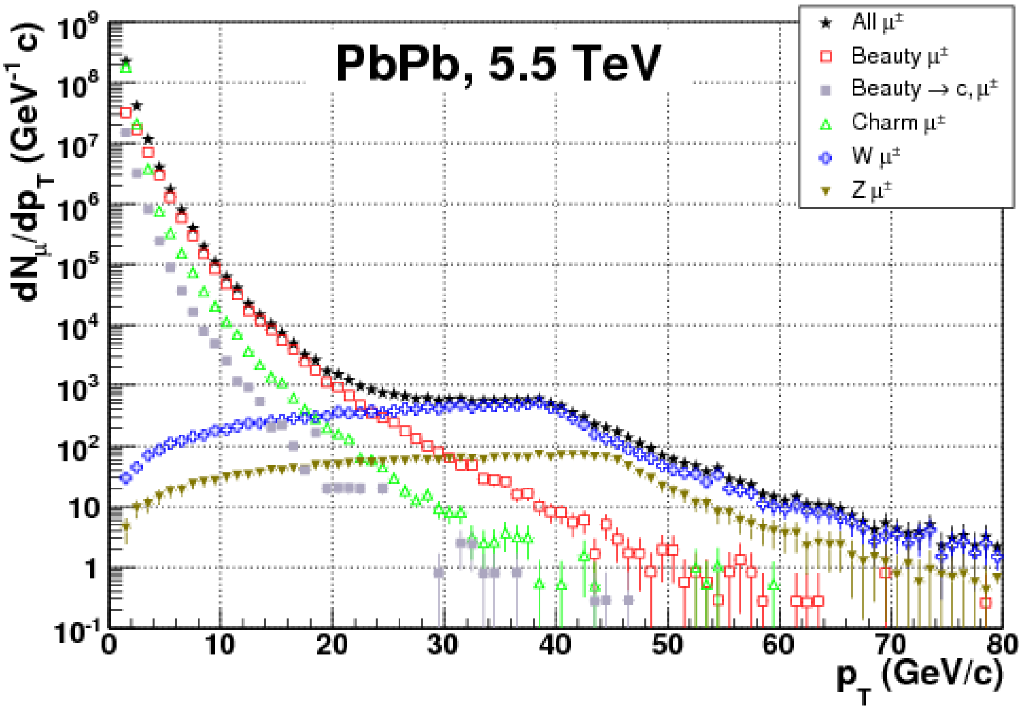

Figure 6.12: Estimated number of reconstructed muons as a function of p_T for Pb-Pb MB collisions at 5.5 TeV.

sources in p-p and Pb-Pb collisions. Remark that the shape differs from that observed in the whole rapidity range, noticeably in the low p_T part of the spectra due to the relative higher influence of beauty and charm decays at mid-rapidity than at high-rapidity and also due to the sharper shape of muons from W decays at high-rapidities. Tab. 6.5 present the estimated

Collision	p_T [GeV/c]	$N^{Reco}_{\mu^+ \leftarrow W}/N^{Reco}_{\mu^- \leftarrow W}$	$N^{Reco}_{\mu^+}/N^{Reco}_{\mu^-}$
p-p at 14 TeV	(15,20)	0.99 ± 0.02	1.02 ± 0.01
	(20,30)	1.25 ± 0.02	1.05 ± 0.01
	(30,40)	1.64 ± 0.02	1.42 ± 0.01
	(35,45)	1.80 ± 0.02	1.57 ± 0.02
	(40,50)	1.98 ± 0.03	1.63 ± 0.02
Pb-Pb at 5.5 TeV	(15,20)	0.33 ± 0.02	0.89 ± 0.01
	(20,30)	0.28 ± 0.01	0.61 ± 0.01
	(30,40)	0.42 ± 0.01	0.48 ± 0.01
	(35,45)	0.56 ± 0.02	0.61 ± 0.02
	(40,50)	0.71 ± 0.03	0.76 ± 0.03

Table 6.5: Estimated reconstructed muon charge asymmetry μ^+/μ^- in the ALICE muon spectrometer as a function of the p_T range and collision type. Errors are just statistical.

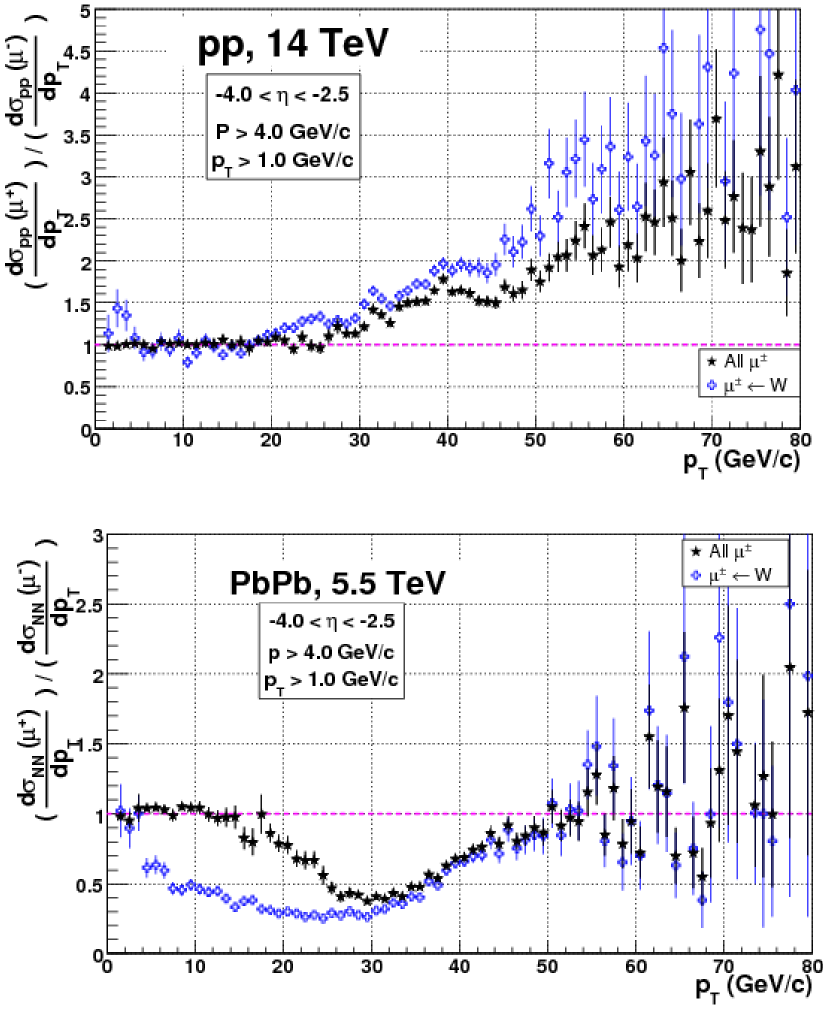

Figure 6.13: Single muon charge asymmetry μ^+/μ^- as a function of p_T for p-p and Pb-Pb collisions in the ALICE muon spectrometer acceptance. The sum of all different sources and also the W contribution are plotted.

muon charge asymmetry expectations for p-p and Pb-Pb collisions in various transverse momenta windows. Contributions from all muons and W muons have been evaluated. Those plots and calculations indicate that ***W muon charge asymmetry and its distinct behavior in p-p and Pb-Pb collisions will be visible in the ALICE muon spectrometer, which converts the muon charge asymmetry in a suitable signal of W production***. Particularly, for $p_T \in (35, 45)$ GeV/c the muon charge asymmetry is expected to amount to about 1.6 in p-p collisions and 0.6 in Pb-Pb collisions.

6.2.2 Muon trigger conditions

It is foreseen that the ALICE muon spectrometer will be able to deal with 1 kHz data-taking rate, and that trigger rates have to be optimized for quarkonia measurements. W produc-

tion should be studied with the sample of high p_T single muon triggered events. Trigger efficiency for high p_T muons has been estimated to be close to 99%, but for the sake of simplicity here we consider it to be equal to 100%.
Results of the muon trigger rates calculations are summarized in Tab. 6.6 from references [Yer05, Gue05, G$^+$06]. However, it should be noticed that those trigger rates assume that beam-gas interactions are fully rejected by the V0 detector of ALICE [G$^+$06]. In the case of p-p collisions at 14 TeV, unlike-sign pair trigger rates are expected to be small, below 30 Hz regardless of the trigger p_T-cut. Single muon low-p_T (SingleLPt) trigger rate in those conditions is close to 500 Hz. The total being below the 1 kHz apparatus capability, we conclude that ***in p-p collisions trigger rates allow to collect all produced high p_T muons***.

		All-Pt [Hz]	Low-Pt [Hz]	High-Pt [Hz]
p-p at 14 TeV	Single	1850 ± 74	508 ± 30	226 ± 20
	Unlike-sign Pair	27 ± 7	10 ± 4	5 ± 3
PbPb at 5.5 TeV	Single	1700	1100	450
	Unlike-sign Pair	930	350	70

Table 6.6: Expected trigger rates in p-p and Pb-Pb collisions for the ALICE muon spectrometer from references [Yer05, Gue05, G$^+$06]. Details of the triggers can be found in Sec. 4.2.1.

For Pb-Pb collisions, unlike-sign pair low-p_T (USPairLPt) trigger rate amounts to ~ 350 Hz, whereas SingleLPt trigger rate is ~ 1100 Hz. In this case, if we consider both triggers we are well above the 1 kHz upper limit. In this circumstances, we should decide between:

1. Scaling-down single muon trigger rates, loosing half of the statistics;
2. Employing the High Level Trigger (HLT) to introduce a higher p_T-cut;
3. Defining different trigger rates as a function of centrality. Take data for one central and one peripheral case. For example, as central we could consider 0-5% centrality class where high-p_T trigger rate amounts to 120 Hz, and for peripheral 40-70% centrality class where it is about 30 Hz. This scenario would allow to compare single muon production in central and peripheral collisions, permitting to study their yields ratio (R_{cp}).

At the present time trigger strategies are still under discussion.

6.3 Preliminary results on Z measurement feasibility

In the previous section we discussed the feasibility of W measurements via the single muon p_T distribution at LHC. Here we briefly examine the feasibility of Z bosons measurements in the ALICE muon spectrometer via their dimuon decay. As usual, the different background muon unlike-sign pair sources, acceptance and efficiency corrections should be considered;

but in this work we will not evaluate the contribution from the background sources to the dimuon spectra. In Fig. 6.6 from reference [B+00] we have an example of the distribution pattern at LHC energies. Nevertheless, we can estimate the number of reconstructed muon pairs from Z decays in different collision types.

In the former section we stated that single muon reconstruction efficiency in the ALICE muon spectrometer follows an approximately flat pattern and amounts to 97% in the $p_T \in (5, 60)$ GeV/c. In Secs. 4.4.3 and 4.5.4 we studied single muon efficiency in the muon spectrometer as a function of the trigger type and concluded that we were able to identify muon charge up to (at least) $p_T \sim$ 60-80 GeV/c. Hence, the spectrometer should be able to reconstruct the unlike-sign dimuon pair distribution from Z decays, and by means of statistics we can evaluate the dimuon reconstruction efficiency to be about 94%[8]. All this and the results exposed in Sec. 5.3 allow us to estimate the reconstructed muon pair statistics from Z production in p-p, p-Pb[9], Pb-Pb and Ar-Ar collisions at 14, 8.8, 6.3 and 5.5 TeV respectively and summarize them in Tab. 6.7. ***Results indicate that the reconstructed statistics is enough to allow Z measurements in p-p, p-Pb and Ar-Ar collisions but to exploit it in Pb-p or Pb-Pb collisions the statistics of several runs should be accumulated***.

Collision	$N_{\mu^+\mu^-\leftarrow Z}$	$N^{Reco}_{\mu^+\mu^-\leftarrow Z}$
p-p at 14 TeV	$5.7 \cdot 10^4$	$2.4 \cdot 10^3$
p-Pb at 8.8 TeV	$2.3 \cdot 10^4$	$1.2 \cdot 10^3$
Pb-p at 8.8 TeV	$2.3 \cdot 10^4$	$3.0 \cdot 10^2$
Ar-Ar at 6.3 TeV	$9.6 \cdot 10^4$	$2.1 \cdot 10^3$
Pb-Pb at 5.5 TeV	$1.4 \cdot 10^4$	$2.3 \cdot 10^2$

Table 6.7: Estimated number of muon pairs from Z decays in ALICE during one year of data-taking. Statistics in $4\,\pi$ ($N_{\mu^+\mu^-\leftarrow Z}$) and evaluated number of reconstructed muon pairs ($N^{Reco}_{\mu^+\mu^-\leftarrow Z}$) in the muon spectrometer.

In addition, preliminary results [Blu06] indicate that the invariant mass full-width-half-maximum could be reconstructed with a resolution of about 5%.

6.4 Conclusions

In this chapter we addressed the feasibility of weak bosons measurement in the ALICE muon spectrometer. For this purpose we studied the different background muon sources contributing to the spectra and we determined the acceptance and the efficiency corrections. From higher to lower transverse momenta we decided to neglect: weak bosons tau and

---

[8] If single track reconstruction efficiency is about 97%, dimuon track reconstruction efficiency amounts to 0.97×0.97, that is 94%.

[9] Preliminary calculations show that the muon spectrometer acceptance for p-Pb and Pb-p collisions at 8.8 TeV is about 5.8% and 1.4% respectively.

charmed decays, light flavor and strange hadrons contributions, all of them populating to the low p_T part of the muon distributions, and also Drell-Yan contribution. We evaluated the single muon p_T distribution and we concluded that in p-p collisions at 14 TeV and for the whole rapidity range charm decays dominate at $p_T \in (2, 4)$ GeV/c, whereas beauty decays are predominant up to $p_T \sim 30$ GeV/c and above that p_T value the W contribution prevails. We observed that those crossing-points evolve smoothly with the collision center-of-mass energy and the pseudo-rapidity window considered. Without trigger considerations we estimated the reconstructed single muon distribution and its associated statistics and deduced that W boson measurements in p-p, p-Pb and Pb-Pb collisions at 14, 8.8 and 5.5 TeV are feasible. Single muon charge asymmetry, i.e. the ratio of the μ^+/μ^- yield at high p_T, proved to be a useful signal of W production. Moreover, this asymmetry varies with the collision type, it becomes larger than unity for p-p collisions and gets smaller than unity for Pb-Pb collisions due to isospin effects. With respect to the trigger, the expected muon trigger rates in p-p collisions should allow to observe the W signal, while the strategies for Pb-Pb collisions have to be further discussed. Finally, we have estimated the expected statistics from Z bosons dimuon decays in the ALICE muon spectrometer and we have concluded that their measurement through the dimuon invariant mass spectrum seems feasible in p-p, p-Pb and Ar-Ar collisions at 14, 8.8 and 6.3 TeV.

Part IV

Discussion

Chapter 7

Probing hot and dense QCD matter with high-p_T muons at the LHC

> *Imagination is more important than knowledge. For knowledge is limited, whereas imagination embraces the entire world, stimulating progress, giving birth to evolution.*
>
> A. Einstein

At this point of the manuscript we would like to concentrate on the study of high-energy muons in heavy-ion collisions. What we could learn from them. Will they be useful to determine the properties of the medium in heavy-ion collisions? In particular, can they tell us something about the possible formation of the QGP and its characteristics? In the previous chapter we learned that weak bosons, and beauty and charm decays are the main contributors for $p_T \gtrsim 30$ GeV/c and $p_T \in (2, 30)$ GeV/c respectively. In Sec. 7.1 we briefly remind the basic differences of heavy quark and weak boson production in nucleon-nucleon collisions and in the presence of a cold nuclear medium. Concerning heavy quarks and quarkonia production, on the first chapter (Sec. 1.3.1) we showed that the $Q\bar{Q}$ pre-resonances are produced early in a time $t_p \ll 1$ fm/c, take around 1-3 fm/c to form a $Q\bar{Q}$ resonance and decay long after ($t_d \sim 1000$ fm/c). If the QGP is created in the most central LHC Pb-Pb collisions and lives about 10 fm/c, the $Q\bar{Q}$ resonance may dissociate in the deconfined medium before decaying, and the single heavy-quarks may lose energy while traversing it. A summary of the present state-of-the-art theoretical formalism to treat heavy quark in-medium energy loss is presented in Sec. 7.2. With regard to weak bosons, they are formed almost instantaneously and decay in about $t_d < 1$ fm/c (see Sec. 2.1); it would then be their decay products who might be affected by the medium. Even though in our case we are interested by the muonic decays and muons do no interact strongly, in Sec. 7.3 we discuss the potential medium influence on high-p_T muons. Later, in Sec 7.4, we make use of all the previous discussions to examine the possibility of high-p_T muon suppression in a QGP with the novelty of considering for the first time weak bosons decays in the calculations. Finally, we mention some possibilities to investigate in-medium effects on Z boson decays (Sec. 7.5).

7.1 Weak boson versus heavy quark production

To go further we need to point out some basic distinctions between heavy quark and weak boson production that have not been specifically highlighted up to now. First their production processes in nucleon-nucleon collisions differ, and secondly they are not influenced in the same way by the presence of a (hot or cold) QCD medium.

7.1.1 Production mechanisms

At LHC energies, heavy quarks are produced via hard processes that occur in the early stage of the collision. They are usually classified as:

- Pair creation: a $Q\,\bar{Q}$ pair is formed either via gluon-gluon fusion ($g\,g \to Q\,\bar{Q}$) or $q\bar{q}$ annihilation ($q\,\bar{q} \to Q\,\bar{Q}$),

- Flavor excitation: an incoming heavy quark scatters on a parton of the other beam: $q\,Q \to q\,Q$, $g\,Q \to g\,Q$,

- Gluon splitting: no heavy flavor is involved in the hard scattering, but a gluon splits into a $Q\,\bar{Q}$ pair: $g \to Q\,\bar{Q}$.

At leading-order heavy quarks are produced via pair creation, mostly by gluon-gluon fusion. On the other hand, at leading-order weak bosons are formed by $q\bar{q}$ annihilation only (see Sec. 5.1.1 for details). In this respect heavy quark production is sensitive to the gluon PDF whereas weak bosons to the quark PDFs.

7.1.2 Nuclear parton distribution functions: nuclear shadowing

EKS98 [EKS99] parameterization of the nuclear modifications of the parton distribution functions are presented in Fig. 7.1. Using this plot we can estimate qualitatively the shadowing factor for heavy quarks and weak bosons via the Bjorken-x values that can be calculated by $x_{1,2} = Q/\sqrt{s} \cdot e^{\pm y}$ as a function of the pair/boson rapidity y and the momentum transferred in the reaction Q. For heavy quarks we shall consider various values of Q, as they vary roughly linearly with the particle transverse momentum ($Q \approx 2p_T$). For weak bosons we suppose $Q \approx M$ and we shall remind that at high-rapidities they are probably produced by valence-sea quark scattering while at mid-rapidity by sea-sea quark collisions. We can also evaluate the mean shadowing factor by computing the ratio of the production cross-sections in p-p and Pb-Pb collisions at the same energy (from Tab. 6.2). Our calculations are summarized in Tab. 7.1 and suggest that the mean shadowing factors for charm, beauty, W and Z are about 0.65, 0.85, 0.9 and 0.9 respectively. Furthermore, ***we observe that the shadowing factor depends on rapidity and transverse momentum. In particular, for high-p_T heavy quarks at mid-rapidity it tends to be larger than one (~ 1.1, anti-shadowing region), while at high-rapidity or for small-p_T it is below one. For weak bosons we remark that it is approximately constant around 0.9.***

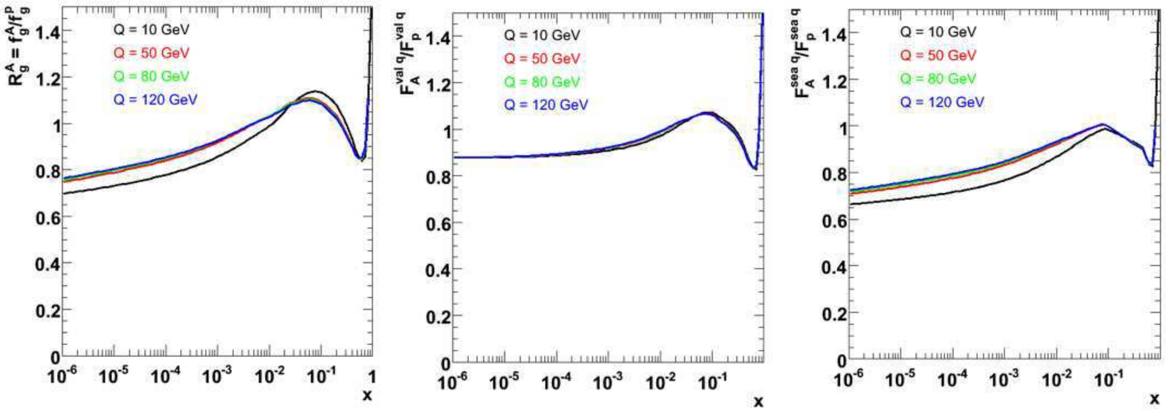

Figure 7.1: Ratio of gluons (left-hand), valence quarks (middle) and sea quarks (right-hand) distributions in Pb nucleus over the ones in the proton (for various values of Q^2) as given by the EKS98 nuclear modifications parameterization. Courtesy of C. Salgado.

	y	p_T	x_1	x_2	$C_{shad}(y,p_T)$	$\langle C_{shad}\rangle$
$c\bar{c}$	0	0	$4{\cdot}10^{-4}$		0.5	0.65
	0	30	10^{-2}		1.1	
	3.0	0	$9{\cdot}10^{-3}$	$2{\cdot}10^{-5}$	0.6	
	3.0	30	$2{\cdot}10^{-1}$	$5{\cdot}10^{-4}$	0.9	
$b\bar{b}$	0	0	$2{\cdot}10^{-3}$		0.8	0.85
	0	30	10^{-2}		1.1	
	3.0	0	$3{\cdot}10^{-2}$	$8{\cdot}10^{-5}$	0.9	
	3.0	30	$2{\cdot}10^{-1}$	$5{\cdot}10^{-4}$	0.9	
W	0	–	$2{\cdot}10^{-2}$		0.9	0.89
	3.0	–	$3{\cdot}10^{-1}$	$7{\cdot}10^{-4}$	0.8	
Z	0	–	$2{\cdot}10^{-2}$		0.9	0.93
	3.0	–	$3{\cdot}10^{-1}$	$8{\cdot}10^{-4}$	0.8	

Table 7.1: Qualitative estimation of Bjorken-x values and EKS98 shadowing factor probed by heavy quarks and weak bosons produced in Pb-Pb collisions at $\sqrt{s_{NN}} = 5.5\ TeV$ as a function of the pair/boson rapidity and transverse momenta.

7.2 Introduction to the theoretical treatment of heavy quark energy loss

In this section we discuss the theoretical framework used to compute the medium energy loss of heavy quarks. We first recall the standard factorization theorem used in QCD to calculate cross-sections, and then we focus on the formalism used to estimate the energy loss.

7.2.1 QCD factorization theorems

Factorization theorems address the problem of calculating QCD high energy cross-sections [CSS88, CSS98]. Factorization theorems explain how to factorize short-distance parton-parton scatterings (calculable via perturbative expansions in α_s), from long-distance physics (for which pQCD can not be used), encoded in universal functions describing the distribution of partons (PDF) in a hadron or the fragmentation of partons (FF) into hadrons.
According to factorization, the cross-section for a hard $A + B \to c + X$ process, with c being for example heavy quarks, may be written as

$$d\sigma_{AB} = \sum_{a,b} \int dx_a dx_b \; \phi_{a/A}(x_a, \mu^2)\, \phi_{b/B}(x_b, \mu^2)\, \widehat{\sigma}_{ab\to c}\Big(\frac{Q^2}{x_a x_b s}, \frac{Q}{\mu}, \alpha_s(\mu)\Big) \; \Big(1 + O\Big(\frac{1}{Q}\Big)\Big) \, , \tag{7.1}$$

where $\phi_{a/A}(x_a, \mu^2)$ describe the a parton distribution function in hadron A as a function of the longitudinal momentum fraction x_a at a given order of α_s and evolves with the factorization scale μ (DGLAP evolution); and $\widehat{\sigma}_{ab\to c}$ is the hard scattering cross section computed in pQCD up to some order of α_s.
The final measured particles are, for example, heavy hadrons whose yields can be determined by including an additional factor in eq. 7.1 related to the parton fragmentation onto the final measured particles, $c \to H + Y \to l + Y'$. The final cross-section can then be expressed in the form

$$d\sigma_{AB} = \sum_{a,b} \int dx_a dx_b \; \phi_{a/A}\, \phi_{b/B}\, \widehat{\sigma}_{ab\to c}\, D_{c\to H}\, D_{H\to l} \, . \tag{7.2}$$

$D_{c\to H}(x, Q)$ gives the probability that a parton c fragments into a hadron H with a momentum fraction x at an scale Q. The Leading-Order (LO) hard scattering elements are available in Monte-Carlo simulators such as PYTHIA or HERWIG. Parton distribution functions are measured in DIS. The distributions are parameterized at an initial scale, and their scale evolution is given by the DGLAP equations. Remark that when dealing with a nucleus-nucleus collision the parton distribution functions may be affected with respect to those measured in DIS ep collisions, thus nuclear corrections are usually taken into consideration, for instance through the EKS98 parameterization. The fragmentation function values are also extracted from fits to e^+e^- hadron production data [KKP01, AKK04] at a low scale and are supposed to evolve in a DGLAP-like form. The former are considered as 'initial-state-effects' and the latter as 'final-state-effects' with respect to the hard reaction.

7.2.2 Medium induced gluon radiation

In 1982 Bjorken [Bjo82] first claimed that the energy of a jet might be degraded in the presence of a QGP. He argued that elastic scattering of the high-p_T partons produced in the reaction with the medium partons might cause energy loss, in a similar way as ionization of charged particles traversing ordinary matter. Later works showed that such elastic scattering processes result in a relatively small energy loss, e.g. of $O(0.1$ GeV/fm$)$ for a 20 GeV

parton in a plasma temperature of $T = 250$ MeV.
In the 90s the effects of radiative (rather than elastic or 'collisional') energy loss drew attention. It was realized that multiple inelastic scattering of partons in the medium induces gluon radiation and thus radiative energy loss, in analogy to the bremsstrahlung of charged particles crossing ordinary matter. Thereafter, a lot of work has been done by the theorists to investigate radiative energy loss. Various approaches have been studied in the literature, and here we will just outline the Parton Quenching Model [DLP05, DLP06], which we will later use to make some predictions, that is based on the BDMPS formalism [BDM$^+$97b, BDM$^+$97a] and includes the so-called dead cone effect [DKT91, DK01] and a realistic collision geometry.

The BDMPS formalism

In the Baier-Dokshitzer-Mueller-Peigné-Schiff (BDMPS) formalism [BDM$^+$97b, BDM$^+$97a], a parton produced in a hard collision suffers multiple scattering with mean free path $\lambda = 1/(\rho\sigma)$ in a medium of length L and density ρ. ***In this process the gluons in the parton wave-function pick-up transverse momentum and may eventually decohere and be radiated***. The scale of the energy loss is determined by the characteristic energy of the radiated gluons

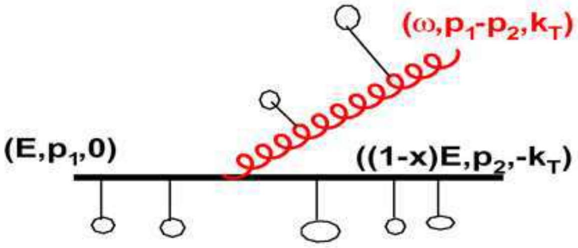

Figure 7.2: Qualitative sketch of the mechanism for radiative energy loss.

$$\omega_c = \frac{1}{2}\widehat{q}L^2\,, \tag{7.3}$$

which depends on L and on the transport coefficient $\widehat{q}$ defined as the typical squared momentum transferred from the medium to the parton per path length unit

$$\widehat{q} = \frac{\langle q_T^2\rangle_{medium}}{\lambda}\,, \tag{7.4}$$

$\widehat{q}$ measures the color field strength of the medium. The energy distribution of the radiated gluons for $\omega \ll \omega_c$ is found to be

$$\omega\frac{dI}{d\omega} \simeq \frac{2\alpha_s C_R}{\pi}\sqrt{\frac{\omega_c}{2\omega}}\,. \tag{7.5}$$

where C_R stands for the QCD (Cassimir) coupling factor between the hard parton and the gluon in the medium ($C_R = 4/3$ for quark-gluon coupling and $C_R = 3$ for gluon-gluon coupling). The energy loss is given by the integral of this expression

$$-\Delta E = \int^{\omega_c} \omega \frac{dI}{d\omega} \propto \alpha_s \, C_R \, \widehat{q} \, L^2 \, . \tag{7.6}$$

In this formalism the energy loss is proportional to α_s, C_R, $\widehat{q}$ and L^2 and is independent of the initial parton energy. Note that parton energy loss is larger for gluons than for light quarks because gluons have a larger color charge.

Dead cone effect

In references [DKT91, DK01] it is argued that due to their large mass heavy quarks gluon-bremsstrahlung differs from that of the light quarks because of its suppression in the angular region $\theta < M/E \equiv \theta_0$ caused by destructive quantum interferences (where M is the heavy quark mass). This effect explains the existence of a cone in the heavy quark forward direction ($\theta < \theta_0$) which is depopulated of gluon-radiation, the so called *dead cone effect*. The gluon emission probability for a heavy quark is related to the standard bremsstrahlung by a factor

$$\left(1 + \frac{\theta_0^2}{\theta^2}\right)^{-2} = \left(1 + \left(\frac{M}{E}\right)^2 \sqrt{\frac{\omega^3}{\widehat{q}}}\right)^{-2} .$$

As a result the leading particle from heavy quark fragmentation carries more energy than the leading particle produced from light quark fragmentation, because for a heavy quark less gluons are radiated.

The Parton Quenching Model

The Parton Quenching Model (PQM) [DLP05, DLP06] is a Monte Carlo model based on the BDMPS formalism and brings a dependence on the initial parton energy (a parton cannot lose more energy than it initially has), includes the collision geometry (the parton energy loss depends on the distance travelled in the medium), and takes into account a realistic energy density profile in the medium.

In reference [SW03] Salgado-Wiedemann bound the transverse momentum of a radiated gluon q_T to be smaller than its characteristic energy ω_c. This constraint is imposed via the dimensionless ratio

$$R = \frac{2\omega_c^2}{\widehat{q}L} = \frac{1}{2}\widehat{q}L^3 \, , \tag{7.7}$$

and allows to extend the BDMPS formalism to $\omega \geq \omega_c$. Note that the BDMPS case corresponds to the limits $R \to \infty$, $L \to \infty$. They define as *quenching weight* the probability that a parton radiates a given energy via scattering, and such weights are computed on the basis of the BDMPS formalism as a function of ω_c and R. Furthermore, with an additional constraint they account for the dead cone effect.

The PQM [DLP05, DLP06] uses the Salgado-Wiedemann *quenching weights* and includes the collision geometry by calculating ω_c and R for each particle within a Glauber model approach (see Appendix D). In fact, they introduce the geometry dependence via a 'local' transport coefficient. In practical terms, the PQM makes use of the factorization theorem by generating first a parton with the PYTHIA event generator for a given PDF, then determine the medium parameters ω_c and R, and with them the *quenching weights* that allow to re-define the parton transverse momentum. Finally fragmentation functions are employed to fragment the parton in a hadron.

This model evaluates parton energy loss traversing a dense medium in the transverse plane, for partons at mid-rapidity. In their approach it is assumed that the parton is produced in the transverse plane, with a distribution of production points that depends on the nuclear overlap function of nuclei A and B separated by an impact parameter b, $T_{AB}(x, y; b)$. This variable being calculated by means of a Glauber model (see Appendix D). Thus they define a 'local' transport coefficient

$$\widehat{q}(\xi; b) = k \times T_{AB}(x', y'; b)\,, \tag{7.8}$$
$$\text{with} \qquad x' = x_0 + \xi \cos\phi_0\,, \qquad y' = y_0 + \xi \sin\phi_0\,,$$

where (x_0, y_0) and $(\cos\phi_0, \sin\phi_0)$ are the parton production point and azimuthal propagation direction. $\widehat{q}(\xi; b)$ depends on the parton trajectory in the medium and k is a free parameter (in fm) that sets the scale of the transport coefficient in GeV^2/fm. Afterwards they evaluate an effective ω_c and R as a function of ξ

$$\omega_c|_{effective} = \frac{1}{2}\widehat{q} L^2 = \int_0^\infty \xi\, \widehat{q}(\xi)\, d\xi, \tag{7.9}$$
$$\text{and} \qquad R|_{effective} = \frac{2\,(\omega_c|_{effective})^2}{\widehat{q}\, L|_{effective}}\,, \qquad \widehat{q}\, L|_{effective} = \int_0^\infty \widehat{q}(\xi)\, d\xi\,.$$

An important characteristic of this model is that it contains one single parameter $\widehat{q}$, which can be estimated from the data. In references [DLP05, DLP06] it is argued that experimental results indicate that $\widehat{q}$ should be set to 4-14 GeV^2/fm for RHIC Au-Au central collisions at $\sqrt{s_{NN}} = 200$ GeV. A $\widehat{q}$ of 25-100 GeV^2/fm is predicted for the LHC Pb-Pb central collisions at $\sqrt{s_{NN}} = 5.5$ TeV assuming $\widehat{q}$ proportionality to the hadron multiplicity. With this single parameter tuned to 14 GeV^2/fm the model describes RHIC results on the nuclear modification factor (centrality dependence and p_T-independence) at high p_T. It also describes the magnitude and centrality dependence of the away-side peak suppression of back-to-back jet-like two-particle correlations. Moreover their analysis suggests that high-p_T hadron production in central nucleus-nucleus collisions occurs predominantly close to the surface.

7.3 Are high-p_T muons affected by the presence of a thermal medium?

The question we try to address in this section is what the energy lost by high energy leptons is while crossing a QGP, i.e. can we ignore the influence of the QGP on leptons going through it? Remember that we are interested in decay muons from weak bosons produced about 0.1 fm/c after the hard interaction (see Sec. 2.1). Theoretical calculations indicate that at

LHC energies the QGP might last about 10 fm/c; consequently muons from weak decays travel quite a large distance in the QGP.

Quantum ElectroDynamics states that when dealing with very energetic leptons crossing a material the predominant process for energy loss is bremsstrahlung[1]. Medium-induced bremsstrahlung can occur if the energetic muon undergoes at least one elastic scattering when traveling in the QGP. We thus need to know the lepton mean free path λ from elastic collisions. Heuristically, if n_q is the density of electromagnetically charged scatters and σ_{el} the elastic cross-section of the lepton, $n_q\,\sigma_{el}\,\lambda \sim 1$. For an ultra-relativistic plasma $n_q \propto T^3$ and $\sigma_{el} \propto \alpha_{em}\,T^{-2}$ [Pei07], then

$$\lambda \propto \frac{1}{\alpha_{em}\,T}\,. \tag{7.10}$$

In the most extreme case we could expect $T \sim 1$ GeV, which would imply $\lambda \sim 27$ fm. As a matter of fact, the accurate calculation of λ is more complex, includes additional terms in the denominator accounting for the long-range magnetic interactions making σ_{el} larger and diminishing the λ value [BI02], so we could expect $\lambda \sim 10$ fm for those conditions [Pei07]. From the latter estimate $\lambda \sim 10$ fm $\sim L_{QGP}$, thus the lepton energy loss can roughly be estimated by assuming that it undergoes in average one elastic scattering. The radiated energy in one elastic scattering $\langle\omega\rangle_1$ is indeed [Pei07]

$$\langle\omega\rangle_1 \;\propto \alpha_{em}\,E\,, \tag{7.11}$$

where E is the lepton energy. A naif interpretation of this relation is that the energy E is radiated with a probability α_{em}. To our concern, we can compute the mean radiative energy loss by muons from W decays[2]. If we consider a muon of $P \sim 40$ GeV/c, we obtain $\langle\omega\rangle_1 \sim 0.3$ GeV and the typical momentum exchange would be $\omega_{typ} \sim 0.1$ GeV [Pei07]. Hence, roughly a muon would lose about 1% of its initial energy through bremsstrahlung when crossing a QGP of $T \sim 1$ GeV.

Nevertheless, if the traversed material length would be larger, we should care about the fact that the radiated photon is not emitted immediately, there exists a formation time. *From an illustrative point of view we can tell that there exists a time interval in which the photon and the lepton travel too close and it is not possible to distinguish them. The* formation time *would then be the time the photon takes to advance the lepton by one reduced wavelength [H$^+$04, H$^+$03, Kle99]. In the ultra-relativistic limit the correspondent lepton travel distance can be expressed as*

$$l_f = \frac{2\,\gamma^2\,c}{\omega}\,, \tag{7.12}$$

where $\gamma = E/mc^2$ is the lepton Lorentz factor related to its energy E and rest mass m, and ω describes the photon energy. During this formation time the lepton may undergo interactions with the medium that could affect the radiation spectrum and might reduce it. As a result of multiple Coulomb scattering in the formation length there might be destructive quantum interferences and the radiation might be suppressed for $\theta > \theta_0 \equiv 1/\gamma$, the so called Landau-Pomeranchuk-Migdal (LPM) effect. Consequently, if the scattering time is smaller than the formation time (i.e. if $\lambda < l_f$) the bremsstrahlung radiation will be suppressed. It is then due to make an approximative estimation of the formation time. If we consider that muons lose a fraction E/n of their initial

---

[1] Note that muon bremsstrahlung occurs much latter than electron bremsstrahlung.

[2] Remark that the mean value of the energy loss does not necessarily correspond to its most probable value. The probability of bremsstrahlung to occur in an elastic scattering is given by α_{em}, thus in most of events the muon does not radiate, and in rare events it emits a highly energetic photon. Here we concentrate on the mean energy loss to give a first estimate, though the most appropriate value should be given by the typical energy loss.

energy the computation gets

$$l_f = \frac{2\,E^2}{m^2\,\omega} \simeq \frac{2\,E^2}{m^2} \times \frac{n}{E} = \frac{2\,E}{m^2} \times n\,, \tag{7.13}$$

For muons with $P \sim 40$ GeV/c, we obtain $l_f \simeq 1.43 \times n$ [pm]. In any case, the formation time is much larger than the scattering time, thus if such energetic muons cross matter under extreme conditions during a large enough length, the bremsstrahlung radiation will be suppressed by the LPM effect. But remind that, as a matter of fact, calculations suggest that if the QGP is formed at LHC energies it will last about 10 fm/c. A large enough length for the bremsstrahlung effect to occur, but not as much for the LPM effect to influence the spectral shape.

In conclusion, at LHC energies energetic muons traversing the QGP might loose energy via bremsstrahlung. We estimate that their mean energy loss through a 10 fm/c plasma of temperature $T \sim 1$ GeV would be small, of about 1%.

7.4 The W reference for high-p_T single muon suppression

Now we know that in-medium weak boson decayed muons do not loose much energy, and we learned how we could estimate heavy quark energy loss, we focus on the methodology and results obtained in reference [DDCdVZ07] and some work in progress [CdVDD+07] in order to calculate the expected single muon suppression in Pb-Pb collisions at 5.5 TeV. On the one hand, weak boson contribution to the spectra is obtained as explained in Chapter 5, and no energy loss is considered for them. On the other hand, heavy quarks[3] are generated with the HVQMNR program up to NLO to reproduce NLO pQCD results of order $O(\alpha_s^3)$. Then, the quenching weights are calculated with the PQM paying attention to a Glauber-based collision geometry (see Sec. 7.2.2). As those quenching weights are evaluated at mid-rapidity and we are interested in the rapidity-dependence, we assume a pseudo-rapidity scaling of the transport coefficient $\widehat{q}$ with the event multiplicity:

$$\widehat{q}(\eta') = \widehat{q}(\eta = 0) \times \left.\frac{dN_{ch}}{d\eta}\right|_{\eta=\eta'} \Big/ \left.\frac{dN_{ch}}{d\eta}\right|_{\eta=0}. \tag{7.14}$$

Moreover, the heavy quarks that loose most of their energy are redistributed according to a thermal distribution

$$\frac{dN_{thermal}}{dm_T} \propto m_T\,exp(-\frac{m_T}{T})\,. \tag{7.15}$$

Finally the heavy quarks are assumed to hadronize following the Peterson fragmentation, and the heavy mesons are supposed to decay according to the spectator model[4] [ACC+82]. The reason to use this procedure and the HVQMNR program to generate heavy quarks lies on the needed CPU time. The generated lepton spectra without considering energy loss

---

[3] We have just considered 'direct' heavy quark decays, i.e. $b \rightarrow \mu\,X$ and $c \rightarrow \mu\,X$, and we have ignored the $b \rightarrow D\,X \rightarrow \mu\,Y$ cascades because their contribution at high-p_T is negligible, as stated in Chapter 6.

[4] The spectator model [ACC+82] addresses the interpretation of the heavy flavor leptonic decays. In this model, heavy mesons disintegrate into a heavy quark plus a spectator quark. The spectator quark is treated as a particle of definite mass and momentum, and the heavy quark is treated as a virtual particle. The heavy quark is then allowed to decay as a free particle with the V-A current.

were compared to those obtained from the PYTHIA tuning (see Sec.6.1.2) demonstrating their agreement [DDCdVZ07].

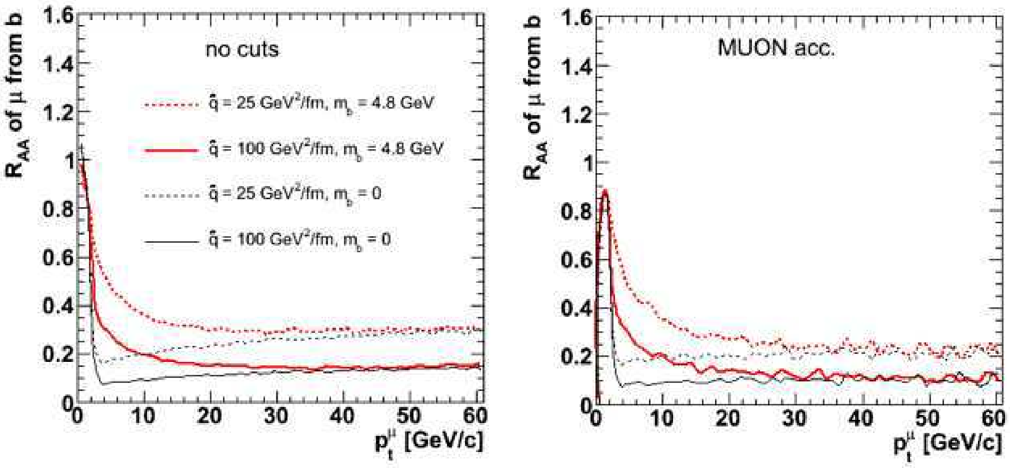

Figure 7.3: Nuclear modification factor for muons from beauty decays with and without mass effect in the whole rapidity range and in the ALICE muon spectrometer acceptance as a function of p_T in Pb-Pb collisions at 5.5 TeV for the 0-10% most central class.

To expose the mass influence on the computations of the energy loss, Fig. 7.3 portrays its effect on the nuclear modification factor of muons from beauty decays in the whole rapidity range and in the ALICE muon spectrometer acceptance. Calculations for $\widehat{q} = 25$ and 100 GeV^2/fm are shown. An overall suppression of around a factor 4 is observed at high-p_T for muons from beauty decays. The relevance of the mass (dead cone effect) is evident at low-p_T.

The results obtained with this framework for the single muon p_T spectra with and without heavy quark energy loss in the whole rapidity range and in the ALICE muon spectrometer acceptance are presented in Fig. 7.4 for the 0-10% most central class. On the left-hand plots the various contributions are unveiled. Solid lines show the spectra without energy loss, and short- and long-dashed lines the computations for $\widehat{q} = 25$ and 100 GeV^2/fm respectively. The right-hand figures present only the global single muon spectra. ***Estimations indicate that the b- and W-muons crossing point shifts down in transverse momenta by*** 5 ***to*** 7 ***GeV/c. Therefore, accurate theoretical predictions of the single muon spectra or p-p data at the same energy would allow to experimentally perform such observation which may sign medium-induced effects on heavy quark production.***

Besides there are different manners to exploit single muon spectra in order to probe beauty and charm energy loss in a hot and dense medium. Below we discuss what information could bring the nuclear modification factor, the central-to-peripheral nuclear modification ratio and the proper muon yield ratios.

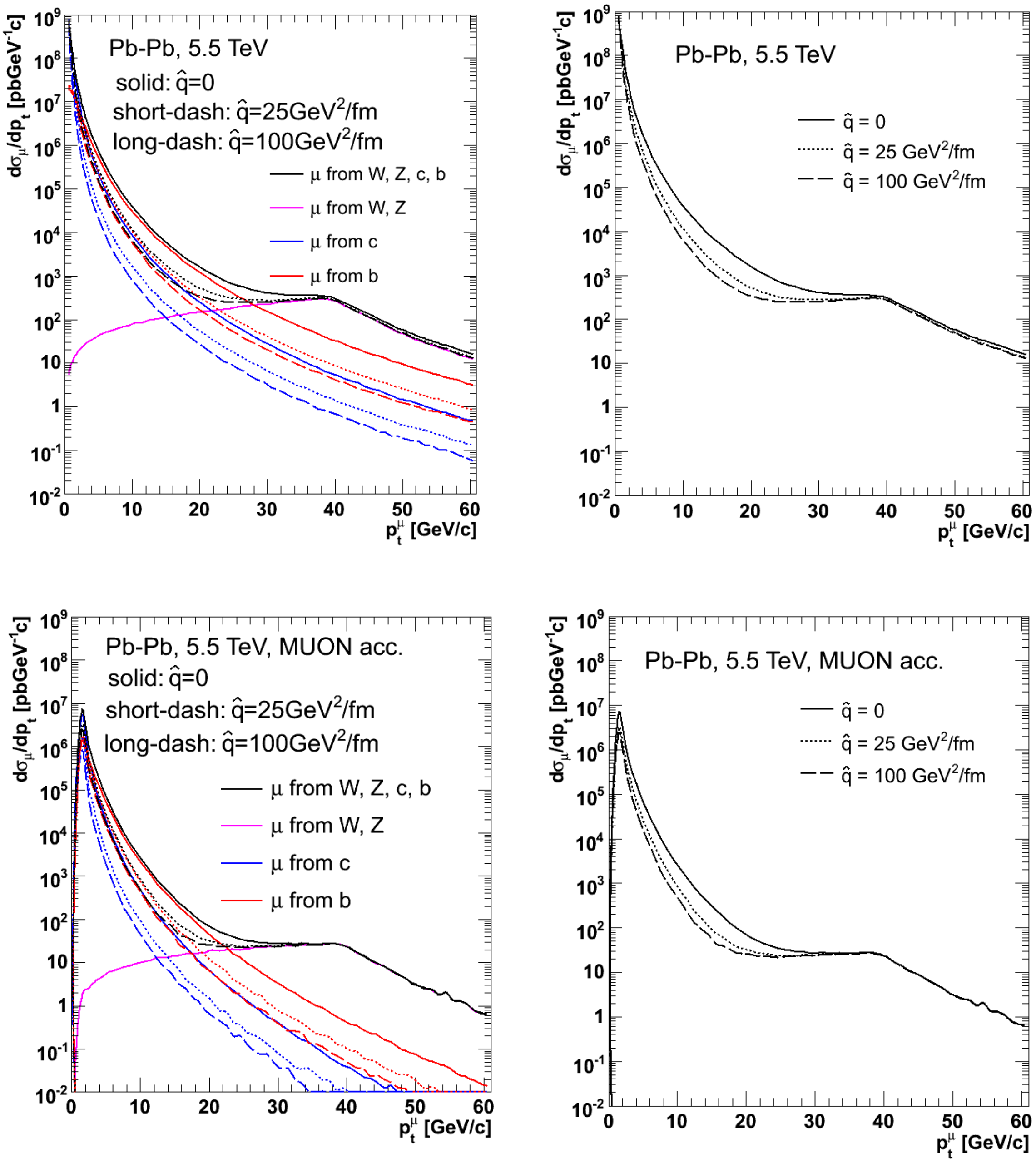

Figure 7.4: Energy loss calculation for the nucleon-nucleon differential production cross-section of single muons in Pb-Pb collisions at 5.5 TeV in the whole rapidity range (upper plots) and in the ALICE muon spectrometer acceptance (bottom plots) for the 0-10% most central class.

7.4.1 Nuclear modification factor: R_{AA}

The nuclear modification factor is defined as the invariant yield ratio in nucleus-nucleus (AA) versus nucleon-nucleon (NN) collisions, and is normalized to the nucleon-nucleon reference by dividing by the mean number of nucleon-nucleon interactions in a AA reaction ($\langle N_{coll} \rangle_{AA}$)

$$R_{AA}(p_T, \eta) = \frac{\left(1/\langle N_{coll} \rangle_{AA}\right) \cdot \left(d^2N/dp_T d\eta\right)_{AA}}{\left(d^2N/dp_T d\eta\right)_{NN}} . \tag{7.16}$$

p-p collisions are commonly used as the NN reference and $\langle N_{coll} \rangle_{AA}$ is usually computed in a Glauber model like basis (see Appendix D). R_{AA} is close to unity when there exists no difference between the production in AA and NN collisions, i.e. when there are no medium-induced effects. In opposition, $R_{AA} > 0$ ($R_{AA} < 0$) reveals an increase (decrease) of the invariant yield with respect to the reference and point out medium-induced effects. Unfortunately medium-induced effects do not only mean effects caused by the formation of a dense and hot matter. So it is extremely important to also check what happens in proton-nucleus collisions to control cold nuclear effects, i.e. the effects of PDF shadowing.

Cold nuclear matter effects

It is interesting to estimate which are the expectations of the single muon nuclear modification factor shape at $\sqrt{s_{NN}} = 5.5$ TeV with this model. Fig. 7.5 exposes our calculation results in the whole rapidity range (upper figures) and in the ALICE muon spectrometer acceptance (bottom figures) for the most central 0-10% Pb-Pb collisions. Solid curves correspond to the calculations without any energy loss. One might observe that the lines position differ from unity. In the whole rapidity range for beauty-decays $R_{AA}(b \to \mu) \sim 1.1$, for charm-decays $R_{AA}(c \to \mu) \sim 1.05$, and for W- and Z-decays $R_{AA}(W \to \mu) \sim 0.9$ at high-p_T. This is what we expect from EKS98 shadowing parameterization. In Tab. 7.1 we qualitatively report the shadowing factor for the different species. We saw that heavy quarks shadowing depends strongly on the interaction energy transfer, i.e. on the transverse momenta, and we found $C_{shad}(y = 0, p_T = 30; HQ) \sim 1.1$ for them, which is in accord to the observed $R_{AA}(HQ)$. On the contrary, on weak bosons production the energy transfer is approximately constant around their mass. A mean shadowing factor of $\langle C_{shad}(W, Z) \rangle \approx 0.9$ was estimated, in agreement to what is displayed in Fig. 7.5. In the muon spectrometer acceptance the beauty and charm R_{AA} diminish. Our calculation at high-rapidity gave $C_{shad}(y = 3, p_T = 30; HQ) \approx 0.9$ seemingly in accord with the plot within statistical fluctuations. The muon pattern from weak bosons at high-rapidity presents variations around its mean value, 0.9. It is superior than 0.9 for $p_T \lesssim 30$ GeV/c and for $p_T > 30$ GeV/c it is smaller than 0.9. A plain explanation resides on the fact that to produce a muon from W decays at high-rapidity a large (small) value of the Bjorken-x of the valence (sea) quark is required. This value must increment (diminish) to generate larger p_T muons. Thus the probed Bjorken-x value of the valence quarks belong to $x \gtrsim 0.1$, the shadowing humpback region. While the sea quark enter in a Bjorken-x range where the shadowing is approximately constant. Hence, the valence quark is first situated in the anti-shadowing region (then $R_{AA} \gtrsim 0.9$) and with the increase of the muon p_T falls steeply in the shadowing domain (then $R_{AA} \lesssim 0.9$).

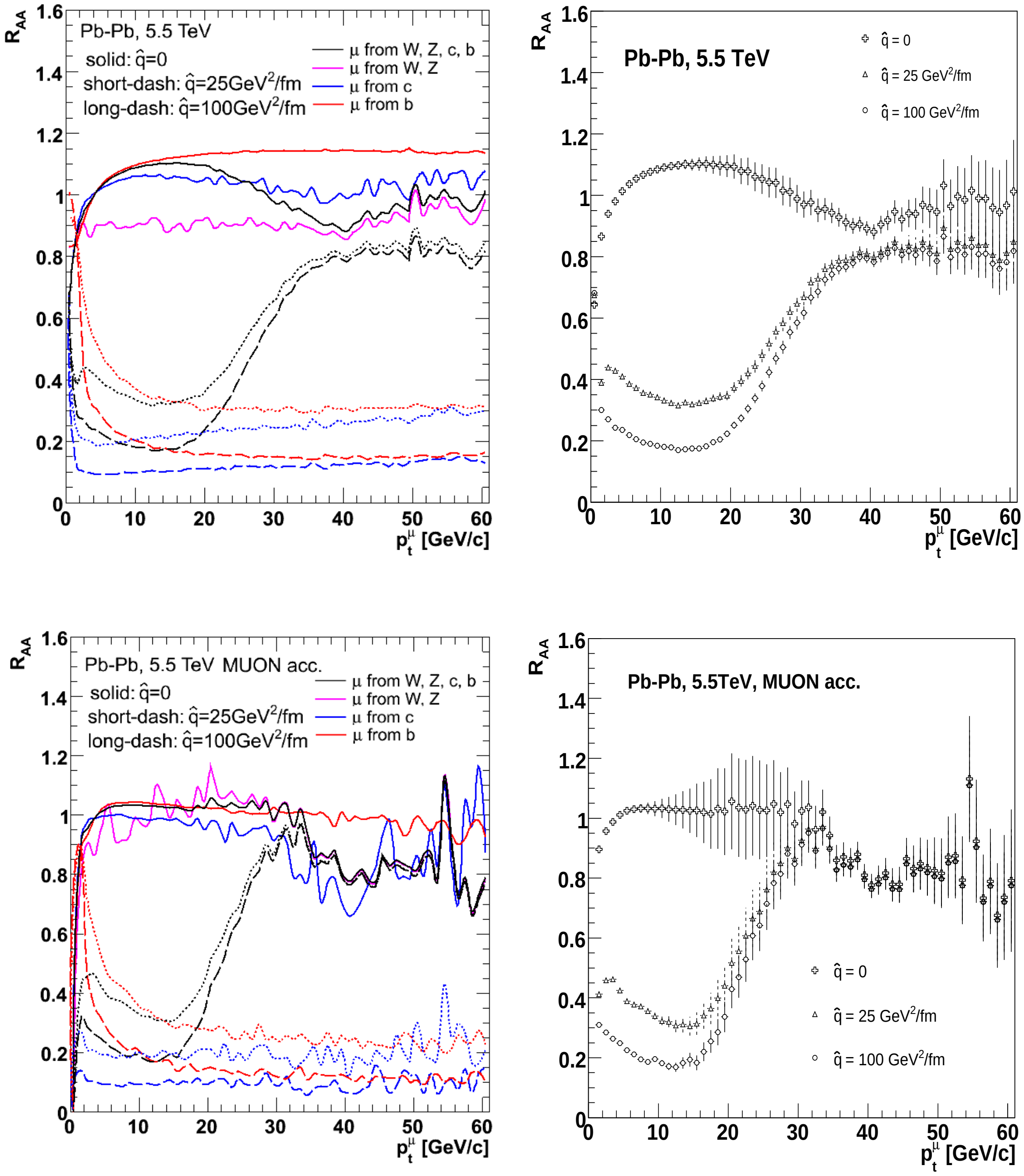

Figure 7.5: Energy loss calculation for the single muon nuclear modification factor for the most central 0-10% Pb-Pb collisions at 5.5 TeV in the whole rapidity range (upper figures) and in the ALICE muon spectrometer acceptance (lower figures). Note that the error bars are just indicative of the calculation uncertainties due to lack of statistics in the simulations. They are not significant neither as statistical nor as systematical errors.

Hot nuclear matter effects

In Fig. 7.5 the results concerning energy loss are displayed with short- and long-dashed lines for the two values of $\widehat{q}$. In the low p_T interval the suppression of charm and beauty quarks differ due to their mass. At intermediate and large p_T the mass does not affect the results, which is commonly interpreted as the beauty and charm quarks behave like massless quarks. Calculations indicate that the heavy quark muon yield would be reduced by a factor from 2 to 4 for $p_T \sim 10$ GeV/c (from 3 to 6 for $p_T \sim 40$ GeV/c). ***The overall muon yield would then be suppressed by about a factor of*** 2-4 ***in the*** $5 \lesssim p_T \lesssim 20$ ***GeV/c range, where heavy quark contribution prevails. Then it rapidly increases in the*** $20 \lesssim p_T \lesssim 35$ ***GeV/c interval and after reaches a plateau at around*** $R_{AA} \sim 0.8$***. For*** $p_T \gtrsim 35$ ***GeV/c its sensitivity to in-medium parton energy loss is of little importance. This*** p_T ***domain can consequently be used as medium-blind reference.*** If data reproduces the pattern in this interval, it would mean that cold nuclear effects, at least for weak bosons production, are under control.

7.4.2 Central versus peripheral nuclear modification factor: R_{CP}

As we just discussed, the difficulty to interpret the nuclear modification factor comes from the fact that also cold nuclear effects are involved. Hence, in a cunning view, the central to peripheral nuclear modification factor is often defined by the invariant yield ratio in central and peripheral collisions, both normalized to the NN reference by the mean number of nucleon-nucleon collisions in their respective centrality classes

$$R_{CP}(p_T,\eta) = \frac{\left(1/\langle N_{coll}\rangle_{Central}\right) \cdot \left(d^2N/dp_T d\eta\right)_{Central}}{\left(1/\langle N_{coll}\rangle_{Peripheral}\right) \cdot \left(d^2N/dp_T d\eta\right)_{Peripheral}} . \tag{7.17}$$

This definition is advantageous as we do not need to have the p-p data at 5.5 TeV available to perform such a calculation. In a first approximation, cold nuclear effects are expected to be equal in central and peripheral collisions[5] [6] then in their ratio they cancel out. The disadvantage is that larger statistics are required. At RHIC it was used, between others issues, to confirm π^0 suppression in central Au-Au collisions.

We decided to estimate it for the 0-10% most central and 40-70% peripheral collisions in order to maximize statistics (see Sec. 6.2.1 and in particular Tab. 6.4 for the expected muon yields in the ALICE muon spectrometer). Fig. 7.6 presents our R_{CP} results with and without including energy loss at 5.5 TeV. ***We conclude that in the*** 0-10% ***most central collisions the invariant yield might be reduced with respect to the*** 40-70% ***peripheral collisions by a factor*** 2-3 ***in the intermediate*** p_T ***range (***$5 \lesssim p_T \lesssim 20$ ***GeV/c). After that it increases sharply between*** $(20, 35)$ ***GeV/c until it attains a plateau governed by the relative proportion of weak bosons and heavy quarks.***

---

[5] As a matter of fact, recent studies [K$^+$07] indicate that the density of protons and neutrons in Pb nuclei vary with the radius (distance to the nuclear center). We could expect a higher density of protons (neutrons) in the Pb nuclei nuclear center (periphery). Thereby one could guess that a relatively larger fraction of protons (neutrons) would interact in central (peripheral) collisions, which could have an impact on the probed PDFs and shadowing region, and may also affect the expected W boson produced charge asymmetry. However this effect is small and we consider that its influence, if any, should not affect our conclusions.

[6] According to references [EKKV99, EKKV00] the shadowing depends on the reaction centrality.

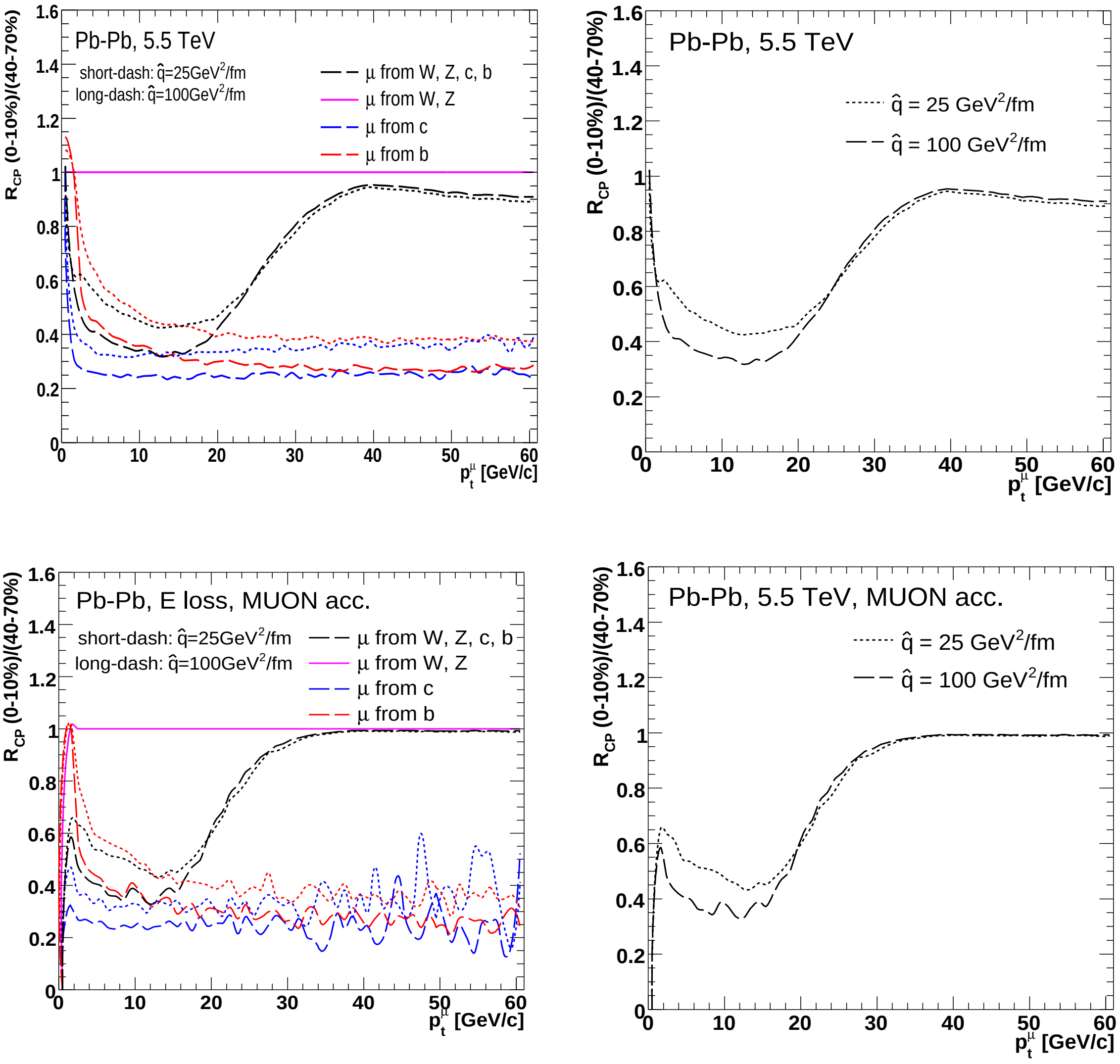

Figure 7.6: Energy loss calculation for the central-to-peripheral (0-10% to 40-70% centrality classes) single muon nuclear modification factor in Pb-Pb collisions at 5.5 TeV in the whole rapidity range (upper plots) and in the ALICE muon spectrometer acceptance (bottom plots).

7.4.3 Muon yield ratios

Despite of the mentioned experimental interest of the R_{AA} and R_{CP} factors, the most direct experimental measurement we could ever do is the proper single muon invariant yield. Hence, we could compare the amount of muons in two transverse momentum intervals, one governed by heavy quarks (e.g. $15 \lesssim p_T \lesssim 20$ GeV/c) sensitive to the in-medium influence, and another where weak bosons prevail (e.g. $30 \lesssim p_T \lesssim 40$ GeV/c), the in-medium blind reference. ***Thereby, we can define a parameter, S, as the ratio of single muon invariant yields in these p_T ranges:***

$$\mathcal{S} = \frac{N_\mu(15,20)}{N_\mu(30,40)} \tag{7.18}$$

$\mathcal{S}$ will then carry information on nuclear effects (both cold and hot nuclear effects). Thus we could expect $\mathcal{S}$ to be reduced in central Pb-Pb collisions with respect to theoretical calculations without hot nuclear effects. For this computation there is no need of the p-p data (in contrast to R_{AA}), larger statistics than for the R_{CP} would a priori be available (we can simply enlarge the studied centrality class), and we could evade the possible experimental bias on the $\langle N_{coll} \rangle$ calculation (needed on both R_{AA} and R_{CP} determination). However, with it we do not get rid of cold nuclear effects such as shadowing, because it varies with p_T and differs for heavy quarks and weak bosons as we previously discussed. Thus it will then be important to evaluate the cold nuclear effects contribution by studying p-A collisions.

From the analysis done in Chapter 6 we have estimated $\mathcal{S}$ to be about 4.8 ± 0.1 (stat) in the ALICE muon spectrometer in absence of the final state effects for minimum bias Pb-Pb collisions. ***If energy loss scenarii are verified, a reduction factor of the order of 3 for $\hat{q} = 25$ GeV^2/fm and 5 for $\hat{q} = 100$ GeV^2/fm could be expected in Pb-Pb 0-10% central collisions*** with respect to theoretical calculations without energy loss.

7.5 Outlook: Z bosons in heavy ion collisions

As W bosons, Z bosons are suitable references to study in-medium properties. We previously exposed the interest of the Z-jet observable to probe the jet quenching phenomena (see Sec. 2). This signature should not be affected by the fact that muons from Z decays loose about $\sim 1\%$ of their energy crossing a QGP; because this might at most influence the dimuon invariant mass by $\sim$ 1-2%, being negligible in this concern. Nevertheless, here we shall concentrate on the information that could be brought by the in-medium modification of Z decays. We do not intend to list and develop all the possible manners in which they can be exploited, we just attempt to describe two possibilities.

7.5.1 Z beauty decay channel

As exposed in Chapter 6 (Sec. 6.1.1) Z bosons have a large branching ratio to $b\bar{b}$ pairs, about 15%. The b-quarks from Z decays might then be formed in the first fm/c and might be sensitive to the in-medium properties before they fragment. For instance we can consider muons or electrons as the final products. If experimentally we are able to tag leptons from b-quarks[7], we should be able to reconstruct the $b\bar{b}$ invariant mass. Then, through kinematics analysis cuts we might be able to unveil the Z invariant mass peak from the continuum of $b\bar{b}$ pairs. Its invariant mass being precisely known, if b-quarks suffer in-medium energy loss, the Z peak of the $b\bar{b}$ invariant mass spectra would be modified[8]. We could then investigate the experimental apparatus sensitivity to this probe.

Although it is a very interesting probe, we must admit that it is first an experimental challenge to apply b-tagging techniques to nucleus-nucleus collisions. Furthermore, we per-

---

[7] The b-tagging technique basically consists on a cut on the distance of closest approach (DCA) to the interaction vertex. B-mesons travel a longer distance than D-mesons before they decay.

[8] Note that both the continuum and the Z peak of the $b\bar{b}$ invariant mass spectra should be modified by in-medium energy loss.

formed a kinematics analysis of the $b\bar{b}$ invariant mass, and our preliminary results indicate that the necessary kinematic cuts to unveil the Z peak appear extremely challenging[9]. Figure 7.7 portrays the obtained $b\bar{b}$ invariant mass applying no cuts and considering the continuum and the Z production; the difficulty to unmask the Z peak becomes obvious. However, such techniques seemed to be appropriate at Tevatron energies [Dor98, D006].

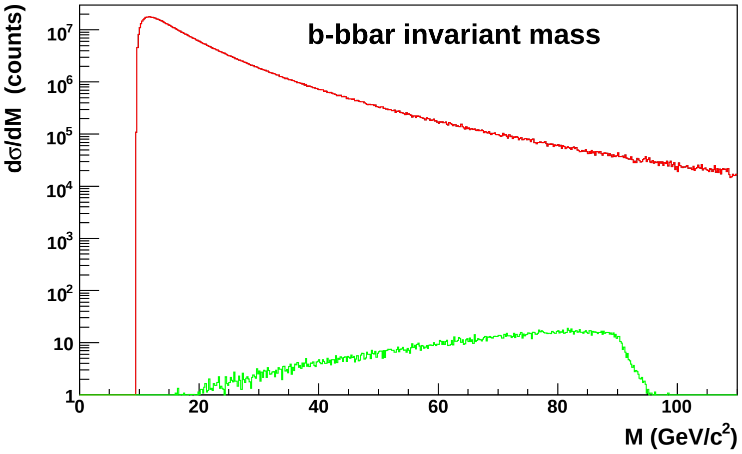

Figure 7.7: Preliminary $b\bar{b}$ invariant mass spectra in Pb-Pb collisions at 5.5 TeV in arbitrary units. Contributions from the continuum and from Z b-decays in the whole phase space are plotted.

7.5.2 Z radiative decays

We understand as radiative decays those where a photon is emitted. In Z dimuon decays, the radiative decay would imply $Z \to \mu^+ \mu^- \gamma$. If a Z boson decays in-medium, the emitted muons might suffer bremsstrahlung, the relative production cross-section of Z radiative decays with respect to non-radiative decays would then increase (with regard to expectations in a cold nuclear medium).

In Sec. 7.3 we argued that the probability that a muon is subjected to bremsstrahlung radiation is related to the interaction length of elastic scatterings λ, and we evaluated $\lambda \sim 10$ fm. We can estimate the probability that at least one of the muons suffers one scattering as the sum of the probabilities that one of those interact and the other does not plus the probability that both interact. That is $P = P_1 \times (1 - P_2) + (1 - P_1) \times P_2 + P_1 \times P_2$, where $P_i = 1 - e^{-L_i/\lambda}$. The in-medium length traversed by the muons L_i is calculated in a Glauber-model-based picture considering a realistic reaction geometry via the collision nuclear overlap zone (see App. D). Fig. 7.8 displays as example the results of the calculation for the correlation of the lengths crossed by the muons in the most central 0-10% Pb-Pb collisions, and the associated interaction probability. This computation suggests that the interaction probability of at least one of

---

[9] The main kinematics cuts applied at Tevatron to disentangle the Z peak are related to the relative angle of the $b\bar{b}$ pairs, the minimum p_T of the parton, and the pair invariant mass.

the muons is about 60%; in 60% of the cases one of the muons will undergo one elastic scattering. The probability that in this scattering a bremsstrahlung occurs is related to α_{em}, it is roughly of about 1%; which would imply a 0.6% probability of in-medium bremsstrahlung. More accurate estimates of the probability of in-medium bremsstrahlung as a function of L are in progress, but at the present time there are still no results available [PMPC07]. However, in order to employ such probe to study the QGP formation, a good understanding of those processes in a cold nuclear medium would be necessary.

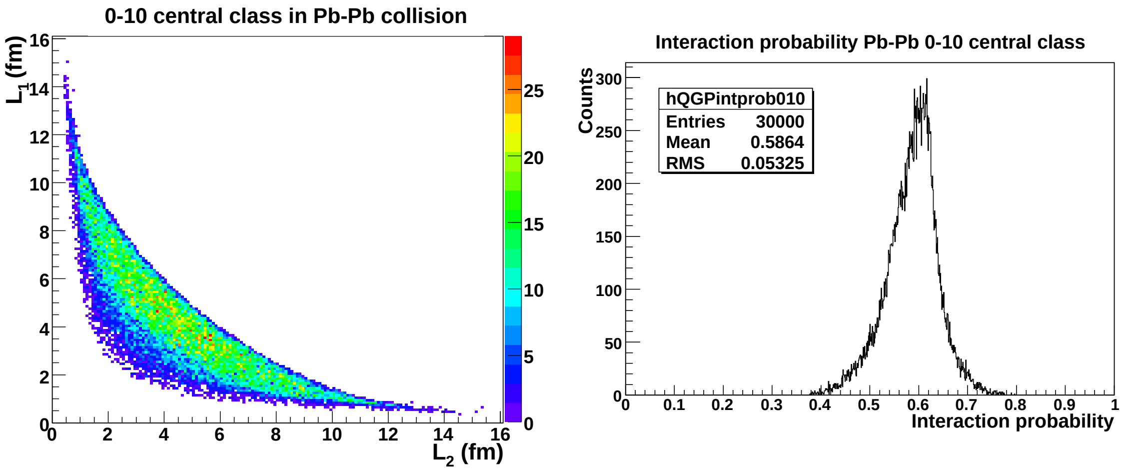

Figure 7.8: Right figure presents the correlation of the lengths traversed by the muons in Pb-Pb 0-10% central collisions. The left plot indicates the associated interaction probability distribution.

Conclusions

The strongest arguments prove nothing so long as the conclusions are not verified by experience. Experimental science is the queen of sciences and the goal of all speculation.

R. Bacon

A conclusion is the place where you got tired of thinking.

A. Bloch

This thesis has been devoted to exploit the expected performances of the ALICE muon spectrometer extending the previous studies up to high transverse momentum, in the region dominated by heavy-quark and gauge boson muonic decays, and investigating weak bosons measurement feasibility and utility in nucleus-nucleus collisions.

Detailed studies of the apparatus capabilities have shown that it should be able to measure muons up to a higher approximative limit of 100 GeV/c (with a resolution of about 10% limited by the detector spatial resolution). The acceptance and efficiency corrections have been discussed and calculated for J/Ψ and high-p_T single muons. The averaged acceptance correction for J/Ψ produced in the rapidity window of the muon spectrometer has been evaluated to be about 40% (5% with respect to the whole phase space) and the mean global efficiency for J/Ψ with the PairUnlineLPt trigger is around 58% for p-p collisions at 14 TeV. For single muons the efficiency has been shown to be approximately constant for $p_T \in (1, 60)$ and about 97% (76%) with the SingleLPt trigger for a flat (realistic) muon distribution. Moreover, a factorization approach has been adapted and developed for this experimental setup. It has been demonstrated useful to unravel the different contributions to the global efficiency and to realize the goodness of simulations with data, while enabling an easier intrinsic chamber efficiency determination. The results obtained with this factorization approach have shown that the apparatus dead zones (by construction) and the intrinsic efficiency will contribute the most to the global efficiency. In addition, with this method we proved that the track reconstruction algorithm is ready for data-taking.

Weak boson production at LHC and their measurement with this experimental setup have been presented. On the one hand, the high-p_T single muon spectra showed to be an appropriate tool to measure W production. Different sources contribution to the spectra have been studied. The distribution is dominated by charm production for $p_T \in (2, 4)$ GeV/c, then by beauty up to $p_T \sim 30$ GeV/c, and later the W contribution prevails. The estimates indicate that about $9 \cdot 10^4$, $2 \cdot 10^4$, 10^4 muons should be reconstructed from W decays in p-p, p-Pb and Pb-Pb collisions respectively during one year of nominal integrated luminosity. Isospin effects in the colliding systems introduce an asymmetry on the positive and negative W production. In addition, parity violation on W decays influences the distribution of positive and negative muons. The calculations have demonstrated that this muon charge asymmetry is not masked neither by beauty nor by charm decayed muons, and can be observed in the ALICE muon spectrometer, being a clear indication of the W origin. On the other hand, Z bosons can be measured via the unlike-sign dimuon invariant mass spectra. Preliminary studies suggest that those measurements could be possible in p-p, p-Pb and Ar-Ar collisions with an expected statistics of about $2 \cdot 10^3$, 10^3 and $2 \cdot 10^3$ reconstructed muon pairs from Z decays respectively, while the estimated $2 \cdot 10^2$ and $3 \cdot 10^2$ reconstructed muon pairs in Pb-Pb and Pb-p collisions demand to accumulate statistics of several runs to perform such measurements. In sum, it has been exposed that weak bosons production could be studied for the first time in heavy-ion collisions at LHC and that the ALICE muon spectrometer can perform such measurements.

If we concentrate on the study of heavy-ion collisions, we shall bear in mind that high-p_T muons mainly come from weak boson and heavy quark decays. As weak bosons are massive, they are formed in the early times of the reaction and decay shortly; it is then their decay products which traverse the medium formed in the collision. A discussion of the QED effects on high-p_T muons have led us conclude that the energy loss through a 10 fm/c QGP would only be of about 1%. Muons from weak decays could then be considered as medium-blind references. On the contrary, charm and bottom quarks are also produced early and traverse the medium during 1-3 fm/c. They might be affected by the QGP due to medium-induced gluon-radiation. Heavy quark in-medium energy loss calculations indicate that the single muon spectra would be suppressed by a factor 2-4 in the most central 0-10% Pb-Pb collisions at 5.5 TeV in the intermediate-p_T of 5-25 GeV/c; while for $p_T > 35$ GeV/c no suppression is expected (weak boson decays being predominant). The estimates evidence that the b- and W-muons crossing point shifts down in transverse momenta by 5 to 7 GeV/c in the most central 0-10% Pb-Pb collisions at 5.5 TeV.

Appendix A

Commonly used abbreviations

- *AGS: Alternate Gradient Synchrotron;*
- *BNL: Brookhaven National Laboratory;*
- *CERN: European Council for Nuclear Research;*
- *CC: Centrality Class;*
- *CPC: Cathode Pad Chambers;*
- *CTP: Central Trigger Processor;*
- *DCA: Distance of Closest Approach;*
- *EW: Electroweak;*
- *Fermilab: Fermi National Accelerator Laboratory;*
- *GMS: Geometry Monitoring System;*
- *HI: Heavy Ion;*
- *HIC: Heavy Ion Collisions;*
- *HQ: Heavy Quark;*
- *IP: Interaction Point;*
- *ITS: Inner Tracking System;*
- *LEP: Large Electron Positron collider;*
- *LHC: Large Hadron Collider;*
- *LINAC: LINnear ACcelerator;*
- *LO: Leading Order;*
- *MIP: Minimum Ionizing Particle;*
- *MRPC: Multi-gap Resistive Plate Chambers;*
- *MWPC: Multi-Wire Pad Chambers;*
- *NLO: Next to Leading Order;*
- *NN: Nucleon-nucleon;*
- *NNLO: Next to Next to Leading Order;*
- *PID: Particle Identification;*
- *PS: Proton Synchroton;*
- *QCD: Quantum ChromoDynamics;*
- *QED: Quantum ElectroDynamics;*
- *QGP: Quark Gluon Plasma;*
- *RHIC: Relativistic Heavy Ion Collider;*
- *RPC: Resistive Plate Chambers;*
- *SPS: Super Proton Synchroton;*
- *TeVaTron: The TEVATRON is Fermilab's super-conducting synchrotron that is four miles in circumference;*
- *TPC: Time Projection Chamber.*

A few experiments acronyms:

- *ALICE: A Large Ion Collider Experiment;*
- *ATLAS: A Toroidal Large ApparatuS;*
- *BRAHMS: Broad RAnge Hadron Magnetic Spectrometers Experiment at RHIC;*
- *CDF: The Collider Detector at Fermilab;*
- *CMS: Compact Muon Solenoid;*
- *LHCb: The Large Hadron Collider beauty experiment;*
- *PHENIX: Pioneering High Energy Nuclear Interaction eXperiment;*
- *PHOBOS: Experiment at RHIC.*
- *STAR: Solenoidal Tracker At RHICH.*

Appendix B

The front absorber influence on the measured track

As explained in Sec. 3.2.3 the mission of the front absorber is to reduce the background from pion and kaon decays in the tracking chambers in order to identify muons. It is made of high density materials such as the Pb and low density materials such as the C. Charged particles crossing the absorber lose energy and might suffer multiple Coulomb scattering. Below we examine those processes in more detail, preventing tracks with momenta lower than 4 GeV/c to reach the muon spectrometer.

B.1 Energy loss

A charged particle passing through a material suffers the electromagnetic interaction between its charge and that of the material bound electrons. Thus it loses energy through many collisions with those bound electrons (by ionization). The energy lost per unit length of material traversed is called stopping power, and the ionization stopping power is characterized by the Bethe-Bloch formula [Wil05]. Moreover, a charged particle moving through the field of atomic nuclei radiates photons and suffers deceleration (by radiative processes). At very high energies the latter phenomenon is predominant and at intermediate energies the energy loss by ionization is the most important process. As an example, Fig. B.1 presents the stopping power of muons in copper, and Fig. B.2 display the muon critical energy for the different chemical elements, defined as the energy at which radiative and ionization loss rates are equal. From the fits exposed in Fig. B.2 we can calculate the muon critical energy in Pb to be about 140 GeV and in C to be around 1.06 TeV. Since the front absorber is mainly composed of C, in the region of interest (p_T from 0 to 100 GeV/c) the ionization energy loss will be predominant, even though the probability of bremsstrahlung for high p_T muons begins to be noticeable in the lead region of the absorber, close to the first tracking station. This justify that in the track reconstruction algorithm just the energy loss by ionization in the absorber has been considered so far for track momenta (up to $p_T \sim 20$ GeV/c). However in our particular case we go up to higher momenta, where the radiative processes begin to have an influence. GEANT includes those effects properly, so in the simulations they are treated correctly and they are thus incorporated into our computed efficiency, but not in the tracking algorithm (at the present time). Further studies are necessary to discern if it would

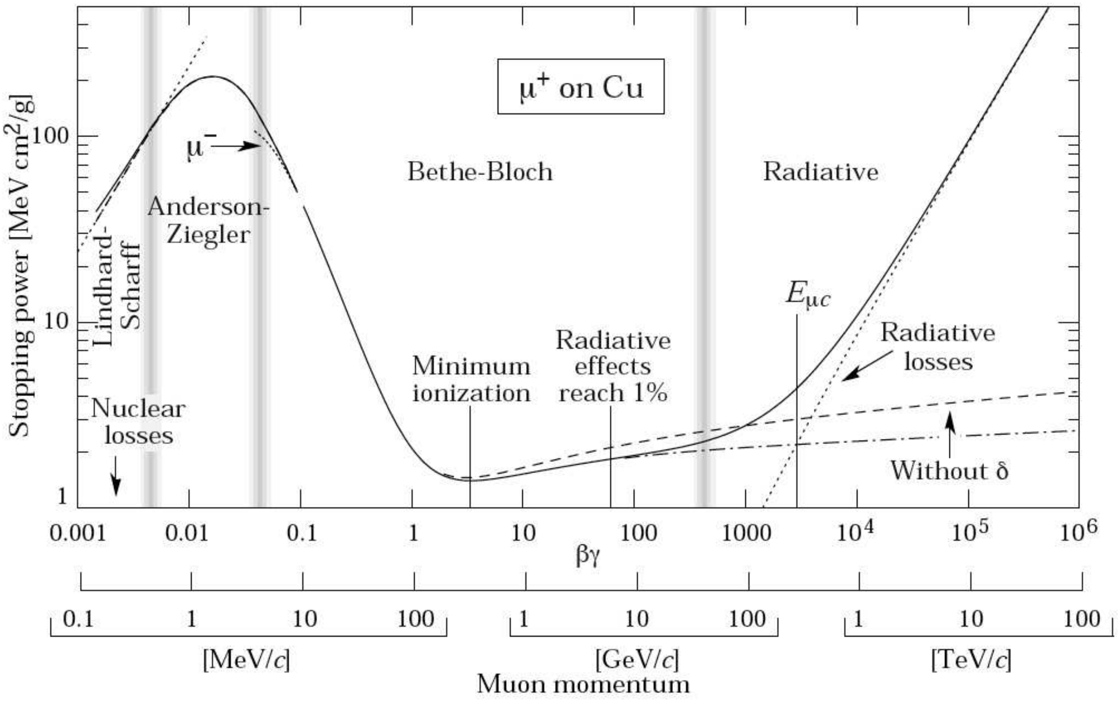

Figure B.1: Stopping power for positive muons in copper as a function of $\beta\gamma = p/Mc$ [Y+06]. Solid curves indicate the total stopping power.

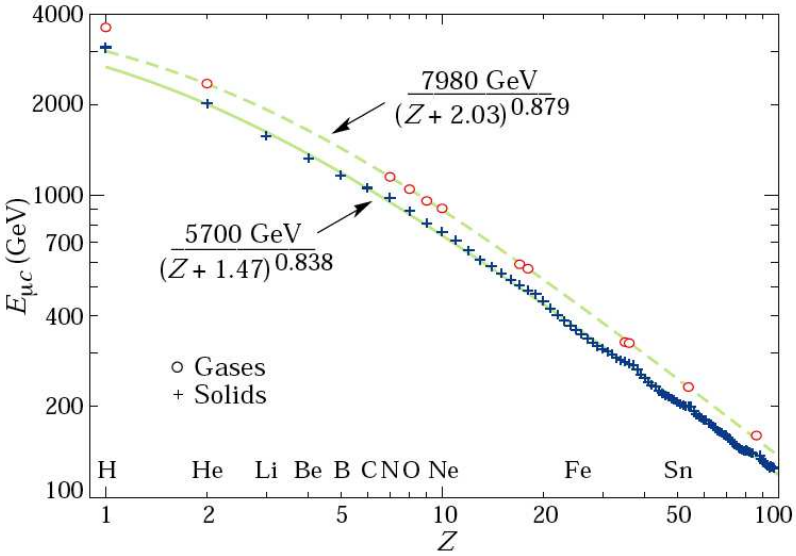

Figure B.2: Muon critical energy for the chemical elements [Y+06]. It is defined as the energy at which radiative and ionization energy loss rates become equal.

be better to correct for bremsstrahlung energy loss via the reconstruction algorithm or if it should just be considered as an inefficiency source.

B.2 Straggling

The energy lost by a particle traversing a medium is of probabilistic nature and, as such, it shows fluctuations around the average values presented in the previous section. We usually refer to this fluctuations as straggling [Wil05]. In very thick absorbers, when the number of collisions is large ($N_{coll} \rightarrow \infty$), the distribution of energy loss is expected to be governed by a Gaussian probability distribution. For thin absorbers the Landau probability distribution describe the process. We can not correct the measured track momenta for this effect, thus it contributes to momenta resolution. If we do consider that the straggling effect does not depend on the initial particle energy, the momenta resolution due to straggling will be determined by the σ of the distribution. The resolution will then be given by a constant that we denote A

$$(\delta P)_{Stragg} \approx A \qquad \longrightarrow \qquad \left(\frac{\delta P}{P}\right)_{Stragg} \approx \frac{A}{P}\,.$$

B.3 Multiple Coulomb scattering

Furthermore, charged particles passing through the absorber and the detection planes might suffer from multiple Coulomb scattering, that might deviate their trajectories. Remark that multiple scattering in the front absorber only affects the initial muon direction measurement. We can partly account for it via the measurement of the interaction vertex position with the SPD detector. In any case, for small angles the Gaussian approximation is valid [Leo93] and the angular width can be described by [Y+06]

$$(\delta\theta)_{Scatt} = \frac{13.6\,\mathrm{MeV}}{\beta c P} z\sqrt{x/X_0}\left(1 + 0.038\, ln\left(\frac{x}{X_0}\right)\right),$$

where βc and z are the velocity and charge of the incident particle and x/X_0 is the thickness of the scattering medium in radiation lengths. From this relationship we can guess the multiple scattering influence on the the measured track momenta to be directly proportional with a proportionality constant B

$$(\delta\theta)_{Scatt} \propto \frac{1}{P} \qquad \longrightarrow \qquad \left(\frac{\delta\theta}{\theta}\right)_{Scatt} \propto \left(\frac{\delta P}{P}\right)_{Scatt} \propto B\,.$$

Appendix C

Parity violation on W decays

Here we outline the effect of parity violation on the angular distribution of W decayed leptons. For this we shall concentrate on the helicity conservation in W bosons production and decay, helping out to interpret the results presented in Chapter 5.

The weak interaction only couples left-handed quarks to right-handed anti-quarks. Following the LO diagram, W bosons will be polarized in the direction of the anti-quark momentum. W bosons emitted at high rapidities will be produced in parton-parton collisions with $x_1 \lesssim 1$ and $x_2 \ll 1$, and partons with $x \sim 1$ will probably be quarks[1]. Therefore, W bosons will tend to be polarized in the opposite direction to its momentum (they will tend to be left-handed). Concerning the decay products, the fact that antineutrinos are right-handed will favor the emission of leptons in the opposite direction of the W^- polarization (i.e. in its momentum direction). On the contrary, the W^+ will mainly emit anti-leptons in its polarization direction (i.e. in opposite direction to its momentum). Visually, Fig. C.1 presents an sketch of W muonic decays, showing that on W decays leptons should be left-handed and anti-leptons right-handed. Figs. C.2 and C.3 represent W production and decay at high-rapidity, in the case $J = -1$. Single lines represent momenta direction and magnitude, the larger the more important. Double lines indicate the helicity state, W bosons being left-handed, as we just exposed. Observe that in the case of W^- decay, angular momentum and helicity conservation push anti-leptons to be produced in its momentum direction (op-

Figure C.1: Sketch of W muonic decay in its rest frame.

---

[1] For instance, W bosons emitted at rapdity $y = 3$ in proton-proton collisions at 14 TeV will be produced by parton collisions with $x_1 = 0.1$ and $x_2 = 3 \cdot 10^{-4}$, and the PDF for quarks is around 5 times larger than the PDF for anti-quarks at $x = 0.1$.

posite to its polarization). While on W^+ decay the situation is more complex. In that case momentum conservation tends to boost leptons in the W^+ direction but helicity conservation pushes them on the opposite sense. In this respect, in W muonic decays, W^- bosons produced at high rapidities will preferably emit negative muons in its momentum direction (in its momentum reference frame) and W^+ bosons will preferably emit positive muons in the opposite direction to its momentum. For this reason, negative muons exhibit a wider rapidity distribution than positive muons. This effect is clearly seen in Pb-Pb collisions (see Figs. 5.13 & 5.14) where W^+ and W^- bosons present a similar rapidity distribution.

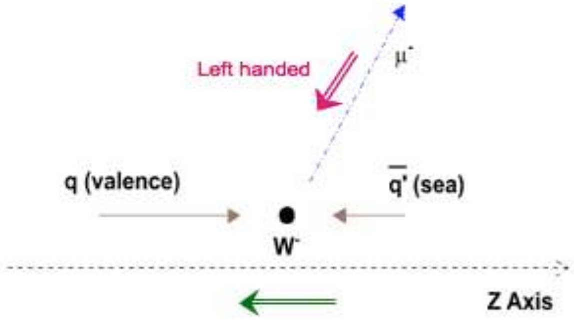

Figure C.2: Sketch of W^- production and muonic decay in its rest frame. Notice that the anti-neutrino has been ignored on that schema, but not its role.

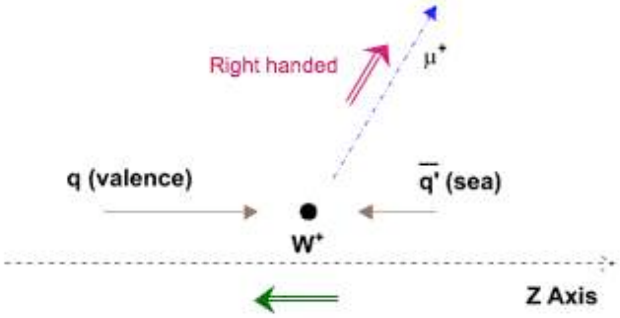

Figure C.3: Sketch of W^+ production and muonic decay in its rest frame. Notice that the neutrino has been ignored on that schema, but not its role.

Appendix D

Centrality determination: the Glauber model

D.1 Introduction

The geometry of heavy ion collisions can be described via the Glauber model as a simple superposition of incoherent nucleon-nucleon (NN) collisions, without taking into account any medium modification. The model introduced by R. J. Glauber [GM70, WS98] in order to analyse the dispersion suffered by protons colliding nucleus, was later adapted for nucleus collisions, and extensively used in high energy collisions. It uses the diffractive approximation[1] and is based in tree main points:

1. The nucleons are distributed following a known density distribution function $\rho(r)$, as a function of their radius, usually measured experimentally;
2. The nucleons travel in straight-line trajectories and their trajectory does not change while passing through the nucleus;
3. The nucleons interact with a nucleon-nucleon inelastic cross section, $\sigma_{NN}(\sqrt{s_{NN}})$, measured in p-p collisions, where $\sqrt{s_{NN}}$ is the energy available in the nucleon-nucleon (NN) center of mass.

The first item deals with the fact that nuclei are not with point like particles, but have a density distribution function. In the case of medium-and large-size nuclei, one considers the *Woods-Saxon distribution function* [Vog99],

$$\begin{aligned} \rho(r) &= \frac{\rho_0}{1+\exp(\frac{r-R}{a})}\,, \\ R &= 1.19\,A^{\frac{1}{3}} - \frac{1.61}{A^{\frac{1}{3}}}(\text{fm})\,, \end{aligned} \tag{D.1}$$

where, for the Au (Pb) case: $R = 6.38$ (6.624) fm, $a = 0.535$ (0.549) fm and $\rho_0 = 0.1693$ (0.1600) fm^{-3}. The distribution for the Au case is represented on figure D.1. The associated radii probability distribution is determined by $P(r)$ [M$^+$02]

$$P(r) = \frac{r^2}{1+\exp(\frac{r-R}{a})}\,.$$

---

[1] In this context, the diffractive approximation deals with the interaction-interference between nuclei and e.g. studies the p-N collisions analyzing the ”perturbation” or ”modification” of N due to p, studying the N spectrum modification when finds p as an obstacle in his way.

This distribution function is not valid for light nuclei. As an example, for the deuterium case we should use the *Hulthén distribution function* [M+02], which indicates the distance between the p and the n on the d, and permits to evaluate the nucleon radii as $\sim \frac{distance}{2}$ (Fig. D.2),

$$d(x) = x^2 \cdot \frac{x_0 \cdot x_1 \cdot (x_0 + x_1)}{2\pi(x_0 - x_1)^2} \cdot \left(\frac{e^{-x_0 x} - e^{-x_1 x}}{x}\right)^2, \tag{D.2}$$

where the parameters are $x_0 = 0.228\ \text{fm}^{-1}$ and $x_1 = 1.18\ \text{fm}^{-1}$.

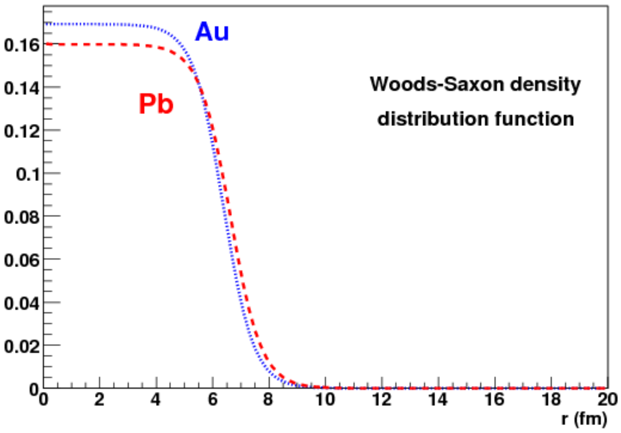

Figure D.1: Woods-Saxon nucleon density distribution function, for the Au and Pb nuclei.

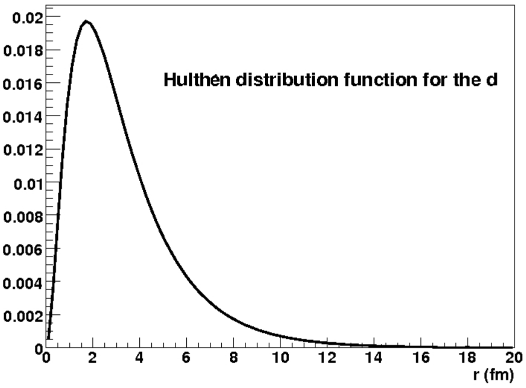

Figure D.2: Hulthén nucleon density distribution function, for the d nuclei.

The Glauber model is a geometrical model that considers that the nucleons travel in straight line trajectories (*eikonal approximation*), and are only deviated by nucleon-nucleon collisions. This model neglects the coulombian repulsion and the existing nuclear mean field. This hypothesis strongly simplify the analysis because a nucleon will only interact with the nucleons that will find in the collision straight line trajectory.

The last item remarks that nucleons interact independently, as an incoherent superposition of NN free collisions, cross section that can be measured in p-p collisions. So there is no correlation between different nucleon collisions.

On the other hand, while studying heavy nuclei collisions at ultra-relativistic energies, the relativistic effect of the Lorentz spatial contraction has to be considered. An A-B collision from the Glauber point of view can be schematically observed on Fig. D.3.

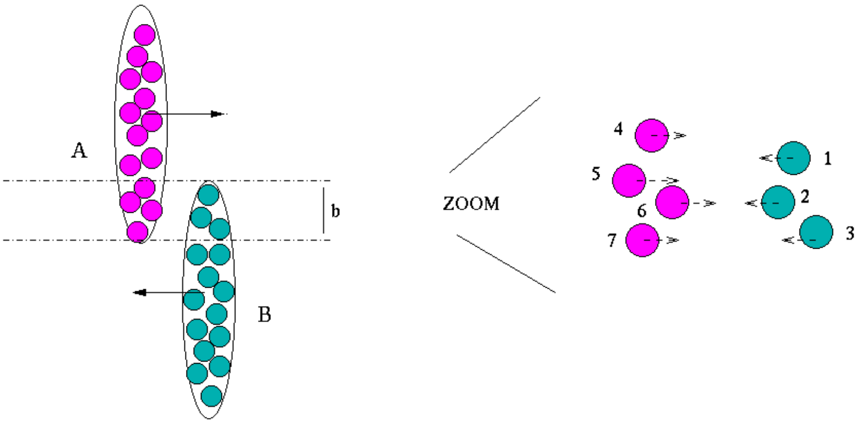

Figure D.3: Schema of a A-B collision from the Glauber model point of view.

From this point of view of the interaction, there are two important parameters to characterize the collision. The **number of nucleon-nucleon collisions** in the interaction, N_{coll}, and the **number of participant nucleons**, N_{part}, that indicates the number of nucleons that participate in at least one collision of the interaction. For instance, on Fig. D.3 there is $N_{part} = 7$ participant nucleons and $N_{coll} = 8$ nucleon-nucleon collisions, as nucleons 1 and 2 interact with three nucleons of A, and the nucleon 3 with two nucleons of A.

D.2 Formalism

D.2.1 Proton-nucleus (p-A) collisions

The Glauber formalism allows to express the p-A inelastic cross section in the eikonal approximation as a function of the corresponding NN inelastic cross section $\sigma_{NN}(\sqrt{s_{NN}})$ at the center of mass energy $\sqrt{s_{NN}}$ [d'E03].

$$\sigma_{pA} = \int \mathrm{d}^2\vec{b} \left[1 - e^{-\sigma_{NN}(\sqrt{s_{NN}})\cdot T_A(b)}\right], \tag{D.3}$$

where $\mathrm{d}^2\vec{b} = 2\pi\, b\, \mathrm{d}b$, and b is the impact parameter of the collisions (see Fig. D.3). The collision geometry is determined by $T_A(b)$, the *nuclear thickness function (or nuclear profile* *function)* of the nucleus A at an impact parameter b,

$$T_A(b) = \int_{-\infty}^{+\infty} \mathrm{d}z\, \rho_A(r)\,, \tag{D.4}$$

where $r = \sqrt{b^2 + z^2}$ and $\rho_A(r)$ is the *nuclear density function*; usually associated to the Woods-Saxon distribution function and normalized so that,

$$\int_0^{+\infty} 2\pi b\, \mathrm{d}b\, T_A(b) = A\,,$$

where A is the nucleus atomic number. As an example, Tab. D.1 presents the $T_A(b)$ values for p-Pb collisions and fixed b values.

b (fm)	$T_A(b)$ (fm^{-2})	b (fm)	$T_A(b)$ (fm^{-2})	b (fm)	$T_A(b)$ (fm^{-2})
0.0	2.12	7.0	$3.05\cdot10^{-1}$	14.0	$1.65\cdot10^{-6}$
1.0	2.09	8.0	$6.65\cdot10^{-2}$	15.0	$2.76\cdot10^{-7}$
2.0	2.02	9.0	$1.19\cdot10^{-2}$	16.0	$4.61\cdot10^{-8}$
3.0	1.88	10.0	$2.04\cdot10^{-3}$	17.0	$7.68\cdot10^{-9}$
4.0	1.67	11.0	$3.47\cdot10^{-4}$	18.0	$1.28\cdot10^{-9}$
5.0	1.34	12.0	$5.85\cdot10^{-5}$	19.0	$2.12\cdot10^{-10}$
6.0	$8.33\cdot10^{-1}$	13.0	$9.84\cdot10^{-6}$	20.0	$3.52\cdot10^{-11}$

Table D.1: Nuclear thickness function $T_A(b)$ obtained with the Glauber model for p-Pb collisions for different values of impact parameter b.

Once the nuclear thickness function is known, the p-A inelastic cross section can be evaluated. As an example, for RHIC energies, $\sqrt{s_{NN}} = 200$ GeV, and considering $\sigma_{NN} = 42$ mb [E+04]. One obtains for p-Au collisions:

$$\sigma_{pAu} \approx 167\, fm^2 = 1.67\, b\,.$$

And for LHC p-Pb collisions at $\sqrt{s_{NN}} = 8.8$ TeV, one obtains:

$$\sigma_{pPb} \approx 190.5\, fm^2 = 1.91\, b \qquad \text{for } \sigma_{NN} = 60\, mb\,,$$

$$\sigma_{pPb} \approx 196.4\, fm^2 = 1.96\, b \qquad \text{for } \sigma_{NN} = 72\, mb\,.$$

D.2.2 Nuclei-nuclei (A-B) collisions

For nuclei collisions, the formalism gives the next equation for the total inelastic A-B cross section:

$$\sigma_{AB} = \int 2\pi b\, \mathrm{d}b \left[1 - e^{-\sigma_{NN}(\sqrt{s_{NN}})\cdot T_{AB}(b)}\right], \tag{D.5}$$

where $T_{AB}(b)$ is the *nuclear overlap function of nuclei A and B separated by an impact parameter b*, which can be expressed as a product of the nuclear thickness function of nuclei A, $T_A(b)$,

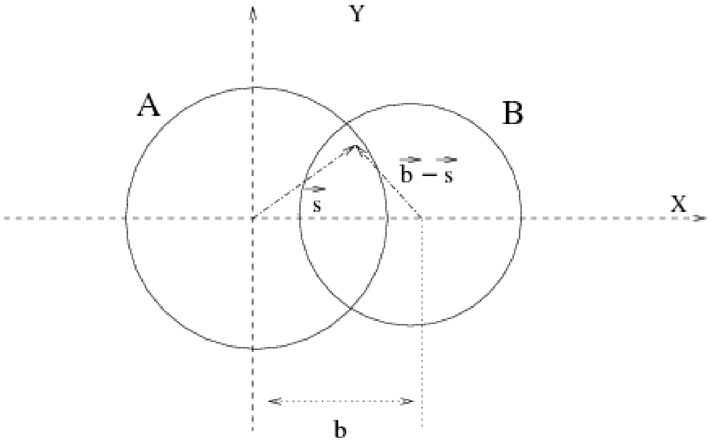

Figure D.4: Scheme of an A-B collision in the transverse plane to the beam line, showing $\vec{b}$ and $\vec{s}$ vectors.

and B, $T_B(b)$, over the element of overlapping area $\mathrm{d}^2\vec{s}$

$$T_{AB}(b) = \int \mathrm{d}^2\vec{s}\, T_A(s)\, T_B(|\vec{b}-\vec{s}|)\,, \tag{D.6}$$

where $\vec{s}$ is a vector in the transverse plane $\vec{s} = (s_x, s_y)$ and $\vec{b}$ is the impact parameter vector between the nuclei center, as can be observed on Fig. D.4. In this case, the normalization is:

$$\int_0^{+\infty} 2\pi b\, \mathrm{d}b\, T_{AB}(b) = A\, B\,.$$

Tab. D.2 presents the nuclear overlap function for different values of the impact parameter b for Pb-Pb collisions.

b (fm)	$T_{AB}(b)$ (fm^{-2})	b (fm)	$T_{AB}(b)$ (fm^{-2})	b (fm)	$T_{AB}(b)$ (fm^{-2})
0.0	304.3	7.0	111.2	14.0	1.04
1.0	297.4	8.0	80.5	15.0	$2.82{\cdot}10^{-1}$
2.0	278.2	9.0	54.3	16.0	$6.79{\cdot}10^{-2}$
3.0	250.2	10.0	33.4	17.0	$1.51{\cdot}10^{-2}$
4.0	216.9	11.0	18.2	18.0	$3.21{\cdot}10^{-3}$
5.0	181.1	12.0	8.50	19.0	$6.55{\cdot}10^{-4}$
6.0	145.2	13.0	3.28	20.0	$1.30{\cdot}10^{-4}$

Table D.2: Nuclear overlap function $T_{AB}(b)$ evaluated by means of the Glauber model for Pb-Pb collisions and different values of the impact parameter b.

The A-B inelastic cross section calculation for Au-Au collisions at RHIC energies, $\sqrt{s_{NN}} = 200$ GeV, considering $\sigma_{NN} = 42$ mb [E+04], gives,

$$\sigma_{AuAu} \approx 705\, fm^2 = 7.05\, b\,.$$

Similarly, for LHC Pb-Pb collisions at $\sqrt{s_{NN}} = 5.5$ TeV, one obtains:

$$\sigma_{PbPb} \approx 782.5\, fm^2 = 7.83\, b \qquad \text{for } \sigma_{NN} = 60\, mb\,,$$

$$\sigma_{PbPb} \approx 795.1\, fm^2 = 7.95\, b \qquad \text{for } \sigma_{NN} = 72\, mb\,.$$

D.2.3 "Hard" collisions

Grosso modo we consider as "hard" collisions the ones where the interaction takes place between partons (quarks and gluons). Their interaction cross section is theoretically calculable by means of perturbative QCD, as the "hard" NN cross section, σ_{NN}^{hard}, is small and allows to expand equations (D.3) and/or (D.5) in serie in orders of $\sigma_{NN}^{hard} \cdot T_{AB}(b)$.

"Hard" p-A collisions

For "hard" p-A collisions equation (D.3) gets simplified on first approximation to:

$$\sigma_{pA}^{hard} \approx \int \mathrm{d}^2\vec{b}\, \sigma_{NN}^{hard}\, T_A(b) \;=\; A \cdot \sigma_{NN}^{hard}\,. \tag{D.7}$$

By definition [d'E03], the mean number of particles produced or **invariant yield**, Y_{pA}^{hard}, is the ratio between the cross section of the "hard" process and the total inelastic cross section,

$$\mathrm{Y}_{pA}^{hard}(b) \equiv \frac{\sigma_{pA}^{hard}}{\sigma_{pA}}\,. \tag{D.8}$$

Equation that can be developed to obtain the relationship between the invariant yield on a p-A "hard" collision and the invariant yield on a NN "hard" collision

$$\mathrm{Y}_{pA}^{hard} = \frac{1}{\sigma_{pA}} \cdot A\, \sigma_{NN}^{hard} = \frac{\sigma_{NN}}{\sigma_{pA}}\, A \cdot \mathrm{Y}_{NN}^{hard}\,, \tag{D.9}$$

where analogously, by definition [d'E03], the invariant yield on a NN "hard" collision is:

$$\mathrm{Y}_{NN}^{hard}(b) \;\equiv\; \frac{\sigma_{NN}^{hard}}{\sigma_{NN}}\,. \tag{D.10}$$

Equation (D.9) allows to interpret the proportionality factor as the mean number of nucleon-nucleon collisions in a *"minimum bias"* p-A collision:

$$\langle N_{coll} \rangle_{pA} = A \cdot \frac{\sigma_{NN}}{\sigma_{pA}}\,. \tag{D.11}$$

Then, for an impact parameter b, the invariant yield is

$$\mathrm{Y}_{pA}^{hard}(b) = \langle N_{coll} \rangle_{pA} \cdot \mathrm{Y}_{NN}^{hard}(b)\,. \tag{D.12}$$

As an example, the mean number of collisions in p-Au interactions at RHIC energies, $\sqrt{s_{NN}} =$ 200 GeV, with the previously evaluated value of σ_{pAu} is

$$\langle N_{coll} \rangle_{pAu} \;=\; 4.95\,.$$

On the other hand, for a given impact parameter, the invariant yield is given by:

$$\frac{\mathrm{dY}_{pA}^{hard}(b)}{\mathrm{d}b} = \frac{\mathrm{d}}{\mathrm{d}b}\left(\frac{\sigma_{pA}^{hard}(b)}{\sigma_{pA}(b)}\right) = \frac{\sigma_{NN}^{hard}\,T_A(b)}{1-e^{-\sigma_{NN}(\sqrt{s_{NN}})\cdot T_A(b)}}\,,$$

$$\frac{\mathrm{dY}_{pA}^{hard}(b)}{\mathrm{d}b} = \frac{\sigma_{NN}\cdot T_A(b)}{1-e^{-\sigma_{NN}(\sqrt{s_{NN}})\cdot T_A(b)}}\cdot \mathrm{Y}_{NN}^{hard}(b) = N_{coll}(b)\cdot \mathrm{Y}_{NN}^{hard}(b)\,. \tag{D.13}$$

Where the number of nucleon-nucleon collisions produced on a "hard" p-A collision at a given impact parameter b, $N_{coll}(b)$, is given by:

$$N_{coll}(b) = \frac{\sigma_{NN}\cdot T_A(b)}{1-e^{-\sigma_{NN}(\sqrt{s_{NN}})\cdot T_A(b)}}\,. \tag{D.14}$$

And the number of participants in a "hard" p-A collision at a given impact parameter b, is:

$$N_{part}(b) = N_{coll}(b) + 1\,. \tag{D.15}$$

Then, the Glauber model permits to express $\mathrm{Y}_{pA}^{hard}(b)$, $N_{coll}(b)$ and $N_{part}(b)$ in p-A collisions as a function of the parameters on NN collisions.
The number of nucleon-nucleon collisions and the number of nucleon participants are then simple parameters to analyse, once the nuclear thickness function is known (Tab. D.1). Tab. D.3 present the results of an evaluation of N_{coll} and N_{part} at $\sqrt{s_{NN}} = 8.8$ TeV for p-Pb collisions at given values of the impact parameter b and $\sigma_{NN} = 60$ mb.

b (fm)	$T_A(b)$ (mb^{-1})	$N_{coll}(b)$	$N_{part}(b)$
0.0	0.212	12.7	13.7
1.0	0.209	12.5	13.5
2.0	0.202	12.1	13.1
3.0	0.188	11.3	12.3
4.0	0.167	10.0	11.0
5.0	0.134	8.0	9.0
6.0	$8.33\cdot10^{-2}$	5.0	6.0
7.0	$3.05\cdot10^{-2}$	2.2	3.2
8.0	$6.65\cdot10^{-3}$	1.2	2.2

Table D.3: Calculated values of $T_A(b)$, $N_{coll}(b)$ and $N_{part}(b)$, by means of the Glauber model for p-Pb collisions at $\sqrt{s_{NN}} = 8.8$ TeV and $\sigma_{NN} = 60$ mb.

"Hard" A-B collisions

Analogously, for "hard" A-B collisions equation (D.5) gets simplified to:

$$\sigma_{AB}^{hard} \approx \int \mathrm{d}^2\vec{b}\, \sigma_{NN}^{hard}\, T_{AB}(b) \;\approx\; A\,B \cdot \sigma_{NN}^{hard}\,. \tag{D.16}$$

The invariant yield is:

$$\mathrm{Y}_{AB}^{hard} = \frac{\sigma_{AB}^{hard}}{\sigma_{AB}} = \frac{A\,B\,\sigma_{NN}}{\sigma_{AB}} \cdot \mathrm{Y}_{NN}^{hard}\,. \tag{D.17}$$

So, the mean number of nucleon-nucleon collisions in a *"minimum bias"* A-B collision can be interpreted as:

$$\langle N_{coll}\rangle_{AB} \;= A\,B\,\frac{\sigma_{NN}}{\sigma_{AB}}\,. \tag{D.18}$$

And the invariant yield can be expressed as:

$$\mathrm{Y}_{AB}^{hard}(b) = \langle N_{coll}\rangle_{AB} \cdot \mathrm{Y}_{NN}^{hard}(b)\,. \tag{D.19}$$

As an example, $\langle N_{coll}\rangle$ in a Pb-Pb interaction at $\sqrt{s_{NN}} = 5.5$ TeV is,

$$\langle N_{coll}\rangle_{PbPb} \;= 332\;(392) \qquad \text{for } \sigma_{NN} = 60\;(72)\; mb\,. \tag{D.20}$$

On the other hand, invariant yield evolves with the impact parameter as,

$$\begin{aligned}\frac{\mathrm{d}\mathrm{Y}_{AB}^{hard}(b)}{\mathrm{d}b} &= \frac{\mathrm{d}}{\mathrm{d}b}\Big(\frac{\sigma_{AB}^{hard}(b)}{\sigma_{AB}(b)}\Big)\\ &= \frac{\sigma_{NN}^{hard}\;\int \mathrm{d}^2\vec{s}\,\int \rho_A(r)\int \rho_B(/\vec{b}-\vec{s}/, z'')\,\mathrm{d}z''\,\mathrm{d}z'}{1-e^{-\sigma_{NN}(\sqrt{s_{NN}})\cdot T_{AB}(b)}}\\ &\equiv \frac{\sigma_{NN}^{hard}\cdot T_{AB}(b)}{1-e^{-\sigma_{NN}(\sqrt{s_{NN}})\cdot T_{AB}(b)}}\,,\end{aligned} \tag{D.21}$$

where equacions (D.6) and (D.4) have been used. Then, the number of inelastic NN collisions produced on a "hard" A-B interaction can be expressed as:

$$(N_{coll})_{AB}(b) = \frac{\sigma_{NN}\cdot T_{AB}(b)}{1-e^{-\sigma_{NN}(\sqrt{s_{NN}})\cdot T_{AB}(b)}} \tag{D.22}$$

So, that we have:

$$\frac{\mathrm{d}\mathrm{Y}_{AB}^{hard}(b)}{\mathrm{d}b} \;=\; (N_{coll})_{AB}(b)\cdot \mathrm{Y}_{NN}^{hard}(b)\,. \tag{D.23}$$

In A-B collisions, the number of participants of nucleus A at a given impact parameter is determined by the sum of the interaction probability of each nucleon of nucleus A with the nucleons of nucleus B

$$N_{part}^{A}(b) = \sum_{i=0}^{A} P_{interaction}^{A\to B}(|\vec{b}-\vec{s}_i|)\,.$$

In the continuum, it gives the next equation for the number of total participants on a "hard" A-B collision [CS01],

$$\begin{aligned} N_{part}(b) &= \int d^2\vec{s}\, T_A(s)\, P_{int}^{A\to B}(|\vec{b}-\vec{s}|) + \int d^2\vec{s}\, T_B(s)\, P_{int}^{B\to A}(|\vec{b}-\vec{s}|) \\ &= \int d^2\vec{s}\, T_A(s) \left(\frac{1-e^{-\sigma_{NN} T_B(|\vec{b}-\vec{s}|)}}{1-e^{-\sigma_{NN}(\sqrt{s_{NN}})\cdot T_{AB}(b)}} \right) + \\ &+ \int d^2\vec{s}\, T_B(s) \left(\frac{1-e^{-\sigma_{NN} T_A(|\vec{b}-\vec{s}|)}}{1-e^{-\sigma_{NN}(\sqrt{s_{NN}})\cdot T_{AB}(b)}} \right). \end{aligned} \qquad \text{(D.24)}$$

Where the existence of two terms comes from the fact that one has to sum over the number of participants of each nuclei on the interaction, the ones of nucleus A, $N_{part}^{A}(b)$, and the ones of nucleus B, $N_{part}^{B}(b)$. Equation that for "hard" A-A collisions gets simplified to

$$N_{part}(b) = 2 \int d^2\vec{s}\, T_A(s) \left(\frac{1-e^{-\sigma_{NN} T_A(|\vec{b}-\vec{s}|)}}{1-e^{-\sigma_{NN}(\sqrt{s_{NN}})\cdot T_{AB}(b)}} \right). \qquad \text{(D.25)}$$

The Glauber model permits then to evaluate the parameters of "hard" A-B collisions as a function of the fundamental NN collisions. As an example, Tab. D.4 presents the calculation of $T_{AB}(b)$, $N_{coll}(b)$ and $N_{part}(b)$ in Pb-Pb collisions at $\sqrt{s_{NN}} = 5.5$ TeV for $\sigma_{NN} = 60$ mb.

b (fm)	$T_{AB}(b)$ (mb^{-1})	$N_{coll}(b)$	$N_{part}(b)$
0.0	30.43	1826 (2191)	405 (407)
1.0	29.74	1784 (2141)	400 (402)
2.0	27.82	1669 (2003)	385 (388)
3.0	25.02	1501 (1801)	359 (364)
4.0	21.69	1301 (1561)	326 (331)
5.0	18.11	1087 (1304)	287 (293)
6.0	14.52	871 (1045)	246 (251)
7.0	11.12	667 (801)	203 (209)
8.0	8.05	483 (580)	162 (168)
9.0	5.43	326 (391)	123 (128)
10.0	3.34	200 (240)	88 (92)
11.0	1.82	109 (131)	58 (62)
12.0	$8.50\cdot10^{-1}$	51 (61)	34 (37)
13.0	$3.28\cdot10^{-1}$	19.7 (23.6)	16.9 (18.5)
14.0	$1.04\cdot10^{-1}$	6.25 (7.49)	6.80 (7.63)
15.0	$2.82\cdot10^{-2}$	2.07 (2.34)	2.20 (2.52)

Table D.4: Calculated values of $T_{AB}(b)$, $N_{coll}(b)$ and $N_{part}(b)$, by means of the Glauber model for Pb-Pb collisions at $\sqrt{s_{NN}} = 5.5$ TeV and $\sigma_{NN} = 60$ (72) mb.

D.2.4 Centrality dependence

Usually one is interested in calculating those parameters for a given centrality class (CC), where the centrality class is defined from the percentage of the inelastic cross section, and it is related to certain values of the impact parameter (b) as follows

$$\sigma_{AB} \times percentage(CC) = \int_0^b 2\pi b \, \mathrm{d}b \left[1 - e^{-\sigma_{NN}(\sqrt{s_{NN}})\cdot T_{AB}(b)}\right].$$

Thereby, for Pb-Pb collisions and $\sigma_{NN} = 60$ mb, the 5% CC corresponds to $b = 3.5$ fm, the 10% CC to $b = 5.0$ fm, the 40% CC to $b = 10.0$ fm, the 50% CC to $b = 11.1$ fm, and the 70% CC to $b = 13.2$ fm.

For a given centrality class $C_1 - C_2$ determined by the impact parameters b_1 and b_2, the hard cross section is

$$\langle \sigma_{AB}^{hard} \rangle_{C_1C_2} \approx \int_{b_1}^{b_2} \mathrm{d}^2\vec{b}\, \sigma_{NN}^{hard}\, T_{AB}(b)\,. \tag{D.26}$$

On the other hand, the number of nucleon-nucleon collisions is

$$\langle N_{coll}^{AB} \rangle_{C_1C_2} \approx \langle T_{AB} \rangle_{C_1C_2} \cdot \sigma_{NN}^{inel}\,, \tag{D.27}$$

where

$$\langle T_{AB} \rangle_{C_1C_2} \equiv \frac{\int_{b_1}^{b_2} \mathrm{d}^2\vec{b}\, T_{AB}}{\int_{b_1}^{b_2} \mathrm{d}^2\vec{b}}\,. \tag{D.28}$$

And the invariant yield can be expressed by:

$$\left\langle \frac{\mathrm{d}^2 N_{AB}^{hard}}{\mathrm{d}y\mathrm{d}p_T} \right\rangle_{C_1C_2} = \langle N_{coll}^{AB} \rangle_{C_1C_2} \cdot \mathrm{Y}_{NN}^{hard} = \langle T_{AB} \rangle_{C_1C_2} \cdot \frac{\mathrm{d}^2\sigma_{NN}^{hard}}{\mathrm{d}y\mathrm{d}p_T}\,. \tag{D.29}$$

And the cross section by:

$$\left\langle \frac{\mathrm{d}^2 \sigma_{AB}^{hard}}{\mathrm{d}y\mathrm{d}p_T} \right\rangle_{C_1C_2} = \langle T_{AB} \rangle_{C_1C_2} \cdot \sigma_{AB}^{inel} \times percentage(CC) \cdot \frac{\mathrm{d}^2\sigma_{NN}^{hard}}{\mathrm{d}y\mathrm{d}p_T}\,. \tag{D.30}$$

Then one can evaluate the mean number of NN collisions for Pb-Pb collisions, and obtain the results of Tab. D.5.

$C_1 - C_2$	$\langle T_{AB} \rangle_{C_1C_2}$ (mb^{-1})	$\langle N_{coll}^{AB} \rangle_{C_1C_2}$
$0\% - 5\%$	26.7	1600
$0\% - 10\%$	23.7	1420
$40\% - 70\%$	1.36	81
$50\% - 70\%$	0.82	49

Table D.5: Calculated values of $\langle T_{AB} \rangle_{C_1C_2}$ and $\langle N_{coll}^{AB} \rangle_{C_1C_2}$ by means of the Glauber model for Pb-Pb collisions at $\sqrt{s_{NN}} = 5.5$ TeV and $\sigma_{NN} = 60$ mb.

It is now evident how one can, for example, calculate the mean number of $c\bar{c}$ pairs produced in different centrality classes by using Tab. D.5 values and for $\sigma_{NN}^{hard} = 4.32$ mb. The results are presented on Tab. D.6.

$C_1 - C_2$	$\langle \mathrm{Y}_{AB}^{hard} \rangle_{C_1 C_2}$
$0\% - 5\%$	115
$0\% - 10\%$	102
$50\% - 70\%$	3.5

Table D.6: Calculated values of the mean number of $c\bar{c}$ pairs produced per CC by means of the Glauber model for Pb-Pb collisions at $\sqrt{s_{NN}} = 5.5$ TeV, $\sigma_{NN} = 60$ mb, and for $\sigma_{NN}^{hard} = 4.32$ mb.

Bibliography

[A$^+$83a] G. Arnison et al. Experimental observation of isolated large transverse energy electrons with associated missing energy at $\sqrt{s} = 540$ GeV. *Phys. Lett. B*, 122(1), Feb. 1983.

[A$^+$83b] G. Arnison et al. Experimental observation of lepton pairs of invariant mass around 95 GeV/c^2 at the CERN SPS collider. *Phys. Lett. B*, 126(5), July 1983.

[A$^+$99] Abbiendi et al. Mesurement of the semileptonic branching ratio of charmed hadrons produced in $Z^0 \to c\bar{c}$ decays. *Eur. Phys. J.*, C8:573–584, 1999.

[A$^+$00a] M. C. Abreu et al. Evidence for deconfinement of quarks and gluons from the J/ψ suppression pattern measured in Pb Pb collisions at the CERN-SPS. *Phys. Lett.*, B477:28–36, 2000.

[A$^+$00b] Anthony A. Affolder et al. Measurement of J/ψ and $\psi(2s)$ polarization in $p\bar{p}$ collisions at $\sqrt{s} = 1.8$ TeV. *Phys. Rev. Lett.*, 85:2886–2891, 2000. arXiv: hep-ph/0004027.

[A$^+$03] S. S. Adler et al. Absence of suppression in particle production at large transverse momentum in $\sqrt{s_{NN}} = 200$ GeV d+Au collisions. *Phys. Rev. Lett.*, 91:072303, 2003. arXiv: nucl-ex/0306021.

[A$^+$05a] John Adams et al. Azimuthal anisotropy in Au+Au collisions at $\sqrt{s_{NN}} = 200$ GeV. *Phys. Rev.*, C72:014904, 2005. arXiv: nucl-ex/0409033.

[A$^+$05b] John Adams et al. Experimental and theoretical challenges in the search for the quark gluon plasma: The STAR collaboration's critical assessment of the evidence from RHIC collisions. *Nucl. Phys.*, A757:102–183, 2005. arXiv: nucl-ex/0501009.

[A$^+$05c] K. Adcox et al. Formation of dense partonic matter in relativistic nucleus nucleus collisions at RHIC: Experimental evaluation by the PHENIX collaboration. *Nucl. Phys.*, A757:184–283, 2005. arXiv: nucl-ex/0410003.

[A$^+$05d] S. S. Adler et al. Centrality dependence of direct photon production in $\sqrt{s_{NN}} = 200$ GeV Au+Au collisions. *Phys. Rev. Lett.*, 94:232301, 2005. arXiv: nucl-ex/0503003.

[A$^+$05e] B. Alessandro et al. A new measurement of j/ψ suppression in Pb-Pb collisions at 158 GeV per nucleon. *Eur. Phys. J.*, C39:335–345, 2005. arXiv: hep-ex/0412036.

[A$^+$05f] R. Arnaldi et al. J/ψ production in indium-indium collisions. *Eur. Phys. J.*, C43:167–172, 2005.

[A$^+$05g] I. Arsene et al. Quark gluon plasma and color glass condensate at RHIC? the perspective from the BRAHMS experiment. *Nucl. Phys.*, A757:1–27, 2005. arXiv: nucl-ex/0410020.

[A$^+$06] B. Alessandro et al. ALICE: Physics performance report, volume II. *J. Phys.*, G32:1295–2040, 2006.

[A$^+$07] R. Arnaldi et al. private communication, 2007.

[ABMRS03] A. Andronic, P. Braun-Munzinger, K. Redlich, and J. Stachel. Statistical hadronization of charm in heavy-ion collisions at SPS, RHIC and LHC. *Phys. Lett.*, B571:36–44, 2003. arXiv: nucl-th/0303036.

[ACC$^+$82] Guido Altarelli, N. Cabibbo, G. Corbo, L. Maiani, and G. Martinelli. Leptonic decay of heavy flavors: A theoretical update. *Nucl. Phys.*, B208:365, 1982.

[ADMP04] Ch. Anastasiou, L. Dixon, K. Melnikov, and F. Petriello. High-precision QCD at hadron colliders: electroweak gauge boson rapidity distributions at NNLO. *Phys. Rev.*, D69:094008, 31 Mar 2004. arXiv: hep-ph/0312266.

[AEGH96] J. F. Amundson, Oscar J. P. Eboli, E. M. Gregores, and F. Halzen. Colorless states in perturbative QCD: Charmonium and rapidity gaps. *Phys. Lett.*, B372:127–132, 1996. arXiv: hep-ph/9512248.

[AEGH97] J. F. Amundson, Oscar J. P. Eboli, E. M. Gregores, and F. Halzen. Quantitative tests of color evaporation: Charmonium production. *Phys. Lett.*, B390:323–328, 1997. arXiv: hep-ph/9605295.

[AKK04] S. Albino, B. A. Kniehl, and G. Kramer. Low x particle spectra in the modified leading logarithm approximation. *Eur. Phys. J.*, C38:177–185, 2004.

[Ali] Alice Experiment: Offline Project. http://aliceinfo.cern.ch/Offline.

[ALI98] *ALICE TDR of the High Momentum Particle Identification Detector*, August 1998. ALICE-DOC-1998-01 CERN/LHCC 98-19.

[ALI99a] *ALICE TDR of the Dimuon Forward Spectrometer*, August 1999. ALICE-DOC-2004-004 CERN/LHCC 99-22.

[ALI99b] *ALICE TDR of the Inner Tracking System*, June 1999. ALICE-DOC-2005-002 CERN/LHCC 99-12.

[ALI99c] *ALICE TDR of the Photon Multiplicity Detector*, September 1999. ALICE-DOC-2004-007 CERN/LHCC 99-32.

[ALI99d] *ALICE TDR of the PHOton Spectrometer*, March 1999. ALICE-DOC-2004-008 CERN/LHCC 99-4.

[ALI99e] *ALICE TDR of the Zero Degree Calorimeter*, March 1999. ALICE-DOC-2004-003 CERN/LHCC 99-5.

[ALI00a] *ALICE Addendum to the TDR of the Dimuon Forward Spectrometer*, December 2000. CERN/LHCC 2000-046.

[ALI00b] *ALICE TDR of the Time Projection Chamber*, January 2000. ALICE-DOC-2004-006 CERN/LHCC 2000-001.

[ALI01] *ALICE TDR of the Transition Radiation Detector*, October 2001. ALICE-DOC-2004-009 CERN /LHCC 2001-021.

[ALI02a] *ALICE Addendum to the TDR of the Time Of Flight System*, April 2002. ALICE-DOC-2004-002 CERN/LHCC 2002-016.

[ALI02b] *ALICE TDR of the Time Of Flight System*, 2002. ALICE-DOC-2006-001.

[ALI03] *ALICE Addendum ot the TDR of the Photon Multiplicity Detector*, September 2003. ALICE-DOC-2005-001 CERN/LHCC 2003-038.

[ALI04] *ALICE TDR of the Forward Detectors: FMD, T0 and V0*, September 2004. ALICE-DOC-2004-010 CERN/LHCC 2004-025.

[Ant07] F. Antinori. Heavy-Ion Physics with ALICE. *arXiv: nucl-ex/0702013*, 2007. To be published in J.P.G.

[B$^+$83a] M. Bagnaia et al. Evidence for $Z^0 \rightarrow e^+e^-$ at the CERN $p\bar{p}$ collider. *Phys. Lett. B*, 129(1,2), Sep. 1983.

[B$^+$83b] M. Banner et al. Observation of single isolated electrons of high transverse momentum in events with missing transverse energy at the CERN $p\bar{p}$ collider. *Phys. Lett. B*, 122(5,6), March 1983.

[B$^+$00] G. Baur et al. Heavy ion physics programme in CMS. *CERN CMS NOTE 2000/060*, 2000.

[B$^+$04] A. Beuret et al. The LHC Lead Ion Injector Chain. 2004. Presented at the 9th European Particle Accelerator Conference (EPAC 2004), Lucerne, Switzerland, 5-9 Jul 2004.

[B$^+$05] B. B. Back et al. The PHOBOS perspective on discoveries at RHIC. *Nucl. Phys.*, A757:28–101, 2005. arXiv: nucl-ex/0410022.

[BBB$^+$03] M. Bedjidian, D. Blaschke, G. T. Bodwin, N. Carrer, B. Cole, P. Crochet, A. Dainese, A. Deandrea, S. Frixione, P. Hoyer, D. Kharzeev, O. L. Kodolova, R. Kvatadze, Jungil Lee, I. P. Lokhtin, M. Mangano, N. Marchal, M. Nardi, G. Nardulli, H. Niemi, S. Peigne', P. Petreczky, A. D. Polosa, H. Satz, H. Takai, S. Tapprogge, R. L. Thews, E. Vercellin, and R. Vogt. Hard probes in heavy ion collisions at the LHC: heavy flavour physics, 2003. arXiv: hep-ph/0311048.

[BDM$^+$97a] R. Baier, Yuri L. Dokshitzer, Alfred H. Mueller, S. Peigne, and D. Schiff. Radiative energy loss and p(t)-broadening of high energy partons in nuclei. *Nucl. Phys.*, B484:265–282, 1997. arXiv: hep-ph/9608322.

[BDM$^+$97b] R. Baier, Yuri L. Dokshitzer, Alfred H. Mueller, S. Peigne, and D. Schiff. Radiative energy loss of high energy quarks and gluons in a finite-volume quark-gluon plasma. *Nucl. Phys.*, B483:291–320, 1997. arXiv: hep-ph/9607355.

[Bet07] Siegfried Bethke. Experimental tests of asymptotic freedom. *Prog. Part. Nucl. Phys.*, 58:351–386, 2007. arXiv: hep-ex/0606035.

[BF95] Eric Braaten and Sean Fleming. Color octet fragmentation and the ψ-prime surplus at the Tevatron. *Phys. Rev. Lett.*, 74:3327–3330, 1995. arXiv: hep-ph/9411365.

[BFL01] Eric Braaten, Sean Fleming, and Adam K. Leibovich. NRQCD analysis of bottomonium production at the Tevatron. *Phys. Rev.*, D63:094006, 2001. arXiv: hep-ph/0008091.

[BHP01] C. Balazs, J. Huston, and I. Puljak. Higgs production: A comparison of parton showers and resummation. *Phys. Rev.*, D63:014021, 2001. arXiv: hep-ph/ph/0002032.

[BI02] J.P. Blaizot and E. Iancu. The quark-gluon plasma: Collective dynamics and hard thermal loops. *Phys. Rept.*, 359:355–528, 2002. arXiv: hep-ph/0101103.

[Bjo82] J. D. Bjorken. Energy loss of energetic partons in quark - gluon plasma: Possible extinction of high p(t) jets in hadron - hadron collisions. 1982. FERMILAB-PUB-82-059-THY.

[Bjo83] J. D. Bjorken. Highly relativistic nucleus-nucleus collisions: The central rapidity region. *Phys. Rev. D*, 27(1):140–151, Jan 1983. APS link.

[BKCS04] E. L. Bratkovskaya, A. P. Kostyuk, W. Cassing, and Horst Stoecker. Charmonium chemistry in A+A collisions at relativistic energies. *Phys. Rev.*, C69:054903, 2004. arXiv: nucl-th/0402042.

[Blu06] N. Blusseau. Master's thesis, Université de Nantes, 2006.

[BM88] Stanley J. Brodsky and Alfred H. Mueller. Using nuclei to probe hadronization in QCD. *Phys. Lett.*, B206:685, 1988.

[Bou04] M. K. Boudjemline. *Étude des chambres de trajectrographie* CPC *du spectromètre dimuon* ALICE. PhD thesis, Université de Nantes, 2004.

[BR96] M. Beneke and I. Z. Rothstein. Hadro-production of quarkonia in fixed target experiments. *Phys. Rev.*, D54:2005–2016, 1996. arXiv: hep-ph/9603400.

[C$^+$04] F. Carminati et al. ALICE: Physics performance report, volume I. *J. Phys.*, G30:1517–1763, 2004.

[Cas07] J. Castillo. private communication, 2007.

[CB05] Gustavo Conesa Balbastre. *Identification of particles and hard processes with the spectrometer PHOS of the ALICE experiment*. PhD thesis, Univ. Valencia and Nantes, 2005. CERN-THESIS-2006-050.

[CdV07] Z. Conesa del Valle. Electroweak boson detection in the ALICE muon spectrometer. *Eur. Phys. J.*, C49:149–154, 2007. arXiv: nucl-ex/0609027.

[CdVDD$^+$07] Z. Conesa del Valle, A. Dainese, H.-T. Ding, G. Martinez, and D. Zhou, 2007. Work in progress.

[CF05] A. Capella and E. G. Ferreiro. J/ψ suppression at $\sqrt{s_{NN}} = 200$ GeV in the comovers interaction model. *Eur. Phys. J.*, C42:419–424, 2005. arXiv: hep-ph/0505032.

[CF06] A. Capella and E. G. Ferreiro. Why does the J/ψ nuclear absorption decrease with increasing energy? 2006. arXiv: hep-ph/0610313.

[CGMP95] Matteo Cacciari, Mario Greco, Michelangelo L. Mangano, and Andrea Petrelli. Charmonium production at the Tevatron. *Phys. Lett.*, B356:553–560, 1995. arXiv: hep-ph/9505379.

[CGMV05] P. Crochet, R. Guernane, A. Morsch, and E. Vercellin. Measuring the b-meson production cross section in 5.5 TeV Pb-Pb collisions using semileptonic decay muons. *CERN ALICE INT 2005/018*, 2005.

[CMAF06] Z. Conesa, G. Martinez, L. Aphecetche, and C. Finck. Production of W vector bosons in p+p and Pb+Pb collisions at LHC energies. W detection in the ALICE muon spectrometer. *CERN ALICE INT 2006/021*, 2006.

[Cro05] P. Crochet. Quarkonia and heavy flavors at the LHC. *European Physical Journal C*, 43:437, 2005. arXiv: nucl-ex/0503008.

[CS01] A. Capella and D. Sousa. Centrality dependence of hadron multiplicities in nuclear collisions in the dual parton model. *Physics Letters B*, 511:185–190, 5 July 2001.

[CS05] A. M. Copper-Sarkar. Low-x physics and W and Z production at LHC. *arXiv: hep-ex/0512228*, 2005.

[CSS88] John C. Collins, Davison E. Soper, and George Sterman. Factorization of hard processes in QCD. *Adv. Ser. Direct. High Energy Phys.*, 5:1–91, 1988. arXiv: hep-ph/0409313.

[CSS98] John C. Collins, Davison E. Soper, and George Sterman. Factorization is not violated. *Phys. Lett.*, B438:184–192, 1998. arXiv: hep-ph/9806234.

[D006] Evidence for Z $\rightarrow b\bar{b}$ decays at D0. 2006. D0 Note 5205-CONF.

[D'A95] G. D'Agostini. A multidimensional unfolding method based on the Bayes' theorem. *N.I.M. A*, 362:487–498, 1995.

[Dai03] A. Dainese. *Charm production and in-medium* QCD *energy loss in nucleus-nucleus collisions with ALICE.* PhD thesis, Università Degli Studi di Padova, 2003. arXiv: nucl-ex/0311004v2.

[DC05] E. Dumonteil and P. Crochet. Measuring the p(t) dependence of the Y′/Y ratio with the ALICE muon spectrometer. 2005. ALICE-INT-2005-002.

[DDCdVZ07] Heng-Tong Ding, Andrea Dainese, Zaida Conesa del Valle, and Daicui Zhou. Studying the energy loss of heavy quarks via single muon production in Pb Pb collisions at $\sqrt{s_{NN}} = 5.5$ TeV. 2007. arXiv: hep-ph/0702118.

[d'E03] David d'Enterria. Hard scattering cross sections at LHC in the Glauber approach: from pp to pA and AA collisions. *nucl-ex*, (0302016), 2003.

[d'E04] David d'Enterria. Hard spectra and QCD matter: experimental review. *nucl-ex*, (0404018), 2004. arXiv: nucl-ex/0404018.

[DHKK07] Matthias Doring, Kay Hubner, Olaf Kaczmarek, and Frithjof Karsch. Color screening and quark-quark interactions in finite temperature QCD. *Phys. Rev.*, D75:054504, 2007. arXiv: hep-lat/0702009.

[DK01] Yuri L. Dokshitzer and D. E. Kharzeev. Heavy quark colorimetry of QCD matter. *Phys. Lett.*, B519:199–206, 2001. arXiv: hep-ph/0106202.

[DKT91] Yuri L. Dokshitzer, Valery A. Khoze, and S. I. Troian. On specific QCD properties of heavy quark fragmentation ('dead cone'). *J. Phys.*, G17:1602–1604, 1991.

[DLP05] A. Dainese, C. Loizides, and G. Paic. Leading-particle suppression in high energy nucleus nucleus collisions. *Eur. Phys. J.*, C38:461–474, 2005. arXiv: hep-ph/0406201.

[DLP06] Andrea Dainese, Constantin Loizides, and Guy Paic. Leading-particle suppression and surface emission in nucleus nucleus collisions. *Acta Phys. Hung.*, A27:245–249, 2006. arXiv: hep-ph/0511045.

[dM72] S. Van der Meer. Stochastic damping of betatron oscillations in the ISR. *Internal report, CERN/ISR PO/73-31*, 1972.

[Dor98] Tommaso Dorigo. Observation of Z decays to b quark pairs at the Tevatron collider. 1998. arXiv: hep-ex/9806022, CDF-PUB-ELECTROWEAK-PUBLIC-4640, FERMILAB-CONF-98-197-E.

[E$^+$04] Eidelman et al. Review of Particle Physics. *Phys. Lett. B*, 592, 2004. and 2005 partial update for the 2006 edition available on the PDG WWW pages *www.pdg.lbl.gov*.

[EKKV99] V. Emel'yanov, A. Khodinov, S. R. Klein, and R. Vogt. Impact parameter dependence of J/ψ and drell-yan production in heavy ion collisions at $\sqrt{s_{NN}} = 17.3$ GeV. *Phys. Rev.*, C59:1860–1863, 1999. arXiv: hep-ph/9809222.

[EKKV00] V. Emel'yanov, A. Khodinov, S. R. Klein, and R. Vogt. The effect of shadowing on initial conditions, transverse energy and hard probes in ultrarelativistic heavy ion collisions. *Phys. Rev.*, C61:044904, 2000. arXiv: hep-ph/9909427.

[EKS99] K. J. Eskola, V. J. Kolhinen, and C. A. Salgado. The scale dependent nuclear effects in parton distributions for practical applications. *Eur. Phys. J. C*, 9:61, 1999. arXiv: hep-ph/9807297.

[FM04] S. Frixione and M. L. Mangano. How accurately can we mesure the W cross section? *arXiv: hep-ph/0405130v1*, 2004.

[FS99] L. Frankfurt and M. Strikman. Diffraction at HERA, color opacity and nuclear shadowing. *Eur. Phys. J.*, A5:293–306, 1999.

[G$^+$95] R. Gavai et al. Quarkonium production in hadronic collisions. *Int. J. Mod. Phys.*, A10:3043–3070, 1995.

[G$^+$06] F. Guerin et al. ALICE muon trigger performance. *CERN ALICE INT 2006/002*, 2006.

[GdC07] Raphael Granier de Cassagnac. Quarkonium suppression from SPS to RHIC (and from p+A to A+A). *Nucl. Phys.*, A783:293–300, 2007. arXiv: nucl-ex/0610003.

[Gei98] Klaus Geiger. QCD space-time analysis of quarkonium formation and evolution in hadronic collisions. *Phys. Rev.*, D57:1895–1919, 1998. arXiv: hep-ph/9706425.

[GHE97] E. M. Gregores, F. Halzen, and Oscar J. P. Eboli. Prompt charmonium production in Z decays. *Phys. Lett.*, B395:113–117, 1997. arXiv: hep-ph/9607324.

[GM70] R. J. Glauber and G. Matthias. High-Energy Scattering of protons by nuclei. *Nucl. Phys. B*, 21:135–157, 1970.

[Gon01] M. Gonin. Conclusions from the SPS heavy ion program. 2001. Prepared for International Nuclear Physics Conference (INPC 2001): Nuclear Physics and the 21st Century, Berkeley, California, 30 Jul - 3 Aug 2001.

[GRB04] Loic Grandchamp, Ralf Rapp, and Gerald E. Brown. In-medium effects on charmonium production in heavy-ion collisions. *Phys. Rev. Lett.*, 92:212301, 2004. arXiv: hep-ph/0306077.

[Gri04] D. Griffiths. *Introduction to Elementary Particles*. WILEY-VCH, 2004.

[Gue05] F. Guerin. Muon trigger performances and rates, in PbPb, ArAr and pp collisions at LHC. Talk given at First ALICE Physics Week; Quarkonia session, Dec. 2005.

[Gue06] F. Guerin. *Sonde muonique et instrumentation associée pour l'étude du plasma de quarks et de gluons dans l'expérience ALICE*. PhD thesis, Université Blaise Pascal, 2006.

[GV90] S. Gavin and R. Vogt. J/ψ suppression from hadron-nucleus to nucleus-nucleus collisions. *Nucl. Phys.*, B345:104–124, 1990.

[GV97] Sean Gavin and Ramona Vogt. Charmonium suppression by comover scattering in Pb+Pb collisions. *Phys. Rev. Lett.*, 78:1006–1009, 1997. arXiv: hep-ph/9606460.

[GW73] D. J. Gross and Frank Wilczek. Ultraviolet behavior of non-abelian gauge theories. *Phys. Rev. Lett.*, 30:1343–1346, 1973.

[H^+03] H. D. Hansen et al. Is the electron radiation length constant at high energies? *Phys. Rev. Lett.*, 91:014801, 2003.

[H^+04] H. D. Hansen et al. Landau-Pomeranchuk-Migdal effect for multihundred GeV electrons. *Phys. Rev.*, D69:032001, 2004.

[Han01] Simon Hands. The phase diagram of QCD. *Contemp. Phys.*, 42:209–225, 2001. arXiv: physics/0105022.

[HJ00] Ulrich Heinz and Maurice Jacob. Evidence for a new state of matter: An assessment of the results from the CERN lead beam programme, 2000. arXiv: nucl-th/0002042.

[HM84] F. Halzen and A. D. Martin. *Quarks and Leptons: An Introductory Course in Modern Particle Physics*. John Wiley and Sons, 1984.

[IK03] B. L. Ioffe and D. E. Kharzeev. Quarkonium polarization in heavy ion collisions as a possible signature of the quark-gluon plasma. *Phys. Rev.*, C68:061902, 2003. arXiv: hep-ph/0306176.

[JPPV07] A. Jakovac, P. Petreczky, K. Petrov, and A. Velytsky. Quarkonium correlators and spectral functions at zero and finite temperature. *Phys. Rev.*, D75:014506, 2007. arXiv: hep-lat/0611017.

[K^+07] B. Klos et al. Neutron density distributions from antiprotonic Pb-208 and Bi-209 atoms. *arXiv: nucl-ex/0702016*, 2007.

[Kal] The Kalman Filter. http://www.cs.unc.edu/ welch/kalman/.

[Kal60] R. E. Kalman. A new approach to linear filtering and prediction problems. *Transactions of the ASME–Journal of Basic Engineering*, 82(Series D):35–45, 1960.

[Kar02] Frithjof Karsch. Lattice results on QCD thermodynamics. *Nucl. Phys.*, A698:199–208, 2002. arXiv: hep-ph/0103314.

[Kar05] Frithjof Karsch. Deconfinement and quarkonium suppression. *Eur. Phys. J.*, C43:35–43, 2005. arXiv: hep-lat/0502014.

[Kar07] Frithjof Karsch. Transition temperature in QCD with physical light and strange quark masses. 2007. arXiv: hep-ph/0701210.

[KKP01] Bernd A. Kniehl, G. Kramer, and B. Potter. Testing the universality of fragmentation functions. *Nucl. Phys.*, B597:337–369, 2001. arXiv: hep-ph/0011155.

[KKS06] F. Karsch, D. Kharzeev, and H. Satz. Sequential charmonium dissociation. *Phys. Lett.*, B637:75–80, 2006. arXiv: hep-ph/hep-ph/0512239.

[KL94] Frithjof Karsch and Edwin Laermann. Susceptibilities, the specific heat and a cumulant in two flavor QCD. *Phys. Rev.*, D50:6954–6962, 1994. arXiv: hep-lat/9406008.

[Kle99] Spencer Klein. Suppression of bremsstrahlung and pair production due to environmental factors. *Rev. Mod. Phys.*, 71(5):1501–1538, Oct 1999.

[KT99] D. Kharzeev and R. L. Thews. Quarkonium formation time in a model-independent approach. *Phys. Rev. C*, 60(4):041901, Sep 1999.

[KTH01] Boris Kopeliovich, Alexander Tarasov, and Jorg Hufner. Coherence phenomena in charmonium production off nuclei at the energies of RHIC and LHC. *Nucl. Phys.*, A696:669–714, 2001.

[L$^+$07] N. LeBris et al. Intrinsic efficiency of the tracking chambers of the muon spectrometer in the ALICE experiment. ALICE Internal Note, 2007.

[Lan05] Jean-Philippe Lansberg. *Quarkonium production at high-energy hadron colliders*. PhD thesis, University of Liège, 2005. arXiv: hep-ph/0507175.

[Lei07] M. J. Leitch. Quarkonia production in p p, p (d) A and AA collisions. *Nucl. Phys.*, A782:319–326, 2007.

[Leo93] W. R. Leo. *Techniques for Nuclear and Particle Physics Experiments*. Springer-Verlag, 1993.

[LHK$^+$97] H. L. Lai, J. Huston, S. Kuhlmann, F. Olness, J. Owens, D. Soper, W. K. Tung, and H. Weerts. Improved parton distributions from global analysis of recent deep inelastic scattering and inclusive jet data. *Phys. Rev. D*, 55:1280, 1997. arXiv: hep-ph/9606399.

[M$^+$02] David Morrison et al. Number of binary collsions and total cross section in d-Au at $\sqrt{s_{NN}} = 200$ GeV. PHENIX Analysis Note 165, 19 December 2002.

[Mar05] Ginés Martinez. Physics of the muon spectrometer of the ALICE experiment. *arXiv: hep-ex/0505021v1*, May 2005.

[Mar06] Ginés Martínez. Introduction à l'étude éxperimentale de la matière hadronique dans les collisions entre ions lourds. Le Plasma de Quarks et de Gluons. HDR Thesis, 2006.

[Mat88] E. Mathieson. Cathode charge distributions in multiwire chambers. 4: Empirical formula for small anode - cathode separation. *Nucl. Instrum. Meth.*, A270:602–603, 1988.

[MCC$^+$07] C. Mironov, M. Castro, P. Constantin, G. J. Kunde, and R. Vogt. Probing the quark-gluon plasma at the LHC with Z0-tagged jets in CMS. *CMS Conference Report*, 2007. To be published in Int. J. of Mod. Phys. E (draft).

[McL03] Larry McLerran. Rhic physics: The quark gluon plasma and the color glass condensate: 4 lectures. 2003. arXiv: hep-ph/0311028.

[MG07] Ginés Martinez Garcia. ALICE potential for heavy-flavour physics. 2007. arXiv: nucl-ex/0702053.

[MRST00] A. D. Martin, R. G. Roberts, W. J. Stirling, and R. S. Thorne. Parton distributions and the LHC: W and Z production. *Eur. Phys. J.*, C14:133, 2000. arXiv: hep-ph/9907231.

[MS86] T. Matsui and H. Satz. J/ψ suppression by quark-gluon plasma formation. *Phys. Lett.*, B178:416, 1986.

[MS99] G. Miu and T. Sjöstrand. W production in an Improved Parton-Shower Approach. *Phys. Lett. B*, 449:313, 1999. arXiv: hep-ph/9812455.

[Mue99] Alfred H. Mueller. Small-x physics, high parton densities and parton saturation in QCD. 1999. arXiv: hep-ph/9911289.

[MV94] Larry D. McLerran and Raju Venugopalan. Gluon distribution functions for very large nuclei at small transverse momentum. *Phys. Rev.*, D49:3352–3355, 1994. arXiv: hep-ph/9311205.

[Nob] All nobel laureates in physics. http://nobelprize.org/nobel_prizes/physics/laureates/.

[Oll92] Jean-Yves Ollitrault. Anisotropy as a signature of transverse collective flow. *Phys. Rev.*, D46:229–245, 1992.

[P^+06] P. Pillot et al. J/ψ production in indium-indium collisions at SPS energies. *AIP Conf. Proc.*, 806:279–285, 2006.

[Pei07] Stéphane Peigné. private communication, 2007.

[PMPC07] Stéphane Peigné, Ginés Martinez, Andre Peshier, and Zaida Conesa. Work in progress, 2007.

[Pol73] H. David Politzer. Reliable perturbative results for strong interactions? *Phys. Rev. Lett.*, 30:1346–1349, 1973.

[PV98] Arthur M. Poskanzer and S. A. Voloshin. Methods for analyzing anisotropic flow in relativistic nuclear collisions. *Phys. Rev.*, C58:1671–1678, 1998.

[S^+02] T. Sjöstrand et al. PYTHIA 6.2 physics and manual. arXiv: hep-ph/0108264, 2002.

[S^+07] D. Stocco et al. Work in progress, 2007.

[Sat06] Helmut Satz. Colour deconfinement and quarkonium binding. *J. Phys.*, G32:R25, 2006. arXiv: hep-ph/0512217.

[Sat07] Helmut Satz. Quarkonium binding and dissociation: The spectral analysis of the QGP. *Nucl. Phys.*, A783:249–260, 2007. arXiv: hep-ph/0609197.

[Sch94] M. Schmelling. The method of reduced cross-entropy. a general approach to unfold probability distributions. *N.I.M. A*, 340:400–412, 1994.

[Sch99] K. Schindl. The injector chain for the LHC. 1999. Given at 9th LEP Performance Workshop, Chamonix, France, 26-29 Jan 1999.

[Sco07] E. Scomparin. J/ψ production in In In and p A collisions. 2007.

[Shu05] Edward V. Shuryak. What RHIC experiments and theory tell us about properties of quark-gluon plasma? *Nucl. Phys.*, A750:64–83, 2005.

[Squ79] E J Squires. The bag model of hadrons. *Reports on Progress in Physics*, 42(7):1187–1242, 1979.

[SVR07] D. Stocco, E. Vercellin, and R.Guernane. Quarkonia detection with the ALICE muon spectrometer in pp collisions at $\sqrt{s}$ =14 TeV. *ALICE Internal Note*, 2007. ALICE-INT-2007-002.

[SW03] Carlos A. Salgado and Urs Achim Wiedemann. Calculating quenching weights. *Phys. Rev.*, D68:014008, 2003. arXiv: hep-ph/0302184.

[TCSG05] A. Tricoli, A. M. Copper-Sarkar, and C. Gwenlan. Uncertainties on W and Z production at LHC. *arXiv: hep-ex/0509002*, 2005.

[The94] R. L. Thews. Formation time scales for quarkonia in a deconfining medium. 1994. arXiv: hep-ph/9409209.

[TM06] R. L. Thews and M. L. Mangano. Momentum spectra of charmonium produced in a quark-gluon plasma. *Phys. Rev.*, C73:014904, 2006. arXiv: nucl-th/0505055.

[Tou07] A. Tournaire. Dimuon parameters geometry-envelopes-positions. Technical report, SUBATECH, 2007. EDMS id 335328: ALI-DIS-SPC-0002.

[Vog99] R. Vogt. Relation of hard and total cross sections to centrality. *nucl-th*, (9903051), 1999.

[Vog01] R. Vogt. Shadowing effects on vector boson production. *Phys. Rev. C*, 64:044901, 2001. arXiv: hep-ph/0011242.

[Vog02] R. Vogt. Testing nuclear shadowing effects on quark distributions at high Q^2. Talk given at 2002 CERN Workshop on Hard Probes in Heavy Ion Collisions at the LHC, 2002.

[WAH+57] C. S. Wu, E. Ambler, R. W. Hayward, D.D. Hoppes, and R. P. Hudson. Experimental test of parity conservation in beta decay. *Phys. Rev.*, 105(4):1413, 1957.

[Wil05] W. S. C. Williams. *Nuclear and Particle Physics*. Oxford Science Press, 2005.

[WS98] T. Wibig and D. Sobczynska. Proton-nucleus cross section at high energies. *J. Phys. G: Nucl. Part. Phys.*, 24:2037–2047, 1998. PII: S0954-3899(98)94375-4.

[Y+06] Yao et al. Review of Particle Physics. *J. Phys. G*, 33, 2006.

[Yer05] F. Yermia. private communication, 2005.

[Z+03a] A. Zinchenko et al. Development of the Kalman filter for tracking in the forward muon spectrometer of ALICE. *ALICE Internal Note*, 2003. ALICE-INT-2003-002.

[Z+03b] A. Zinchenko et al. A new approach to cluster finding and hit reconstruction in muon chambers of ALICE. *ALICE Internal Note*, 2003. ALICE-INT-2003-006.

Index

Performance of the ALICE muon spectrometer. Weak boson production and measurement in heavy-ion collisions at LHC.

Zaida Conesa del Valle

Resum

La QCD en xarxa prediu una transició d'una fase hadrònica a una fase de Plasma de Quarks i Gluons, QGP, per a temperatures superiors a 10^{13} K. Les col·lisions d'ions pesants han estat proposades per tal de recrear-la al laboratori. Amb aquest objectiu, el LHC proporcionarà col·lisions Pb-Pb a 5.5 TeV/u, i l'experiment ALICE permetrà explorar-les. En particular, l'espectròmetre de muons d'ALICE permetrà investigar les sondes muòniques (quarkonia, bellesa oberta,...). En aquest document es discuteixen les característiques de funcionament del detector per mesurar muons i dimuons. S'empra una tècnica de factorització per tal de separar les diverses contribucions a l'eficiència global. Els resultats indiquen que el detector hauria d'ésser capaç de mesurar muons fins a $p_T \sim 100$ GeV/c amb una resolució entorn del 10%. Mostrem que els bosons febles podran ésser mesurats per primer cop en les col·lisions d'ions pesants. La producció de W i Z serà sondejada per la distribució de muons simples en p_T i la massa invariant de dimuons. Com que la zona intermitja de p_T de 5-25 GeV/c estarà majoritàriament poblada per muons dels decaïments de quarks b i c, els càlculs de pèrdua d'energia mostren que l'espectre de muons simples podria ésser suprimit per un factor 2-4 en les col·lisions Pb-Pb 0-10% més centrals a 5.5 TeV. D'altra banda, per $p_T > 35$ GeV/c els decaïments dels bosons febles són predominants, i no s'espera cap supressió. Les estimacions indiquen que el punt de creuament entre els muons de b i W disminuirà en p_T de 5 a 7 GeV/c en les col·lisions Pb-Pb 0-10% més centrals a 5.5 TeV.

Paraules clau: Plasma de Quarks i Gluons, col·lisions d'Ions Pesants, LHC, ALICE, Espectròmetre de muons, Bosons Febles, Funcionament del detector.

Resumen

La QCD en red predice una transición de una fase hadrónica a una fase de Plasma de Quarks y Gluones, QGP, para temperaturas superiores a 10^{13} K. Las colisiones de iones pesados han sido propuestas para recrearla en el laboratorio. Con tal objectivo, el LHC proporcionará colisiones Pb-Pb a 5.5 TeV/u, y el experimento ALICE permitirá explorarlas. En particular, el espectrometro de muones de ALICE permitirá investigar las sondas muónicas (quarkonia, belleza abierta,...). En este documento se discuten las características de funcionamento del detector para medir muones y dimuones. Se utiliza una técnica de factorización para separar las diversas contribuciones a la eficiencia global. Los resultados indican que el detector debería ser capaz de medir muones hasta un $p_T \sim 100$ GeV/c con una resolución entorno del 10%. Mostramos que los bosons débiles podran ser medidos por primera vez en las colisiones de iones pesados. La producción de W y Z será sondeada por la distribución de muones simples en p_T y la massa invariante de dimuones. Como la zona intermedia de p_T de 5-25 GeV/c estará mayoritariamente poblada por muones de los decaimientos de quarks b y c, los cálculos de pérdida de energía muestran que el espectro de muones simples podría ser suprimido por un factor 2-4 en las colisiones Pb-Pb 0-10% más centrales a 5.5 TeV. Por otro lado, para $p_T > 35$ GeV/c los decaimientos de los bosons débiles son predominantes, y no se espera ninguna supresión. Las estimaciones indican que el punto de cruce entre los muones de b y W disminuirá en p_T de 5 a 7 GeV/c en las colisiones Pb-Pb 0-10% más centrales a 5.5 TeV.

Palabras llave: Plasma de Quarks y Gluones, colisiones de Iones Pesados, LHC, ALICE, Espectrómetro de muones, Bosons Débiles, Funcionamento del detector.

Performance of the ALICE muon spectrometer. Weak boson production and measurement in heavy-ion collisions at LHC.

Zaida CONESA DEL VALLE

Abstract

Lattice QCD predicts a transition from a hadronic phase to a Quark Gluon Plasma phase, QGP, for temperatures above 10^{13} K. Heavy-ion collisions are proposed to recreate it in the laboratory. With such a purpose, the LHC will provide Pb-Pb collisions at 5.5 TeV/u, and the ALICE experiment will permit to explore them. In particular, the ALICE muon spectrometer will permit to investigate the muon related probes (quarkonia, open beauty,...). The expected apparatus performances to measure muons and dimuons are discussed. A factorization technique is employed to unravel the different contributions to the global efficiency. Results indicate that the detector should be able to measure muons up to $p_T \sim 100$ GeV/c with a resolution of about 10%. We show that weak bosons production could be measured for the first time in heavy-ion collisions. Single muon p_T and dimuons invariant mass distributions will probe W and Z production. As mainly muons from b- and c-quarks decays will populate the intermediate-p_T of 5-25 GeV/c, heavy quark in-medium energy loss calculations indicate that the single muon spectra would be suppressed by a factor 2-4 in the most central 0-10% Pb-Pb collisions at 5.5 TeV. However, for $p_T > 35$ GeV/c the weak boson decays are predominant, and no suppression is expected. Estimations indicate that the b- and W-muons crossing point shifts down in transverse momenta by 5 to 7 GeV/c in the most central 0-10% Pb-Pb collisions at 5.5 TeV.

Keywords: Quark Gluon Plasma, Heavy Ion collisions, LHC, ALICE, Muon spectrometer, Weak bosons, Detector performance.

Résumé

La QCD sur réseau prédit la transition d'une phase hadronique vers le Plasma de Quarks et Gluons (PQG) pour des températures au-dessus de 10^{13} K. Pour le recréer en laboratoire, des collisions d'ions lourds ont été proposées. Dans cette optique, le LHC produira des collisions Pb-Pb à 5.5 TeV/u, qui seront étudiées notamment auprès de l'expérience ALICE. En particulier, son spectromètre à muons permettra d'examiner les sondes muoniques (quarkonia, beauté ouverte, ...). Les performances attendues de ce dispositif pour mesurer des muons et des dimuons sont ici discutées. Des techniques de factorisation sont employées pour différencier les contributions à l'efficacité globale. Les résultats indiquent que le détecteur devrait être capable de mesurer des muons jusqu'à $p_T \sim 100$ GeV/c avec une résolution proche de 10%. On montre que la production des bosons faibles pourra être mesurée pour la première fois dans des collisions d'ions lourds. Les distributions de muons simples en p_T et de la masse invariante des dimuons sonderont le W et le Z. Comme les muons issus des décroissances de quarks b et c peupleront principalement le domaine intermédiare en p_T de 5-25 GeV/c, les calculs de perte d'énergie des quarks lourds dans le milieu indiquent que le spectre devrait être supprimé d'un facteur 2-4 dans les collisions Pb-Pb les plus centrales 0-10% à 5.5 TeV. Néanmoins, pour $p_T > 35$ GeV/c la production des bosons faibles predomine, et aucune suppression n'est attendue. Des estimations indiquent que le point de croisement entre des muons issus de b et de W diminuera en p_T de 5 à 7 GeV/c dans les collisions Pb-Pb les plus centrales 0-10% à 5.5 TeV.

Mots clé: Plasma de Quarks et de Gluons, Collisions d'Ions Lourds, LHC, ALICE, Spectromètre à muons, Bosons faibles, Performances du détecteur.